Inaugural-Dissertation

zur
Erlangung der Doktorwürde
der
Naturwissenschaftlich-Mathematischen Gesamtfakultät
der
Ruprecht-Karls-Universität
Heidelberg

vorgelegt von

Matthias Klinger

aus Magdeburg

Tag der mündlichen Prüfung: _____

Variational Methods for the Estimation of Transport Fields with Application to the Recovery of Physics-Based Optical Flows Across Boundaries

Betreuer: Prof. Dr. Dr. h. c. R. Rannacher
Priv.-Doz. Dr. C. Garbe

Abstract

In this thesis we develop a method for the estimation of the flow behaviour of an incompressible fluid based on observations of the brightness intensity of a transported visible substance which does not influence the flow. The observations are given in a subregion of the flow as a sequence of discrete images with in- and outflow across the image boundaries. The resulting mathematical problem is ill-posed and has to be regularised with information of the underlying fluid flow model.

We consider a constrained optimisation problem, namely the minimisation of a tracking type data term for the brightness distribution and a regularisation term subject to a system of weakly coupled partial differential equations. The system consists of the time-dependent incompressible Navier-Stokes equations coupled by the velocity vector field to a convection-diffusion equation, which describes the transport of brightness patterns in the image sequence.

Due to the flow across the boundaries of the computational domain we solve a boundary identification problem. The usage of (strong) Dirichlet boundary controls for this purpose leads to theoretical and numerical complications, so that we will instead use Robin-type controls, which allow for a more convenient theoretical and numerical framework. We will prove well-posedness and investigate the functionality of the proposed approach by means of numerical examples. Furthermore, we discuss the connection to Dirichlet-control problems, e. g. the approximation of Dirichlet-controls by the so-called penalised Neumann method, which is based on the Robin-type controls for a varying penalty parameter.

We will show via numerical tests that Robin-type controls are suitable for the identification of the correct fluid flow. Moreover, the examples indicate that the underlying physical model used for the regularisation influences the flow reconstruction process. Thus appropriate knowledge of the model is essential, e. g. the viscosity parameter. For a time-independent example we will present a heuristic, which, beside the boundary identification, automatically evaluates the viscosity in case the parameter is unknown.

The developed physics-based optical flow estimation approach is finally used for the data set of a prototypical application. The background of the application is the approximation of horizontal wind fields in sparsely populated areas like desert regions. A sequence of satellite images documenting the brightness intensity of an observable substance distributed by the wind (e. g. dust plumes) is thereby assumed to be the only available data. Wind field information is for example needed to simulate the distribution of other, not directly observable, substances in the lower atmosphere. For the prototypical example we compute a high quality reconstruction of the underlying fluid flow by a (discrete) sequence of consecutive spatially distributed brightness intensities. Thereby, we compare three different models (heat equation, Stokes system and the original fluid flow model) in the reconstruction process and show that using as much model knowledge as possible is essential for a good reconstruction result.

Zusammenfassung

In dieser Arbeit entwickeln wir eine Methode zur Schätzung des Strömungsverhaltens eines inkompressiblen Fluids anhand von Beobachtungen der Helligkeitsintensität eines transportierten sichtbaren Stoffes, welcher die Strömung nicht beeinflusst. Die Beobachtungen in einem Teilgebiet der Strömung sind gegeben als eine Folge diskreter Bilder, mit Ein- und Ausströmung über die Bildränder. Das resultierende mathematische Problem ist schlecht gestellt und muss deshalb regularisiert werden. Wir verwenden zur Regularisierung Informationen des zugrunde liegende physikalische Modell.
Wir betrachten ein restringiertes Optimierungsproblem, das aus der Minimierung eines Kostenfunktionals mit einem Tracking-Datenterm für die Helligkeitsintensität und einem Regularisierungsterm besteht und ein System schwach gekoppelter partieller Differentialgleichungen als Nebenbedingung hat. Das System besteht aus den instationären inkompressiblen Navier-Stokes-Gleichungen, die durch das Geschwindigkeitsfeld an eine instationäre Konvektions-Diffusions-Gleichung gekoppelt ist, welche den Transport von Helligkeitsmustern in der Bildfolge beschreibt.
Aufgrund der Überströmung an den Rändern des Rechengebiets handelt es sich um ein Randidentifikationsproblem. Die Verwendung von (starken) Dirichlet-Randkontrollen für diesen Zweck führt zu theoretischen und numerischen Schwierigkeiten, sodass wir stattdessen Robin-artige Kontrollen verwenden, die einen passenderen theoretischen und numerischen Rahmen bieten. Wir beweisen die Wohlgestelltheit und untersuchen anhand von numerischen Beispielen die Funktionalität des vorgeschlagenen Ansatzes. Des weiteren diskutieren wir die Verbindung zu Dirichlet-Kontrollproblemen durch die sogenannte "penalised Neumann"-Methode, die auf Robin-artigen Kontrollen mit einem variierenden Strafparameter basiert.
Wir werden zeigen, dass durch die Robin-artigen Kontrollen adäquate Fluidströmungen identifiziert werden können. Darüber hinaus zeigen die Beispiele, dass das in der Regularisierung verwendete zugrunde liegende physikalische Modell den Rekonstruktionsprozess beeinflusst. Daher ist adäquates Modellwissen entscheidend, z. B. über den Viskositätsparameter. Für ein zeitunabhängiges Beispiel werden wir eine Heuristik vorstellen, die neben der Randidentifikation auch noch automatisch den Viskositätsparameter bestimmt, im Fall, dass der Parameter unbekannt ist.
Der entwickelte Ansatz für einen physikalischen optischen Fluss-Schätzer wird am Ende auf den Datensatz einer prototypischen Anwendung angewendet. Der Hintergrund der Anwendung ist die Approximation horizontaler Windfelder in dünn besiedelten Gebieten, wie zum Beispiel Wüsten. Eine Folge von Satellitenbildern, welche die Verteilung einer beobachtbaren Substanz durch deren Helligkeitsintensität dokumentiert (z. B. Sandstaubfahne) wird dabei als einzige verfügbare Datenquelle angenommen. Die Windinformationen werden beispielsweise für die Simulation der Verteilung anderer, nicht sichtbarer, Schadstoffe in der erdnahen Atmosphäre benötigt. Für das prototypische Beispiel können wir eine qualitativ hochwertige Rekonstruktion des Strömungsfelds aus einer Folge (diskreter) aufeinander folgender, örtlich verteilter Helligkeitsintensitäten berechnen. Dabei vergleichen

wir drei unterschiedliche Modelle (Wärmeleitungsgleichung, Stokes-Gleichungen und das ursprüngliche Modell) im Rekonstruktionsprozess und zeigen, dass die Verwendung von möglichst viel Modellwissen entscheidend für eine gute Rekonstruktion ist.

Contents

1. Introduction

1.1. Motivation

In the past fifty years, the investigation of complex fluid flows received more and more interest in a wide range of different scientific areas, e. g. fluid mechanics or meteorological flows. The analysis of the considered flows uses measurement and simulation techniques. However, for some realistic fluid flows neither good direct measurements can be performed, nor are appropriate data (boundary conditions, initial values etc.) available for direct numerical simulations. This is the case, e. g., for meteorological flows, for which, especially in desert or maritime regions, no dense measurement grids are available.

Nevertheless, we can observe atmospheric flows indirectly by aerosols, which are transported by the wind like a tracer. Desert dust is an example for such an aerosol, which is uplifted in deserts and then transported over great distances (Tegen et al. [98]). Assuming a straightforward connection between the mean dust load density in a vertical column and the corresponding aerosol optical thickness, the movement of such airborne dust plumes can be observed by satellite remote sensing techniques (Schepanski et al. [94] and the literature cited therein). Moreover, the atmospheric wind system is transporting other substances like harmful pollutants, which possibly cannot be observed directly. We assume that we are interested in the temporal evolution of the spatial distribution of such a pollutant in a certain domain of interest, which is an artificial truncation of the original flow domain. It is questionable if we can use a temporally sparse sequence of intensity functions (sequence of images) documenting the movement of dust plumes to reconstruct a reliable fluid flow field, which describes the non observable pollutant transport accurately. However, the complexity of this sophisticated real world application lies beyond the scope of this thesis, so that we will consider a simplified prototypical setting, which focuses on fundamental aspects for optimisation problems with physical models as constraints and the numerical treatment of such mathematically complex problems.

A first idea of the approximation of the underlying atmospheric flow is to estimate the so called optical flow field from the given image sequence. Image processing tools like variational optical flow estimation techniques were developed over the last decades to recover flow behavior of passive tracers like dye or particles in a fluid flow (e.g. Heitz et al. [51], Liu et al. [71]). These techniques could also be used for the analysis of satellite observation of meteorological flows (for example Corpetti et al. [25], Héas et al. [49], Papadakis et al. [83]). The fundamental equation in this context is the so called "physics-based optical flow" equation (Heitz et al. [51]), which describes the change of brightness intensity in a sequence of consecutive images, caused by a transport field which is directly correlated to an

underlying fluid flow. The mathematical structure of this equation is a parabolic partial differential equation (PDE), more precisely a convection-diffusion equation. The estimation of an unknown transport field based on this equation is an ill-posed problem (inverse problem theory: cf. Engl et al. [31]) and requires the use of regularisation techniques, like for example the famous Tikhonov regularisation.

Thanks to the progression of computational power after the turn of the millennium a next step was to design methods based on PDE-constrained optimisation, also called "optimal control", formulations for the recovering of the optical flow. These involved methods constitute also the framework of the present thesis. Therefore we mention two fundamental directions of optimal control based optical flow estimation. The first one uses the (physics-based) optical flow equation as a side condition to avoid filtering of the given image data (approximating the spatial and temporal derivative) and decouples the sampling rate of the image sequence and the time step size of the used numerical time stepping scheme (cf. Borzí et al. [16], Chen et al. [22], [23]), which stabilses the numerical process. The other approach treats the underlying physical model as a PDE-constraint for an appropriate regularisation of the optimisation problem (cf. Ruhnau et al. [91], [92]).

We suggest in this work a combination of these two directions. First, because we want to apply the physical model and second, we want to take into account that the given image data is only available with a sparse temporal resolution. As side condition for our PDE-constrained optimisation problem we obtain a weakly coupled combined model of the physics-based optical flow equation describing the change of the intensity function of the tracer and the Navier-Stokes equations describing the fluid flow.

Another fundamental aspect our method has to deal with is the assumption that the given images are only truncations of more complex flow configurations. Thus the fluid moves across the image boundaries and transports also the observed tracer over these boundaries. We will present a method which is also able to recover the flow of the tracer across the image domain boundaries. Therefore we use so called "boundary controls" in our PDE-constrained optimisation problems, which represent distributed functions on the boundary. The aim is then to identify appropriate functions, which yield the expected movement of the tracer.

The treatment of the boundary controls, especially the use of Dirichlet controls, is widely considered in the optimal control literature (cf. Fursikov et al. [38], [39], Gunzburger et al. [45], Ito et al. [58]), since it arouses some complications. We will discuss the use of Dirichlet controls and their approximation by Robin-type controls in the case of convection-diffusion problems and for the Navier-Stokes equations (cf. Hou et al. [55], [56]). In the end we will apply these concepts of boundary controls for the combined approach and suggest a novel approach for physically based image interpolation and flow estimation with respect to in- and outflow of the observed tracer across the boundaries. We will develop the mathematical theory for the resulting sophisticated PDE-constrained optimisation problem and solve a bunch of prototypical examples numerically by a Newton-type method. Based on these examples we will also discuss heuristics to choose an appropriately small regularisation parameter for the identification process in an automatic way. Moreover,

we will suggest a segregation loop which yields, besides the boundary conditions, also an estimate for the Reynolds-number of the fluid flow model.

The outline of the work is as follows:

The **first chapter** presents the description of the problem. We will discuss optical flow and physics-based optical flow and present prototypical applications. Afterwards, we introduce some common optical flow estimation techniques and sketch how we combine them to a novel approach, which is well suited for the prototypical examples.

In the **second chapter** we discuss the standard theory of the equations which are used throughout this thesis. Therefore we briefly introduce the used notation. Furthermore, we present the classical existence and uniqueness theory for time-dependent convection-diffusion equations and the time-dependent Navier-Stokes system in two space dimensions. We also dedicate a section to the discussion of the purely linear transport equation, since this equation is the fundamental optical flow equation in image processing. The last section provides the theory for a system of equations weakly coupling the Navier-Stokes equation to a convection-diffusion equation for a passive tracer by the fluid flow vector field.

The **third chapter** is devoted to the numerical treatment of our model equations. Since we solve our time-dependent problems with Rothe's method, we start with the time discretisation. Afterwards, we discuss the spatial discretisation of the quasi-stationary problems arising in each time step. We will use standard bilinear finite elements on quadrilaterals. Then we specify the boundary conditions in a weak sense by a stabilised Robin approach. The next topic we have to consider is the use of transport stabilisation techniques in the case of convection dominance. Furthermore, the overhead needed for solving the Navier-Stokes system is described. The solution process of this nonlinear problem involves Newton's method. Moreover, we use a pressure stabilisation technique by local projections, since we have to fix the lack of inf-sup stability in the case of equal order approaches for the velocity components and the pressure. All presented techniques are also verified by numerical calculations of test examples. At the end of the chapter we combine all presented techniques to solve a test case for the weakly coupled system.

The **fourth chapter** deals with general PDE-constrained optimisation problems. We will first discuss the abstract theory of general optimisation problems with a linear time-dependent PDE constraint. The optimality conditions, among them the optimality system, are also mentioned. Based on the reduced approach we describe in the second part of the chapter a Newton-type algorithm to solve the discussed general optimisation problems. Here we have to represent the derivatives in the Newton algorithm by solutions of additional PDE problems. We will also briefly discuss the structure of these subproblems. The chapter relies essentially on the work of Becker [8], Meidner [77] and Vexler [102], since these three authors designed the software library RoDoBo [88], which was the basis for almost all calculations in this thesis.

In the **fifth chapter** we concretise the abstract setting from before for boundary control problems. While Neumann or Robin controls are easy to handle, Dirichlet controls are comparably difficult, since they require an appropriate choice of the control space. The space $H^{\frac{1}{2}}$ is the natural choice from the theoretical point of view, but it is hard to handle

the implementation of functions from this space from a computational point of view, since the use of the $H^{\frac{1}{2}}$-norm requires either the evaluation of complicated boundary integrals or the solution of additional problems increasing the computational complexity. We would therefore like to use L^2-controls, which are easy to implement. On the other hand L^2-traces have in general no H^1-extension into the domain Ω, although every H^1-function has a trace in $L^2(\partial\Omega)$. A way out of this dilemma is the use of the Dirichlet control problem with a very weak formulation of the original problem as side condition (cf. May et al. [76]). This leads in general to a well-posed formulations. However, this approach is also very sophisticated from the computational point of view. Fortunately there is a close connection between very weakly formulated Dirichlet control problems and Robin control problems. For the very simple case of the Poisson problem as side condition and a tracking type cost functional it can be shown that a solution sequence of the Robin-type approach converges to a solution of the very weakly formulated problem (cf. Belgacem et al. [13]). We will present the enhancement of this result to the time-dependent convection-diffusion equation and the linearised Navier-Stokes system (e. g. Oseen and Stokes). For the Navier-Stokes equations it becomes more sophisticated since we have no very weak L^2-solution for L^2-boundary data (cf. Farwig et al. [34], Marušic-Paloka et al. [75]). However, we will show that using the theoretically justified Robin boundary condition leads to reliable approximations of the original flow field, by presenting numerical calculations for a fluid flow in a backward facing step with a rough boundary.

The **sixth chapter** collects all developed techniques for the theoretical justification of a sophisticated optimisation problem with a weakly coupled PDE system, consisting of the Navier-Stokes system and a convection dominant convection-diffusion equation, as side condition. After formulating the problem correctly, we prove existence of at least one solution of the optimisation problem. In a second step we verify the method by means of a numerical example, where brightness patterns move across the boundary of the computational domain. The developed method is able to reconstruct an intensity function out of sparsely given observations of the intensity distribution.
By a further synthetic numerical test case we investigate quantitatively the numerical behaviour of the suggested approach. We will show that we can use the developed method to reconstruct drag and lift coefficients of a fluid flow in a benchmark channel, where only observations of the intensity functions are available and the flow field on the lower boundary is unknown, due to a unknown roughness of the original flow domain. In the context of a time-independent version of this example we discuss also a heuristic technique, which choose an appropriately small regularisation parameter in a homotopy-type method. Moreover, we show that knowledge of the underlying flow model (e. g. the Reynolds number) is essential for a good reconstruction result. However, with the appropriate geometry it is also possible to estimate the correct Reynolds number. We segregate both processes and end up with a method which is able to estimate both the model parameter and an appropriate boundary function. At the end of the chapter we consider a fully time-dependent example and present the functionality of our methodology for such a highly complex framework.

The final **seventh chapter** is devoted to the prototypical application oriented at the meteorological problem mentioned at the beginning of this motivation. The first objective is to combine the aspects from the synthetic examples of the last chapter in one comprehensive

example and to show that our method is able to deal with all complexities at once. The second and more important aspect is to compare the influence of the fluid flow model as regulariser. We will therefore consider the reconstruction with three different fluid models. The first one is the original model of the forward calculation. The second one is the linearised Stokes system. The third model is the simple heat equation, which in principle introduces only temporal and spatial regularity for the flow field. We will show by this comparison that the reconstruction quality is clearly influenced by using as much model knowledge as possible. Thus the large computational effort in case of the fully nonlinear physical model is justified.

1.2. Problem Description

In this section we will develop the problem under consideration. We will define the (physics-based) optical flow and present related prototypical examples, which we use later on for the validation of the developed methodologies.

1.2.1. Optical Flow

As optical flow we understand the velocity vector field, which describes the visible motion of photometric patterns in a sequence of consecutive images (cf. Horn et al. [54] or Heitz et al. [51]). It is possible to obtain information on the spatial arrangements of objects and their temporal change in an observed scenery by the change of photometric patterns representing these objects. Under several assumptions, such as uniform illumination of the scenery and nearly no reflectance of the objects, the brightness change is described by

$$\partial_t I + \boldsymbol{w} \cdot \nabla I = 0, \qquad \text{in } \Omega \times (0, T]. \tag{1.1}$$

This so called "optical flow equation" (also BCCE, "brightness change constraint equation") states that the total time derivative of the brightness intensity at each temporal and spatial point $(t, \boldsymbol{x})$ is zero, which means that the brightness is a conserved quantity. Thus the brightness value at a certain point $\boldsymbol{x}$ in the image $\mathcal{I}_k := I(\boldsymbol{x}, t_k)$ keeps constant along a trajectory on which the value is moved to the consecutive image $\mathcal{I}_{k+1} := I(\boldsymbol{x}, t_{k+1})$. In this context the two dimensional vector field $\boldsymbol{w}$ describing the transport is called the "optical flow field".

The function

$$I : \Omega \times [0, T] \to \mathbb{R}^+$$

described by the above equation is called (brightness) intensity function. As in several other publications we will treat this function as a continuous quantity for all our theoretical considerations, although the given data, the images, are of course discrete samples in space and time.

From the mathematical point of view equation (1.1) represents a hyperbolic PDE, which is known as linear transport equation.

The optical flow equation is used for very general brightness distributions observing any objects in a given scenery. However, our focus is on the observation of a passive tracer in a fluid flow. This concrete application is also discussed in the literature. An impressive application was given in the article of Papadakis et al. [83]. The authors present how imaging techniques can be used for the flow analysis of a cyclone, which was observed by an image sequence given by a satellite. Here the brightness intensity distribution of infrared images of the moving water clouds acts as a passive tracer and a direct connection between optical flow in the image sequence and the underlying physical flow is assumed.

A connection between fluid and related optical flow in an image sequence was also discussed in various other publications, where the authors developed the concept of the so called "physics-based optical flow equation". In the next subsection we will present this concept.

1.2.2. Physics-Based Optical Flow

Liu et al. [71] and Heitz et al. [51] as well as the literature cited therein give a good summary of the topic. The aim is to find a connection between the observed fluid flow and the optical flow, since it would be very promising to use optical flow methods to derive qualitatively and quantitatively good estimations of the fluid flow field.

During the last decade the optical flow equation (1.1) turned out not to be an accurate model for image-based fluid measurements. Liu et al. [71] developed models for a bunch of different fluid flow scenarios. One of these scenarios considers the transport of a passive scalar tracer by the underlying fluid flow. The passive scalar has the property of attenuating the wavelength of light rays transmitting through it. In case that the fluid itself is not light absorbing and the scalar does not change the fluid's density the authors derived the following equation

$$\partial_t g + \nabla_{x,y}(g\boldsymbol{u}_{x,y}) = \varepsilon\Delta_{x,y} g - c_B B(\Gamma_1, \Gamma_2), \qquad g = \ln\left(\frac{L}{L_0}\right)$$

for the radiance $L(x, y, t)$ which reaches the camera through the scalar. The vector field $\boldsymbol{u}_{x,y}$ represents the planar components of the three dimensional flow field. The term $B(\Gamma_1, \Gamma_2)$ indicates boundary conditions on the so-called control surfaces between which the fluid is moving. If the control surfaces are solid this term vanishes. In case of "virtual control surfaces" the boundary terms are negligible, if we have small relative velocities related to the distance between the control surfaces and the camera apparatus. The latter case occurs for satellite image observations of the lower atmosphere's wind system. Furthermore the connection between radiance and intensity function is given by

$$\ln\left(\frac{L}{L_0}\right) = \ln\left(\frac{I}{I_0}\right).$$

That means the brightness intensity is described by the following convection-diffusion equation

$$\partial_t I - \varepsilon\Delta I + \boldsymbol{w} \cdot \nabla I = 0, \qquad \text{in } \Omega \times (0, T],$$

with an optical flow field $\boldsymbol{w}$ which is directly related to the planar components of the fluid flow $\boldsymbol{u} = (u, v, w)^T$ in the following way

$$\boldsymbol{w} = c\boldsymbol{u}_{x,y}, \qquad \text{with } \boldsymbol{u}_{x,y} = (u, v)^T.$$

Often the mentioned connection between optical flow and fluid flow requires a very specific analysis of the real world application and even then further problems come up, such as model uncertainties in the flow model (e. g. the wind model for atmospheric flows) or the optical flow model (e. g. varying illumination of the images) or measurement errors. Since these aspects are beyond the scope of this thesis we will present prototypical examples, which on the one hand motivate interesting applications and on the other hand omit all uncertainties so that we can directly focus on the development of our methodology.

In connection to the real world application mentioned in the motivation we will concentrate on some fundamental problems in physics-based optical flow estimation. Our prototypical test cases should be designed in such a way that they exhibit these special problem structures.

The problems our method should deal with are the following:

i) The image sequence represents only an aperture of the original flow domain. Thus we have flow of intensity signals across the boundaries. The method must be able to recover the flow field at the boundary as well as the signal movement across the boundary.

ii) The sequence is assumed to be temporally sparse. Thus the method should be able to interpolate between consecutive images.

iii) Assuming the knowledge of an appropriate physical model for the fluid flow, our physics-based optical flow estimation process should be able to integrate this knowledge.

iv) We want to suggest a framework, which is flexible in terms of integrating further information (e. g. model information, measurements in parts of the domain or on parts of the boundary).

1.2.3. Synthetic Numerical Examples and Prototypical Applications

We present three examples. The first example concerns the interpolation aspect for a sparsely given image sequence. An essential advantage of our method is the possibility of interpolating an intensity signal across the computational boundary. For regularisation we already use a physical model, although it does not exhibit its positive effect on the estimation, due to the simplicity of the chosen original flow field.
In the second example, we consider a time-dependent (laminar) flow scenario, which is motivated by the standard benchmark channel (cf. Schäfer [93]) and a modification mentioned in Vexler [102]. Here the focus is on the application of the model for the regularisation and the possibility to estimate further indirectly observed quantities like the pressure function

and, through this, the drag and lift coefficients of an obstacle.
However, both examples will be used to verify the numerics behind the two main functionalities of the suggested approach, signal interpolation across the boundaries and the estimation of time-dependent boundary functions in a physically based framework.
Finally, a third prototypical example is oriented towards atmospheric flows, as mentioned in the motivation of this thesis. The aim is here to reconstruct the distribution of a not directly observable passive tracer (some kind of pollutant) by a given sequence of intensity functions documenting the movement of an observable passive tracer (dust plumes). This application will combine the aspects presented in the other two examples. Moreover, it has the advantage that it presents the flexibility to integrate different types of information in our method and it yields an idea for possible further interdisciplinary research. However, the main objective of this example is to emphasise that using appropriate model knowledge of the underlying fluid model leads to a clear improvement of the reconstruction results, which justifies the increased numerical effort of working with such nonlinear and time-dependent models. In the following, we briefly summarise the three examples.

First Example: Interpolation Across the Image Boundaries

Starting point for this example is the optical flow equation

$$\partial_t I + \boldsymbol{u} \cdot \nabla I = 0, \qquad \Omega \times (0, T].$$

By choosing appropriate data functions, this equation yields a space-time evolution $I(\boldsymbol{x}, t)$. We will generate a temporal sequence of intensity functions as given data, by setting $\mathcal{I}_k := I(\boldsymbol{x}, t_k)$. Thereby the temporal grid is sparse.

Figure 1.1 shows six intensity functions documenting the movement of a bulb signal in the domain $\Omega = (0, 1) \times (0, 1)$ on a certain time interval $[0, T]$. The bulb was moved by the solenoidal flow field

$$\boldsymbol{u}(\boldsymbol{x}, t) = \kappa(-y, x)^T.$$

We consider the following question:

Problem: *Assuming only the six images as given data, without any knowledge of the flow field, except that the vector field is divergence free, the aim is to reconstruct (interpolate) the movement of the signal on a finer resolution, of the time grid.*

The mathematical task behind this problem is to prescribe appropriate boundary data for the intensity function on the computational domain. Furthermore, we have to approximate a reliable vector field, which transports the signal throughout the domain also by the reconstruction of appropriate boundary conditions.

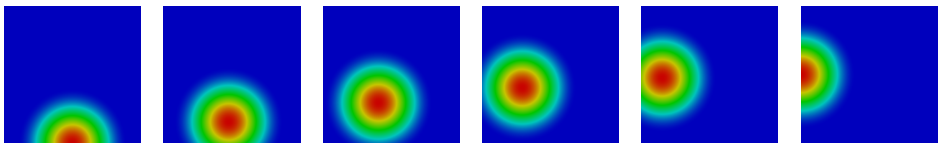

Figure 1.1. Intensity function sequence: $\hat{I} = (\mathcal{I}_k)_{k=1}^{6}$.

Second Example: Drag and Lift Estimation in a Channel with Unknown Roughness

In this numerical test the underlying fluid flow is described by the two dimensional time-dependent Navier-Stokes equations

$$\begin{aligned} \partial_t \boldsymbol{u} - \nu \Delta \boldsymbol{u} + \boldsymbol{u} \cdot \nabla \boldsymbol{u} + \nabla p &= \boldsymbol{f}, && \text{in } \Omega \times (0,T], \\ \nabla \cdot \boldsymbol{u} &= 0, && \text{in } \Omega \times (0,T], \end{aligned}$$

which are discussed in detail in the next chapter. We assume that no body forces ($\boldsymbol{f} = 0$) act on the fluid. Thus the whole flow is driven by the choice of the boundary conditions

$$\begin{aligned} B_I(\boldsymbol{u}; I, q_I) &= 0, && \partial\Omega \times (0,T], \\ B_{\boldsymbol{u}}(\boldsymbol{u}, \boldsymbol{q}_{\boldsymbol{u}}) &= 0, && \partial\Omega \times (0,T], \end{aligned}$$

with functions q_I and $\boldsymbol{q}_{\boldsymbol{u}}$, which have to be specified.

We assume a straightforward connection of the optical flow to the underlying fluid flow, that means it is directly proportional to the fluid velocity

$$\boldsymbol{w} = c\boldsymbol{u}.$$

Thus, the optical flow is described by the physics-based optical flow equation (cf. Heitz [51])

$$\partial_t I - \varepsilon \Delta I + \boldsymbol{w} \cdot \nabla I = 0.$$

Assuming that $\boldsymbol{w} = \boldsymbol{u}$ we end up with the following system of equations

$$\begin{aligned} \partial_t I - \varepsilon \Delta I + \boldsymbol{u} \cdot \nabla I &= 0, \\ \partial_t \boldsymbol{u} - \nu \Delta \boldsymbol{u} + \boldsymbol{u} \cdot \nabla \boldsymbol{u} + \nabla p &= 0, && \text{in } \Omega \times (0,T], \\ \nabla \cdot \boldsymbol{u} &= 0, \end{aligned} \tag{1.2}$$

which describes the evolution of the pressure p, the velocity field $\boldsymbol{u}$ and the brightness intensity function I. The system is weakly coupled by $\boldsymbol{u}$, that means $\boldsymbol{u}$ influences the physics-based optical flow equation without I influencing the Navier-Stokes system.

We want to emphasise that a mathematically correct statement requires also the choice of appropriate initial data. We postpone an accurate formulation and the discussion of the mathematical theory of the problem to the next chapter.

We consider a benchmark channel Ω_{Ben} consisting of an inflow boundary on the left and outflow boundary on the right and rigid walls on the top and the bottom of the channel. In

the front segment of the channel an obstacle with rigid boundary is fixed. In this channel, an incompressible fluid is moving from the left to the right transporting two tracer signals twisting around the obstacle. In general, walls in channels are not smooth so that we assume an unknown roughness at the lower boundary. The question is then the following:

Problem: *Reconstruct the drag and lift coefficients of the obstacle only by a given (temporally sparse) sequence of brightness functions I_k observing the passive tracer at discrete time points.*

For the evaluation of the two quantities of interest we need to reconstruct the velocity vector field of the fluid and the corresponding pressure function.

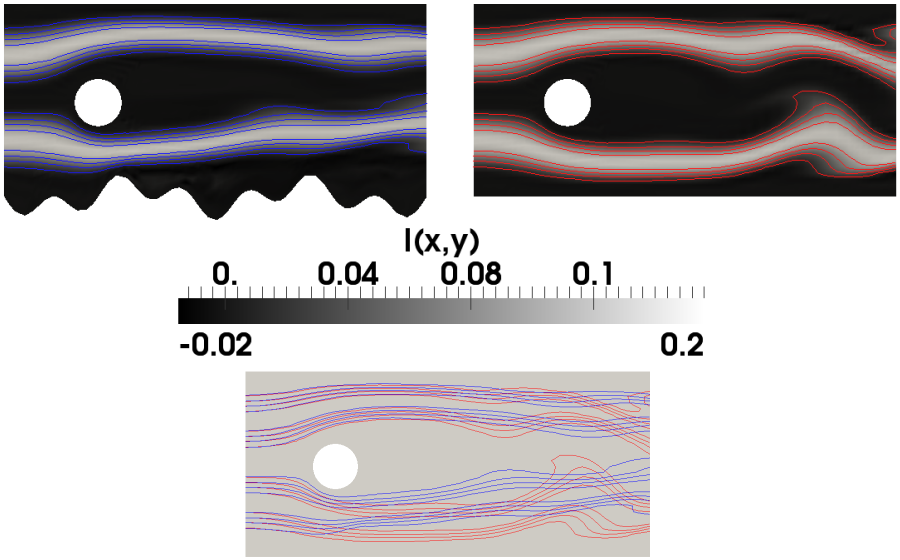

Figure 1.2. Brightness function $I(\boldsymbol{x}, t)$ of a passive tracer transported by a time-dependent incompressible fluid flow visualised at a fixed time point. Top left: Rough lower boundary. Top right: Even wall on the lower boundary. Bottom picture: Overlap of the contour lines of the both brightness functions (blue: rough, red: smooth).

Working with a direct numerical simulation is not possible, due to the fact that the roughness of the lower boundary is assumed to be unknown. The flow in a channel with a flat bottom wall leads to a completely different flow behaviour. This is indicated by the intensity functions in a rough and a smooth channel visualised in Figure 1.2.

We will introduce an artificial smooth boundary at the bottom of the computational domain and use physics-based optical flow estimation techniques to reconstruct the desired quantities. The usage of the fluid model, described by the system of equations (1.2), will be crucial for the reconstruction to achieve both a reliable flow field and pressure function.

Third Example: Reconstruction of a Pollutant

As mentioned in the motivation of this thesis, an interesting idea is to use physics-based optical flow estimation to compute a reliable vector field for ground-based atmospheric flows in deserts only by using intensity function sequences obtained by satellite remote sensing.

As an example we take the country Egypt, whose territory is almost completely located in the desert ($> 95\%$). We assume that the wind system can only be measured in certain small areas as the Nil valley in the east and the shore line to the Mediterranean sea in the north. In the rest of the country the measurement of the wind system is not possible. Nevertheless, a certain knowledge about the wind system in deserts could be of interest, since the wind potentially distributes harmful substances into populated areas. An example for such a substance could be residues of fertilisers used in intensive industrial agriculture projects in the south of the country in the middle of the desert. By satellite remote sensing we can obtain information of a "natural" passive tracer, which is transported by the wind system, namely the desert sand dust. The dust plumes have a so-called optical thickness (cf. Schepanski et al. [94]), which influences the brightness intensities in the infrared satellite images.

However, formulating and solving a real world application like this would require a whole team of interdisciplinary scientists.

It should be demonstrated by the following prototypical example that the developed techniques are able to cope with several aspects of this fictitious application.

Therefore we assume that the ground-based atmospheric wind system is described by the Navier-Stokes equations, and neglect the influence of temperature, humidity, vertical flows etc. Considering appropriate physical units it will turn out that the kinematic viscosity is very small and thus we work in principle with a time-dependent Euler system, which is then numerically stabilised for the solution process.
Since a connection between the dust plumes and their brightness intensity in the satellite images is a topic for research by itself, for simplicity we assume again a direct connection to the intensity function of our passive tracer. Hence, we will work with the system (1.2), with a very small ν, to generate an intensity function sequence for our artificial sand problem. We visualised the solution of a forward calculation in a quadratic aperture (cf. Figure 1.3), which will be specified later.

Although the simplifications are significant in comparison to the real world problem the main aspects like flow across the boundaries and also the application of model knowledge can be investigated in this setting.

While the first row of pictures in Figure 1.3 shows the intensity distribution and the corresponding flow field at three different time points, the second row indicates the distribution of the concentration $c(\boldsymbol{x}, t)$ of a pollutant, which has its source in the lower half of the computational domain.

For this setting we formulate the following problem:

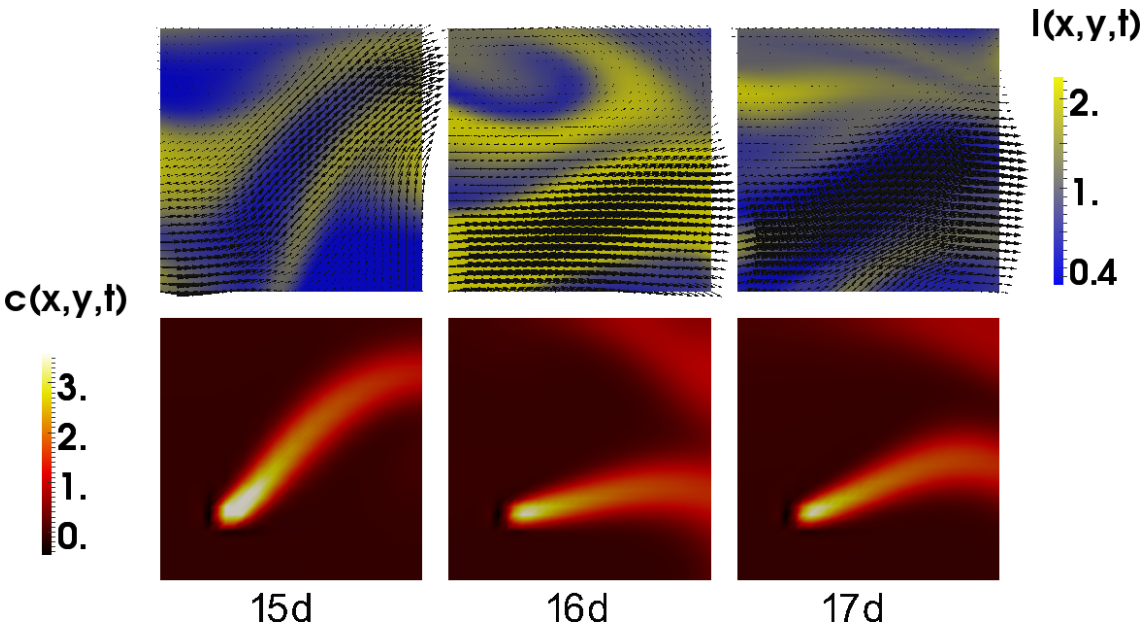

Figure 1.3. From left to right: $t = 15d$, $t = 16d$ and $t = 17d$. Upper row: Blue-yellow plot indicates the dust distribution. The black arrows visualise the transport vector field. Lower row: Distribution of a pollutant also transported by the above indicated vector field.

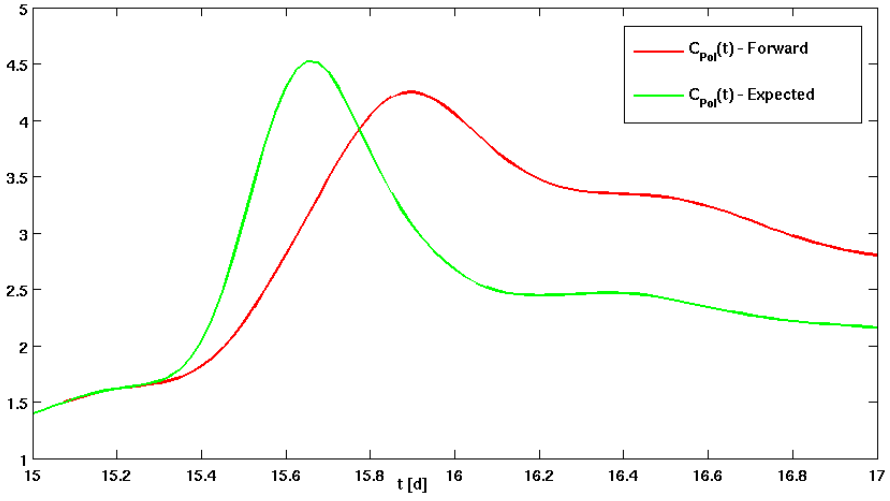

Figure 1.4. Temporal evolution of the mean value for the concentration c in a domain of interest Ω_{Det}. Green curve: Expected value. Red curve: Forward calculation without boundary identification.

Problem: *Reconstruct the temporal evolution of the mean value of the pollutant in a certain subdomain of interest Ω_{Det} by a (temporally sparse) sequence of intensity functions.*

The significant influence of the transport field to the mean value of the concentration $c(\boldsymbol{x}, t)$ can be observed in Figure 1.4. The red curve shows a forward calculation, where no appropriate boundary functions were available, while the green curve shows the evolution with the expected boundary functions.

1.3. Variational Optical Flow Estimation Techniques

In this subsection, we present the common state of the art of optical flow estimation techniques and develop our approach which is classified into the common techniques. The most famous methods for estimating the optical flow are the Lucas and Kanade method (cf. Lucas et al. [73]) and the Horn and Schunck method (cf. Horn et al. [54]). Both methods were developed in the 1980s. In the past 30 years they have been enhanced to a certain extent. For a broad overview see Beauchemin et al. [6], Barron et al. [5] or the monograph of Jähne [60]. We want to introduce the Horn and Schunck approach briefly ,since it is a variational based technique, which represents the basic structure for the optimisation problems presented later.

The Horn and Schunck Method

The Horn and Schunck method is based on the minimisation of the following functional

$$J_{HS}(\boldsymbol{u}) = \sum_{k=1}^{N} \left(\|\partial_t \hat{I}(t_k) + \boldsymbol{u}(t_k) \cdot \nabla \hat{I}(t_k)\|^2_{L^2(\Omega)} + \frac{\alpha}{2} \|\nabla \boldsymbol{u}(t_k)\|^2_{L^2(\Omega)} \right), \tag{1.3}$$

whereas the terms $\partial_t \hat{I}(t_k)$ and $\nabla \hat{I}(t_k)$ must be approximated by the given image sequence $(\mathcal{I}_k)_{k=1}^N$. Usually one uses finite differences for the latter. With the temporal and spatial sample rates dt, dx and dy, we have for example

$$\begin{aligned}
\partial_t \hat{I} &= \frac{1}{dt} \left(\mathcal{I}(i, j, t_k + dt) - \mathcal{I}(i, j, t_k) \right), \\
\partial_x \hat{I} &= \frac{1}{2dx} \left(\mathcal{I}(i + dx, j, t_k) - \mathcal{I}(i - dx, j, t_k) \right), \\
\partial_y \hat{I} &= \frac{1}{2dy} \left(\mathcal{I}(i, j + dy, t_k) - \mathcal{I}(i, j - dy, t_k) \right).
\end{aligned}$$

The index k indicates a discrete time point $t_k \in [0, T]$ at which the brightness intensity function, the image, is given.

We want to emphasise that large spatial or temporal derivatives lead to possibly bad approximations of the image derivatives. Thus, heuristic 'Coarse-to-Fine' motion estimation methods (cf. Ruhnau [90], Brox et al. [21]) were developed in the last decades. Unfortunately, estimation errors on a coarse resolution are propagated to the finest resolution and

therefore we have no guarantee for good approximations of the optical flow field. We will later on present a technique, which avoids the approximation of derivatives, but first we discuss the functionality of the two terms in the cost functional (1.3).

Remark 1.1 (Data Term).
The first term in parentheses of equation (1.3) is called the data term since it involves the given image data. It expreses the fact that we are looking for a transport field which provides an approximation of the optical flow equation

$$\partial_t I + \boldsymbol{u} \cdot \nabla I = 0, \quad \text{in } \Omega \times (0,T]$$

as good as possible. In the context of observations of fluid flows it is more reliable to work with an approximation of the physics-based optical flow equation in the data term:

$$\sum_{k=1}^{N} \|\partial_t \hat{I}(t_k) - \varepsilon \Delta \hat{I}(t_k) + \boldsymbol{u}(t_k) \cdot \nabla \hat{I}(t_k)\|^2_{L^2(\Omega)}.$$

Remark 1.2 (Regularisation Term).
The second term in parentheses of equation (1.3) is a regularisation which has to be added due to the ill-posed character of the scalar (physics-based) optical flow equation

$$\partial_t I - \varepsilon \left(\partial_{xx} I + \partial_{yy} I\right) + u \partial_x I + v \partial_y I = 0, \qquad \text{in } \Omega \times (0,T],$$

with respect to the estimation of the two dimensional flow field $\boldsymbol{u} = (u,v)^T$.

The whole functional (1.3) can be interpreted as an inverse problem with Tikhonov regularisation.

By using calculus of variations,

$$\frac{d}{d\varepsilon} J_{HS}(\boldsymbol{u} + \varepsilon \boldsymbol{\varphi})|_{\varepsilon=0} = 0, \quad \forall \boldsymbol{\varphi} \in H$$

we derive a necessary and sufficient condition for a minimiser $\boldsymbol{u}$ in the vector space H, which has to be specified. The variational derivative yields a system of PDEs in each time point t_k:

$$\begin{aligned} &\alpha(\nabla u_1, \nabla \varphi_1) + 2(u_1 \partial_x \hat{I} + u_2 \partial_y \hat{I}, \partial_x \hat{I} \varphi_1) = -2(\partial_t \hat{I}, \partial_x \hat{I} \varphi_1), \\ &\alpha(\nabla u_2, \nabla \varphi_2) + 2(u_1 \partial_x \hat{I} + u_2 \partial_y \hat{I}, \partial_y \hat{I} \varphi_2) = -2(\partial_t \hat{I}, \partial_y \hat{I} \varphi_2), \end{aligned} \qquad \forall \boldsymbol{\varphi} = (\varphi_1, \varphi_2)^T \in H.$$

We rewrite the above equation in the following short notation:

$$\alpha(\nabla \boldsymbol{u}, \nabla \boldsymbol{\varphi}) + (B\boldsymbol{u}, \boldsymbol{\varphi}) = (\boldsymbol{f}, \boldsymbol{\varphi}), \quad \forall \boldsymbol{\varphi} \in H,$$

with

$$B = \begin{pmatrix} (\partial_x \hat{I})^2 & (\partial_x \hat{I})(\partial_y \hat{I}) \\ (\partial_x \hat{I})(\partial_y \hat{I}) & (\partial_y \hat{I})^2 \end{pmatrix}, \quad \boldsymbol{f} = -2\partial_t \hat{I} \begin{pmatrix} \partial_x \hat{I} \\ \partial_y \hat{I} \end{pmatrix}.$$

Hence, we derive a weak formulation of a steady elliptic diffusion-reaction equation in each time point t_k.

Remark 1.3 (Small Diffusion).
Setting $\alpha = 0$ shows that the two equations degenerate to the same equation, which emphasises the ill-posed character of estimating the flow field out of the scalar transport equation. Thus, the diffusive term in the equations, introduced by the regularisation term, is necessary for the solution process.

The diffusive term leads essentially to a spatial smoothing of the solution. Unfortunately, this "smoothing" of the transport smears sharp edges in the brightness distribution, so that we have a blurring effect, which makes a "perfect" match in the data term nearly impossible. Thus, the regularisation parameter α is a sensitive tool to adjust a good trade-off between matching of the data term and regularisation of the solution. Developing appropriate strategies to choose α automatically is a delicate matter, which will be discussed later on in another context.

We now present a methodology based on PDE-constrained optimisation which has several advantages in comparison to the Horn and Schunck method.

Optimal Control Approach for Optical Flow Estimation

Borzi et al. [16] formulated the following optimisation problem:

Optimisation Problem 1.4 (Optimal Control Optical Flow Estimation).
We wish to find $\boldsymbol{u} \in \mathcal{Q}$ and $I \in \mathcal{V}$ such that

$$J(\boldsymbol{u}, I) = \frac{1}{2} \sum_{k=1}^{N} \|I(t_k) - \mathcal{I}_k\|_2^2 + \mathcal{R}(\boldsymbol{u})$$

is minimised subject to an appropriate mathematical formulation of the optical flow equation

$$\partial_t I + \boldsymbol{u} \cdot \nabla I = 0, \qquad \text{in } \Omega \times (0, T], \tag{1.4}$$

$$I(0) = \mathcal{I}_1, \qquad \text{in } \Omega. \tag{1.5}$$

The above mentioned authors choose as regularisation term

$$\mathcal{R}(\boldsymbol{u}) = \frac{\alpha}{2} \int_0^T \int_\Omega \Phi\left(|\partial_t \boldsymbol{u}|^2\right) \, d\boldsymbol{x} \, dt + \frac{\beta}{2} \int_0^T \int_\Omega \Psi\left(|\nabla \boldsymbol{u}|^2\right) \, d\boldsymbol{x} \, dt + \frac{\gamma}{2} \int_0^T \int_\Omega |\nabla \cdot \boldsymbol{u}|^2 \, d\boldsymbol{x} \, dt,$$

with non-negative parameters α, β and γ. The first two terms are introduced to achieve spatial and temporal regularisation needed since the given image data is under-determined. The choice of the appropriate functions $\Phi(\cdot)$ and $\Psi(\cdot)$ is complicated, and we refer the interested reader to the above cited literature. The last term is a penalisation term, which guarantees that the velocities on the border of small subregions have the same value as in the interior of the subregion. This term leads to an extrapolation of flow information into regions without any brightness information. The usage of such a term is also common in the classical optical flow estimation literature.

Another approach for the regularisation term was presented by Chen et al. [22]. They use as regularisation

$$\mathcal{R}(\boldsymbol{u}) = \frac{\alpha}{2} \int_0^T \|\nabla \Delta \boldsymbol{u}(t)\|_2^2 \, dt \tag{1.6}$$

and add the divergence-free constraint

$$\nabla \cdot \boldsymbol{u} = 0, \quad \text{in } \Omega$$

to the state equation (1.4).

Remark 1.5 (Choice of the Control Space).
The authors choose a highly regular control space by taking the above mentioned semi-norm in equation (1.6), which is equivalent to the norm of the space $H^3(\Omega)^2 \cap H^1_{0,\text{div}}(\Omega)^2$ *(see next chapter for definitions of the spaces), when using homogeneous Dirichlet boundary data. The regularity is needed to guarantee the solvability of the state equation (cf. Chapter 2.2.2).*

Both references introduce a new class of optimal flow estimators based on optimal control approaches. This concept leads to fundamental advantages as the authors mentioned in their contributions:

i) Decoupling of the sampling rate from the images and time step size for the temporal discretisation to enable even the treatment of large deviations of brightness patterns.

ii) No differentiation of the data is needed. Depending on the sampling rate the approximation of the image derivatives is considerably bad and therefore only poor estimates would be possible in the usual approaches using the approximative optical flow equation in the data term.

iii) Using the divergence of the optical flow field for the regularisation leads to extrapolation of flow information into regions without image information.

iv) We can use this approach not only for the estimating the optical flow but also for reconstructing the image function $I(\boldsymbol{x}, t)$ and therefore for the temporal interpolation of the images.

v) The authors showed for common benchmark examples that their optimal control approach is superior to the usual Horn and Schunck technique.

The first two aspects are closely connected. Borzi et al. [16] discussed that the process of estimating a reliable velocity field by the classical Horn and Schunck approach yields only good results as long as for the sampling rates dx, dy and dt good approximations

$$\boldsymbol{u} = \begin{pmatrix} u_1(x,y,t) \\ u_2(x,y,t) \end{pmatrix} \approx \begin{pmatrix} \frac{dx}{dt} \\ \frac{dy}{dt} \end{pmatrix}$$

are available. This is due to the Courant-Friedrich-Levy condition

$$C_{\mathrm{CFL}} = u_1 \frac{dt}{dx} + u_2 \frac{dt}{dy} \leq 1,$$

which has to be fulfilled for a reliable numerical solution of the linear transport equation (cf. Großmann et al. [44]).

In the classical method the temporal sample rate dt and the time step are the same, while in the optimal control approach we can use a finer time discretisation, fulfilling the above condition for the state equation independent of the temporal difference of two consecutive images $\mathcal{I}_k$ and $\mathcal{I}_{k+1}$. In this sense the method is more flexible when we want to handle image sequences with large deviations from the observed brightness patterns between two given images.

In the approach of Chen et al. [22] the choice of the regularisation was justified by the required regularity of the flow field in the linear transport equation. This property can also be achieved by a combined approach, which is on the one hand more complex but on the other hand more flexible.

1.4. Coupled Approach

We formulate a more sophisticated optimisation problem.

Optimisation Problem 1.6 (Optimal Control Optical Flow Estimator II). *Find $\boldsymbol{q} \in \mathcal{Q}$ and $(\boldsymbol{u}, p, I) \in \mathcal{V}_{\boldsymbol{u}} \times \mathcal{V}_p \times \mathcal{V}_I$ such that*

$$J(\boldsymbol{q}, I) = \frac{1}{2} \sum_{k=1}^{N} \|I(t_k) - \mathcal{I}_k\|_2^2 + \frac{\alpha}{2} \int_0^T \|\boldsymbol{q}\|_2^2 \, dt$$

is minimised subject to an appropriate mathematical formulation of the following system of equations

$$\begin{aligned} \partial_t I + \boldsymbol{u} \cdot \nabla I &= 0, \\ \partial_t \boldsymbol{u} - \Delta \boldsymbol{u} + \nabla p &= \boldsymbol{q}, \qquad && \text{in } \Omega \times (0, T], \\ \nabla \cdot \boldsymbol{u} &= 0, \end{aligned}$$

with homogeneous boundary conditions and sufficiently regular initial data for I and $\boldsymbol{u}$.

The state equation of this optimal control approach with distributed domain control is coupled by the velocity field, which is described by the time-dependent Stokes equation, to the linear transport equation. In the context of boundary control optical flow estimation this approach was already presented by Klinger [67].

In the next chapter we will show that we can achieve the regularity properties

$$\{I, \boldsymbol{u}\} \in L^\infty \left(0, T; H_0^1(\Omega)\right) \times L^\infty \left(0, T; H^3(\Omega)^2 \cap H_{0,\mathrm{div}}^1(\Omega)^2\right)$$

for this approach, which are essentially the same properties as in Chen et al. [22] except for the additional temporal regularity in the approach above.

A major drawback of this formulation is that we introduce an additional variable p and that we expand the system from two to four equations, which will increase the computational cost for the solution process of this optimisation problem.

However, the proposed method shows also several advantages:

i) If we observe a laminar fluid flow the Stokes equations

$$\begin{aligned} \partial_t \boldsymbol{u} - \Delta \boldsymbol{u} + \nabla p &= \boldsymbol{q}, && \text{in } \Omega \times (0,T], \\ \nabla \cdot \boldsymbol{u} &= 0, && \text{in } \Omega \times (0,T] \end{aligned}$$

constitutes the correct physical model. In this situation the additional variable p gets a physical meaning and can also be evaluated by this approach.

ii) We can substitute the Stokes system by other flow models (e. g. by the nonlinear and time-dependent Navier Stokes equations) and use therefore further a priori knowledge of the underlying fluid flow or evaluate even not directly observed quantities.

iii) We can also substitute the equation for the brightness intensity function by an appropriate model for the brightness evolution. This can be used for example to detect sources for intensity changes which localise sources of the tracer (e. g. pollutants acting as tracer in the atmospheric wind system).

iv) We can choose different types of control functions q (e. g. boundary controls) and adapt this choice also to our particular situation.

v) We can apply different data sources. For example if we have measurements of the transport field in a subdomain Ω_{Sub} of the image domain Ω_{Img}, we can easily couple this information to the optimisation by extending the cost functional by a further term, e. g.

$$\int_0^T \|\boldsymbol{u}(t) - \hat{\boldsymbol{u}}(t)\|^2_{L^2(\Omega_{\text{Sub}})^2} \, dt.$$

To apply more knowledge about the underlying fluid flow in the case of optical fluid flow estimation as indicated in points i) and ii) was already suggested by other authors (cf. Papadakis et al. [83], Ruhnau et al. [91, 92] and Ruhnau [90].). There, optimal control approaches with different fluid flow models as PDE-constraints are used with an approximation of the (physics-based) optical flow equation as data term as in the Horn and Schunck case. In this sense, the proposed methodology is a combination of two common directions of optimal control based optical flow estimation.

However, the above mentioned advantages are very abstract. To fix ideas we will focus on an approach which is able to cope with the different problems, which are specified by the prototypical examples (see Section 1.2.3).

We formulate the following optimisation problem:

Optimisation Problem 1.7 (Boundary Control Optical Flow Estimator).
Find $\boldsymbol{q} \in \mathcal{Q}$ *and* $(\boldsymbol{q}, p, I) \in \mathcal{V}_{\boldsymbol{u}} \times \mathcal{V}_p \times \mathcal{V}_I$ *such that*

$$J(\boldsymbol{u}, I) = \frac{1}{2} \sum_{k=1}^{N} \|I(t_k) - \mathcal{I}_k\|_2^2 + \frac{\alpha}{2} \int_0^T \|\boldsymbol{q}\|_{\mathcal{Q}}^2 \, dt$$

is minimised subject to an appropriate mathematical formulation of the following system of equations

$$\begin{aligned} \partial_t I - \varepsilon I + \boldsymbol{u} \cdot \nabla I &= 0, \\ \partial_t \boldsymbol{u} - \nu \Delta \boldsymbol{u} + \boldsymbol{u} \cdot \nabla \boldsymbol{u} + \nabla p &= 0, \qquad \text{in } \Omega \times (0, T], \\ \nabla \cdot \boldsymbol{u} &= 0, \end{aligned}$$

with sufficiently regular initial conditions for I *and* $\boldsymbol{u}$ *and the following abstract boundary conditions*

$$\begin{aligned} B_I(\boldsymbol{u}; I, q_I) &= 0, \qquad \Gamma_C \times (0, T], \\ B_{\boldsymbol{u}}(\boldsymbol{u}, \boldsymbol{q}_{\boldsymbol{u}}) &= 0, \qquad \Gamma_C \times (0, T] \end{aligned}$$

involving the boundary control $\boldsymbol{q} = (q_I, \boldsymbol{q}_{\boldsymbol{u}})$ *on* $\Gamma_C \subset \partial\Omega$*. Also, boundary conditions on* $\partial\Omega \setminus \Gamma_C$ *have to be specified.*

From the mathematical point of view a fundamental question for this sophisticated boundary control-type problem arose:

Question: *What is an appropriate choice for the boundary conditions* $B_I(\cdot; \cdot, \cdot)$ *and* $B_{\boldsymbol{u}}(\cdot, \cdot)$ *and their associated vector spaces to obtain on the one hand a mathematically well-posed formulation of the optimisation problem and on the other hand a practicable method from the computational point of view?*

In the next chapters we will discuss and answer this question. The result will be a novel approach for physics-based optical flow estimation with image interpolation across boundaries. Afterwards we will use this technique to solve the three prototypical problems and investigate the behaviour of the methodology.

2. Governing Equations

The Optimisation Problem 1.7 relies on the system of equations (1.2). The aim of this chapter is to present the standard theory of this system of equations consisting of the time-dependent fully nonlinear incompressible Navier-Stokes equations and a convection-diffusion equation describing the transport of a passive tracer caused by the Navier-Stokes vector field. Hence, we want to briefly discuss existence and uniqueness theory and the influence of the data, especially boundary data. We will need the techniques summerised in this chapter for the theoretical analysis of the resulting boundary control problems in the later chapters.

2.1. Preliminaries and Notation

In the following we introduce briefly the basic notation for the theory of partial differential equations.

We will always assume Ω as a *bounded domain* with *Lipschitz boundary* (cf. Sohr [97], I.3.2.). In many cases Ω will be additionally polygonal and convex.

The notation for the standard *Lebesgue* and *Sobolev spaces*, $L^p(\Omega)$ and $W^{m,p}(\Omega)$, corresponds to the notation in Adams et al. [1]. Furthermore the *Hilbert space* $W^{m,2}(\Omega)$ is denoted by $H^m(\Omega)$. For $m < \infty$ we denote by

$$(u,v) = \int_\Omega u(x) \cdot v(x)\, dx, \qquad (u,v)_{H^m(\Omega)} = \sum_{0\le|\alpha|\le m} \int_\Omega D^\alpha u(x) D^\alpha v(x)\, dx$$

the usual *scalar products*. The *norms* of the Hilbert spaces are given by

$$\|u\|^2_{L^2(\Omega)} = (u,u)\,, \qquad \|u\|^2_{H^m(\Omega)} = (u,u)_{H^m(\Omega)}$$

and the norms for $L^\infty(\Omega)$ and $W^{m,\infty}(\Omega)$ are

$$\|u\|_{L^\infty(\Omega)} = \operatorname*{ess\,sup}_{x\in\Omega} |u(x)|, \quad \|u\|_{W^{m,\infty}(\Omega)} := \max_{|\alpha|\le m} \|D^\alpha u\|_{L^\infty(\Omega)}.$$

For the L^2-scalar product on a part of the boundary $\Gamma \subset \partial\Omega$ we will use the notation

$$\langle u,v\rangle_\Gamma = \int_\Gamma u(s) \cdot v(s)\, ds$$

to avoid confusions with the usual duality pairing, which will be introduced below.

We will also distinguish between *vector* and *scalar valued* functions by using bold face for vector valued variables and superscripts for the space, e. g.

$$\boldsymbol{x} \in \mathbb{R}^n, \quad \boldsymbol{u}(\boldsymbol{x}) \in L^p(\Omega)^n.$$

For time-dependent functions we use the standard notation of *Bochner functions* (cf. Gajewski et al. [40]), where for $[a, b] \subset \mathbb{R}$ the symbol $L^p(a, b; X)$ with $1 \leq p < \infty$ denotes the space of Bochner measurable functions with the property

$$\int_a^b \|u(t)\|_X^p dt < \infty.$$

Furthermore, we follow Dobrowolski [29] and use the notation

$$\langle x, f \rangle = f(x) \in \mathbb{R}$$

to describe a duality mapping from $X \times X'$, where X' denotes the dual space of the normed space X. Hence we have also the mapping

$$f \mapsto \langle x, f \rangle, \quad X' \to \mathbb{R}$$

for every $x \in X$. Therefore we call $\langle \cdot, \cdot \rangle$ a *duality pairing*.

2.2. Convection-Diffusion Equation

The convection-diffusion equation describes the dispersion of a given initial concentration, temperature or brightness intensity distribution $u^0(x)$ over a certain time interval $(0, T]$. Therefore this type of equation is involved in general when we observe a passive tracer in a flow. We sum up some fundamental properties of this kind of equation.

In the classical form this equation is written as

$$\begin{aligned} \partial_t u(\boldsymbol{x}, t) - \nu(\boldsymbol{x}, t)\Delta u(\boldsymbol{x}, t) + \boldsymbol{\beta}(\boldsymbol{x}, t) \cdot \nabla u(\boldsymbol{x}, t) &= f(\boldsymbol{x}, t), && \text{in } \mathcal{Q} := \Omega \times (0, T], \\ u(\boldsymbol{x}, t) &= g(\boldsymbol{x}, t), && \text{on } \Sigma := \partial\Omega \times (0.T], \\ u(\boldsymbol{x}, 0) &= u^0(\boldsymbol{x}), && \text{in } \Omega. \end{aligned} \tag{2.1}$$

This equation is a parabolic partial differential equation as long as $\nu(\boldsymbol{x}, t)$ stays positive and thus the spatial part with the operator

$$Lu := -\nu(\boldsymbol{x}, t)\Delta u(\boldsymbol{x}, t) + \boldsymbol{\beta}(\boldsymbol{x}, t) \cdot \nabla u(\boldsymbol{x}, t)$$

is elliptic.

2.2.1. Existence and Uniqueness

The existence and uniqueness results rely on the following weak formulation of the problem.

Weak Formulation 2.1.
Let $f \in L^2\left(0,T;L^2(\Omega)\right)$. *Find* $u \in L^2\left(0,T;H_0^1(\Omega)\right)$ *with* $\partial_t u \in L^2\left(0,T;H^{-1}(\Omega)\right)$ *such that*

$$(\partial_t u, \varphi) + (\nu \nabla u, \nabla \varphi) + (\boldsymbol{\beta} \cdot \nabla u, \varphi) = (f, \varphi), \quad \forall \varphi \in H_0^1(\Omega) \tag{2.2}$$

for almost every $t \in (0,T]$ *and*

$$u(\boldsymbol{x}, 0) = u^0 \in L^2(\Omega).$$

Remark 2.2 (Prescription of Inhomogeneous Dirichlet Conditions (Strong)).
The above weak formulation does not consider the case of inhomogeneous Dirichlet boundary conditions. Anyway, this general case can easily be transformed into the above formulation. We follow Schweizer [96] to describe the concept.

If we assume enough regularity of the boundary data $g(\boldsymbol{x},t)$, *especially regularity in time then, we are looking for a generalised solution of the homogeneous problem*

$$\partial_t w(\boldsymbol{x},t) + Lw(\boldsymbol{x},t) = f(\boldsymbol{x},t) - \partial_t \tilde{g}(\boldsymbol{x},t) - L\tilde{g}(\boldsymbol{x},t) =: \tilde{f}, \quad \text{in } \Omega$$

for almost every $t \in (0,T]$ *and*

$$w(\boldsymbol{x},t) = 0, \quad \text{on } \partial\Omega, \quad w(\boldsymbol{x},0) = u^0(\boldsymbol{x}) - \tilde{g}(\boldsymbol{x},0), \quad \text{in } \Omega,$$

where $\tilde{g}$ *is an appropriate extension of* $g(\boldsymbol{x},t)$ *into the domain.*

The solution of the inhomogeneous problem can then be calculated by

$$u(\boldsymbol{x},t) = w(\boldsymbol{x},t) + \tilde{g}(\boldsymbol{x},t).$$

The minimum requirement for the boundary data is

$$g(\boldsymbol{x},t) \in H^{\frac{1}{2}}(\partial\Omega), \quad \text{with} \quad H^{\frac{1}{2}}(\partial\Omega) = \{\varphi \in L^2(\partial\Omega) : \ \exists \omega \in H^1(\Omega), \varphi = \mathcal{T}(\omega)\},$$

where $\mathcal{T}$ *denotes the trace operator* $\mathcal{T} : H^1(\Omega) \to L^2(\partial\Omega)$.

Remark 2.3 (Continuity in Time).
The initial condition is meaningful in the sense that $u \in C\left([0,T];L^2(\Omega)\right)$. *This follows with a standard result (see Theorem 3, 5.9.2 Evans [33]), when*

$$u \in L^2\left(0,T;H_0^1(\Omega)\right) \ \text{ and } \ \partial_t u \in L^2\left(0,T;\left(H_0^1(\Omega)\right)'\right).$$

Considering the fact that we later on assume that the underlying transport field results from an incompressible fluid flow we will have the additional assumption

$$\nabla \cdot \boldsymbol{\beta}(\boldsymbol{x}, t) = 0, \qquad \text{in } \mathcal{Q}$$

in an appropriate weak sense. For these so called "solenoidal" flow fields we have a special property of the weak transport term.

Lemma 2.4 (cf. Lemma 2.1 Galdi [41, Chapter VIII.2]).
Let $\Omega \subset \mathbb{R}^2$ be a bounded Lipschitz domain. We have

$$\begin{aligned} (\boldsymbol{u} \cdot \nabla v, v) &= 0, \\ (\boldsymbol{u} \cdot \nabla v, w) + (\boldsymbol{u} \cdot \nabla w, v) &= 0 \end{aligned}$$

for all $\boldsymbol{u} \in H^1_{\text{div}}(\Omega)^n = \{\boldsymbol{u} \in H^1(\Omega)^n \ : \ \nabla \cdot \boldsymbol{u} = 0$ in a weak sense$\}$ and $v, w \in H^1_0(\Omega)$.

The proof of the existence of a solution works now in the standard way by using Galerkin's method (also called energy method), which is based on the following steps (cf. Evans [33] or Schweizer [96])

1. Construction and existence of a finite-dimensional approximation $u^{(m)}$ of the continuous solution u for $m \in \mathbb{N}$.
2. Calculation of appropriate uniform energy estimates for $u^{(m)}$.
3. By compactness arguments, due to the uniform boundedness of $u^{(m)}$ we select subsequences, which converge to a certain weak solution u for $m \to \infty$.
4. Showing that u fulfils the original equation.

By this proceeding we derive following result:

Theorem 2.5 (Existence and Uniqueness of Solutions).
The domain $\Omega \subset \mathbb{R}^n$, with $n = 2, 3$, is bounded with Lipschitz boundary. Moreover we have for the initial condition $u^0 \in L^2(\Omega)$ and the final time point $T > 0$. The operator L is elliptic and we have one of the following conditions:

1. $\boldsymbol{\beta}(\boldsymbol{x}, t) \in L^\infty\left(0, T; L^\infty(\Omega)^n\right)$,
2. $\boldsymbol{\beta}(\boldsymbol{x}, t) \in L^2\left(0, T; H^1_{\text{div}}(\Omega)^n\right)$.

Furthermore $f \in L^2\left(0, T; H^{-1}(\Omega)\right)$.

Then there exists a unique weak solution $u \in L^2\left(0, T; H^1_0(\Omega)\right)$ of equation (2.2).

Proof. The details of the proof are given in Evans [33, Chapter 7.1].

The second possibility for the regularity of $\boldsymbol{\beta}$ requires a modification of the second step of Galerkin's method, the evaluation of an uniform energy bound. This is straightforward by testing the weak formulation with $u(t)$ itself

$$\frac{1}{2}\frac{d}{dt}\|u(t)\|_2^2 + \nu\|\nabla u(t)\|_2^2 + (\boldsymbol{\beta}(t)\cdot\nabla u(t), u(t)) = (f(t), u(t))$$

for almost every $t \in (0,T]$. Using Lemma 2.4 and Young's inequality we obtain the inequality

$$\frac{1}{2}\frac{d}{dt}\|u(t)\|_2^2 + \nu\|\nabla u(t)\|_2^2 \leq C_1\|u(t)\|_2^2 + C_2\|f(t)\|_2^2.$$

By using Gronwalls inequality the energy estimates can be generated in a standard way (cf. Evans [33, Chapter 7, THEOREM 2]). □

This weak solution can have a higher regularity under certain assumptions on the data and the domain. We cite therefore the following

Theorem 2.6 (cf. THEOREM 5 Evans [33, Chapter 7.1.3.]).
Let Ω be either a bounded domain with a smooth boundary $\partial\Omega$ or a convex polygon with

$$u^0 \in H_0^1(\Omega), \quad f \in L^2\left(0,T;L^2(\Omega)\right).$$

Moreover $\boldsymbol{\beta} \in L^\infty\left(0,T;L^\infty(\Omega)^n\right)$. Then

$$u \in L^2\left(0,T;H^2(\Omega)\right) \cap L^\infty\left(0,T;H_0^1(\Omega)\right), \quad \textit{and} \quad \partial_t u \in L^2\left(0,T;L^2(\Omega)\right).$$

Furthermore we have the following estimate

$$\begin{aligned}\operatorname*{ess\,sup}_{0\leq t\leq T}\|u(t)\|_{H_0^1(\Omega)} + \int_0^T \left(\|u(t)\|_{H^2(\Omega)}^2 + \|\partial_t u(t)\|_{L^2(\Omega)}^2\right) dt \\ \leq C\left(\int_0^T \|f(t)\|_{L^2(\Omega)}^2\, dt + \|u^0\|_{H_0^1(\Omega)}\right),\end{aligned} \tag{2.3}$$

with C depending on Ω, ν and $\boldsymbol{\beta}$.

Hence, under appropriate assumptions the weak solution is more regular and therefore we can show, by using the fundamental theorem of the calculus of variations (cf. Dacorogna [26]), that the weak solution of equation (2.2) is also a solution to the classical formulation in equation (2.1).

2.2.2. Linear Transport Equation (Optical Flow Constraint)

The transport of intensity patterns in a generic image sequence is described by the the optical flow equation

$$\begin{aligned} \partial_t u(\boldsymbol{x},t) + \boldsymbol{\beta}(\boldsymbol{x},t)\cdot\nabla u(\boldsymbol{x},t) &= 0, && \text{in } \Omega\times(0,T], \\ u(\boldsymbol{x},0) &= u^0, && \text{in } \Omega, \end{aligned} \tag{2.4}$$

with a plane optical flow field $\boldsymbol{\beta}$ (cf. Jähne [60]). From the mathematical point of view this is a linear transport equation. Though it fits at first glance into the above presented setting of general convection-diffusion equations by choosing $\nu = 0$ and $f = 0$, the character of this partial differential equation is completely different, since the spatial operator

$$Lu(\boldsymbol{x},t) := \boldsymbol{\beta}(\boldsymbol{x},t)\cdot\nabla u(\boldsymbol{x},t)$$

is no longer elliptic. Hence, also the theoretical background changes.

The classical theory of linear transport equations is closely related to the theory (of system) of ordinary differential equations

$$\frac{d}{dt}X(t) = \boldsymbol{\beta}(t,X(t)), \quad \text{with } \ t\in[0,T], \quad \text{and } X(0) = X^0,$$

where $\boldsymbol{\beta}$ is required to be Lipschitz continuous in space and must be integrable in time. Then we can apply the classical theorem of Picard-Lindelöf to obtain unique existence of a solution $X(t)$. These requirements are somehow eased for fields $\boldsymbol{\beta}$ with bounded divergence and some Sobolev type regularity in DiPerna et al. [28]. The authors derive

$$\boldsymbol{\beta}\in W^{1,1}_{\mathrm{loc}}(\mathbb{R}^n), \quad \nabla\cdot\boldsymbol{\beta}\in L^\infty(\mathbb{R}^n)$$

if the following conditions are fulfilled:

$$\boldsymbol{\beta} = \boldsymbol{\beta}_1 + \boldsymbol{\beta}_2, \quad \boldsymbol{\beta}_1\in L^p(\mathbb{R}^n), \quad \text{for } 1\le p\le\infty, \quad \frac{\boldsymbol{\beta}_2}{1+|x|}\in L^\infty(\mathbb{R}^n).$$

Unfortunately, the above result covers neither the usual H^1-regularity of the transport field nor the divergence free condition in a weak sense. On the other hand the above mentioned conditions are not appropriate for our later purposes. Hence, we will present a well-posedness result for a special configuration.

We want to mention two articles in the literature considering the linear transport equation in the context of optical flows. Chen et al. [22] assumes H^3-regular flow fields $\boldsymbol{\beta}$ to have an embedding into $W^{1,\infty}(\Omega)$ and thus into the space of Lipschitz-continuous functions. Furthermore, the fields are solenoidal. Then authors are able to prove existence of a unique BV-regular solution, as long as the initial value is in BV (see the definition below for this space).

Remark 2.7 (Spaces for Image Processing Applications).
In image processing usually the space of functions with bounded variations is used:

$$BV(\Omega) = \{u \in L^1(\Omega) \ : \ \Phi(u) < \infty\},$$

with $\Phi(u) := \sup\{\int_\Omega u(x)\,(\nabla \cdot \phi(x))\ dx \ : \ \phi \in C_0^\infty(\Omega), \|\phi\|_\infty \leq 1\}$.

The reason for this is that on the one hand it contains functions which have more regularity than a statistical noise but on the other hand discontinuities (sharp edges in an image) are allowed. $BV(\Omega)$ *is an extension of the Sobolev space*

$$W^{1,1}(\Omega) = \{u \in L^1(\Omega) \ : \ \nabla u \in L^1(\Omega)\}.$$

Hence, together with the result in Bergounioux [14] we have the following chain of embeddings in two space dimensions

$$H^1(\Omega) \subset W^{1,1}(\Omega) \subset BV(\Omega) \subset L^2(\Omega). \tag{2.5}$$

In contrast, Borzi et al. [16] assume directly $C^{0,1}$-regular flows which are not necessarily divergence free to transport $W^{1,p}$-regular initial values into $W^{1,p}$-regular solutions in a unique way, where $p \geq 2$.

We will briefly show with the same technique that a H^3-regular flow field $\boldsymbol{\beta}$, which is solenoidal in a weak sense, generates a unique H^1-regular solution of the transport equation, as long as the initial value is in $H^1(\Omega)$. The starting point is again the weak formulation of the problem.

Weak Formulation 2.8.
Find $u \in L^2(0,T;H_0^1(\Omega))$ *such that*

$$(\partial_t u(t), \varphi) + (\boldsymbol{\beta}(t) \cdot \nabla u(t), \varphi) = 0, \quad \forall \varphi \in H_0^1(\Omega)$$

for almost every $t \in [0,T]$ *and with* $\boldsymbol{\beta} \in L^2\left(0,T;H^1_{\mathrm{div}}(\Omega)^n\right)$.

For this weak formulation we have the following theorem:

Theorem 2.9.
Let $\Omega \subset \mathbb{R}^2$ *be a bounded domain with* C^2*-boundary or convex polygonal structure. The initial value function* u^0 *belongs to the space* $H_0^1(\Omega)$ *and* $T > 0$*. For the transport field we have*

$$\boldsymbol{\beta} \in L^2\left(0,T;H^3(\Omega)^2 \cap H^1_{\mathrm{div}}(\Omega)^2\right).$$

Then we obtain a unique weak solution $u \in L^\infty\left(0,T;H_0^1(\Omega)\right) \cap H^1\left(0,T;L^2(\Omega)\right)$.

Proof. To prove uniqueness is standard using Lemma 2.4, since $\boldsymbol{\beta}$ is solenoidal.

So we will only describe the existence proof. It is based on the "vanishing viscosity" method, where we introduce a diffusion term in the weak formulation so that we are looking for a ε-dependent solution u_ε of

$$(\partial_t u_\varepsilon(t), \varphi) + \varepsilon\,(\nabla u_\varepsilon(t), \nabla\varphi) + (\boldsymbol{\beta}(t)\cdot\nabla u_\varepsilon(t), \varphi) = 0, \quad \forall\varphi \in H_0^1(\Omega) \tag{2.6}$$

for almost every $t \in (0,T]$ and with $0 < \varepsilon < 1$. This formulation fits perfectly to the assumptions of Theorem 2.5. Moreover $\boldsymbol{\beta}(t) \in H^3(\Omega)^2$ is embedded in $L^\infty(\Omega)^2$ (see Adams [1, Theorem 4.12 CASE A]). Hence we can also use Theorem 2.6. Altogether we obtain for a fixed ε the existence of a unique solution u_ε belonging to the following spaces

$$u_\varepsilon \in L^2\left(0,T; H_0^1(\Omega)\right), \quad u_\varepsilon \in L^2\left(0,T; H^2(\Omega)\right), \quad \frac{d}{dt}u_\varepsilon \in L^2\left(0,T; L^2(\Omega)\right). \tag{2.7}$$

We want to emphasise that the estimate (2.3) cannot be an energy bound for the sequence u_ε, since the constant C of the energy bounds in the above mentioned theorems is indirectly proportional to ε ($C \sim \frac{1}{\varepsilon}$).

Hence, we have to prove energy estimates with uniform bounds:

1. Testing with the solution itself

   $$\frac{1}{2}\frac{d}{dt}\|u_\varepsilon(t)\|_2^2 + \varepsilon\|\nabla u_\varepsilon(t)\|_2^2 + \underbrace{(\boldsymbol{\beta}(t)\cdot\nabla u_\varepsilon(t), u_\varepsilon(t))}_{=0} = 0, \quad \forall\varphi \in H_0^1(\Omega)$$

   due to Lemma 2.4. With

   $$\operatorname*{ess\,sup}_{t\in[0,T]} \|u_\varepsilon(t)\|_2^2 \le 2\|u^0\|_2^2 \quad \text{and} \quad \int_0^T \varepsilon\|\nabla u_\varepsilon(t)\|_2^2\,dt \le \|u^0\|_2^2 \tag{2.8}$$

   we then obtain the first two estimates.

2. Testing with $\Delta u_\varepsilon(t)$, which is possible due to the above mentioned regularity properties, we obtain

   $$\frac{1}{2}\frac{d}{dt}\|\nabla u_\varepsilon(t)\|_2^2 + \varepsilon\|\Delta u_\varepsilon(t)\|_2^2 \le |\,(\boldsymbol{\beta}(t)\cdot\nabla u_\varepsilon(t), \Delta u_\varepsilon(t))\,|.$$

   A simple calculation with integration by parts shows that the right hand side can be controlled by

   $$\frac{1}{2}\frac{d}{dt}\|\nabla u_\varepsilon(t)\|_2^2 + \varepsilon\|\Delta u_\varepsilon(t)\|_2^2 \le \|\nabla\boldsymbol{\beta}(t)\|_{L^\infty(\Omega)^2}\|\nabla u_\varepsilon(t)\|_2^2.$$

   Using Gronwall's inequality and the Sobolev imbedding $H^3(\Omega) \hookrightarrow W^{1,\infty}$ we obtain

   $$\|\nabla u_\varepsilon(t)\|_2^2 \le \|\nabla u^0\|_2^2 \exp\left(\int_0^t \|\boldsymbol{\beta}(s)\|_{H^3(\Omega)^2}\,ds\right).$$

3. Testing with $\partial_t u_\varepsilon$ results in

$$\|\partial_t u_\varepsilon\|_2^2 + \frac{1}{2}\frac{d}{dt}\varepsilon\|\nabla u_\varepsilon(t)\|_2^2 \leq \frac{1}{2}\|\boldsymbol{\beta}(t)\|_{L^\infty(\Omega)^2}^2\|\nabla u_\varepsilon(t)\|_2^2 + \frac{1}{2}\|\partial_t u_\varepsilon(t)\|_2^2$$

and further with the bound of $\|\nabla u_\varepsilon(t)\|_2^2$ we obtain

$$\|\partial_t u_\varepsilon\|_2^2 + \frac{d}{dt}\varepsilon\|\nabla u_\varepsilon(t)\|_2^2 \leq c\|\boldsymbol{\beta}(t)\|_{L^\infty(\Omega)^2}^2.$$

After integration in time w get

$$\int_0^T \|\partial_t u_\varepsilon\|_2^2 \, dt \leq \|\nabla u^0\|_2^2 + c\int_0^T \|\boldsymbol{\beta}(t)\|_{L^\infty(\Omega)^2}^2 \, dt.$$

Now we know that u_ε is uniformly bounded in $L^\infty\left(0,T;H_0^1(\Omega)\right) \cap H^1\left(0,T;L^2(\Omega)\right)$. So there exists a weakly$\star$-convergent subsequence of u_ε converging to $u \in L^\infty\left(0,T;H_0^1(\Omega)\right)$. Further we can choose a subsequence of this sequence which converges weakly to $u \in H^1\left(0,T;L^2(\Omega)\right)$. Together with the uniform boundedness of $\varepsilon\int_0^T \|\nabla u_\varepsilon(t)\|_2^2 \, dt$ we can send ε to zero in equation (2.6) and obtain the result of the theorem. □

2.3. Navier-Stokes Equations

In this section we will shortly summarise the theory of the Navier-Stokes equations, which later on describe the underlying flow in the complete system of equations.

The classical form of the system is given by

$$\begin{aligned} \partial_t \boldsymbol{u}(\boldsymbol{x},t) - \nu\Delta\boldsymbol{u}(\boldsymbol{x},t) + \boldsymbol{u}(\boldsymbol{x},t)\cdot\nabla\boldsymbol{u}(\boldsymbol{x},t) + \nabla p(\boldsymbol{x},t) &= \boldsymbol{f}(\boldsymbol{x},t), \quad \text{in } \mathcal{Q}, \\ \nabla\cdot\boldsymbol{u}(\boldsymbol{x},t) &= 0, \quad \text{in } \mathcal{Q}, \\ \boldsymbol{u}(\boldsymbol{x},t) &= \boldsymbol{g}(\boldsymbol{x},t), \quad \text{on } \Sigma, \end{aligned}$$

with the viscosity parameter $\nu > 0$. Hereby we have a system of parabolic equations with saddle point character (cf. Girault et al. [42]). A main issue is the nonlinear term, which essentially affects all theoretical aspects.

Remark 2.10 (Inhomogeneous Dirichlet Data).
As before we state here all theoretical results for homogeneous boundary data. Inhomogeneous boundary data are treated in the same fashion as for convection-diffusion equations (cf. Remark 2.2).

A possible way to transform the non homogeneous case to a homogeneous one is given in the article of Raymond [86]. Then, we are searching for a solution $\boldsymbol{u}(\boldsymbol{x},t) = \boldsymbol{w}(\boldsymbol{x},t) + \boldsymbol{v}(\boldsymbol{x},t)$*, where* $\boldsymbol{w}(\boldsymbol{x},t)$ *is an appropriate* H^1*-regular solenoidal extension of the boundary function* $\boldsymbol{g}(\boldsymbol{x},t)$*.*

Moreover, we have to solve the system

$$\begin{aligned} \partial_t \boldsymbol{v} - \nu\Delta\boldsymbol{v} + \boldsymbol{w}\cdot\nabla\boldsymbol{v} + \boldsymbol{v}\cdot\nabla\boldsymbol{w} + \boldsymbol{v}\cdot\nabla\boldsymbol{v} + \nabla\rho &= \boldsymbol{f} - \partial_t\boldsymbol{w} - \boldsymbol{w}\cdot\nabla\boldsymbol{w}, && \text{in } \Omega, \\ \nabla\cdot\boldsymbol{v} &= 0, && \text{in } \Omega, \\ \boldsymbol{v} &= 0, && \text{on } \partial\Omega. \end{aligned}$$

A slight modification of the solution theory presented below will yield also the existence and uniqueness of a solution of this system of equations.

The above strongly formulated problem can be transformed to the following weak formulation by using the space

$$H^1_{0,\mathrm{div}}(\Omega)^n := \{\boldsymbol{\varphi} \in H^1(\Omega)^n \ : \ \boldsymbol{\varphi}|_{\partial\Omega} = 0,\ \nabla\cdot\boldsymbol{\varphi} = 0 \text{ in a weak sense}\}. \tag{2.9}$$

Weak Formulation 2.11.
Find $\boldsymbol{u}(\boldsymbol{x},t) \in L^2\left(0,T; H^1_{0,\mathrm{div}}(\Omega)^n\right)$ *such that*

$$\begin{aligned} (\partial_t\boldsymbol{u}(t),\boldsymbol{\varphi}) + (\nabla\boldsymbol{u}(t),\nabla\boldsymbol{\varphi}) + (\boldsymbol{u}(t)\cdot\nabla\boldsymbol{u}(t),\boldsymbol{\varphi}) &= (\boldsymbol{f}(t),\boldsymbol{\varphi}), \qquad \forall\boldsymbol{\varphi} \in H^1_{0,\mathrm{div}}(\Omega)^n, \\ \boldsymbol{u}(0,\cdot) &= \boldsymbol{u}_0. \end{aligned} \tag{2.10}$$

Here we have $\boldsymbol{u}_0 \in L^2_{\mathrm{div}}(\Omega)^n$ *and* $\boldsymbol{f} \in L^2\left(0,T; L^2(\Omega)^n\right)$.

The following Lemma describes in which sense a pressure is associated to a solution of the Weak Formulation 2.11 and therefore guarantees that the weak formulation is equivalent to the classical one, if sufficient regularity of the solution is available.

Lemma 2.12 (cf. Sohr, [97, Lemma 2.1.1 (b)]).
Again $\Omega \subset \mathbb{R}^n$, *with* $n = 2, 3$, *is a domain with Lipschitz boundary. Further we have* $\boldsymbol{l} \in H^{-1}(\Omega)^n := \mathcal{L}\left(H^1_0(\Omega)^n, \mathbb{R}\right)$ *with*

$$\boldsymbol{l}(\boldsymbol{\varphi}) = 0, \qquad \forall\boldsymbol{\varphi} \in H^1_{0,\mathrm{div}}(\Omega)^n.$$

Then the relation

$$\boldsymbol{l}(\boldsymbol{\varphi}) = (-\nabla\cdot\boldsymbol{\varphi}, p), \quad \forall\boldsymbol{\varphi} \in C^\infty_0(\Omega)^n$$

is valid, with $p \in L^2(\Omega)$ *and* $\int_\Omega p\, d\boldsymbol{x} = 0$.

Remark 2.13 (Application of Lemma 2.12 to Instationary Equations).
The pressure in the time-dependent case is introduced by applying Lemma 2.12 to a time-integrated version of equation (2.10). The proceeding is analogously to the proof of Proposition 3.1.1 in Temam [99].

The existence of solutions can now be obtained from the Weak Formulation 2.11 by the Galerkin method described in section 2.2.1. Crucial for the argumentation is the condition

$$(\boldsymbol{u}(t)\cdot\nabla\boldsymbol{v}(t),\boldsymbol{v}(t)) = 0, \qquad \forall\boldsymbol{v}(t) \in H^1_0(\Omega)^n, \quad \text{(especially if } \boldsymbol{v}(t) = \boldsymbol{u}(t) \in H^1_{0,\mathrm{div}}(\Omega)^n)$$

for the nonlinearity resulting from Lemma 2.4. We have

Theorem 2.14 (cf. Temam,[99, Chapter 3.3. Theorem 3.1]).
As before the domain $\Omega \subset \mathbb{R}^n$ $(n = 2, 3)$ has a Lipschitz boundary. For the data we have

$$\boldsymbol{f} \in L^2\left(0, T; (H^1_{0,\mathrm{div}}(\Omega)^n)'\right), \qquad \text{and} \qquad \boldsymbol{u}_0 \in L^2_{\mathrm{div}}(\Omega)^n.$$

Then there exists at least one solution $\boldsymbol{u} \in L^2\left(0, T; H^1_{0,\mathrm{div}}(\Omega)^n\right)$, which satisfies the Weak Formulation 2.11.

Proving the uniqueness of a solution is now based on Gronwall's inequality. Since the nonlinearity is no longer vanishing we have to estimate it. In two space dimensions we can use for this purpose an interpolation inequality which yields

$$\|\boldsymbol{u}\|^2_{L^4(\Omega)^2} \leq c\|\boldsymbol{u}\|_{L^2(\Omega)^2}\|\nabla \boldsymbol{u}\|_{L^2(\Omega)^2}, \tag{2.11}$$

which fits perfectly and allows to prove the following theorem.

Theorem 2.15 (Temam,[99, Chapter 3.3. Theorem 3.2]).
For $n = 2$ the solution from Theorem 2.14 is unique. Furthermore it is almost everywhere equal to a continuous function from $[0, T]$ into the space $L^2_{\mathrm{div}}(\Omega)^2$.

In contrast to this result in the three dimensional case inequality (2.11) is changing and we are no longer able to prove uniqueness or further regularity results. However, for our further considerations this big gap (cf. Millennium problem [35]) will not be crucial, since we want to investigate at first only the two dimensional case.

We present another result, which yields more regularity of the solution.

Theorem 2.16 (Higher Regularity).
The bounded domain $\Omega \subset \mathbb{R}^2$ has a C^2-boundary or is convex polygonal. Moreover

$$\boldsymbol{f} \in L^2\left(0, T; (H^1_{0,\mathrm{div}}(\Omega)^2)'\right) \cap L^\infty\left(0, T; L^2_{\mathrm{div}}(\Omega)^2\right), \quad \text{and} \quad \boldsymbol{u}_0 \in H^2(\Omega)^2 \cap H^1_{0,\mathrm{div}}(\Omega)^2.$$

It follows that

$$\boldsymbol{u} \in L^\infty\left(0, T; H^2(\Omega) \cap H^1_{0,\mathrm{div}}(\Omega)^2\right).$$

Proof. In the case of a C^2-boundary this can be found in Temam [99, Chapter 3.3. Theorem 3.6].

For the case of a convex polygonal domain we have to replace the proposition of the afore mentioned proof, which requires the indicated smoothness of the boundary, by a result (Theorem 3) from Kellogg et al. [65]. The rest of the argumentation is then completely analogous. □

Remark 2.17 (Higher Regularity via Streamline Formulation).
Another possibility to prove more regularity of the solution is to argue the streamline formulation of the two dimensional Navier-Stokes problem. Hereby we consider the biharmonic operator Δ^2 and via the regularity theory for this operator given in Blum et al. [15] we obtain in some situations even more regular solutions.

For example in the case of the domain $\Omega = (0,1) \times (0,1)$ we obtain for the stream function H^4-regularity and therefore H^3 for the original field, which is given by

$$\boldsymbol{u} = \mathit{curl}\, \boldsymbol{\psi} = (\psi_2, -\psi_1).$$

Remark 2.18 (Inhomogeneous Boundary Data and Higher Regularity).
Since we have for boundary functions $g \in H^{\frac{1}{2}}(\partial\Omega)$ only a H^1-extension it is clear that the composed solution of an non homogeneous problem (cf. Remark 2.10) cannot admit H^2 regularity. We want to emphasise that we also need an increase of the regularity of the boundary function.

2.4. Coupled System

In the following chapters we are interested in optimisation problems with a system of partial differential equation as side condition consisting of the transport of a passive tracer and a flow equation describing the transport field, in our case the fully nonlinear, time-dependent and incompressible Navier-Stokes equations. The tracer being passive means mathematically that the function is not coupling back to the flow model, so that we have the following system of equations:

$$\begin{aligned} \partial_t I(\boldsymbol{x},t) - \varepsilon \Delta I(\boldsymbol{x},t) + \boldsymbol{u}(\boldsymbol{x},t) \cdot \nabla I(\boldsymbol{x},t) &= 0, && \text{in } \mathcal{Q}, \\ \partial_t \boldsymbol{u}(\boldsymbol{x},t) - \nu \Delta \boldsymbol{u}(\boldsymbol{x},t) + \boldsymbol{u}(\boldsymbol{x},t) \cdot \nabla \boldsymbol{u}(\boldsymbol{x},t) + \nabla p(\boldsymbol{x},t) &= \boldsymbol{f}(\boldsymbol{x},t), && \text{in } \mathcal{Q}, \\ \nabla \cdot \boldsymbol{u}(\boldsymbol{x},t) &= 0, && \text{in } \mathcal{Q}. \end{aligned} \tag{2.12}$$

Further theoretical investigations of more general systems of this kind, which are fully coupled are considered in the works of Diaz et. al. [27] or Norman [81].

We will consider only our particular situation, with the following weak formulation.

Weak Formulation 2.19.
Find

$$I(\boldsymbol{x},t) \in L^2\left(0,T; H_0^1(\Omega)\right) \;\; \textit{and} \;\; \boldsymbol{u}(\boldsymbol{x},t) \in L^2\left(0,T; H_{0,\mathrm{div}}^1(\Omega)^n\right),$$

so that

$$\begin{aligned} \left(\partial_t I(t), \psi\right) + \varepsilon \left(\nabla I(t), \nabla \varphi\right) + \left(\boldsymbol{u}(t) \cdot \nabla I(t), \psi\right) &= 0, && \forall \psi \in H_0^1(\Omega), \\ \left(\partial_t \boldsymbol{u}(t), \boldsymbol{\varphi}\right) + \nu \left(\nabla \boldsymbol{u}(t), \nabla \boldsymbol{\varphi}\right) + \left(\boldsymbol{u}(t) \cdot \nabla \boldsymbol{u}(t), \boldsymbol{\varphi}\right) &= \left(\boldsymbol{f}(t), \boldsymbol{\varphi}\right), && \forall \boldsymbol{\varphi} \in H_{0,\mathrm{div}}^1(\Omega)^n \end{aligned}$$

and

$$I(\boldsymbol{x},0) = I^0(\boldsymbol{x}) \quad \in H_0^1(\Omega), \qquad \boldsymbol{u}(\boldsymbol{x},0) = \boldsymbol{u}^0(\boldsymbol{x}) \quad \in L_{\mathrm{div}}^2(\Omega).$$

Under the assumption of sufficient regularity of the solution pair this weak formulation is again equivalent to the classical formulation. The pressure is treated as in Lemma 2.12.

Theorem 2.20 (Existence and Uniqueness Coupled System).
The domain $\Omega \subset \mathbb{R}^2$ is bounded and has a Lipschitz boundary. Moreover we have

$$\boldsymbol{f} \in L^2\left(0,T;(H_0^1(\Omega)^2)'\right), \qquad \boldsymbol{u}^0 \in L^2_{\mathrm{div}}(\Omega)^2, \qquad I^0 \in L^2(\Omega)$$

for $T > 0$ and we have $\varepsilon, \nu \in \mathbb{R}^+ \setminus \{0\}$. Then there exists a unique solution pair

$$\{I, \boldsymbol{u}\} \in L^2\left(0,T;H_0^1(\Omega)\right) \times L^2\left(0,T;H^1_{0,\mathrm{div}}(\Omega)^2\right).$$

Proof. Since the solution of the parabolic convection-diffusion equation is not coupling back to the Navier-Stokes system, we can deduce this easily by the previously stated existence results.

Starting from the Navier-Stokes part of the system

$$(\partial_t \boldsymbol{u}(t), \boldsymbol{\varphi}) + \nu\left(\nabla \boldsymbol{u}(t), \nabla \boldsymbol{\varphi}\right) + \left(\boldsymbol{u}(t) \cdot \nabla \boldsymbol{u}(t), \boldsymbol{\varphi}\right) = \left(\boldsymbol{f}(t), \boldsymbol{\varphi}\right), \qquad \forall \boldsymbol{\varphi} \in H^1_{0,\mathrm{div}}(\Omega)^n$$

we know that for the assumed regularity of the data and the domain we obtain a flow field $\boldsymbol{u} \in L^2(0,T;H^1_{0,\mathrm{div}}(\Omega)^2)$ due to Theorem 2.14.

With this $\boldsymbol{u}$ all assumptions of Theorem 2.5 are fulfilled and we have also the existence of a unique $I \in L^2(0,T;H_0^1(\Omega))$. □

Remark 2.21 (Inhomogeneous Dirichlet Data for the Coupled System).
Inhomogeneous Dirichlet data are again handled as in the sections before. We can establish $\boldsymbol{u} \in L^2\left(0,T;H^1_{\mathrm{div}}(\Omega)^2\right)$ in Remark 2.10. Moreover, Theorem 2.5 is also valid for $\boldsymbol{u} \in L^2\left(0,T;H^1_{\mathrm{div}}(\Omega)^2\right)$ and with Remark 2.2 we extend the result for functions $I(\boldsymbol{x},t)$ with non homogeneous boundary data.

Thus we showed, that the theory of the coupled approach can be handled by a slight technical extension of the presented standard theory. This is changing if we want to work with pure transport in the passive tracer equation, which means $\varepsilon = 0$.

Nevertheless, due to the increased regularity properties of the Navier-Stokes solution we can obtain the existence of a unique vector field with

$$\boldsymbol{u} \in L^\infty\left(0,T;H^3(\Omega)^2 \cap H^1_{0,\mathrm{div}}(\Omega)^2\right)$$

for very special situations (cf. Remark 2.17). Then the assumption on the transport term stated in Theorem 2.9 would be fulfilled and we could obtain a unique

$$I \in L^2\left(0,T;H_0^1(\Omega)\right).$$

The next example shows a setting of assumptions for which the above sketch of the solution theory will work.

Example 2.22.
Let $\Omega = (0,1) \times (0,1)$. Moreover, we have

$$\begin{aligned} \boldsymbol{f} &\in L^2\left(0,T;(H_0^1(\Omega)^2)'\right) \cap L^\infty\left(0,T;L^2_{\mathrm{div}}(\Omega)^2\right), \\ \boldsymbol{u}^0 &\in H^3(\Omega)^2 \cap H^1_{0,\mathrm{div}}(\Omega)^2, \\ I^0 &\in H_0^1(\Omega) \end{aligned}$$

for $T > 0$ and we have $\nu \in \mathbb{R}^+ \setminus \{0\}$. Then there exists a unique solution pair

$$\{I, \boldsymbol{u}\} \in L^\infty\left(0,T;H_0^1(\Omega)\right) \times L^\infty\left(0,T;H^3(\Omega)^2 \cap H^1_{0,\mathrm{div}}(\Omega)^2\right).$$

Remark 2.23 (Boundary Control or Identification).
A big problem considering boundary control and identification problems is that non homogeneous boundary data, with a strongly prescribed boundary function $g \in H^{\frac{1}{2}}(\Omega)^2$ cannot be treated in this way.

In this case, we have only H^1-regularity (see Remark 2.10) of the transport field $\boldsymbol{u}$, which is not sufficient for Theorem 2.9.

For a proper well-posedness theory we have either to guarantee higher regularity of the boundary function g or to use other types of boundary conditions.

3. Discretisation and Numerical Treatment

In this chapter we will present all necessary techniques for the numerical calculation of the coupled system given in equation (2.12) in Chapter 2.4.

Since the equations are time-dependent we discuss the Rothe method for time discretisation with the implicit Euler or the Crank-Nicholson scheme. By this we obtain quasi stationary partial differential equations in each time step, which are then solved by the finite element method (FEM) with bilinear elements. Since we want to solve each component with the same class of elements we have to introduce stabilisation techniques to guarantee inf-sup stability. We use the local projection stabilisation (LPS) for this. Furthermore we describe Newton's method for solving the arising nonlinear system and present two common techniques for the stabilisation of transport dominant processes, the SUPG and a slightly modified LPS technique. For us it seems advisable to use the LP stabilisation, since it yields just as good results as the SUPG, but it has the property that *Discretise-then-Optimise* and *Optimise-then-Discretise* interchange with each other in context of PDE constrained optimisation problems.

Special attention is paid to the implementation of given boundary data. The reason is that weakly treated boundaries are easy to handle from a numerical point of view and very useful in the treatment of boundary control problems, which we will consider in Chapter 5. Here we extend a special suggestion for the Poisson problem from the literature to general convection-diffusion-reaction equations and the Navier-Stokes equations. By a bunch of numerical example we will show that weak implemented boundary conditions are almost equal to the strong implementation in terms of quality and quantity, even for transport dominant processes and the mentioned coupled system from Chapter 2.4.

3.1. Time Stepping Schemes

We use Rothe's method (cf. Grossmann et al. [44, Chapter 5.1.5]) for the time discretisation of the PDE problems discussed in the last chapter.

In a general form this PDE is usually given with the solution variable $u(t, \boldsymbol{x})$, which fulfils the following weak formulation

$$\begin{aligned} (\partial_t u(t), \varphi) + a\left(u(t), \varphi\right) &= \left(f(t), \varphi\right), \quad \forall \varphi \in V, \\ u(0) &= u^0 \end{aligned} \tag{3.1}$$

for almost all t in the time interval $I = (0, T]$. Here $a(\cdot, \cdot)$ denotes a bilinear form. The general case of semilinear forms can be reduced to this case (see Section 3.5.2).

We split the time interval I into subintervals of the form

$$I = \{0\} \cup I_1 \cup I_2 \cup \ldots \cup I_{M-1} \cup I_M,$$

with $I_m = (t_{m-1}, t_m]$, where $k_m := t_m - t_{m-1}$ represents the size of the mth subinterval and the time points are distributed in the following way

$$0 = t_0 < t_1 < \ldots < t_{M-1} < t_M = T.$$

Hence, the mentioned partition gives us the temporal grid.

For our theoretical discussion we discretise the weak formulation from formula (3.1) via the θ-method (cf. Grossmann et al. [44]):

For $m > 0$ we seek for a solution $u(t_m, \boldsymbol{x})$ in the time point t_m for a given $u(t_{m-1}, \boldsymbol{x})$, which fulfils

$$\frac{1}{k_m}\left(u(t_m) - u(t_{m-1}), \varphi\right) = \theta\left(\left(f(t_m), \varphi\right) - a(u(t_m), \varphi)\right) + \\ + (1-\theta)\left(\left(f(t_{m-1}), \varphi\right) - a(u(t_{m-1}), \varphi)\right), \quad \forall \varphi \in V.$$

By certain choices of θ we obtain classical time stepping schemes. We want to present three well-known examples:

1. For $\theta = 1$ we obtain the backward Euler scheme. Then, on every time point t_m with $m > 0$ we have to solve

   $$\left(u(t_m), \varphi\right) + k_m a\left(u(t_m), \varphi\right) = k_m\left(f(t_m), \varphi\right) + u(t_{m-1}, \varphi), \quad \forall \varphi \in V.$$

   The backward Euler method is a strongly A-stable, implicit time stepping scheme of first order accuracy. It damps out oscillations very quickly, but also oscillatory parts of the solution.

2. For the choice of $\theta = 0.5$ we obtain the Crank-Nicolson scheme (CN scheme). Here, we have to solve for every time point t_m, with $m > 0$, the equation

   $$\left(u(t_m), \varphi\right) + \frac{k_m}{2} a\left(u(t_m), \varphi\right) = \left(u(t_{m-1}) + \frac{k_m}{2}\left(f(t_m) + f(t_{m-1})\right), \varphi\right) \\ - \frac{k_m}{2} a\left(u(t_{m-1}), \varphi\right), \quad \forall \varphi \in V.$$

   This time-stepping scheme has an temporal accuracy of second order. It is also implicit, but only A-stable, which means that it preserves oscillating solutions since it has almost no dissipation. This property cause an advantage, but also a drawback for errors introduced by initial values or produced during the solution process. The CN scheme is not able to damp errors during the calculation and therefore disturbs our approximation.

3. A method suggested by Rannacher [85] yields better aproximations of our solutions. Therefore, we choose a fixed amount of backward Euler steps (e. g. two steps) at the beginning of the time stepping scheme and then switch over to the CN scheme simply by changing the parameter θ:

$$\theta_m = \begin{cases} 1, & \text{if } m < K, \\ 0.5, & \text{if } m \geq K. \end{cases}$$

This procedure is still accurate of second order, but in contrast to the pure CN scheme it damps out error contents of the initial solution.

Remark 3.1 (Further Time Stepping Techniques).
The shifted θ scheme adds $\frac{1}{k_m}$ to $\theta = 0.5$. It can be used for damping computational errors arising during long time computations (see Heywood et al. [52]), without losing the second order of convergence.

The Fractional-Step-θ scheme combines the positive aspects of the backward Euler and the CN scheme in a more complex way (see Bristeau et al. [20]).

Remark 3.2 (Time Discretisation for Optimisation Problems).
Meidner [77] uses Galerkin discretisations in time and space to guarantee the same discrete system independent in which order discretisation and optimisation is performed. The spatial discretisation with a Galerkin approach is presented in the next section. For the time discretisation we have the possibility to use either a discontinuous Galerkin method $dG(r)$ or a continuous Galkerin method $cG(r)$.
The $cG(r)$ method uses continuous trial functions of degree r and discontinuous test functions of degree $r-1$, while the $dG(r)$ method is based on the usage of discontinuous trial and test functions of degree r (see Erikson et al. [32, Chapter 9.2.1 & 9.2.2] for a detailed discussion).
However, we want to emphasise that the $dG(0)$ method, where all occurring integrals are evaluated with the box rule, leads directly to the above stated backward Euler scheme ($\theta = 1$ in the θ-scheme).
Furthermore the $cG(1)$ method, where all occurring temporal integrals are approximated with the trapezoidal rule, generates the CN scheme ($\theta = 0.5$).
For almost all optimisation problems consider in this work we will work with the dG(0) method for the temporal discretisation.

3.2. Finite Element Discretisation in Space

A well-established method for spatial discretisation is the finite element method (FEM). It is based on the discretisation of the following weak formulation of an general elliptic PDE or an elliptic part of a parabolic PDE, after discretisation in time has been performed by the methods presented in the last subsection.

Weak Formulation 3.3.
Find a suitable $u \in V$ such that

$$a(u, \varphi) = l(\varphi), \quad \forall \varphi \in V, \tag{3.2}$$

with a bilinear form $a(u, \varphi)$ and the linear form $l(\varphi)$.

Remark 3.4 (Nonlinear Equations).
We concentrate at first on the linear case. The general nonlinear case can be treated by Newton's method discussed later on.

The above stated weak formulation will now be discretised by searching a discrete solution u_h in the finite dimensional subspace $V_h \subset V$ which fulfils

$$a(u_h, \varphi_h) = l(\varphi_h), \quad \forall \varphi \in V_h. \tag{3.3}$$

The character of the discrete space V_h and its connection to the finite element method will be described below. Firstly, we describe how to derive an algebraic system of equations from equation (3.3). Therefore, we choose a basis $\xi_h^{(1)}, \ldots, \xi_h^{(N)}$ of V_h with $\dim(V_h) = N$. With this basis we have the following representation of the discrete solution

$$u_h = \sum_{i=1}^{N} \alpha_i \xi_h^{(i)}. \tag{3.4}$$

Substitution of this representation into the discrete weak formulation for each of the N basis functions leads to the following discrete system

$$A_h \boldsymbol{\alpha} = \boldsymbol{b}_h, \quad \text{or in more detail} \quad \sum_{i=1}^{N} \alpha_i a(\xi_h^{(i)}, \xi_h^{(j)}) = l(\xi_h^{(j)}), \quad j = 1, \ldots, N.$$

This system can now be solved by an arbitrary linear solver and the discrete solution can be generated by substitution of the solution vector α into the representation formula (3.3).

The essential part of the above mentioned discretisation is the choice of appropriate basis functions for the ansatz space V_h. In the finite element method we use polynomial functions for the approximation on a decomposition of the computational domain into subdomains of similar form and size (e.g. triangles or quadrilaterals in two space dimensions).

Throughout this work we will choose an ansatz space containing continuous functions, which are piecewise bilinear polynomials in $Q_1 = \text{span}\{1, x, y, xy\}$ on a grid of (regular) quadrilaterals (cf. Braess [18] and Brenner et al. [19]):

$$V_h := \{u_h : \bar{\Omega} \to \mathbb{R} \mid u_h \in C(\bar{\Omega}),\ u_h|_T \in Q_1\}.$$

3.3. Boundary Conditions with Weak Implementation

Later on we will consider the estimation of boundary conditions to recover a certain flow situation from given data of a passive tracer. Therefore the prescription of boundary data is a major aspect of this thesis.

We will describe in this subsection the concept of weakly formulated boundary conditions. This formulation has two positive aspects for us. At first, it is simple to handle for the implementation of the boundary conditions. The second aspect will be revealed in the later chapters, when we consider optimisation problems. We will see that the control variable, the distributed boundary function, enters directly in the optimisation framework, without using any sophisticated extension operators. Furthermore the connection to Robin-type boundary controls will become more obvious.

For starting the proceeding of weakly imposed boundary conditions we state the following strongly formulated Poisson problem:

$$\begin{aligned} -\Delta u &= f, && \text{in } \Omega, \\ \partial_n u &= \frac{1}{\mu}\left(q_D - u\right) + q_N, && \text{on } \partial\Omega. \end{aligned}$$

Then the weak formulation is given by searching a solution $u \in H^1(\Omega)$ such that

$$(\nabla u, \nabla \varphi) - \frac{1}{\mu}\left\langle q_D - u, \varphi \right\rangle_{\partial\Omega} - \left\langle q_N, \varphi \right\rangle_{\partial\Omega} = (f, \varphi), \quad \forall \varphi \in H^1(\Omega). \tag{3.5}$$

The parameter μ is crucial. If μ tends to infinity we see directly that the above weak formulation reduces to the weak formulation of a Poisson problem with Neumann boundary conditions.
On the other hand if $\mu \to 0$ the Dirichlet part, that means $q_D - u$, on the boundary becomes dominant.
This limit process can be used for the approximation of Dirichlet boundaries and is known as the penalty or penalised Neumann method in the literature. It goes back to the work of Babuška [2]. The big advantage of this weak implementation of Dirichlet boundary data is the computational simplicity, since we do not have to set the matrix values for the boundary in a strong manner. The drawback of this approach is that it leads to more and more ill-conditioned discrete problems when μ is chosen too small.

To overcome this difficulty Juntunen et al. [63] suggested a consistent stabilised version of the penalty method. They use the following weak formulation for the discretised problem:

Weak Formulation 3.5.
Find $u_h \in V_h$ such that

$$(\nabla u_h, \nabla \varphi_h) + b(q_{D,h}; u_h, \varphi_h) = (f, \varphi_h) + b_f(q_{N,h}; \varphi_h), \quad \forall \varphi_h \in V_h,$$

with

$$\begin{aligned} b(q_{D,h};u_h,\varphi_h) := &-\frac{\delta}{\mu+\delta}\left(\langle\partial_n u_h,\varphi_h\rangle_{\partial\Omega}+\left\langle u_h-q_{D,h},\partial_n\varphi_h\right\rangle_{\partial\Omega}\right)\\ &+\frac{1}{\mu+\delta}\left\langle u_h-q_{D,h},\varphi_h\right\rangle_{\partial\Omega}-\frac{\mu\delta}{\mu+\delta}\langle\partial_n u_h,\partial_n\varphi_h\rangle_{\partial\Omega} \end{aligned} \tag{3.6}$$

and

$$b_f(q_{N,h};\varphi_h) := \frac{\mu}{\mu+\delta}\left\langle q_{N,h},\varphi_h\right\rangle_{\partial\Omega}-\frac{\mu\delta}{\mu+\delta}\left\langle q_{N,h},\partial_n\varphi_h\right\rangle_{\partial\Omega}, \tag{3.7}$$

where $\delta>0$ is a user specified parameter.

Now we are able to choose $\mu=0$ for a fixed $\delta>0$. Then, by prescribing δ by a function depending on the mesh size $\delta:=\gamma(h)$ we obtain the well known Nitsche method [79]

$$\begin{aligned} (\nabla u_h,\nabla\varphi_h)-\langle\partial_n u_h,\varphi_h\rangle_{\partial\Omega}-\left\langle u_h-q_{D,h},\partial_n\varphi_h\right\rangle_{\partial\Omega}&\\ +\frac{1}{\gamma(h)}\left\langle u_h-q_{D,h},\varphi_h\right\rangle_{\partial\Omega}=(f,\varphi_h),\quad \forall\varphi_h\in V_h.& \end{aligned} \tag{3.8}$$

This approach is often used for the prescription of Dirichlet boundary values in a weak sense. Hence Babuška's penalty method and the Nitsche technique are connected via the above mentioned method.

This concept carries also over to the general convection-diffusion-reaction equation. For simplicity we consider here only the case, when $q_N=0$ and examine the formulation

$$-\nu\Delta u+\beta\cdot\nabla u+cu=f, \qquad \text{in } \Omega, \tag{3.9}$$

$$\nu\partial_n u=\frac{1}{\mu}(q_D-u)+\frac{1}{2}(\boldsymbol{\beta}\cdot\boldsymbol{n})\,u, \quad \text{on } \partial\Omega, \tag{3.10}$$

where the special form of the Robin-type boundary condition is needed for the solution theory.

Remark 3.6 (Solution Theory).
The solution theory for a fixed $\mu>0$ is obtained by a straightforward modification of the standard techniques mentioned in Chapter 2 and is presented in another context in the proof of Theorem 5.21 in Chapter 5.

For abbreviation purposes we skip now the index h. By introducing the bilinear form

$$a(u,\varphi):=\nu(\nabla u,\nabla\varphi)+(\beta\cdot\nabla u,\varphi)+(cu,\varphi)$$

and for the boundary part

$$\begin{aligned} b(q_D;u,\varphi):=&-\frac{\nu\delta}{\mu+\delta}\left(\langle\partial_{\boldsymbol{n}}u,\varphi\rangle_{\partial\Omega}+\langle u-q_D,\partial_{\boldsymbol{n}}\varphi\rangle_{\partial\Omega}\right)+\frac{1}{\mu+\delta}\langle u-q_D,\varphi\rangle_{\partial\Omega}\\ &-\frac{\nu\mu\delta}{\mu+\delta}\langle\partial_{\boldsymbol{n}}u,\partial_{\boldsymbol{n}}\varphi\rangle_{\partial\Omega}-\frac{\mu}{2(\mu+\delta)}\langle(\boldsymbol{\beta}\cdot\boldsymbol{n})u,\varphi\rangle_{\partial\Omega}\\ &+\frac{\delta\mu}{2(\mu+\delta)}\langle(\boldsymbol{\beta}\cdot\boldsymbol{n})u,\partial_{\boldsymbol{n}}\varphi\rangle_{\partial\Omega}, \end{aligned}$$

We finally obtain the weak formulation

$$a(u,\varphi) + b(q_D; u, \varphi) = (f, \varphi), \quad \forall \varphi \in V. \tag{3.11}$$

Lemma 3.7. *A solution of problem (3.9)-(3.10) also satisfies equation (3.11).*

Proof. Firstly, equation (3.9) is integrated over the domain after multiplying with an arbitrary test function $\varphi \in V$. Integration by parts yields

$$a(u,\varphi) - \nu \langle \partial_{\boldsymbol{n}} u, \varphi \rangle_{\partial\Omega} = (f, \varphi)\,. \tag{3.12}$$

We multiply now formula (3.10) with the same test function and integrate over the boundary. Then multiplication with

$$\frac{1}{\mu + \delta}$$

leads to

$$\frac{\mu\nu}{\mu+\delta} \langle \partial_{\boldsymbol{n}} u, \varphi \rangle_{\partial\Omega} = \frac{1}{\mu+\delta} \langle q_D - u, \varphi \rangle_{\partial\Omega} + \frac{\mu}{2(\mu+\delta)} \langle (\boldsymbol{\beta}\cdot\boldsymbol{n}) u, \varphi \rangle_{\partial\Omega}\,. \tag{3.13}$$

Doing the same again with the test function $\partial_{\boldsymbol{n}}\varphi$ and the factor

$$-\frac{\delta}{\mu+\delta}$$

we get

$$-\frac{\delta\nu\mu}{\mu+\delta} \langle \partial_{\boldsymbol{n}} u, \partial_{\boldsymbol{n}}\varphi \rangle_{\partial\Omega} = -\frac{\delta}{\mu+\delta} \langle q_D - u, \partial_{\boldsymbol{n}}\varphi \rangle_{\partial\Omega} - \frac{\delta\mu}{2(\mu+\delta)} \langle (\boldsymbol{\beta}\cdot\boldsymbol{n}) u, \partial_{\boldsymbol{n}}\varphi \rangle_{\partial\Omega}\,. \tag{3.14}$$

The equation (3.11) is now the sum of equations (3.12), (3.13) and (3.14). □

Again we can consider the case $\mu = 0$ for the bilinear form $b(q_D; u, \varphi)$ and obtain a Nitsche-type formulation for the convection-diffusion equation

$$b_{\mathrm{Ni}}(q_D; u, \varphi) = -\nu \left(\langle \partial_{\boldsymbol{n}} u, \varphi \rangle_{\partial\Omega} + \langle u - q_D, \partial_{\boldsymbol{n}}\varphi \rangle_{\partial\Omega} \right) + \frac{1}{\delta} \langle u - q_D, \varphi \rangle_{\partial\Omega}\,, \tag{3.15}$$

with an appropriate choice of δ in dependence of the mesh size h.

Remark 3.8 (Time-Dependent Equations).
As mentioned in the section about the time stepping schemes in the beginning of this chapter in the Rothe method we have to solve in each time step a quasi-stationary equation, with an additional reaction-type part

$$\frac{1}{k_m} (u(t_m), \varphi)\,.$$

This equation fits in the discussed setting and therefore we can apply the implementation of weak boundary conditions also to time-dependent convection-diffusion equations.

Remark 3.9 (Consistency to the Linear Transport Equation).
Chosing $\nu = 0$ we have the linear transport equation. In this case the boundary form $b(q_D; u, \varphi)$ degenerates to

$$b(q_D; u, \varphi) = \frac{1}{\mu + \delta} \left(\langle u - q_D, \varphi \rangle_{\partial\Omega} - \frac{\mu}{2} \langle (\boldsymbol{\beta} \cdot \boldsymbol{n})\, u, \varphi \rangle_{\partial\Omega} + \frac{\delta\mu}{2} \langle (\boldsymbol{\beta} \cdot \boldsymbol{n})\, u, \partial_{\boldsymbol{n}} \varphi \rangle_{\partial\Omega} \right).$$

Without the stabilisation, $\delta = 0$, we obtain

$$b(q_D; u, \varphi) = \frac{1}{\mu} \langle u - q_D, \varphi \rangle_{\partial\Omega} - \frac{1}{2} \langle (\boldsymbol{\beta} \cdot \boldsymbol{n})\, u, \varphi \rangle_{\partial\Omega}.$$

Setting $\mu = 0$ and $\delta \geq \delta_0 > 0$ we yield a Nitsche-type formulation for the weak prescription of Dirichlet boundary data

$$b(q_D; u, \varphi) = \frac{1}{\delta} \langle u - q_D, \varphi \rangle_{\partial\Omega}.$$

Furthermore we have the opportunity to prescribe only the inflow boundary condition on Γ_{In}, that means all $\boldsymbol{x} \in \partial\Omega$, such that $\boldsymbol{\beta} \cdot \boldsymbol{n} < 0$. By choosing the positive parameter δ as follows

$$0 < \delta := -\frac{1}{(\boldsymbol{\beta} \cdot \boldsymbol{n})}$$

we obtain

$$b(q_D; u, \varphi) := -\left\langle (\boldsymbol{\beta} \cdot \boldsymbol{n})(u - q_D), \varphi \right\rangle_{\Gamma_{In}}. \tag{3.16}$$

This formulation is consistent with a suggestion for Nitsche-type inflow presented in the work of Freund et al. [36].

Now we are able to prescribe different kinds of boundary conditions at different parts of the domain's boundary simply by the choice of μ and δ. Hence, boundary conditions can be handled very elegantly from a computational point of view.
Moreover, in the case of the Laplace equation it was shown in the cited literature, that there are almost no differences in terms of the accuracy or convergence properties, between the strong or the weak implementation of the Dirichlet boundary data.

The following examples indicate that this is also valid for the time-dependent convection-diffusion-reaction equation:

Example 3.10.
For our example we choose the following parameters:

$$\nu = 0.1, \qquad \boldsymbol{\beta} = (-y, x)^T, \qquad c = 0 \qquad \text{and} \qquad f = 0.$$

On the outflow boundary, $\boldsymbol{\beta} \cdot \boldsymbol{n} > 0$, we prescribe zero Neumann conditions and the Dirichlet condition is given by

$$q_D^{(1)} = \begin{cases} -16(x - \frac{1}{4})(x - \frac{3}{4}), & \text{if } y = 0 \text{ and } x \in [\frac{1}{4}, \frac{3}{4}], \\ 0, & \text{if } y = 0 \text{ and } x \in [0, \frac{1}{4}) \cup (\frac{3}{4}, 1], \text{ or } y = 1 \text{ and } x \in [0, 1]. \end{cases}$$

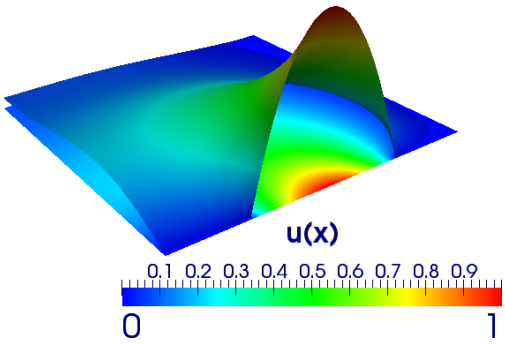

Figure 3.1. Reference solution u_{h_9} at the end time point $T = 1$. It was calculated on an equidistant time grid with $k = 0.01$ and 262144 spatial nodes.

The time interval is given by $I = [0, 1]$ *and the initial function* u^0 *is zero, except from the above mentioned boundary part. For the time discretisation we use the time-step size* $k = 0.01$. *Then Figure 3.1 visualises the solution for a fine spatial discretisation.*

Table 3.1. Approximation error for the Babuška approach with $\delta = 0$ and either $\mu = h$ (denoted by $u_{h_i}^{(I)}$) or $\mu = h^2$ (denoted by $u_{h_i}^{(II)}$).

n		$\|u_{h_9}(1) - u_{h_i}^{((\mathrm{I}))}(1)\|_{L^2(\Omega)}$	**(rate)**	$\|u_{h_9}(1) - u_{h_i}^{((\mathrm{II}))}(1)\|_{L^2(\Omega)}$	**(rate)**
16	(h_2)	$5.4805 \cdot 10^{-2}$		$3.7324 \cdot 10^{-2}$	
64	(h_3)	$3.6551 \cdot 10^{-2}$	**(0.58)**	$9.5563 \cdot 10^{-3}$	**(1.98)**
256	(h_4)	$2.5465 \cdot 10^{-2}$	**(0.52)**	$2.2491 \cdot 10^{-3}$	**(2.04)**
1024	(h_5)	$1.5941 \cdot 10^{-2}$	**(0.68)**	$5.1633 \cdot 10^{-4}$	**(2.06)**
4096	(h_6)	$9.1364 \cdot 10^{-3}$	**(0.80)**	$1.2110 \cdot 10^{-4}$	**(2.05)**
16384	(h_7)	$4.9378 \cdot 10^{-3}$	**(0.89)**	$2.8686 \cdot 10^{-5}$	**(2.04)**
		$\approx$	1	$\approx$	2

Tables 3.1 and 3.2 show the comparison of the strong implementation of Dirichlet boundary conditions (as given in the used software library Gascoigne [12]) to the weak implementation presented in this subsection (we perform the weak implementation in the same FEM library). We see that all approaches, the strong implementation, the Babuška technique and Nitsche's method, behave equally well under mesh refinement. The drawback of Babuška's method is that the system matrix becomes more and more ill-conditioned as μ *tends to zero. This can be observed if we work with an iterative linear solve (e.g. GMRES or multi grid method) and document the number of iterations to reach a required tolerance. The number of steps increases for a decreasing* μ. *At a certain point, we are not able to drop below the chosen tolerance.*

Table 3.2. Comparison between the solutions of a strong implementation ($u_{h_i}^{(s)}$ left) and weak implementation ($u_{h_i}^{(w)}$ right) of Dirichlet data for the above mentioned example. We choose the parameters $\mu = 0$ and $\delta = \frac{h}{2 \cdot 10^6}$ in the computation with the weak boundary conditions.

n		$\|u_{h_9}(1) - u_{h_i}^{(s)}(1)\|_{L^2(\Omega)}$	**(rate)**	$\|u_{h_9}(1) - u_{h_i}^{(w)}(1)\|_{L^2(\Omega)}$	**(rate)**
16	(h_2)	$3.6920 \cdot 10^{-2}$		$3.3736 \cdot 10^{-2}$	
64	(h_3)	$1.0511 \cdot 10^{-2}$	**(1.81)**	$7.0302 \cdot 10^{-3}$	**(2.26)**
256	(h_4)	$2.8277 \cdot 10^{-3}$	**(1.89)**	$1.6388 \cdot 10^{-3}$	**(2.09)**
1024	(h_5)	$7.4948 \cdot 10^{-4}$	**(1.92)**	$4.2435 \cdot 10^{-4}$	**(1.96)**
4096	(h_6)	$1.9902 \cdot 10^{-4}$	**(1.91)**	$1.1114 \cdot 10^{-4}$	**(1.93)**
16384	(h_7)	$5.5419 \cdot 10^{-5}$	**(1.84)**	$2.8843 \cdot 10^{-5}$	**(1.95)**
		$\approx$	2	$\approx$	2

Now we consider a discontinuous boundary condition to confirm the same behaviour of both methods under mesh refinement, although the order of convergence is reduced in this case.

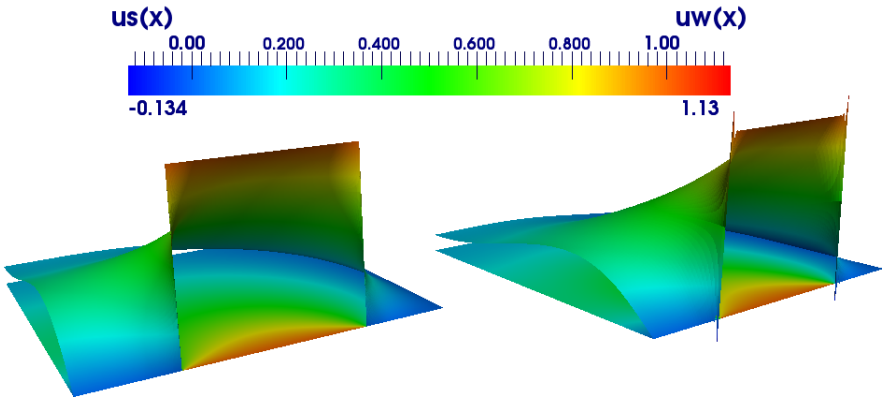

Figure 3.2. Left: Reference solution. Right: Weak approximative solution.

Example 3.11.
We make the same general assumptions as in the first example:

$$\nu = 0.1, \qquad \boldsymbol{\beta} = (-y, x)^T, \qquad c = 0 \qquad \text{and} \qquad f = 0.$$

On the outflow boundary we prescribe zero Neumann conditions and the Dirichlet condition is given by

$$q_D^{(2)} = \begin{cases} 1, & \text{if } y = 0 \text{ and } x \in [\frac{1}{4}, \frac{3}{4}], \\ 0, & \text{if } y = 0 \text{ and } x \in [0, \frac{1}{4}) \cup (\frac{3}{4}, 1], \quad \text{or } y = 1 \text{ and } x \in [0, 1]. \end{cases}$$

The left figure in Figure 3.2 shows the solution calculated with a high resolution in space

and time. The right picture shows the approximative solution with the weak implementation of the boundary data $u_{h_7}^{(w)}$.

Table 3.3. Comparison between the solutions of a strong realisation ($u_h^{(s)}$ left) and weak implementation ($u_h^{(w)}$ right) of Dirichlet data given by $q_D^{(2)}$. Here $e_i(1)$ denotes the L^2-error for the following three cases: $(i = 1)$ strong implementation, $(i = 2)$ weak implementation with $\mu = 0$ and $\delta = \frac{h}{2 \cdot 10^6}$ (Nitsche) and $(i = 3)$ weak implementation with $\mu = h^2$ and $\delta = 0$ (Babuška).

n		$e_1(1)$	**(rate)**	$e_2(1)$	**(rate)**	$e_3(1)$	**(rate)**
16	(h_2)	$9.8953 \cdot 10^{-2}$		$9.0139 \cdot 10^{-2}$		$8.5817 \cdot 10^{-2}$	
64	(h_3)	$6.2585 \cdot 10^{-2}$	**(0.63)**	$4.4553 \cdot 10^{-2}$	**(1.02)**	$4.3177 \cdot 10^{-2}$	**(0.99)**
256	(h_4)	$3.5042 \cdot 10^{-2}$	**(0.84)**	$2.2277 \cdot 10^{-2}$	**(1.00)**	$2.1727 \cdot 10^{-2}$	**(0.99)**
1024	(h_5)	$1.8528 \cdot 10^{-2}$	**(0.92)**	$1.1231 \cdot 10^{-2}$	**(0.99)**	$1.1069 \cdot 10^{-2}$	**(0.97)**
4096	(h_6)	$9.2703 \cdot 10^{-3}$	**(1.00)**	$5.7986 \cdot 10^{-3}$	**(0.95)**	$5.7568 \cdot 10^{-3}$	**(0.94)**
16384	(h_7)	$4.2118 \cdot 10^{-3}$	**(1.14)**	$3.2087 \cdot 10^{-3}$	**(0.85)**	$3.2014 \cdot 10^{-3}$	**(0.85)**
		$\approx$	1	$\approx$	1	$\approx$	1

Table 3.3 compares the strong implementation of the above given discontinuous Dirichlet boundary conditions to the weak implementation with Nitsche's and Babuška's method. Although the order of convergence reduces to one the methods behave equally well under mesh refinement. The reason for the order reduction is the reduced regularity of the solution in this case. We want also to emphasise that the weak solution shows a slightly oscillatory behaviour in the vicinity of the discontinuities on the boundary, which is not the case in the strong implementation (see Figure 3.2).
At first glance this seems like a drawback, since we want to conserve positivity of the intensity function in our application later on, but on the other hand the oscillation only affects the patch of cells around the discontinuities on the boundary and smooths out in the interior of the domain. Hence, the influence of these artefacts gets lost under mesh refinement.

With the last example we want to investigate the behavior of the solution for different choices of the parameter δ.

Example 3.12. *Therefore we choose the same configuration as in Example 3.10 and observe the changes of the discrete solution on the* 4096*-node grid while we change* δ_0 *in*

$$\delta = \frac{h}{\delta_0}.$$

Table 3.4. Changing parameter $\delta = \frac{h}{\delta_0}$.

δ_0	$\|u_{h_9}(T) - u_{h_6}^{(\mathrm{w})}(T)\|_{L^2(\Omega)}$
1	$1.7905 \cdot 10^{-2}$
10	$1.8813 \cdot 10^{-3}$
100	$1.7988 \cdot 10^{-4}$
1000	$1.0500 \cdot 10^{-4}$
10000	$1.1067 \cdot 10^{-4}$
100000	$1.1137 \cdot 10^{-4}$

Table 3.4 gives us an overview of the quality of the approximation if we increase δ_0. Obviously the approximation becomes better for larger δ_0 and stays qualitatively on the same level also for choices of huge values for δ_0. So we decide to skip any further investigation of an appropriate choice of δ_0 and take big values for this parameter.

To sum up we have discussed a methodology to implement Dirichlet, Neumann or Robin boundary conditions in a weak sense, by prescribing two parameters, for a general time-dependent convection-diffusion equation. In the case of Dirichlet boundary conditions we observed by numerical experiments almost equally well behaviour in terms of convergence and quality of the approximation in comparison to the strong implementation. We assume therefore that the theoretical results presented in the literature for the Poisson problem and the time-independent convection-diffusion equation carry over to our case, and skip a further investigation.

We will now concentrate on another important aspect, when dealing with the approximation of convection-diffusion equations. Since we want to work with continuous finite elements, we have to introduce transport stabilisation in the case of dominant convection.

3.4. Stabilisation for Transport-Dominated Flows

Starting point is again the weak formulation of a convection-diffusion equation

$$(\partial_t u(t), \varphi) + \varepsilon \left(\nabla u(t), \nabla \varphi\right) + \left(\boldsymbol{\beta}(t) \cdot \nabla u(t), \varphi\right) = \left(f(t), \varphi\right), \quad \forall \varphi \in V.$$

For us, the case $f = 0$ and $\varepsilon \ll 1$ is of special interest, since it corresponds to the (physics-based) optical flow equation, which we will use in our later investigations. For notational brevity we therefore choose $f = 0$ and remark that the argumentation will be straightforward with a general right hand side.

With Rothe's method from Section 3.1 we generate the following quasi-stationary equation

$$\begin{aligned}(u_m, \varphi) + k_m\theta \left(\varepsilon \left(\nabla u_m, \nabla \varphi\right) + \left(\boldsymbol{\beta}_m \cdot \nabla u_m, \varphi\right)\right) \\ = (u_{m-1}, \varphi) + k_m(1-\theta) \left(\varepsilon \left(\nabla u_{m-1}, \nabla \varphi\right) + \left(\boldsymbol{\beta}_{m-1} \cdot \nabla u_{m-1}, \varphi\right)\right)\end{aligned}$$

for all $\varphi \in V$, where $u_m = u(t_m)$.

Hence we have to solve an elliptic convection-diffusion-reaction equation of the form

$$\hat{\varepsilon}\left(\nabla u, \nabla\varphi\right) + \left(\hat{\boldsymbol{\beta}} \cdot \nabla u, \varphi\right) + \left(u, \varphi\right) = \left(g, \varphi\right), \quad \forall \varphi \in V \tag{3.17}$$

in every time-step, where

$$\hat{\varepsilon} = k_m \theta \varepsilon, \qquad \hat{\boldsymbol{\beta}} = k_m \theta \boldsymbol{\beta},$$
$$\left(g, \varphi\right) = \left(u_{m-1}, \varphi\right) + k_m(1-\theta)\left(\varepsilon\left(\nabla u_{m-1}, \nabla\varphi\right) + \left(\boldsymbol{\beta}_{m-1} \cdot \nabla u_{m-1}, \varphi\right)\right).$$

This convection-diffusion-reaction equation is also well-posed (cf. Evans [33, Chapter 6]) since $\nabla \cdot \boldsymbol{\beta} = 0$.

We now consider a finite element approximation $u_h \in V_h$ of equation (3.17)

$$\hat{\varepsilon}\left(\nabla u_h, \nabla\varphi_h\right) + \left(\hat{\boldsymbol{\beta}} \cdot \nabla u_h, \varphi_h\right) + \left(u_h, \varphi_h\right) = \left(g, \varphi_h\right), \quad \forall \varphi_h \in V_h.$$

It is well known that spurious ocsillations can be introduces in the approximation, when we work with a continuous finite element ansatz space V_h for the mentioned convection dominant problem. Thus we need to stabilise the discretisation by techniques, which are presented in the next subsection.

3.4.1. Streamline-Upwind-Petrov-Galerkin

The SUPG-method (Streamline-Upwind-Petrov-Galerkin) is based on adding the term

$$s(u_h, \varphi_h) := \sum_{T \in \mathbb{T}_h} \delta_T \left(\mathrm{Res}(u_h), \hat{\boldsymbol{\beta}} \cdot \nabla\varphi_h\right)$$

to the left hand side of equation (3.17). Here $\mathrm{Res}(\cdot)$ denotes the residual of equation (3.17)

$$\mathrm{Res}(u) = -\hat{\varepsilon}\Delta u + \hat{\boldsymbol{\beta}} \cdot \nabla u + u - g. \tag{3.18}$$

The essential term which is responsible for the stabilisation is

$$\left(\hat{\boldsymbol{\beta}} \cdot \nabla u_h, \hat{\boldsymbol{\beta}} \cdot \nabla\varphi_h\right).$$

The other terms only guarantee the consistency of the method since the bilinear form $s(\cdot,\cdot)$ should become small for a good approximation u_h to the solution u.

Unfortunately the computation of the whole residual is costly and with bilinear elements even impossible, due to the appearing Laplacian. That is the reason why we will work with a quasi-consistent SUPG method, where we avoid the diffusion term in equation (3.18). Therefore we modify the discrete version of equation (3.17) by

$$\hat{\varepsilon}\left(\nabla u_h, \nabla\varphi_h\right) + \left(\hat{\boldsymbol{\beta}} \cdot \nabla u_h + u_h, \varphi_h\right) + s(u_h, \varphi_h) = \left(g, \varphi_h\right), \quad \forall \varphi_h \in V_h. \tag{3.19}$$

The convergence of the method is then guaranteed by the choice of the parameter

$$\delta_T = \min\left\{\frac{h}{2|\hat{\boldsymbol{\beta}}|}, \frac{h^2}{\theta k_m \varepsilon}, 1\right\},$$

where $|\cdot|$ denotes the Euclidean norm. It holds $\delta \sim h$ and therefore the stabilisation term tends to zero with h tending to zero for better approximations. For further details of this method see the monograph of Kuzmin [70].

3.4.2. Local Projection Stabilisation for Convection Dominance

Another possibility for the convection stabilisation was introduced in the work of Becker et al. [10]. In this work the authors analyse a stabilisation based on local projections (LPS) for the steady problem

$$u + (\boldsymbol{\beta} \cdot \nabla)\, u = f, \quad \text{in } \Omega.$$

As mentioned before we obtain exactly this formulation in every time step, after using the θ-method for time-discretisation. See therefore equation (3.19) with $\hat{\varepsilon} = 0$. We set

$$s(u_h, \varphi_h) = s_{\mathrm{LPS}}(u_h, \varphi_h) := \sum_{T \in \mathcal{T}_h} \delta_T \left(\pi_h \left(\boldsymbol{\beta} \cdot \nabla u_h\right), \pi_h \left(\boldsymbol{\beta} \cdot \nabla \varphi\right)\right)$$

as stabilisation term. The operator $\pi_h = I - \mathcal{P}_{2h}$ consists of the difference of the identity operator and a projection operator

$$\mathcal{P}_{2h} : V_h \to V_{2h}$$

defining a mapping of the current trial function space V_h onto the coarser one V_{2h}. The so defined mapping measures fluctuations of the convection term. The parameter δ_T is chosen as follows

$$\delta_T = \delta_0 \frac{h}{k\theta|\boldsymbol{\beta}|}.$$

This scheme also stabilise the original unstable problem in almost the same quality like the SUPG scheme as the following benchmark examples indicates. However, an import advantage is that the procedures “optimise” and “discretise” can be interchanged for the LPS approach, which makes the LPS approach more reliable for our optimisation problems later on.

3.4.3. Numerical Examples

In the literature stabilisation techniques are usually compared through several benchmark tests. We want to present calculations for the above two stabilisation techniques to show that both methods work equally well. Therefore we present briefly the results of both techniques for the slotted disc benchmark, which can also be found in John et al. [62].

Example 3.13 (Slotted Disc Benchmark).
In the slotted disc benchmark three different structures are rotated in the computational domain $\Omega = [0,1]^2$ *by the divergence free transport field* $\boldsymbol{\beta} = (0.5 - y, x - 0.5)$ *on the time interval* $[0,T]$. *Furthermore* $\varepsilon \approx 0$ *and* $f = 0$. *The initial value* u^0 *represents three structures, which have the form of a slotted cylinder, a cone and a hump (see Figure 3.3).*

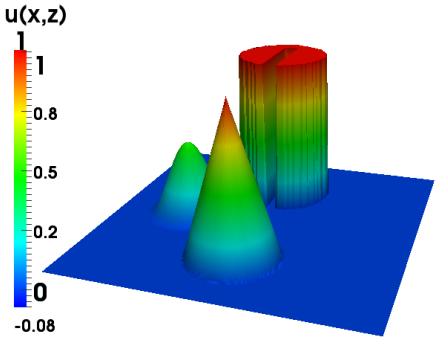

Figure 3.3. Initial configuration: $u(\boldsymbol{x}, 0)$. Slotted disc benchmark.

The computed solution u_h is then compared after a whole rotation $T = 2\pi \approx 6.28$ to the initial value. We made two calculations with a CN-scheme initiated by two Euler steps on a 129×129 nodes grid with 1000 time steps. The first one is the 'quasi-consistent' version of the SUPG method, where only the Laplacian is not taken into account due to the choice of bilinear trial functions (cf. discussion above).
The second method is the LPS technique described in the last subsection. In this situation we choose the stabilisation parameter $\delta_0 = 0.3$.

Figure 3.4 shows the results of these calculations (Left: SUPG. Right: LPS). Qualitatively there is almost no difference between these two methods. Hence, we will prefer the LPS method for the optimisation problems, due to the mentioned advantage in the context of optimisation problems.

Furthermore Figure 3.4 (bottom) shows that smooth structures like the hump are not affected by the stabilisation. In fact for C^∞-structures we need no stabilisation at all. Without stabilisation the transport of the cone structure leads to serious oscillations, which propagate through the whole computational domain. This effect can be captured by both methods equally well. In contrast the sharp edges of the slotted cylinder pollute the solution of the transport process, unless we choose very fine spatial and temporal grids. In view of image processing applications this is a serious issue, since in general sharp edges in an intensity distribution are given in most cases.

With the second example we want to emphasise that the weak formulation of the boundary data (see last section) does not essentially influence the behaviour of the LPS method.

Example 3.14 (LPS and Weak Boundary Conditions).
Here we use the flow field $\boldsymbol{\beta} = (-y, x)^T$. *The parameter* ε *is chosen very small and* $f = 0$.

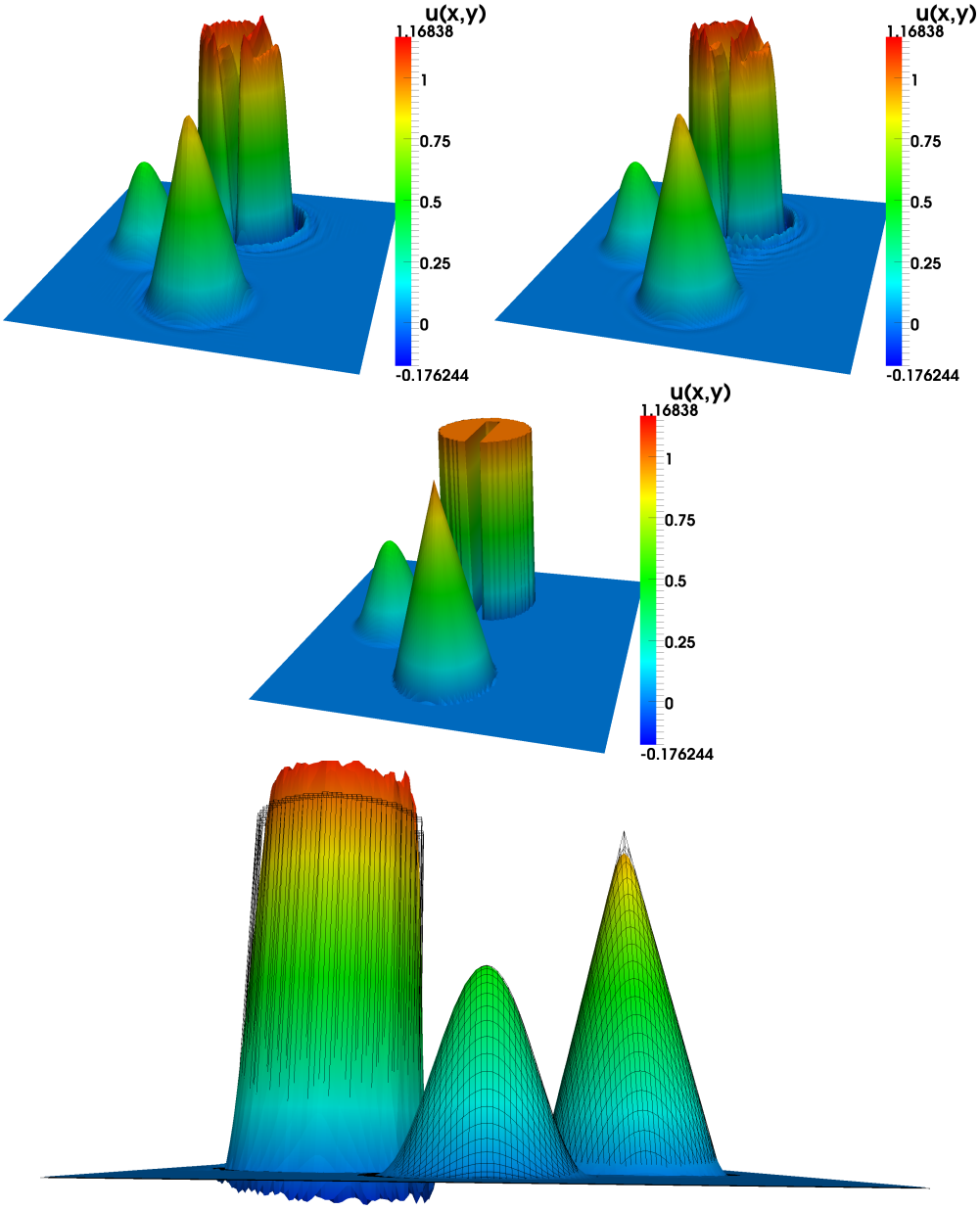

Figure 3.4. Benchmark after one rotation.
Top Left: SUPG method. Error: $\|u_h(T) - \hat{u}\|_2 = 6.596e-2$ and Var= $\max(u_h(T)) - \min(u_h(T)) = 1.35$.
Top Right: LPS method. Error: $\|u_h(T) - \hat{u}\|_2 = 6.913e-2$ and Var= 1.29.
Center: Expected solution for comparison.
Bottom: Comparison between the LPS solution and the expected one. The hump structure is unaffected by the stabilisation. Also the cone structure is almost exactly transported, while the slotted disc is heavily disturbed.

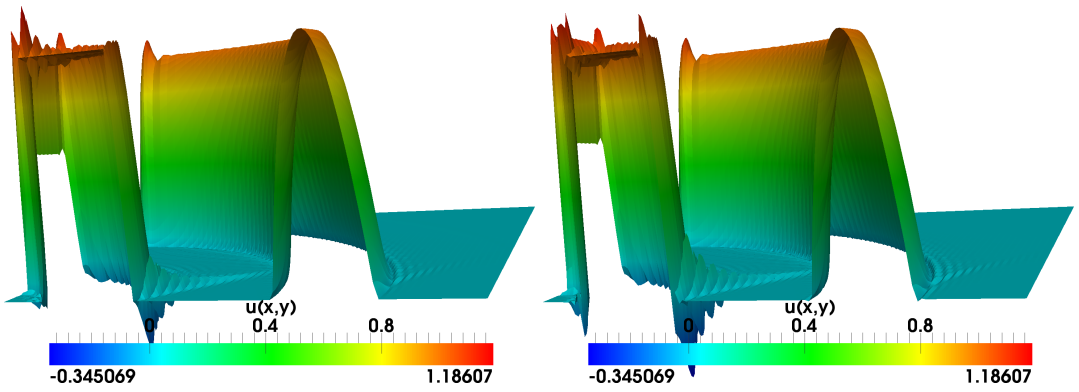

Figure 3.5. LP-stabilisation for a time-dependent convection-diffusion equation. Left: Strongly implemented boundary data on the inflow boundary. Right: Weakly formulated boundary conditions on the inflow boundary.

We consider the time interval $[0, \frac{\pi}{4}]$ *with 1000 time steps and a spatial resolution with 129×129 nodes. We set the boundary on the inflow boundary (*$\Gamma_{in} = [0, 1]$*)*

$$g(x,y) = \begin{cases} 1, & \forall x \in [0.1, 0.3], \\ -100(x-0.6)\cdot(x-0.8), & \forall x \in [0.6, 0.8], \\ 0, & else, \end{cases}$$

which is transported into the computational domain. As stabilisation we use LPS.

The results for a strong implementation of the above given boundary function (left picture) and a weak formulation of the boundary data (right picture) are given in Figure 3.5. The smooth part of the boundary function is transported in the same way for both formulations. However, the box signal shows peaks in the discontinuities on the boundary, but the LPS technique damps this oscillations in the interior of the domain. Thus, the transport of the signal into the interior of the domain is almost similar.

3.5. Nonstationary Navier-Stokes Equations

The Navier-Stokes system bears several difficulties we have to deal with, due to its saddle point character and its nonlinearity. We start with the continuous weak formulation

$$\begin{aligned} (\partial_t \boldsymbol{u}(t), \boldsymbol{\varphi}) + \nu\,(\nabla \boldsymbol{u}(t), \nabla \boldsymbol{\varphi}) + (\boldsymbol{u}(t)\cdot\nabla \boldsymbol{u}(t), \boldsymbol{\varphi}) - (p(t), \nabla\cdot\boldsymbol{\varphi}) &= (\boldsymbol{f}(t), \boldsymbol{\varphi})\,, \quad \forall \boldsymbol{\varphi} \in V, \\ (\mu, \nabla\cdot\boldsymbol{u}(t)) &= 0, \qquad\qquad \forall \mu \in M, \end{aligned}$$

with V denoting the test space for the velocity components, which is chosen as $H_0^1(\Omega)^n$ as long as we use homogeneous boundary data, and M the space for the pressure component,

which is usually $L^2(\Omega) \setminus \mathbb{R}$. By setting

$$a(\boldsymbol{u})(\boldsymbol{\varphi}) := \nu \left(\nabla \boldsymbol{u}(t), \nabla \boldsymbol{\varphi}\right) + \left(\boldsymbol{u}(t) \cdot \nabla \boldsymbol{u}(t), \boldsymbol{\varphi}\right) - \left(p(t), \nabla \cdot \boldsymbol{\varphi}\right)$$

we can use the Rothe technique from Section 3.1 by applying the θ-method to the differential part of the equation system so that we obtain the quasi stationary problem

$$\begin{aligned} \left(\boldsymbol{u}_m, \boldsymbol{\varphi}\right) + k_m \theta \left(\nu \left(\nabla \boldsymbol{u}_m, \nabla \boldsymbol{\varphi}\right) + \left(\boldsymbol{u}_m \cdot \nabla \boldsymbol{u}_m, \boldsymbol{\varphi}\right) - \left(p_m, \nabla \cdot \boldsymbol{\varphi}\right)\right) &= \left(\mathcal{F}, \boldsymbol{\varphi}\right), \\ \left(\mu, \nabla \cdot \boldsymbol{u}_m\right) &= 0 \end{aligned} \tag{3.20}$$

for all $\boldsymbol{\varphi} \in V$ and $\mu \in M$, with an $\mathcal{F}$ which consists of the known problem data and the already calculated solution $u_{m-1} := u(t_{m-1})$.

We deal with the nonlinearity by using Newton's method. For the resulting linear subproblems we will discuss the stabilisation of the pressure approximation, since we work with an equal order approximation for pressure and velocity, which is not inf-sup stable, by itself.

3.5.1. Weak Boundary Conditions

We want to describe how Nitsche's method can be applied to the nonstationary Navier-Stokes system. The main issues are already developed in an article and the habilitation thesis of Becker (cf. [7] and [8]) for the stationary Navier-Stokes equations.

Starting point for our considerations is a quasi-stationary problem (3.20) in an arbitrary time-step t_m.

For abbreviation purposes we skip the index m and divide the whole equation by $k_m\theta$. Hence we obtain

$$\begin{aligned} \nu \left(\nabla \boldsymbol{u}, \nabla \boldsymbol{\varphi}\right) + \left(\boldsymbol{u} \cdot \nabla \boldsymbol{u}, \boldsymbol{\varphi}\right) - \left(p, \nabla \cdot \boldsymbol{\varphi}\right) + \kappa \left(\boldsymbol{u}, \boldsymbol{\varphi}\right) &= \left(\boldsymbol{f}, \boldsymbol{\varphi}\right), && \forall \boldsymbol{\varphi} \in V, \\ \left(\nabla \cdot \boldsymbol{u}, \psi\right) &= 0, && \forall \psi \in M, \end{aligned}$$

where $\kappa > 1$, since we assume that $k_m\theta \in (0, 1]$. This weak formulation is only appropriate as long as we have $V = H_0^1(\Omega)^n$. In the case $V = H^1(\Omega)^n$ we have to add the boundary bilinear form

$$b(\{\boldsymbol{u}, p\}, \boldsymbol{\varphi}) := -\nu \left\langle \partial_{\boldsymbol{n}} \boldsymbol{u}, \boldsymbol{\varphi} \right\rangle_{\partial\Omega} + \left\langle p\boldsymbol{n}, \boldsymbol{\varphi} \right\rangle_{\partial\Omega} \tag{3.21}$$

due to integration by parts.

Moreover, we define the following (semi-) linear forms

$$\begin{aligned} a(\boldsymbol{u})(\boldsymbol{\varphi}) &:= \nu \left(\nabla \boldsymbol{u}, \nabla \boldsymbol{\varphi}\right) + \left(\boldsymbol{u} \cdot \nabla \boldsymbol{u}, \boldsymbol{\varphi}\right) + \kappa \left(\boldsymbol{u}, \boldsymbol{\varphi}\right), \\ c(p, \boldsymbol{\varphi}) &:= -\left(p, \nabla \cdot \boldsymbol{\varphi}\right) \end{aligned}$$

and have

$$\begin{aligned} a(\boldsymbol{u})(\boldsymbol{\varphi}) + b(\{\boldsymbol{u}, p\}, \boldsymbol{\varphi}) + c(p, \boldsymbol{\varphi}) &= \left(\boldsymbol{f}, \boldsymbol{\varphi}\right), && \forall \boldsymbol{\varphi} \in V, \\ -c(\mu, \boldsymbol{u}) &= 0, && \forall \mu \in M. \end{aligned} \tag{3.22}$$

We can now in general act as in Section 3.3 and introduce a weak implementation of the boundary data by replacing $b(\cdot,\cdot)$ by an appropriate formulation of the strongly formulated boundary data

$$\nu\partial_{\boldsymbol{n}}\boldsymbol{u} - p\boldsymbol{n} = \frac{1}{\mu}(\boldsymbol{q}_D - \boldsymbol{u}) + \frac{1}{2}(\boldsymbol{u}\cdot\boldsymbol{n})\,\boldsymbol{u}. \tag{3.23}$$

Remark 3.15 (Connection to the Solution Theory).
The second part of the right hand side of equation (3.23) is introduced for the solution theory of the resulting modification of the Navier-Stokes system, since

$$(\boldsymbol{u}\cdot\nabla\boldsymbol{u},\boldsymbol{u}) = \frac{1}{2}\langle(\boldsymbol{u}\cdot\boldsymbol{n})\boldsymbol{u},\boldsymbol{u}\rangle_{\partial\Omega}$$

cancels out in the usual argumentation of finding appropriate uniform bounds in the Galerkin technique presented in Chapter 2.2.1. For a fixed $\mu > 0$ we obtain therefore also unique solvability.

After discretizing in space we can also introduce a stabilised penalty approach for the calculation, since we have again ill-conditioned problems for very small μ like in the case of the convection-diffusion equation (cf. Section 3.3). The stabilised semilinear form is given by

$$\begin{aligned} b_\mu^\delta(\boldsymbol{q}_D;\boldsymbol{u})(\boldsymbol{\varphi}) := &-\frac{\delta}{\mu+\delta}\left(\langle\nu\partial_{\boldsymbol{n}}\boldsymbol{u} - p\boldsymbol{n},\boldsymbol{\varphi}\rangle_{\partial\Omega} + \langle\boldsymbol{u}-\boldsymbol{q}_D,\nu\partial_{\boldsymbol{n}}\boldsymbol{\varphi}+\psi\boldsymbol{n}\rangle_{\partial\Omega}\right)\\ &+\frac{1}{\mu+\delta}\langle\boldsymbol{u}-\boldsymbol{q}_D,\boldsymbol{\varphi}\rangle_{\partial\Omega} - \frac{\mu}{2(\mu+\delta)}\langle(\boldsymbol{u}\cdot\boldsymbol{n})\boldsymbol{u},\boldsymbol{\varphi}\rangle_{\partial\Omega}\\ &-\frac{\delta\mu}{\delta+\mu}\langle\nu\partial_{\boldsymbol{n}}\boldsymbol{u} - p\boldsymbol{n},\nu\partial_{\boldsymbol{n}}\boldsymbol{\varphi}+\psi\boldsymbol{n}\rangle_{\partial\Omega}\\ &+\frac{\delta\mu}{2(\delta+\mu)}\langle(\boldsymbol{u}\cdot\boldsymbol{n})\boldsymbol{u},\nu\boldsymbol{\varphi}+\psi\boldsymbol{n}\rangle_{\partial\Omega}. \end{aligned} \tag{3.24}$$

While $b_\mu^0(\cdot;\cdot)(\cdot)$ corresponds to the penalty formulation the parameter choice $\mu = 0$ and $\delta = \gamma(h)$ results in a kind of Nitsche formulation for the Navier-Stokes system

$$b_0^{\gamma(h)}(\boldsymbol{q}_D;\boldsymbol{u})(\boldsymbol{\varphi}) := -\langle\partial_{\boldsymbol{n}}\boldsymbol{u} - p\boldsymbol{n},\boldsymbol{\varphi}\rangle_{\partial\Omega} - \langle\boldsymbol{u}-\boldsymbol{q}_D,\partial_{\boldsymbol{n}}\boldsymbol{\varphi}+\psi\boldsymbol{n}\rangle_{\partial\Omega} + \frac{1}{\gamma(h)}\langle\boldsymbol{u}-\boldsymbol{q}_D,\boldsymbol{\varphi}\rangle_{\partial\Omega},$$

which looks almost like the one Becker obtained in [8]. Like for the convection-diffusion equation we find the following result:

Lemma 3.16.
A solution pair $\{\boldsymbol{u},p\}$ of the strong formulation

$$\begin{aligned} -\nu\Delta\boldsymbol{u} + \boldsymbol{u}\cdot\nabla\boldsymbol{u} + \nabla p + \kappa\boldsymbol{u} &= \boldsymbol{f}, && \text{in } \Omega,\\ \nabla\cdot\boldsymbol{u} &= 0, && \text{in } \Omega, \end{aligned}$$

which fulfils the boundary condition (3.23) satisfies also the equation

$$\begin{aligned} a(\boldsymbol{u})(\boldsymbol{\varphi}) + b_\mu^\delta(\{\boldsymbol{u},p\},\boldsymbol{\varphi}) + c(p,\boldsymbol{\varphi}) &= (\boldsymbol{f},\boldsymbol{\varphi}), && \forall\boldsymbol{\varphi}\in V,\\ -c(\mu,\boldsymbol{u}) &= 0, && \forall\mu\in M. \end{aligned}$$

Proof. By multiplying the classical Navier-Stokes equation with appropriate test functions $\boldsymbol{\varphi}$ and ψ, integration over the domain Ω and partial integration we obtain equation (3.22) with $b(\boldsymbol{q}_D;\boldsymbol{u})(\boldsymbol{\varphi})$ as in equation (3.21).

Afterwards the boundary condition is multiplied with $\boldsymbol{\varphi}$ and integrated over the boundary. We obtain after multiclation with $\frac{1}{\mu+\delta}$

$$\frac{\mu}{\mu+\delta}\left\langle \nu\partial_{\boldsymbol{n}}\boldsymbol{u}-p\boldsymbol{n},\boldsymbol{\varphi}\right\rangle_{\partial\Omega}+\frac{1}{\mu+\delta}\left\langle \boldsymbol{u}-\boldsymbol{q}_D,\boldsymbol{\varphi}\right\rangle_{\partial\Omega}-\frac{\mu}{2(\mu+\delta)}\left\langle (\boldsymbol{u}\cdot\boldsymbol{n})\boldsymbol{u},\boldsymbol{\varphi}\right\rangle_{\partial\Omega}=0. \quad (3.25)$$

Furthermore, we multiply the boundary condition with the test function

$$\nu\partial_{\boldsymbol{n}}\boldsymbol{\varphi}+\psi\boldsymbol{n} \quad (3.26)$$

and integrate over the boundary and multiply with the factor $-\frac{\delta}{\mu+\delta}$. This yields

$$\begin{aligned}-\frac{\mu\delta}{\mu+\delta}\left\langle \nu\partial_{\boldsymbol{n}}\boldsymbol{u}-p\boldsymbol{n},\nu\partial_{\boldsymbol{n}}\boldsymbol{\varphi}+\psi\boldsymbol{n}\right\rangle_{\partial\Omega}-\frac{\delta}{\mu+\delta}\left\langle \boldsymbol{u}-\boldsymbol{q}_D,\nu\partial_{\boldsymbol{n}}\boldsymbol{\varphi}+\psi\boldsymbol{n}\right\rangle_{\partial\Omega}\\ +\frac{\delta\mu}{2(\mu+\delta)}\left\langle (\boldsymbol{u}\cdot\boldsymbol{n})\boldsymbol{u},\nu\partial_{\boldsymbol{n}}\boldsymbol{\varphi}+\psi\boldsymbol{n}\right\rangle_{\partial\Omega}=0.\end{aligned}$$

Adding up equations (3.21), (3.25) and (3.26) leads directly to $b_\mu^\delta(\boldsymbol{q}_D;\boldsymbol{u})(\boldsymbol{\varphi})$ together with the (semi-) linear forms for the interior of the domain we obtain that $\{\boldsymbol{u},p\}$ also fulfils the weak formulation. □

Remark 3.17 (Time-Independent Navier Stokes System).
The case $\kappa=0$ represents the case of the steady Navier-Stokes system.

We want to present a few numerical examples which involve this possibility to prescribe the boundary data. But at first we want to describe how we deal with the nonlinearity in the Navier-Stokes system and we want also to discuss stabilisation aspects.

3.5.2. Newton's Method

We assume we are in a fixed time step, so that we can skip for abbreviation t_m. Furthermore we set $k_m=1$ and decide to work with $\theta=1$. Then, we consider the equation (3.22)

$$\begin{aligned}a(\boldsymbol{u})(\boldsymbol{\varphi})+b_\mu^\delta(\boldsymbol{q}_D;\boldsymbol{u})(\boldsymbol{\varphi})+c(p,\boldsymbol{\varphi})&=(\boldsymbol{f},\boldsymbol{\varphi}), &&\forall\boldsymbol{\varphi}\in\boldsymbol{V},\\ -c(\mu,\boldsymbol{u})&=0, &&\forall\mu\in M,\end{aligned}$$

which involves the nonlinearities

$$(\boldsymbol{u}\cdot\nabla\boldsymbol{u},\boldsymbol{\varphi}) \quad \text{and} \quad -\frac{\mu}{2(\mu+\delta)}\left(\left\langle (\boldsymbol{u}\cdot\boldsymbol{n})\boldsymbol{u},\boldsymbol{\varphi}\right\rangle_{\partial\Omega}-\delta\left\langle (\boldsymbol{u}\cdot\boldsymbol{n})\boldsymbol{u},\boldsymbol{\varphi}\right\rangle_{\partial\Omega}\right)$$

in the semilinear forms $a(\cdot)(\cdot)$ and $b(\cdot;\cdot)(\cdot)$.

We will linearise this equation using Newton's method by stating the following problem:

Find $\boldsymbol{x} = (\boldsymbol{u}, p) \in X = V \times M$, so that

$$g(\boldsymbol{x})(\boldsymbol{\tau}) = 0, \quad \forall \tau = (\boldsymbol{\varphi}, \mu) \in X,$$

with

$$g(\boldsymbol{x})(\boldsymbol{\tau}) := a(\boldsymbol{u})(\boldsymbol{\varphi}) + b_\mu^\delta(\boldsymbol{q}_D; \boldsymbol{u})(\boldsymbol{\varphi}) + c(p, \boldsymbol{\varphi}) - c(\mu, \boldsymbol{u}) - (\boldsymbol{f}, \boldsymbol{\varphi}) = 0.$$

With the Fréchet derivative we can state Newton's method in update-form for this problem:

$$\text{Compute } \boldsymbol{\delta}^{(k)} \text{ from } \frac{d}{d\eta} g(\boldsymbol{x}^{(k)} + \eta \boldsymbol{\delta}^{(k)})(\boldsymbol{\tau})\Big|_{\eta=0} = -g(\boldsymbol{x}^{(k)})(\boldsymbol{\tau}),$$
$$\boldsymbol{x}^{(k+1)} = \boldsymbol{x}^{(k)} + \lambda_k \boldsymbol{\delta}^{(k)}.$$

With the damping parameter $\lambda_k \in (0, 1]$ we can globalise the convergence of the otherwise only locally convergent Newton method. The price of the globalisation is the loss of quadratic convergence of the method, which reduces to superlinear convergence.

In the linear parts of the above mentioned Fréchet derivative we can substitute $\boldsymbol{u}$ by $\boldsymbol{\delta}_{\boldsymbol{u}}$ and p by δ_p, where $\boldsymbol{\delta}_{\boldsymbol{u}}^{(k)}$ and $\delta_p^{(k)}$ are the defects for velocity and pressure. The nonlinear part has the following form

$$\frac{d}{d\eta} (\boldsymbol{u} \cdot \nabla \boldsymbol{u}, \boldsymbol{\varphi})\Big|_{\eta=0} = \left(\boldsymbol{\delta}_{\boldsymbol{u}}^{(k)} \cdot \nabla \boldsymbol{u}^{(k)}, \boldsymbol{\varphi}\right) + \left(\boldsymbol{u}^{(k)} \cdot \nabla \boldsymbol{\delta}_{\boldsymbol{u}}^{(k)}, \boldsymbol{\varphi}\right).$$

Moreover the boundary part has a similar structure.

Thus, we have to solve in each step of Newton's method a linearised PDE with the finite element method in the unknown variable $\boldsymbol{\delta}^{(k)}$ until the residual of the original system is sufficiently reduced.

3.5.3. Inf-Sup Stability for Equal Order Approach

Using the finite element method from Section 3.2 for the spatial discretisation of the Navier-Stokes equations can lead to further trouble in the pressure approximation. The problem becomes already obvious in the case of the linear Stokes system with homogeneous Dirichlet data.

We consider the saddle point system (cf. Girault et. al. [42])

$$\begin{aligned} a(\boldsymbol{u}, \boldsymbol{\varphi}) + c(\boldsymbol{\varphi}, p) &= (\boldsymbol{f}, \boldsymbol{\varphi}), & \forall \boldsymbol{\varphi} \in V, \\ -c(\boldsymbol{u}, \mu) &= 0, & \forall \mu \in M \end{aligned} \tag{3.27}$$

given in an abstract notation, where

$$\begin{aligned} a(\boldsymbol{u}, \boldsymbol{\varphi}) &:= (\nabla \boldsymbol{u}, \nabla \boldsymbol{\varphi}), \\ c(\boldsymbol{u}, \mu) &:= -(\mu, \nabla \cdot \boldsymbol{u}). \end{aligned}$$

The aim is then to find a pair $\{\boldsymbol{u}, p\} \in V \times M$ such that the above system is fulfilled.

For the discretisation we have to choose appropriate finite element spaces V_h and M_h and solve the linear algebraic system resulting from the discrete counterpart of the above problem

$$\begin{aligned} a(\boldsymbol{u}_h, \boldsymbol{\varphi}_h) + c(\boldsymbol{\varphi}_h, p_h) &= (\boldsymbol{f}, \boldsymbol{\varphi}_h), \quad \forall \boldsymbol{\varphi}_h \in V_h, \\ - c(\boldsymbol{u}_h, \mu_h) &= 0, \qquad\quad \forall \mu_h \in M_h. \end{aligned}$$

For a reasonable approximation of the pressure p_h we need in this context a further condition

$$\min_{\mu_h \in M_h} \left(\max_{\boldsymbol{\varphi}_h \in V_h} \frac{c\left(\boldsymbol{\varphi}_h, \mu_h\right)}{\|\boldsymbol{\varphi}_h\|_{V_h} \|\mu_h\|_{M_h}} \right) \geq \gamma_h \geq \gamma > 0.$$

which is called the discrete "inf-sup"-condition.

There exist pairs of finite elements connected to appropriate spaces V_h and M_h like the Taylor-Hood element, which obey these conditions.

However, we want to work for computational simplicity with bilinear finite elements $\mathcal{Q}_1 = \text{span}\{1, x, y, xy\}$ for both the pressure and the velocity approximation. Then we have $V_h = \hat{V}_h^2$ and $M_h = \hat{V}_h$ with

$$\hat{V}_h := \{\varphi_h : \bar{\Omega} \to \mathbb{R} \;\Big|\; \varphi_h|_T \in \mathcal{Q}_1 \text{ and } \varphi_h \in C(\Omega)\}.$$

For this choice the inf-sup-condition is not fulfilled and requires therefore an adequate stabilisation. This stabilisation effect can be achieved by using again a stabilisation with local projection. The procedure is for example described in Braack [9].

The concept is to add the bilinear form

$$s_{LPS}(\{\boldsymbol{u}_h, p_h\}, \{\boldsymbol{\varphi}_h, \mu_h\}) = \sum_{T \in \mathcal{T}_h} \alpha_T \left(\nabla \left(\pi_h p_h \right), \nabla \left(\pi_h \mu_h \right) \right)$$

to the left hand side of the divergence equation of the weak formulation in formula (3.27). The fluctuation operator π_h is defined as in Section 3.4.2, where we used the LPS method for the convection stabilisation. The parameter

$$\alpha_T = \frac{h_T^2}{\nu}$$

is a piecewise constant function controlling the influence of the stabilisation.

Remark 3.18 (Two-Level LPS).
The presented technique is called the two-level LPS approach. It can also be used to stabilise the convection term in the Navier-Stokes equation, which works essentially the same way as presented in Section 3.4.2 or as described in the work of Braack et al. [17]. In the mentioned article also other applications of stabilisation techniques are discussed.

3.6. Numerical Examples for the Coupled System

We will finish this chapter by a numerical example for the fully nonlinear and time-dependent two dimensional Navier-Stokes equations, which is coupled to the pure transport equation. That means the resulting velocity field transports a passive tracer through the computational domain Ω. The resulting system of equations consists of four components in this situation. It is solved in a monolithic way with help of the techniques presented in this chapter. Special attention is paid again to the application of weakly imposed boundary data.

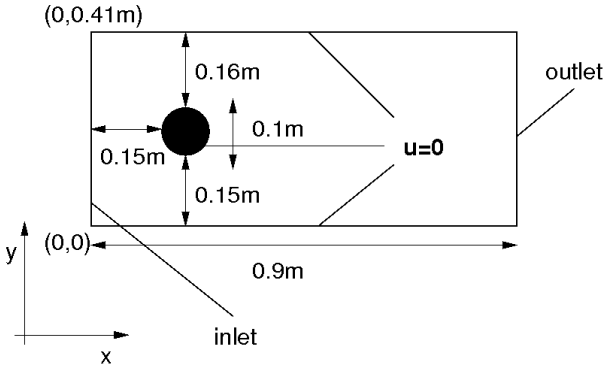

Figure 3.6. Computational domain for the benchmark problem.

Starting point is the famous CFD benchmark, which is for example presented in Schäfer [93]. We will now briefly describe the configuration.

We want to solve the system in (2.12) in the computational domain Ω, which is drawn in Figure 3.6. We modified here the length of the channel in comparison to the original channel. The left boundary of the channel is the inflow boundary and the right one the outflow boundary. On the inlet we prescribe

$$\boldsymbol{u}(\boldsymbol{x},t) = \left(\frac{4\bar{u}y(0.41-y)\sin(\frac{\pi t}{8})}{0.41^2}, 0 \right)^T$$

for the velocity $\boldsymbol{u}$. Here $\bar{u}$ denotes an averaged velocity of $1.5\frac{m}{s}$. Furthermore, we set

$$I(\boldsymbol{x},t) = \begin{cases} 0.1\min(t,1)\left(1+\cos\left(\frac{\pi}{r}\sqrt{(y-y_i)^2}\right)\right), & \text{for all } y \text{ with } |y-y_i| < r, \\ 0, & \text{else} \end{cases}$$

on the inflow boundary for the passive tracer $I(\boldsymbol{x},t)$. We specify the value of the radius as $r = 0.075m$. Furthermore we have $y_1 = 0.12m$ and $y_2 = 0.3m$. The outflow on the outlet is a Neumann type boundary condition for both parts, the Navier-Stokes part and the transport part of the system. In the Navier-Stokes case this type of boundary is also known

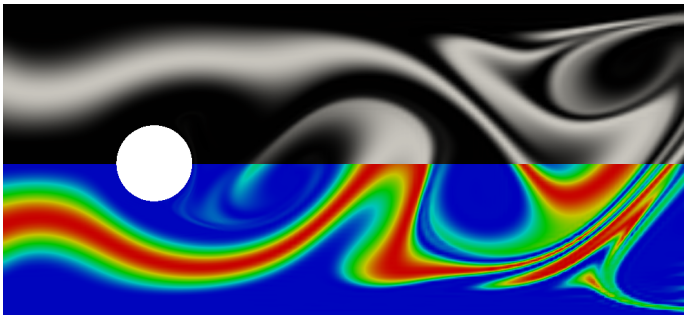

Figure 3.7. Forward calculation: Result of the intensity function $I(\boldsymbol{x}, 8)$ for the described configuration. Upper half: Interpreted as grey scale image. Lower half: Colored scalar bar for a better visualisation of the solution.

as "do nothing"-boundary condition (cf. Heywood et al. [53]). For the above described configuration we choose the initial conditions

$$\boldsymbol{u}^0(\boldsymbol{x}, t) = 0, \qquad I^0(\boldsymbol{x}, t) = 0.$$

Moreover we set the parameters $\nu = 10^{-3}\frac{m^2}{s}$ and $\varepsilon = 0$ in the system (2.12). That means that the system of equations describes the flow of a fluid with the fluid density $\rho = 1\frac{kg}{m^3}$. The Reynolds number is defined as

$$\mathrm{Re} = \frac{\boldsymbol{u}^c d}{\nu},$$

with a time dependent mean velocity $\boldsymbol{u}^c$ and a characteristic diameter $d = 0.1m$. Hence on the time interval $[0, 8s]$ we have for the above configuration a varying Reynolds number

$$\mathrm{Re} \in [0, 100].$$

The result of a calculation on a mesh with 41504 spatial nodes and a temporal time step size of $k = 2.5 \cdot 10^{-3}$ at the endtime point $t = 8$ is visualised in Figure 3.7. Here we use in the bottom half a color map visualisation, while in the upper half a visualisation by a grey-value scale was used. The reason is that we want to emphasise that we interpret $I(\boldsymbol{x}, t)$ as a grey value image later on, although we usually use a colored scale for a better visualisation of the results.

We used the Crank-Nicolson scheme with two initial Euler steps as time stepping scheme (cf. Section 3.1). For all components of the system we used the LP stabilisation for convection stabilisation and to guarantee the inf-sup stability. We used the following parameter choices:

$$\text{Pressure: } \alpha = 0.3\frac{h^2}{\nu}, \qquad \text{Velocity: } \delta_{\boldsymbol{u}} = 0.2\frac{h}{k\theta\|\boldsymbol{u}\|_2}, \qquad \text{Intensity: } \delta_I = 0.3\frac{h}{k\theta\|\boldsymbol{u}\|_2}.$$

In Figure 3.9 we visualised the solution of the intensity component $I(\boldsymbol{x}, t)$ of the system for

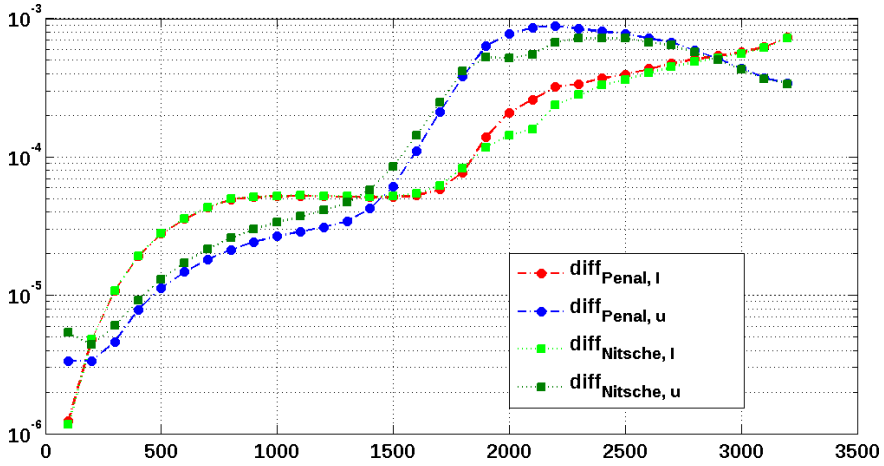

Figure 3.8. Lines with box: Difference between the approximation with strong implemented boundary conditions and the one with Nitsche-type boundary data. The x-axis denotes here the number of the time step t_i for $i = 1, \dots, 3200$. Light green: $\|I_{h,\mathrm{Str}}(t) - I_{h,\mathrm{Nit}}(t)\|_2$. Dark green: $\|\boldsymbol{u}_{h,\mathrm{Str}}(t) - \boldsymbol{u}_{h,\mathrm{Nit}}(t)\|_2$. Lines with circle: The same for the penalised approach $I_{h,\mathrm{Pen}}$ and $\boldsymbol{u}_{h,\mathrm{Pen}}$.

four different time points $t = 2, 4, 6, 8$ and for three different techniques of prescribing the boundary condition: The Nitsche approach was used in the upper row ($\mu = 0$ and $\delta = \frac{h}{100}$). The Neumann penalisation technique was applied in the middle row ($\mu = h^2$ and $\delta = 0$) and in the bottom row we used a strong implementation of the boundary data. On first glance we see no qualitative difference between the three different techniques. In fact there is a difference if we compare the solutions of the weak approaches in the L^2-norm to the strong solution for different time points. A plot of these differences for $t = 0.25i$ with $i = 1, \dots, 32$ is given in Figure 3.8. We see that the weak implementations produce almost the same solution as the strong implementation up to a certain discretisation error in the laminar phase of our solution. With beginning of the dynamic behaviour at $t \approx 3.75$ the difference between the weak implementations and the strong implementation increases. This is quite certainly due to the stabilisation effects, since small differences between the solutions on the boundary are differently prolongated through the computational domain.

However the weak implementations produce solutions which are equal to the strong implementation up to a marginal difference of 10^{-3} over the whole computational domain. Due to the convergence properties of the weak implementations (c.f. Section 3.3) we can expect that this difference is decreasing under mesh refinement. Hence the weak implementations constitute equally good ways to implement boundary conditions.

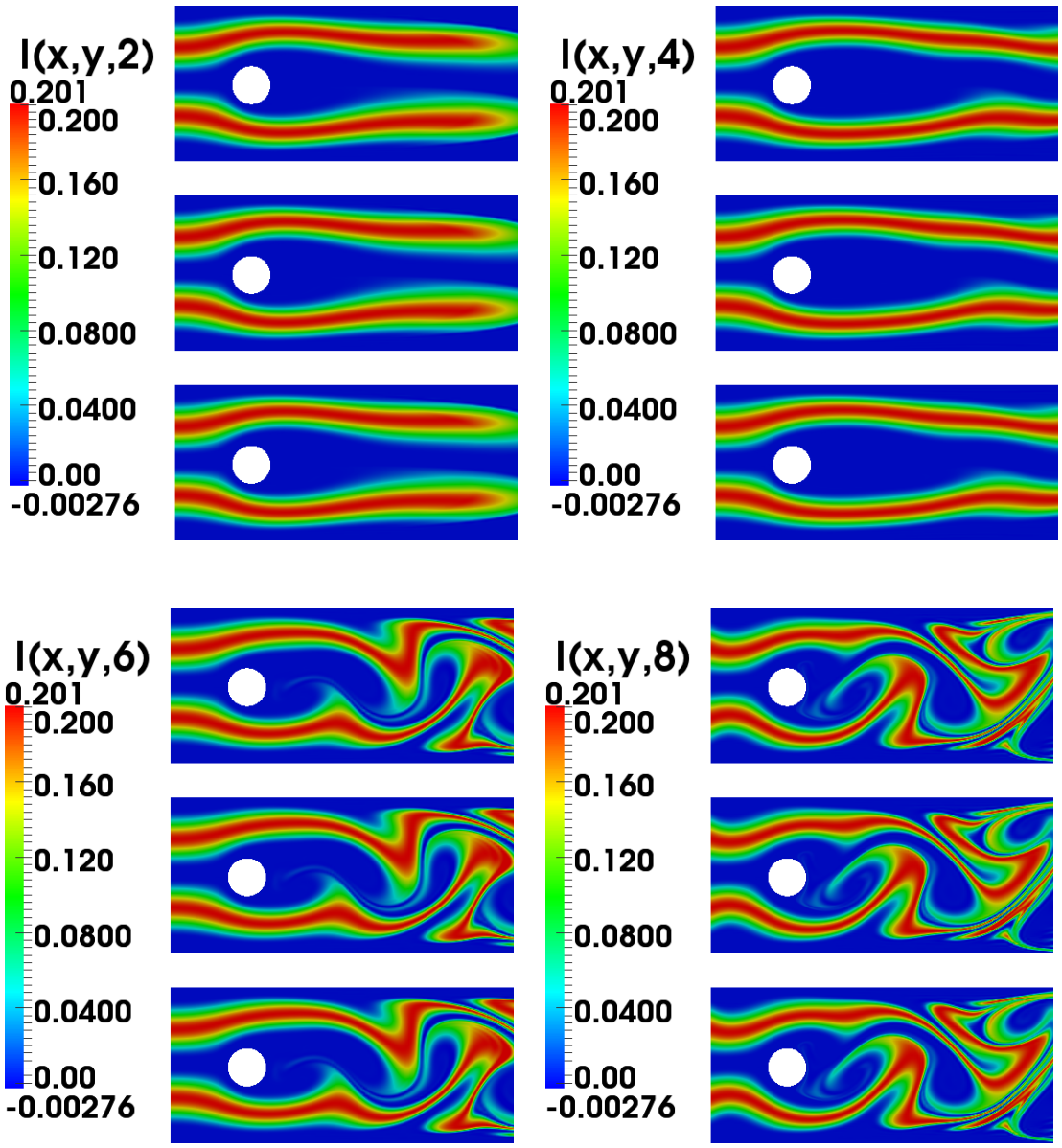

Figure 3.9. Results: $I(\boldsymbol{x}, t)$ for $t = 2, 4, 6, 8$ in groups of three graphs from top left to bottom right. Each graph represents one of three different techniques for the implementation of the boundary conditions: (top) Nitsche approach ($\delta = \frac{h}{100}$, $\mu = 0$), (middle) penalisation approach ($\delta = 0$, $\mu = h^2$) and (bottom) strong implementation.

4. PDE Constrained Optimisation

In this chapter we want to present the general formulation of PDE constrained optimisation problems. We need this concept to deal with the application mentioned in the introduction. We will start with a brief theoretical introduction into the topic. Starting point is the reduced approach, which is based on a reduction of the originally constrained problem to an unconstrained optimisation problem introducing a solution operator and treating therefore the state variable implicitly. During our discussion we mention existence and uniqueness results and derive optimality conditions. Finally we will describe a numerical algorithm to solve PDE constrained optimisation problems.

4.1. Theoretical Considerations

In this section we introduce the notation and the conceptual background of PDE constrained optimisation. The problems will be stated in an abstract way and a few basic theoretical results will be presented (existence, uniqueness). We follow essentially the theses of Becker [8], Meidner [77], Vexler [102] and the monograph of Tröltzsch [100] .

We will later on investigate identification or inverse problems, where we are interested in the recovering of a distributed quantity. The formulation of such problems fits into the following abstract setting of a PDE-constrained optimisation problem:

Optimisation Problem 4.1.
We search for a minimal value of the cost functional $J(\cdot)$ depending on the state function $u \in \mathcal{X}$ and control function $q \in \mathcal{Q}$:

$$J(u,q) = \kappa_1 \int_0^T j_t(u(t))dt + \kappa_2 j_T(u(T)) + \frac{\alpha}{2} \int_0^T r(q(t))\, dt$$

such that u and q also fulfill the PDE side condition

$$\left(\!\left(\partial_t u, \varphi\right)\!\right) + a(q;u)(\varphi) + b(q;u)(\varphi) + \Big(u(0) - u^0, \varphi(0)\Big) = \left(\!\left(f, \varphi\right)\!\right), \qquad \forall \varphi \in \mathcal{X}. \tag{4.1}$$

Now we want to discuss the elements of the above formulation in a general and abstract way. In the further chapters of the work we will consider concrete optimisation problem, which can be embedded in this abstract setting.

The cost functional has two essential parts: The data or fitting terms and the regularisation term. The first two terms in $J(u,q)$ are the fitting terms for an observable quantities. In view of identification problems we will also refer to these terms as data terms. The parameters κ_1, κ_2 are either zero or one and switch between data terms at the end time or for the whole time evolution. . The aim is to minimise these fitting terms.

Remark 4.2 (Observation Operator).
Often the fitting terms are in least squares form, sometimes involving a so called observation operator $M : \mathcal{X} \to Y$

$$j_T := \|M(u(T)) - \hat{M}\|_Y^2, \qquad j_t(t) := \|M(u(t)) - \hat{M}(t)\|_Y^2.$$

The last term in $J(u,q)$ is called the regularisation or control term $r(\cdot)$. It is in general of Tikhonov type:

$$r(q) := \|q - q^\star\|_Q^2,$$

with Q denoting the spatial space of the control $q(t)$.

The parameter $\alpha \geq 0$ is the regularisation parameter, by which we can choose the influence of the regularisation. The regularisation especially stabilises ill-posed problems, which occur for example in theory of inverse problems (cf. Engl et al. [31]). In the control community this term has the functionality to adjust the cost of the control.

As a side condition for the above mentioned minimisation of the cost functional in general we will have a system of partial differential equations. The parabolic equation in (4.1) is called the state equation. The term $a(q;u)(\varphi)$ is a semilinear form in the interior of the domain, and $b(q,u)(\varphi)$ is the boundary counterpart of $a(\cdot;\cdot)(\cdot)$.

Remark 4.3 (Boundary Control Formulation).
Throughout this work we will consider boundary control problems. Therefore we assume the term $b(\cdot,\cdot)(\cdot)$ to contain always the control q, while $a(\cdot)(\cdot)$ depends only on the state. The concrete form of this term for different problems is extensively discussed in the next chapter.

The last aspect is the choice of function spaces. We have to take special care if we want to find theoretical justified formulations. We start with the spatial space for the state variable, which we denote by V. Then V' denotes the dual space of the Hilbert space V. If there exists another Hilbert space H with a dense embedding of the form

$$V \hookrightarrow H \hookrightarrow V', \qquad \text{(Gelfand triple)}.$$

Then an essential result yields that

$$\mathcal{X} := \{\boldsymbol{u} : \boldsymbol{u} \in L^2(0,T;V),\ \partial_t \boldsymbol{u} \in L^2(0,T;V')\}$$

is continuously embedded in $C([0,T],H)$ (see Remark 2.3 for a concrete example).

The Hilbert space $\mathcal{Q}$ for the control variable is generally given as a subspace of $L^2(0,T;Q)$, where we have to specify the special structure of the spatial Hilbert Space Q for the concrete situations later on.

4.1.1. Existence and Uniqueness

Now we examine the existence and uniqueness of a solution of the optimisation problem. Therefore we define what we mean by the term solution.

Definition 4.4 (Solution of the Optimisation Problem).
A pair $(\hat{u}, \hat{q}) \in \mathcal{X} \times \mathcal{Q}$, which fulfils equation (4.1) is called a 'local solution' of the abstract Optimisation Problem 4.1, if there exists $U_u \subset \mathcal{X}$ and $U_q \subset \mathcal{Q}$ such that

$$J(u, q) \geq J(\hat{u}, \hat{q})$$

for all solutions of equation (4.1) with $(u, q) \in U_u \times U_q$. If $U_u \times U_q = \mathcal{X} \times \mathcal{Q}$ we call the pair $(\hat{u}, \hat{q})$ a 'global solution'.

Furthermore, we describe the set of admissible functions $\mathcal{F}_{ad}$ by

$$\mathcal{F}_{ad} := \{(u, q) \in \mathcal{X} \times \mathcal{Q} : \ J(u, q) < \infty, \text{ equation (4.1) is fulfiled}\}.$$

Theorem 4.5 (Existence Theory: Abstract Linear Optimisation Problem)).
We assume the following:

1. *The functionals $j_t(u)$ and $j_T(u)$ are convex with respect to u:*

   $$j_\tau(\lambda u_1 + (1-\lambda)u_2) \leq \lambda j_\tau(u_1) + (1-\lambda) j_\tau(u_2), \qquad \text{with } \ \lambda \in [0,1] \ \text{ and } \ \tau = t, T.$$

2. *The functional $r(q)$ is convex with respect to q*

   $$r(\lambda q_1 + (1-\lambda)q_2) \leq \lambda r(q_1) + (1-\lambda) r(q_2),$$

3. *$J(u, q)$ is coercive with respect to q :*

   $$J(u, q) \geq \alpha \|q\|_{\mathcal{Q}} + \kappa, \qquad \forall q \in \mathcal{Q},$$

   with $\alpha > 0$ and $\kappa \in \mathbb{R}$.

4. *The state equation (4.1) admits a unique solution, and the terms*

   $$a(u)(\varphi) = a(u, \varphi), \qquad b(q, u)(\varphi) = b(q; u, \varphi)$$

   are linear.

Then there exists at least one local optimal solution $(u, q) \in \mathcal{F}_{ad}$, which solves the Optimisation Problem 4.1.

Proof. Given the unique solvability of the state equation we can introduce a linear and continuous solution operator

$$S : \mathcal{Q} \to \mathcal{X}, \qquad u(t) = S(q(t)).$$

By substituting this expression into the cost functional we obtaine the reduced cost functional

$$j(q) = J(S(q), q)$$

and have thus reformulated the problem as an unconstrained optimisation problem. The coercivity is transfered to the reduced cost functional

$$j(q) \geq \alpha \|q\|_{\mathcal{Q}} + \kappa.$$

Hence $j(\cdot)$ is bounded from below, and we define

$$\theta := \inf_{q \in \mathcal{Q}} j(q).$$

Now we introduce a minimizing sequence $q^{(n)}$:

$$\lim_{n \to \infty} j(q^{(n)}) = \theta.$$

By using the coercivity we get for all $n > N$, with N large enough

$$\|q^{(n)}\|_{\mathcal{Q}} \leq B,$$

with an uniform bound B. Due to the Hilbert space structure of $\mathcal{Q}$ we derive the existence of a weakly convergent subsequence such that

$$q^{(n_k)} \rightharpoonup q \in \mathcal{Q}. \tag{4.2}$$

The reduced cost functional $j(q)$ is also convex, due to the convexity of j_t, j_T and r. Furthermore $j(q)$ is continuous, due to the continuity of S and the used functionals j_t, j_T and r.

With these properties j is lower semicontinuous (generalisation of Tröltzsch [100, Satz 2.12] for Bochner spaces), which means that

$$\lim \inf_{n \to \infty} j(q^{(n)}) \geq j(q).$$

The latter results from the weak convergence in equation (4.2). The last inequality yields directly that q must be the minimum of $j(q)$. Since $u = S(q)$ is a unique solution of the state equation, $(u, q) \in \mathcal{F}_{ad}$ is a minimiser of $J(u, q)$. □

Remark 4.6 (Nonlinear State Equation).
The treatment of nonlinearities in the semilinear forms $a(\cdot)(\cdot)$ and $b(\cdot,\cdot)(\cdot)$ can also be presented in a general framework (see Tröltzsch [100]) with further assumptions on the forms. However this lies beyond the scope of this introduction. Therefore we postpone the discussion of the existence theory for a concrete boundary control problem with the fully nonlinear and nonstationary Navier-Stokes equations as PDE constraints to the next chapter.

Remark 4.7 (Uniqueness).
We assume the individual parts of the cost functional to have better properties so that the reduced cost functional is additionally to the above mentioned properties strongly convex

$$j(\lambda q + (1-\lambda)p) < \lambda j(q) + (1-\lambda)j(p)$$

for all $\lambda \in (0,1)$ and $q, p \in \mathcal{Q}$, with $p \neq q$. Then the solution of Theorem 4.5 is unique.

The reason is that for two minima in $p \neq q$ we have $j(p) = j(q) = \min_{\tilde{q}\in\mathcal{Q}} j(\tilde{q})$. Due to the assumed strong convexity we obtain immediately the contradiction

$$j(\lambda q + (1-\lambda)p) < \lambda j(q) + (1-\lambda)j(p) = \min_{\tilde{q}\in\mathcal{Q}} j(\tilde{q}).$$

Example 4.8 (Setting with a Unique Solution).
The cost functional which we will use very often in this work is given by

$$\kappa_1 = 0, \quad \kappa_2 = 1, \quad j_T(u(t)) := \frac{1}{2}\|u(T) - \bar{u}\|_2^2 \quad \textit{and} \quad r(q(t)) = \|q(t)\|^2_{L^2(\partial\Omega)}.$$

with $\mathcal{Q} = L^2(0,T;L^2(\partial\Omega))$. Hence, we have

$$J(u,q) = \frac{1}{2}\|u(T) - \bar{u}\|_2^2 + \frac{\alpha}{2}\|q\|^2_{L^2(0,T;L^2(\partial\Omega))}.$$

It is easy to show that

$$\|u(T) - \bar{u}\|_2^2, \quad \textit{and} \quad \|q\|^2_{L^2(0,T;L^2(\partial\Omega))}$$

are strictly convex with respect to u and q. Furthermore $J(u,q)$ is coercive due to

$$\begin{aligned} J(u,q) &= \underbrace{\frac{1}{2}\|u(T) - \bar{u}\|_2^2}_{\geq 0} + \frac{\alpha}{2}\|q\|^2_{L^2(0,T;L^2(\partial\Omega))} \\ &\geq \frac{\alpha}{2}\|q\|^2_{L^2(0,T;L^2(\partial\Omega))} \geq \alpha\|q\|_{L^2(0,T;L^2(\partial\Omega))} - \frac{\alpha}{2}. \end{aligned}$$

Thus as long as the state equation is linear and admits a unique solution for this particular choice of the control space, Theorem 4.5 will give us the existence of a solution, which is unique due to Remark 4.7.

4.1.2. Optimality Conditions and Lagrange Principle

As before we still hypothesise the existence of a unique solution operator S in this section. S gives us then a one-to-one and onto correspondence between the control q and the state u. That means we can still introduce a reduced cost functional like in the proof of Theorem 4.5

$$j(q) := J(S(q), q).$$

Hence, we reduced our constrained optimisation problem to an unconstrained one for which we can formulate first- and second-order necessary optimality conditions with the help of the following definitions (see Werner [104]):

Definition 4.9 (Differentiability Concepts).
Let X and Y be normed spaces with $U \subset X$ nonempty and open and

$$f : U \to Y.$$

1. *The mapping f is called "Gâteaux" differentiable in $x \in U$, if there exists a continuous linear mapping $T \in L(X, Y)$ with*

$$\lim_{h \to 0} \frac{f(x + h\delta x) - f(x)}{h} = T\delta x, \quad \forall \delta x \in X. \tag{4.3}$$

   For the mentioned continuous linear mapping T we will also write

$$f'(x)(\delta x) := T\delta x.$$

2. *If the convergence in equation (4.3) is uniform with respect to the direction, that means*

$$\lim_{\|\delta x\|_X \to 0} \frac{\|f(x + \delta x) - f(x) - T\delta x\|_Y}{\|\delta x\|_X} = 0.$$

   Then the mapping f is called "Fréchet" differentiable.

With these definitions we can formulate optimality conditions as follows.

Theorem 4.10 (Necessary Optimality Conditions).
Let the functional j be twice continuously Fréchet differentiable in a neighborhood of a local solution $q \in \mathcal{Q}$ of the unconstrained optimisation problem

$$\min_{q \in \mathcal{Q}} j(q). \tag{4.4}$$

Then we have

First-order necessary Condition*:*

$$j'(q)(\delta q) = 0 \quad \forall q \in \mathcal{Q}. \tag{4.5}$$

Then q is called a stationary point of $j(\cdot)$.

Second-order necessary Condition*:*

$$j''(q)(\delta q, \delta q) \geq 0, \qquad \forall \delta q \in \mathcal{Q}.$$

That means that $j''(\cdot)$ is positive semidefinite in q.

This theorem reflects common knowledge and its proof can be found in the standard literature, see for instance Tröltzsch [100] or Nocedal et al. [80].

Also from the standard literature we cite the sufficient optimality conditions:

Theorem 4.11 (Sufficient Optimality Conditions).
Let the functional j be twice continuously Fréchet differentiable in a neighborhood of the control q. The first order necessary optimality condition in equation (4.5) is fulfilled. Moreover, there exists a $\gamma > 0$ such that:

$$j''(q)(\delta q, \delta q) \geq \gamma \|\delta q\|_Q^2, \qquad \forall \delta q \in Q, \tag{4.6}$$

which means the second-order sufficient condition is fulfilled.

Then the unconstrained optimisation problem in (4.4) admits a local minimum in q.

4.2. Optimisation Algorithm

Starting from the derived conditions efficient algorithms can be developed to solve the optimisation problem. Therefore a representation of the first and second derivatives of $j(\cdot)$ is needed.

We follow in this subsection the work of Meidner [77] and Becker [8], since they described the optimisation algorithm used in the Software library *RoDoBo* [88], which we used for the calculations presented later on.

4.2.1. Representation of First Order Derivatives

We can obtain such representations by the useful identity:

$$j(q) = J(q, u) = \mathcal{L}(q, u, z), \tag{4.7}$$

where $\mathcal{L}(\cdot, \cdot, \cdot)$ denotes the Lagrangian, which is defined as

$$\mathcal{L}(q, u, z) := J(q, u) - (\!(\partial_t u, z)\!) - a(q; u)(z) - b(q; u)(z) - \Big(u(0) - u^0, z(0)\Big) + (\!(f, z)\!)$$

by the difference between the cost functional and the state equation. Thereby the auxiliary variable z denotes the adjoint state.

By identity (4.7) we see that the first derivative of $j(\cdot)$ is given by

$$j'(q)(\delta q) = \mathcal{L}'_q(q, u, z)(\delta q) + \mathcal{L}'_u(q, u, z)(\delta u) + \mathcal{L}'_z(q, u, z)(\delta z) = 0, \tag{4.8}$$

where $\delta u = S'(q)(\delta q)$ and δz is the q-derivative of z in direction δq.

Remark 4.12 (Optimality System).
The first-order necessary condition is equivalent to the existence of a triple

$$(q, u, z) \in Q \times X \times X,$$

which solves the optimality system of the Lagrangian $\mathcal{L}(\cdot,\cdot,\cdot)$ for the constrained problem. In terms of the Lagrangian we can state the optimality system in the following way:

$$\mathcal{L}'_z(q,u,z)(\varphi) = 0, \quad \forall \varphi \in X, \quad \textit{(state equation)}, \tag{4.9}$$
$$\mathcal{L}'_u(q,u,z)(\psi) = 0, \quad \forall \psi \in X, \quad \textit{(dual equation)}, \tag{4.10}$$
$$\mathcal{L}'_q(q,u,z)(\rho) = 0, \quad \forall \rho \in X, \quad \textit{(gradient equation)}. \tag{4.11}$$

Furthermore, we found a representation of the first derivative

$$j'(q)(\delta q) = \mathcal{L}'_q(q,u,z)(\delta q)$$

by the solutions u and z of the state and the dual (or adjoint) equation

$$\mathcal{L}'_z(q,u,z)(\varphi) = 0, \quad \forall \varphi \in \mathcal{X}, \quad \text{and} \quad \mathcal{L}'_u(q,u,z)(\varphi) = 0, \quad \forall \varphi \in \mathcal{X}.$$

We will use this representation to formulate a Newton-type method to calculate a solution of the optimisation problem in the next section.

4.2.2. Representation of Second Order Derivatives

To formulate a Newton-type algorithm we need also a representation of the second order derivative. This is again derived by the identity (4.7). A large amount of terms occur if we take the derivatives with respect to q, since z and u depend on the control q in an implicit way. We find the following representation

$$j''(q)(\delta q, \tau q) = \mathcal{L}''_{qq}(q,u,z)(\delta q, \tau q) + \mathcal{L}''_{uq}(q,u,z)(\delta u, \tau q) + \mathcal{L}''_{zq}(q,u,z)(\delta z, \tau q). \tag{4.12}$$

if we assume that the following two identities hold:

$$\mathcal{L}''_{qz}(q,u,z)(\delta q, \varphi) + \mathcal{L}''_{uz}(q,u,z)(\delta u, \varphi) = 0, \quad \forall \varphi \in X,$$
$$\mathcal{L}''_{qu}(q,u,z)(\delta q, \varphi) + \mathcal{L}''_{uu}(q,u,z)(\delta u, \varphi) + \mathcal{L}''_{zu}(q,u,z)(\delta z, \varphi) = 0, \quad \forall \varphi \in X.$$

The first one is the so called tangent or linearised state equation and the second one is called the additional adjoint equation.

These two additional equations can be used to calculate δu and δz. Hence, for two given directions δq and τq we can express the second order derivative with respect to the two given directions by equation (4.12). Therefore we have to solve the tangent and the additional adjoint equation. For a rigorous justification of equation (4.12) we refer the reader to Meidner [77].

4.2.3. Newton-CG Method

Newton's method for the calculation of a root of the first order derivative for the reduced cost functional is given by the following iteration

$$\begin{aligned} j''(q^{(k)})(\delta q^{(k)}, \eta) &= -j'(q^{(k)})(\eta), \quad \forall \eta \in \mathcal{Q}, \\ q^{(k+1)} &= q^{(k)} + \lambda_k \delta q^{(k)}, \end{aligned}$$

which starts with a good initial choice for q^0 and terminates after an appropriate stopping criterion is fulfilled.

We will concretise the situation now for the Optimisation Problem 4.1 with $\kappa_1 = 1$, $\kappa_2 = 0$, set

$$\tilde{j}(u) := j_t(u), \qquad \rho(q, q) := \frac{\alpha}{2} \int_0^T r(q(t), q(t))\, dt$$

and assume furthermore that $r(\cdot, \cdot)$ is a symmetric and positive definite bilinear form. Hence, also $\rho(\cdot, \cdot)$ is symmetric and positive definite. Moreover, the control is only part of the boundary semilinear form $b(q; u)(\varphi)$ in the state equation (4.1). Then, for the first order derivative we obtain

$$j'(q)(\delta q) = \mathcal{L}'_q(q, u, z)(\delta q) = \rho(q, \delta q) - b'_q(q, u)(\delta q, z).$$

The adjoint variable z is evaluated from the adjoint equation

$$-\big((\partial_t z, \varphi)\big) + \big(z(T), \varphi(T)\big) + a'_u(u)(\varphi, z) + b'_u(q, u)(\varphi, z) = j'_u(u)(\varphi) \quad \forall \varphi \in V, \tag{4.13}$$

which means that we integrate backward in time with the initial condition $z(T) = 0$.

The second order derivative is given by

$$j''(q)(\delta q, \tau q) = \rho(\delta q, \tau q) - b''_{q,q}(q, u)(\delta q, \tau q, z) - b''_{u,q}(q, u)(\delta u, \tau q, z) - b'_q(q, u)(\tau q, \delta z).$$

At first we have to solve the tangent equation

$$\begin{aligned} \big((\partial_t \delta u, \varphi)\big) + \big(\delta u(T), \varphi(T)\big) + a'_u(u)(\delta u, \varphi) \\ + b'_u(q, u)(\varphi) = -b'_q(q, u)(\delta q, \varphi), \quad \forall \varphi \in V. \end{aligned}$$

Afterwards we solve the additional adjoint equation

$$\begin{aligned} -\big((\partial_t \delta z, \varphi)\big) + \big(\delta z(T), \varphi(T)\big) + a'_u(u)(\varphi, \delta z) \\ + b'_u(q, u)(\varphi, \delta z) = &-a''_{uu}(u)(\delta u, \varphi, z) - b''_{uu}(u)(\delta u, \varphi, z) \\ &-b''_{qu}(q, u)(\delta q, \varphi, z) + j''(u)(\varphi, \delta u), \\ &\forall \varphi \in V. \end{aligned} \tag{4.15}$$

Now, we can sum up all steps of the optimisation loop in Algorithm 4.1.

Algorithm 4.1. Optimisation loop

1. Choose an initial $\boldsymbol{q}^0 \in \mathcal{Q}_h$, $\mu_0 \in \mathbb{R} \cup \{+\infty\}$ and set $k = 0$.
2. Solve the state equation (4.1).
3. Evaluate the cost functional.
4. Evaluate the residual $\hat{f}_i := -j'(q^k))(\delta q_i^{(k)})$ for $i = 1, 2, \ldots, \dim \mathcal{Q}_d$:
   4.1 Solve the adjoint equation.
   4.2 Compute:
   $$j'(q^{(k)})(\delta q_i^{(k)}) = r(q^{(k)}, \delta q_i^{(k)}) - b'_q(q^{(k)}, u^{(k)})(\delta q_i^{(k)}, z^{(k)}).$$
5. Stop if $\|\hat{f}_i\| < tol$ (norm $\|\cdot\|$ must be specified).
6. Solve the linear system
   $$j''(q^{(k)})(\delta q_i^{(k)}, \tau q_j^{(k)}) = -j'(q^{(k)})(\tau q_j^{(k)}) \tag{4.16}$$
   without assembling of the matrix:
   6.1 Solve the tangent equation (4.14).
   6.2 Solve the additional adjoint equation (4.14).
   6.3 Evaluate the matrix-vector product
   $$\begin{aligned} j''(q)(\delta q, \tau q_i) = r(\delta q, \tau q_i) - b''_{q,q}(q, u)(\delta q, \tau q_i, z) \\ - b''_{u,q}(q, u)(\delta u, \tau q_i, z) - b'_q(q, u)(\tau q_i, \delta z). \end{aligned}$$
   and perform a step of the CG-method.
   6.4 Repeat from Step 6.1 until:
   i) a chosen tolerance for (4.16) is reached, or
   ii) a fixed ammount of steps was performed.
7. Update the control: $q^{(k+1)} = q^{(k)} + \lambda_k q^{(k)}$.
8. Go back to Step 2.

Remark 4.13 (CG-Method for the Linear System (Step 6)).
Although the matrix $A_{ij} := j''(q)(\delta q_i, \delta q_j)$ is not assembled in the algorithm it is indirectly involved in each Newton step. The CG method requires positive definiteness of this matrix, which is especially the case in the neighborhood of a local minima. However, the positivity of (Aq, q) can be generated by choosing greater values for α, such that the computational process becomes more stable. Unfortunately we are often interested in choosing small values for α, especially in the case of identification problems.
In such cases we try for example to work with a so called "Inexact-Newton method", where the residuum of the linear system is not sufficiently reduced in each Newton step. In this case we will usually have a much higher amount of Newton steps to reduce the Newton residuum.
Hence, in such cases another possibility is to work with a homotopy method in α, where we start with a larger value of α to generate a better initial value q^0 for a second calculation. If the calculated value q is closer to the local minimum we can use it as initial value for a calculation with a reduced regularisation parameter.

Remark 4.14 (Line Search (Step 7)).
The relaxation parameter λ_k is needed for the globalisation of the convergence area of Newton's method. It can be evaluated by line search techniques (cf. Nocedal et al.[80] for details).

5. Boundary Control Problems

After presenting the theory and numerics for abstract PDE-constrained optimisation problems we want to concretise the topic in this chapter and discuss so called "boundary control" problems, which we need to deal with the questions mentioned in the introduction of this thesis (cf. Chapter 1).
One fundamental assumption in our prototypical application was that we observe an aperture of a bigger flow domain. Then, in absence of external forces the flow is completely described by the unknown boundary conditions. Now, boundary control formulations can be used to recover these conditions.

Thus, a main objective of this chapter is to present a boundary control formulation, which is well suited for our application, theoretically justified and can be easily handled from the computational point of view.

To re-establish the unknown boundary functions it seems likely to work with a Dirichlet control approach. However, this approach leads to complications either in the theoretical justification or in the numerical treatment. We will describe these contrary propositions by considering an Dirichlet control problem, with the simple Poison equation as PDE side condition.
An interesting approach discussed in the literature over the last two decades is that using a Robin-type approach

$$\partial_{\boldsymbol{n}} u = \frac{1}{\mu}(q - u)$$

for the description of the boundary data leads to a theoretically justified approach, which yields also a reliable approximation of the original Dirichlet control problem.
We will use this idea also for the time-dependent convection-diffusion equation and the (linearised) Navier-Stokes system. We will show well-posedness for the boundary control formulations for these PDE constraints. Furthermore, we will discuss the connection of the μ-dependent solutions of the Robin-type problems to Dirichlet control problems for the respective equations. For the time-dependent convection-diffusion equation and the linearised Navier-Stokes system we will be able to prove that the solutions of the Robin-type problems converging to a solution of a Dirichlet control problem, when μ tends to zero. For the fully nonlinear Navier-Stokes system we will present the obstacles for proving such a result.
However, we will confirm by numerical test cases that the Robin-type approach with a fixed and small μ is well suited for our reconstruction purposes for the mentioned types of PDEs.

5.1. Survey of Dirichlet Control Approaches for Elliptic Equations

Before we consider Dirichlet control problems for time-dependent convection-diffusion and the Navier-Stokes equations, we first sum up theoretical aspects of the state of the art literature.

At first let us state the problem:

Optimisation Problem 5.1 (Dirichlet Control Problem (Poisson Equation)). *We want to find $q \in \mathcal{Q}$ so that the cost functional*

$$\mathcal{J}(u,q) = \frac{1}{2}\|u - \bar{u}\|_2^2 + \frac{\alpha}{2}\langle A(q-\bar{q}), q-\bar{q}\rangle_\Gamma$$

becomes minimal, under the side condition that a sufficiently regular u fulfils the Poisson equation

$$\begin{aligned} -\Delta u &= f, \quad \text{in } \Omega, \\ u &= q, \quad \text{on } \Gamma, \\ u &= g, \quad \text{on } \partial\Omega \setminus \Gamma \end{aligned}$$

for given functions f and g, which are also sufficiently regular. Hereby $\bar{u} \in L^2(\Omega)$ and $\bar{q} \in \mathcal{Q}$ are given functions.

Remark 5.2.
In the following we assume that the control boundary Γ is the whole boundary of the computational domain. The general case can be treated in the same way as described in the next sections by slightly modifying the notation and the argumentation.

The appropriate space for the boundary functions, and therefore the control, is the space $H^{\frac{1}{2}}(\Gamma)$. However we will see that this space increases the numerical effort drastically and therefore discuss L^2-controls and their approximations.

5.1.1. $H^{\frac{1}{2}}$-Control

For notational brevity we set $\bar{q} = 0$ and remark that the general case is also working in the same manner.

Then we need an operator with the property

$$A : H^{\frac{1}{2}}(\partial\Omega) \to H^{-\frac{1}{2}}(\partial\Omega)$$

such that

$$|\cdot|_A^2 := \langle A\cdot, \cdot\rangle$$

defines a seminorm which is equivalent to the $H^{\frac{1}{2}}(\partial\Omega)$-seminorm

$$|u|_{H^{\frac{1}{2}}(\partial\Omega)^n} = \int_{\partial\Omega} \left(\int_{\partial\Omega} \frac{|u(y) - u(y^\star)|^2}{|y - y^\star|^n} \, d\sigma_y \right) d\sigma_{y^\star}, \quad \text{(see Galdi [41, p. 44 ff])}. \tag{5.1}$$

For example Of et al. [82] and John [72] work with the Steklov-Poincaré operator for this purpose. In the following we will briefly describe this approach.

It is clear that the homogeneous Poisson problem

$$\begin{aligned} -\Delta\omega &= 0, \qquad \text{in } \Omega, \\ \omega &= g, \qquad \text{on } \partial\Omega \end{aligned} \tag{5.2}$$

admits a unique solution in $H^1(\Omega)$ for $g \in H^{\frac{1}{2}}(\Gamma)$. As figured out for example in Menad [78] the Steklov-Poincaré operator is now defined as a mapping

$$\mathcal{P}_{\text{SP}} : H^{\frac{1}{2}}(\partial\Omega) \to H^{-\frac{1}{2}}(\partial\Omega), \quad \text{with} \quad g \mapsto \partial_{\boldsymbol{n}}\omega.$$

The so defined operator is symmetric with respect to the L^2 inner product on the boundary and furthermore positive definite. Hence, we have

$$|q|^2_{H^{\frac{1}{2}}(\partial\Omega)} = \langle \mathcal{P}_{SP} q, q \rangle = \langle \partial_{\boldsymbol{n}}\omega, q \rangle_{\partial\Omega}.$$

Due to the unique solvability of the state equation for $g \in H^{\frac{1}{2}}(\partial\Omega)$ we can introduce a solution operator $\mathcal{S}(q) = u$ and formulate the reduced cost functional

$$j(q) = J(\mathcal{S}(q), q) = \frac{1}{2}\|\mathcal{S}(q) - \bar{u}\|^2_{L^2(\Omega)} + \frac{\alpha}{2}|q|^2_{H^{\frac{1}{2}}(\partial\Omega)},$$

which admits a unique solution due to Theorems 4.5 and 4.7.

Remark 5.3 (Increased Numerical Effort for $H^{\frac{1}{2}}$-Controls).
The resulting optimality condition is only a slight modification of the gradient equation in contrast to the choice of other possible control spaces. We therefore postpone the statement of the optimality system. However, we want to emphasise that either the complicated boundary integral in equation (5.1) has to be calculated or the auxiliary variable ω is needed in the solution process and therefore the Poisson equation 5.2 has to be solved, which obviously increases the costs of the numerical calculation (especially in view of further time dependent systems of equations).

5.1.2. L^2-Control

We have seen that the use of the space $H^{\frac{1}{2}}(\partial\Omega)$ necessitates the solution of an auxiliary problem or the calculation of complicated boundary integrals. Therefore, we prefer to simply use the space $L^2(\partial\Omega)$ for the control to avoid this problem.

How to use this control space was for example described by May et al. [76] and Belgacem et al. [13]. For this purpose the authors used the very weak formulation of the Poisson equation:

Very Weak Formulation 5.4 (Poisson Equation).
For given $q \in L^2(\partial\Omega)$ find $u \in L^2(\Omega)$ in a way that

$$-(u, \Delta\varphi) + \langle q, \partial_n\varphi\rangle = (f, \varphi)$$

is fulfilled for all $\varphi \in H_0^1(\Omega) \cap H^2(\Omega)$.

Here the control is in $L^2(\partial\Omega)$ and the optimal control problem admits also for this formulation a unique solution $(u, q) \in L^2(\Omega) \times L^2(\partial\Omega)$, since we have for the very weak formulation the existence of a solution operator (see the above mentioned literature)

$$S : L^2(\partial\Omega) \to L^2(\Omega)$$

and we are therefore able to embed the problem into the abstract setting of Theorem 4.5.

Remark 5.5 (Equivalence to Weak Formulation).
In case that the solution admits higher regularity (for example $u \in H^1(\Omega)$) we have the equivalence between the above mentioned very weak formulation and the usual weak formulation:

Find $u \in Bq + H_0^1(\Omega)$ such that

$$(\nabla u, \nabla\varphi) = (f, \varphi), \qquad \forall\varphi \in H_0^1(\Omega),$$

where B is an extension operator, which prolongates boundary functions into the interior of the domain.

The introduction of the very weak formulation has the big advantage that the control enters now the variational setting in a direct way as in the case of Neumann or Robin controls.

Hence the optimality system is given by

$$\begin{aligned}
-(u, \Delta\varphi) + \langle q, \partial_n\varphi\rangle &= (f, \varphi), && \forall\varphi \in H_0^1(\Omega) \cap H^2(\Omega), && \text{(Primal equation)},\\
-(\hat{\varphi}, \Delta z) - (u, \hat{\varphi}) &= -(\bar{u}, \hat{\varphi}), && \forall\hat{\varphi} \in L^2(\Omega), && \text{(Dual equation)},\\
\alpha\langle q, \rho\rangle - \langle \partial_n z, \rho\rangle &= 0, && \forall\rho \in L^2(\partial\Omega), && \text{(Control equation)}.
\end{aligned} \tag{5.3}$$

The system admits a unique solution $\{u, q, z\} \in L^2(\Omega) \times L^2(\Gamma) \times H^2(\Omega) \cap H_0^1(\Omega)$.

Under the assumption of higher regularity for the state solution u, the dual solution z and the control q we obtain the classical formulation of the above mentioned optimality system

$$\begin{aligned}
-\Delta u &= f, && \text{in } \Omega,\\
u &= q, && \text{on } \partial\Omega,\\
-\Delta z - u &= -\bar{u}, && \text{in } \Omega,\\
z &= 0, && \text{on } \partial\Omega,\\
\alpha q - \partial_n z &= 0, && \text{on } \partial\Omega.
\end{aligned} \tag{5.4}$$

Remark 5.6 (Optimality System for $H^{\frac{1}{2}}$).
The optimality system for the $H^{\frac{1}{2}}$-formulation differs from system (5.4) only in the control equation:

$$\alpha \mathcal{P}_{SP} q - \partial_n z = 0, \qquad \text{on } \partial\Omega,$$

where $\mathcal{P}_{SP}$ constitutes the Steklov-Poincaré operator mentioned in the section before.

In contrast, a big disadvantage of the very weak formulation is that it is not easy to handle from the numerical point of view. For example we have no chance to solve this problem with bilinear finite elements due to the Laplacian acting on the test functions.

A way out of this dilemma is presented by Belgacem et al. [13], who uses a Neumann penalisation of the Dirichlet condition like we present it in Chapter 3.3 for the Poisson equation. The technique is closely related to another approach of proving existence of a very weak solution $u \in L^2(\Omega)$ presented for example by Marusic-Paloka [74].
In this approach the following penalisation of the state equation

$$\begin{aligned} -\Delta u_\mu &= f, && \text{in } \Omega, \\ \partial_n u_\mu &= \frac{1}{\mu}(q - u_\mu), && \text{on } \Gamma \end{aligned} \tag{5.5}$$

is used to show existence of a solution of the very weak formulation by proving uniform boundedness of u_μ in $L^2(\Omega)$ and $L^2(\partial\Omega)$ with respect to μ.

Belgacem et al. [13] realise that it seems very promising to work with this approach also for numerical calculations of Dirichlet control problems. The advantage is that this approach is very easy to implement and has good convergence properties which we presented in Chapter 3.3.

We will now present the theoretical background of this approach. Here we employ argumentation techniques used in the articles of Hou et al. [55], [56] which are different to the argumentation chosen in the paper of Belgacm et al. [13]. The advantage is that the presented argumentation is more flexible for the extension to more complicated time-dependent boundary control problems, which we will show in the subsequent sections.

Starting point is the following perturbed optimisation problem. We will briefly discuss the (unique) existence of a solution and afterwards answer the question if a μ-dependent solution convergences to a solution of the optimisation problem with the very weak formulation as side condition.

Optimisation Problem 5.7 (Poisson Equation with Robin-Type Control).
We seek $(u_\mu, q_\mu) \in H^1(\Omega) \times L^2(\partial\Omega)$ such that the cost functional

$$\mathcal{J}(u_\mu, q_\mu) = \frac{1}{2}\|u_\mu - \bar{u}\|_2^2 + \frac{\alpha}{2}\|q_\mu - \bar{q}\|_{L^2(\partial\Omega)}$$

is minimal subject to the following Weak Formulation 5.8, where $f \in L^2(\Omega)$, $\bar{u} \in L^2(\Omega)$ and $\bar{q} \in L^2(\partial\Omega)$ are given functions.

Weak Formulation 5.8 (Poisson Equation with Robin-Type Boundary).
Find $u_\mu \in H^1(\Omega)$ such that

$$(\nabla u_\mu, \nabla \varphi) - \frac{1}{\mu} \langle (q_\mu - u_\mu), \varphi \rangle = (f, \varphi), \qquad \forall \varphi \in H^1(\Omega).$$

For a fixed $0 < \mu \leq 1$ and $q_\mu \in L^2(\partial\Omega)$ we have

$$\|\nabla u_\mu\|_2^2 + \frac{1}{\mu}\|u_\mu\|_{L^2(\partial\Omega)}^2 \leq \|f\|_2 \|u_\mu\|_2 + \frac{1}{\mu}\|q_\mu\|_{L^2(\partial\Omega)} \|u_\mu\|_{L^2(\partial\Omega)}$$

and with the general Poincaré inequality (cf. Brenner [19, formula (5.3.3.)])

$$\|\omega\|_2 \leq C \left(\|\nabla \omega\|_2 + \|\omega\|_{L^2(\partial\Omega)} \right) \tag{5.6}$$

and Young's inequality we obtain the a priori bound

$$\frac{3}{4}\|\nabla u_\mu\|_2^2 + \frac{1}{2\mu}\|u_\mu\|_{L^2(\partial\Omega)}^2 \leq \frac{C}{2}\|f\|_2^2 + \frac{1}{\mu}\|q_\mu\|_{L^2(\partial\Omega)}^2. \tag{5.7}$$

With this bound we can obtain by standard argumentations the existence and uniqueness of the state equation (see the Galerkin method in Chapter 2.2.1). Hence there exists a solution operator $u_\mu = S(q_\mu)$ and by Theorem 4.5 and Remark 4.7 we get the existence of a unique minimiser $(\tilde{u}_\mu, \tilde{q}_\mu) \in H^1(\Omega) \times L^2(\Omega)$.

By the corresponding Lagrangian

$$\mathcal{L}(u_\mu, q_\mu, z_\mu) = J(u_\mu, q_\mu) - (\nabla u_\mu, \nabla z_\mu) + \frac{1}{\mu} \langle (q_\mu - u_\mu), z_\mu \rangle + (f, z_\mu)$$

we derive the optimality system

$$\begin{aligned}
(\nabla u_\mu, \nabla \varphi) - \frac{1}{\mu} \langle q_\mu - u_\mu, \varphi \rangle &= (f, \varphi), && \forall \varphi \in H^1(\Omega), && \text{(Primal equation)}, \\
(\nabla \hat{\varphi}, \nabla z_\mu) + \frac{1}{\mu} \langle \hat{\varphi}, z_\mu \rangle - (u_\mu, \hat{\varphi}) &= -(\bar{u}, \hat{\varphi}), && \forall \hat{\varphi} \in H^1(\Omega), && \text{(Dual equation)}, \\
\alpha \langle q_\mu, \rho \rangle + \frac{1}{\mu} \langle z_\mu, \rho \rangle &= 0, && \forall \rho \in L^2(\Gamma), && \text{(Control equation)}.
\end{aligned} \tag{5.8}$$

The solution pair (u_μ, q_μ) of the optimisation problem is then characterised by the triplet (u_μ, q_μ, z_μ) which solves the above system. Therefore the existence of $z_\mu \in H^2 \cap H_0^1(\Omega)$ is needed.

Now we have to check that $\{u_\mu, q_\mu, z_\mu\}$ converges to a solution of the optimal control problem.

Theorem 5.9 (Convergence Properties).
For an arbitrary μ the triplet (u_μ, q_μ, z_μ) is a solution of the optimisation problem 5.7.

Furthermore we assume that Ω is convex and polygonal. For the triplet sequence $(u_\mu, q_\mu, z_\mu)_\mu$ we have then the following convergence properties

$$q_\mu \rightharpoonup \tilde{q} \in L^2(\partial\Omega), \tag{5.9}$$
$$u_\mu \rightharpoonup \tilde{u} \in L^2(\Omega), \tag{5.10}$$
$$z_\mu \rightharpoonup \tilde{z} \in H_0^1(\Omega), \tag{5.11}$$

when $\mu \to 0$.

Proof. We will use three steps to prove these properties.

1. If we choose $q = 0$ we know that their exists a unique solution of the Weak Formulation 5.8, which we indicate by $\hat{u}$. Since (u_μ, z_μ, q_μ) is the minimum, we have

$$J(u_\mu, q_\mu) \leq J(\hat{u}, 0) \quad \Rightarrow \quad \frac{1}{2}\|u_\mu - \bar{u}\|_2^2 + \frac{\alpha}{2}\|q_\mu\|_{L^2(\partial\Omega)}^2 \leq \frac{1}{2}\|\hat{u}\|_2^2 + \|\bar{u}\|_2^2,$$

   after using the triangle inequality on the right hand side.

   Furthermore, we obtain for $q = 0$ and the corresponding solution $\hat{u}$ by the a priori bound in formula (5.7) and the inequality (5.6) the following estimate

$$\|\hat{u}\|_2^2 \leq C\left(\|\nabla\hat{u}\|_2^2 + \|\hat{u}\|_{L^2(\partial\Omega)}^2\right) \leq C\|f\|_2^2.$$

   Combining the last two estimates yields the following uniform bound for q_μ

$$\|q_\mu\|_{L^2(\partial\Omega)} \leq \frac{C_{f,\bar{u}}}{\alpha}. \tag{5.12}$$

2. Now we want to prove that u_μ is uniformly bounded in the L^2 norm. Therefore we have again a look at the a priori bound (5.7). With the bound for the control q_μ in formula (5.12) we obtain now

$$\frac{3}{4}\|\nabla u_\mu\|_2^2 + \frac{1}{2\mu}\|u_\mu\|_{L^2(\partial\Omega)}^2 \leq \frac{C}{2}\|f\|_2^2 + \frac{C_{f,\bar{u},\alpha}}{\mu}.$$

   Hence, we have

$$\|u_\mu\|_{L^2(\partial\Omega)} \leq C_{f,\bar{u},\alpha} \quad \text{and} \quad \|\nabla u_\mu\|_2 \leq \frac{C_{f,\bar{u},\alpha}}{\sqrt{\mu}}. \tag{5.13}$$

   The first inequality yields again uniform boundedness of u_μ in L^2 on the boundary. The second bound is not uniform. Anyhow, for a fixed μ we can use the inequalities for a duality argument to obtain uniform boundedness in $L^2(\Omega)$.

   We introduce the auxiliary dual problem

$$\begin{aligned} -\Delta\lambda &= u_\mu, \quad \text{in } \Omega, \\ \lambda &= 0, \quad \text{on } \partial\Omega. \end{aligned}$$

From the classical regularity theory of elliptic operators (see Satz 7.6 in Dobrowolski [29]) we have

$$\|\lambda\|_{H^2} \leq C\|u_\mu\|_2, \tag{5.14}$$

since Ω is a convex polygon.

Now we test the dual problem with u_μ and integrate over the domain. After integration by parts we get

$$\|u_\mu\|_2^2 = (\nabla\lambda, \nabla u_\mu) - \langle \partial_{\boldsymbol{n}}\lambda, u_\mu\rangle_{\partial\Omega}\,.$$

Using the Weak Formulation 5.8 again yields

$$\|u_\mu\|_2^2 = (f,\lambda) - \langle \partial_{\boldsymbol{n}}\lambda, u_\mu\rangle_{\partial\Omega} \leq \|f\|_2\|\lambda\|_2 + \|\partial_{\boldsymbol{n}}\lambda\|_{L^2(\partial\Omega)}\|u_\mu\|_{L^2(\partial\Omega)}.$$

And finally by the uniform bound for the boundary norm for u_μ and the estimate we obtain (5.14)

$$\|u_\mu\|_2^2 \leq \Big(C\|f\|_2 + C_{f,\bar{u},\alpha}\Big)\,\|\lambda\|_{H^2(\Omega)} \leq C_{f,\bar{u},\alpha}\|u_\mu\|_2$$

and with this the uniform bound

$$\|u_\mu\|_2 \leq C_{f,\bar{u},\alpha}.$$

3. Finally we discuss the sequence of the dual variable z_μ. Therefore, we test the dual equation with z_μ. Afterwards we apply with the usual inequalities used throughout this proof and get $\|u_\mu - \bar{u}\|_2 \leq C$, which is a consequence of the first step of this proof. We find

$$\begin{aligned}\|\nabla z_\mu\|_2^2 + \frac{1}{\mu}\|z_\mu\|_{L^2(\partial\Omega)}^2 &\leq \|u_\mu - \bar{u}\|_2\|z_\mu\|_2 \leq C_{f,\bar{u},\alpha}\|z_\mu\|_2 \\ &\leq C_{f,\bar{u},\alpha} + \frac{1}{2C}\|z_\mu\|_2^2 \leq C_{f,\bar{u},\alpha} + \frac{1}{2}\|\nabla z_\mu\|_2^2 + \frac{1}{2}\|z_\mu\|_{L^2(\partial\Omega)}^2.\end{aligned}$$

Because of $1 \leq \frac{1}{\mu}$ we get the inequality

$$\|\nabla z_\mu\|_2^2 + \frac{1}{\mu}\|z_\mu\|_{L^2(\partial\Omega)}^2 \leq C_{f,\bar{u},\alpha},$$

which yields

$$\|z_\mu\|_{L^2(\partial\Omega)} \leq \sqrt{\mu}C_{f,\bar{u},\alpha}, \quad \text{and} \quad \|\nabla z_\mu\|_2 \leq C_{f,\bar{u},\alpha}.$$

We have

$$z_\mu \rightharpoonup \tilde{z} \in H^1(\Omega)$$

and

$$z_\mu \rightharpoonup \tilde{z} \in L^2(\partial\Omega)$$

because of $\|z_\mu\|_{L^2(\partial\Omega)} \leq C$, since $\sqrt{\mu} \leq 1$ and z_μ converges weakly in L^2 to zero on the boundary:

$$\lim_{\mu\to 0}\langle z_\mu, \rho\rangle_{\partial\Omega} \leq \lim_{\mu\to 0}\|z_\mu\|_{L^2(\partial\Omega)}\|\rho\|_{L^2(\partial\Omega)} \leq \lim_{\mu\to 0}\sqrt{\mu}C = 0, \quad \forall\rho \in L^2(\partial\Omega).$$

Hence, the limit value $\tilde{z}$ is in $H_0^1(\Omega)$. □

Remark 5.10 (Other Regularity Results).
By the last theorem we can guarantee that the sequence of optimal solutions (u_μ, z_μ, q_μ) in μ converges to a limit $(\tilde{u}, \tilde{z}, \tilde{q}) \in L^2(\Omega) \times H_0^1(\Omega) \times L^2(\Gamma)$ for $\mu \to 0$. We will use this result to check if the limit is a solution of the optimality system that arises from the optimisation problem with the very weak formulation. Thus we will see that the dual solution $\tilde{z}$ admits even more regularity since we work with a convex polygon as computational domain.

We also want to mention that under the assumption of further regularity of the domain (e. g. C^2 boundaries) we have even higher regularity of the limit function. See for example the following theorem, which also yields a qualitative statement about the convergence in μ.

Theorem 5.11 (Theorem 4.2, Belgacem et al. [13]).
The domain Ω is smooth (C^2-regular) and $\bar{u} \in L^2(\Omega)$. With $s \in [0,1]$ we have

$$\|z_\mu - \tilde{z}\|_{H^{1+s}(\Omega)} + \|q_\mu - \tilde{q}\|_{H^{-\frac{1}{2}+s}(\partial\Omega)} \leq C\mu^{1-s}\|\bar{u}\|_2.$$

Moreover, we have

$$\|u_\mu - \tilde{u}\|_{H^s(\Omega)} \leq C\mu^{1-s}\|\bar{u}\|_2,$$

were both constants are independent of μ.

Thus, by this theorem we obtain the weak convergence of the sequence $(u_\mu, z_\mu, q_\mu)_\mu$ to $(\tilde{u}, \tilde{z}, \tilde{q}) \in H^1(\Omega) \times H^2(\Omega) \times H^{\frac{1}{2}}(\partial\Omega)$ for the limit case $s = 1$.

Once we have shown that this sequence converges to a solution of the optimisation problem with the very weak formulation as side condition we know that this solution admits more regularity and therefore we can also work with the usual weak formulation from Remark 5.5.

However, we want to emphasise again that for general polygonal domains we lose the above stated regularity $H^1(\Omega) \times H^2(\Omega) \times H^{\frac{1}{2}}(\partial\Omega)$ of the triplet $(\tilde{u}, \tilde{z}, \tilde{q})$, since $\partial_{\boldsymbol{n}} z$ does not longer belong to $H^{\frac{1}{2}}(\partial\Omega)$ due to the corner points of the domain. Nevertheless for special situations we can still obtain higher regularity results, see therefore Remark 2 in May et al. [76] or the discussion in Section 4.2 in Belgacem et al. [13].

We can easily check that the obtained limit triplet is also a solution of the optimality system (5.3).

By partial integration in the primal equation of (5.8) and choosing the subset

$$H^2(\Omega) \cap H_0^1(\Omega) \subset H^1(\Omega)$$

we obtain

$$-(\tilde{u}_\mu, \Delta\varphi) + \langle \tilde{u}_\mu, \partial_{\boldsymbol{n}}\varphi \rangle_{\partial\Omega} = (f, \varphi), \quad \forall \varphi \in H^2(\Omega) \cap H_0^1(\Omega).$$

The convergence of the first term is clear. The second term can be obtained by the following identity

$$\langle \tilde{u}_\mu - \tilde{q}, \rho \rangle_{\partial\Omega} = \langle \tilde{u}_\mu - \tilde{q}_\mu, \rho \rangle_{\partial\Omega} + \langle \tilde{q}_\mu - \tilde{q}, \rho \rangle_{\partial\Omega}, \quad \forall \rho \in L^2(\partial\Omega).$$

The second term of the right hand side tends to zero, due to the convergence properties of $\tilde{q}_\mu$. The first term can be obtained by estimating the primal equation and using the second estimate in formula (5.13)

$$\frac{1}{\mu} \langle \tilde{u}_\mu - \tilde{q}_\mu, \varphi \rangle_{\partial\Omega} \leq \|f\|_2 \|\varphi\|_2 + \|\nabla u_\mu\|_2 \|\nabla\varphi\|_2 \leq \frac{C}{\sqrt{\mu}} \quad \Rightarrow \quad \langle \tilde{u}_\mu - \tilde{q}_\mu, \varphi \rangle_{\partial\Omega} \leq \sqrt{\mu} C.$$

Thus, we get

$$-(\tilde{u}, \Delta\varphi) + \langle \tilde{q}, \partial_{\boldsymbol{n}} \varphi \rangle_{\partial\Omega} = (f, \varphi), \quad \forall \varphi \in H^2(\Omega) \cap H_0^1(\Omega). \tag{5.15}$$

Now we have a look at the convergence in the dual equation of (5.8).

$$(\nabla \tilde{z}_\mu, \nabla\varphi) + \frac{1}{\mu} \langle \tilde{z}_\mu, \varphi \rangle_{\partial\Omega} - (\tilde{u}_\mu, \varphi) = -(\bar{u}, \varphi), \quad \forall \varphi \in H^1(\Omega).$$

For each $\mu \in (0, 1]$ the equation is also valid for the subspace $H_0^1(\Omega) \subset H^1(\Omega)$

$$(\nabla \tilde{z}_\mu, \nabla\varphi) - (\tilde{u}_\mu, \varphi) = -(\bar{u}, \varphi).$$

By the convergence properties of Theorem 5.9 we obtain that the limit functions $\tilde{z} \in H_0^1(\Omega)$ and $\tilde{u} \in L^2(\Omega)$ fulfil the equation

$$(\nabla \tilde{z}, \nabla\varphi) - (\tilde{u}, \varphi) = -(\bar{u}, \varphi).$$

This is due to the regularity theory of elliptic operators on a convex polygon equivalent to the classical formulation

$$\begin{aligned} -\Delta\tilde{z} &= \tilde{u} - \bar{u}, && \text{a. e. in} \quad \Omega, \\ \tilde{z} &= 0, && \text{a. e. on} \quad \partial\Omega, \end{aligned} \tag{5.16}$$

with $\tilde{z} \in H^2(\Omega) \cap H_0^1(\Omega)$. Hence, $\tilde{z}$ and $\tilde{u}$ fulfil especially the dual equation in system (5.3).

Finally, we have to check the convergence to the optimality condition in the system (5.3). We start with the optimality condition for the perturbed problem

$$\alpha \langle q_\mu, \rho \rangle_{\partial\Omega} = -\frac{1}{\mu} \langle z_\mu, \rho \rangle_{\partial\Omega}.$$

The convergence on the left hand side to the limit $q \in L^2(\partial\Omega)$ is clear. Only the convergence of the boundary form on the right hand side remains. Therefore we multiply the classical formulation in equation (5.16) with $\varphi \in H^1(\Omega)$ and obtain after integration over the domain the equivalent weak formulation

$$(\nabla \tilde{z}, \nabla\varphi) - \langle \partial_{\boldsymbol{n}} \tilde{z}, \varphi \rangle_{\partial\Omega} - (\tilde{u}, \varphi) = -(\bar{u}, \varphi), \quad \forall \varphi \in H^1(\Omega).$$

Using this weak formulation and the one for the dual problem in system (5.8) we find

$$\frac{1}{\mu}\langle \tilde{z}_\mu, \varphi\rangle_{\partial\Omega} - (-\langle \partial_{\boldsymbol{n}}\tilde{z}, \varphi\rangle_{\partial\Omega}) = -(\nabla\tilde{z}_\mu, \nabla\varphi) + (\tilde{u}_\mu - \bar{u}, \varphi) + (\nabla\tilde{z}, \nabla\varphi) - (\tilde{u} - \bar{u}, \varphi).$$

Thus

$$\left|\frac{1}{\mu}\langle \tilde{z}_\mu, \varphi\rangle_{\partial\Omega} - (-\langle \partial_{\boldsymbol{n}}\tilde{z}, \varphi\rangle_{\partial\Omega})\right| \leq \left|(\nabla(\tilde{z} - \tilde{z}_\mu), \nabla\varphi)\right| + \left|((\tilde{u}_\mu - \tilde{u}, (\varphi)\right| \tag{5.17}$$

for all $\varphi \in H^1(\Omega)$. Due to the convergence properties of the terms on the right hand side of the last estimate we get

$$\lim_{\mu\to 0}\frac{1}{\mu}\langle \tilde{z}_\mu, \varphi\rangle_{\partial\Omega} = -\langle \partial_{\boldsymbol{n}}\tilde{z}, \varphi\rangle_{\partial\Omega}, \quad \forall\rho \in L^2(\partial\Omega),$$

which means that the limit of the triplet also fulfils the control equation of the optimality system (5.8).

Hence, we have shown that the sequence of solution pairs $(u_\mu, q_\mu)_\mu$ of the Robin-type boundary control problem converges to a solution of the Dirichlet control problem with the very weak formulation as PDE side condition. That means especially that we can use the Robin-type controls for the approximation of Dirichlet controls.

Numerical Example

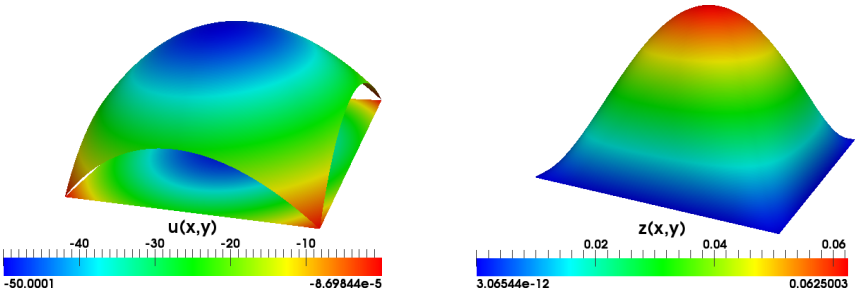

Figure 5.1. Example 5.12, left: State solution $\hat{u}(\boldsymbol{x})$. Right: Adjoint solution $\hat{z}(\boldsymbol{x})$. Note that the two bulges show in different directions due to the values of the scalar bar.

We confirm the utility of the above mentioned approximation approach by a numerical example in this context taken from the numerical test chapter of the work of May et al. [76].

Example 5.12.
We have the initial configuration

$$f = -\frac{4}{\alpha}, \qquad \bar{u} = -(2 + \frac{1}{\alpha})(x(1-x) + y(1-y)), \qquad \bar{q} = 0, \quad \alpha = 0.01.$$

As a result the unique analytical solution of the optimality system (5.4) is given by

$$\begin{aligned}\hat{q} &= -\frac{1}{\alpha}(x(1-x)+y(1-y)), \quad \text{on } \Gamma,\\ \hat{u} &= -\frac{1}{\alpha}(x(1-x)+y(1-y)), \quad \text{in } \Omega,\\ \hat{z} &= xy(1-x)(1-y), \qquad\qquad \text{in } \Omega.\end{aligned}$$

We visualised the solutions in Figure 5.1.

Table 5.1. For a fixed uniform discretisation of the unit square $(0,1)^2$ into 16384 cells we compare in this table the approximations u_μ, q_μ and z_μ of the Dirichlet control problem of Example 5.12 for $\mu_i = 0.1 \cdot 2^{-i}$ (bisection of 0.1).

i	$\|\hat{u}-u_{h,\mu}\|_{L^2(\Omega)}$	**(rate)**	$\|\hat{q}-q_{h,\mu}\|_{L^2(\Omega)}$	**(rate)**	$\|\hat{z}-z_{h,\mu}\|_{L^2(\Omega)}$	**(rate)**
0	$5.4918{\cdot}10^{-1}$		$2.5365{\cdot}10^{0}$		$5.2399{\cdot}10^{-3}$	
1	$2.9194{\cdot}10^{-1}$	**(0.87)**	$1.5121{\cdot}10^{0}$	**(0.75)**	$3.6127{\cdot}10^{-3}$	**(0.54)**
2	$1.5164{\cdot}10^{-1}$	**(0.92)**	$8.6644{\cdot}10^{-1}$	**(0.80)**	$2.3058{\cdot}10^{-3}$	**(0.65)**
3	$7.7501{\cdot}10^{-2}$	**(0.95)**	$4.8019{\cdot}10^{-1}$	**(0.85)**	$1.2893{\cdot}10^{-3}$	**(0.83)**
4	$3.9184{\cdot}10^{-2}$	**(0.97)**	$2.5871{\cdot}10^{-1}$	**(0.89)**	$6.7921{\cdot}10^{-4}$	**(0.92)**
5	$1.9671{\cdot}10^{-2}$	**(0.99)**	$1.3626{\cdot}10^{-1}$	**(0.93)**	$3.4789{\cdot}10^{-4}$	**(0.97)**
6	$9.8268{\cdot}10^{-3}$	**(0.99)**	$7.0585{\cdot}10^{-2}$	**(0.95)**	$1.7759{\cdot}10^{-4}$	**(0.99)**
7	$4.8855{\cdot}10^{-3}$	**(1.08)**	$3.6211{\cdot}10^{-2}$	**(0.96)**	$8.7771{\cdot}10^{-5}$	**(1.00)**

We insert now the identity for the control q_μ, which is described by the control equation in the system (5.8), into the primal equation. This is possible since the test functions of the primal equation are in $H^1(\Omega)$ and therefore have at least an L^2-trace on $\partial\Omega$. Then we derive the coupled system:

Find $(u_\mu, z_\mu) \in H^1(\Omega) \times H^1(\Omega)$ such that

$$\begin{aligned}(\nabla u_\mu, \nabla\varphi) + \frac{1}{\mu}\langle u_\mu, \varphi\rangle + \frac{1}{\alpha\mu^2}\langle z_\mu, \varphi\rangle &= (f,\varphi), \qquad \forall\ \varphi \in H^1(\Omega),\\ (\nabla z_\mu, \nabla\hat{\varphi}) + \frac{1}{\mu}\langle z_\mu, \hat{\varphi}\rangle - (u_\mu, \hat{\varphi}) &= -(\bar{u}, \hat{\varphi}), \qquad \forall\ \hat{\varphi} \in H^1(\Omega).\end{aligned} \tag{5.18}$$

This system (5.18) is discretized with bilinear finite elements (for details see Chapter 3).

Remark 5.13 (Newton-CG). *The Optimisation Problem 5.7 can be solved of course also with the Newton-CG method presented in the Chapter 4. Nevertheless we solve the optimality system directly, since we consider an easy convex optimisation problem with a stationary PDE as side condition, where the unique solution of the optimisation problem is described by the optimality system, which can be reduced to the system (*5.18*) due to the structure of the control equation.*

The number of unknowns is doubled in comparison to the original state equation and the above system is now nonlinear. But with a usual Newton method for nonlinear systems (like it is used for example for calculations of the Navier-Stokes equation, see Chapter 3.5.2) this system can be solved easily and efficiently.

On the other hand the Newton-CG method requires in each CG step the solution of two additional PDEs with the complexity of the original state equation plus a further additional computation of the dual equation in each Newton step. Each of these equations is in our particular case linear and therefore easy to solve by a usual linear solver. However in our experience at least two Newton steps with several CG-steps are necessary to achieve a sufficient accuracy, so that the direct calculation via the above mentioned system is in general more efficient than the Newton-CG method in this context.

This is changing drastically when we are working with time-dependent equations, since we cannot directly solve the optimality system due to forward and backward integration in time. Treating the time as a third spatial dimension would increase essentially the complexity, so that in this case the Newton-CG method is a very efficient means to calculate the solution of the optimisation problem.

Table 5.2. The table documents the error evolution under mesh refinement for $\mu = h^2$.

cells	$\|\hat{u} - u_{h,\mu}\|_{L^2(\Omega)}$	**(rate)**	$\|\hat{q} - q_{h,\mu}\|_{L^2(\Omega)}$	**(rate)**	$\|\hat{z} - z_{h,\mu}\|_{L^2(\Omega)}$	**(rate)**
64	$8.3277{\cdot}10^{-2}$		$8.5997{\cdot}10^{-1}$		$1.3383{\cdot}10^{-3}$	
256	$2.0916{\cdot}10^{-2}$	**(1.99)**	$2.2927{\cdot}10^{-1}$	**(1.91)**	$3.6281{\cdot}10^{-4}$	**(1.88)**
1024	$5.1813{\cdot}10^{-3}$	**(2.01)**	$5.9050{\cdot}10^{-2}$	**(1.96)**	$9.2573{\cdot}10^{-5}$	**(1.97)**
4096	$1.2896{\cdot}10^{-3}$	**(2.01)**	$1.4862{\cdot}10^{-2}$	**(1.99)**	$2.3262{\cdot}10^{-5}$	**(1.99)**
16348	$3.2240{\cdot}10^{-4}$	**(2.00)**	$3.7117{\cdot}10^{-3}$	**(2.00)**	$5.8232{\cdot}10^{-6}$	**(2.00)**
65536	$8.0659{\cdot}10^{-5}$	**(2.00)**	$9.2659{\cdot}10^{-4}$	**(2.00)**	$1.4563{\cdot}10^{-6}$	**(2.00)**
262144	$2.0173{\cdot}10^{-5}$	**(2.00)**	$2.3149{\cdot}10^{-4}$	**(2.00)**	$3.6409{\cdot}10^{-7}$	**(2.00)**

We make two experiments for the above mentioned optimality system. The first one considers the parameter μ and the quality of the approximations to the analytic solutions of the Dirichlet control problem in the example. The second one considers the convergence under mesh refinement for the convenient choice h^2 for μ, as mentioned in Example 3.10 in Chapter 3.3.

In both cases we compute (u_μ, z_μ) directly from system (5.18) by bilinear finite elements and compare them to the analytic solution in the L^2-norm. For the control q_μ we compare the state solution on the boundary $u|_{\partial\Omega}$ to the analytic solution $\hat{q}$ in the L^2-norm on the boundary.

In Table 5.1 we see that we achieve better approximations of the Dirichlet control problem for decreasing μ. At first glance it seems like a good idea to work with this Robin-type

approach to generate approximations of Dirichlet control problems. But we also want to emphasise that the numerical problem gets more and more ill-conditioned for decreasing μ. If we drop the value of μ under 10^{-8} the residual of our problem becomes larger, which is an indicator that our approximation has lost its accuracy. Hence the problem is not solved properly and the approach is not able to resolve the Dirichlet control problem up to any given accuracy.

The second test which is documented in Table 5.2 shows that the approximation is converging to the expected solution under mesh refinement if we choose $\mu = h^2$. We achieve the same quadratic convergence properties in h as May et al. [76] for this particular example with a strong implementation of the L^2-Dirichlet control. Also for this parameter choice the problem remains, that the system becomes ill-conditioned for small μ, which means here the choice of very fine meshes.

However, the fact that we cannot solve the system for arbitrarily small μ is unsatisfactory. Since this effect was already observed for the discretisation of the state equation (cf. Chapter 3.3), we are able to avoid this problem by working with the stabilisation of the Neumann penalisation in the discretised version of the optimality system. Thus, we write the discrete optimality system as

$$\begin{aligned} (\nabla u_h, \nabla\varphi) + b(q_h; u_h, \varphi) &= (f, \varphi)\,, && \forall \varphi \in V_{\mathcal{X}}, \\ (\nabla z_h, \nabla\hat{\varphi}) + b(0; z_h, \hat{\varphi}) &= (u_h - \bar{u}, \hat{\varphi})\,, && \forall \hat{\varphi} \in V_{\mathcal{X}}, \\ \alpha \langle q_h, \rho\rangle_{\partial\Omega} &= -\, b(0; z_h, \rho), && \forall \rho \in V_{\mathcal{Q}}, \end{aligned}$$

with

$$b(q; u, \varphi) = \frac{1}{\mu} \langle u - q, \varphi\rangle_{\partial\Omega}\,.$$

Afterwards, we substitute $b(q; u, \varphi)$ by the stabilised version

$$\begin{aligned} b(q; u, \varphi) = &- \frac{\delta}{\mu + \delta} \left(\langle \partial_{\boldsymbol{n}} u, \varphi\rangle_{\partial\Omega} + \langle u - q, \partial_{\boldsymbol{n}}\varphi\rangle_{\partial\Omega} \right) + \frac{1}{\mu + \delta} \langle u - q, \varphi\rangle_{\partial\Omega} \\ &- \frac{\mu\delta}{\mu + \delta} \langle \partial_{\boldsymbol{n}} u, \partial_{\boldsymbol{n}}\varphi\rangle_{\partial\Omega}\,, \end{aligned} \tag{5.19}$$

which is for $\delta = 0$ equal to the original form.

By setting $\mu = 0$ and $\delta = \frac{h}{\gamma}$ we implement the Nitsche method to realise the Dirichlet data in a weak sense. We yield the discrete optimality system

$$\begin{aligned} (\nabla u_h, \nabla\varphi) - \langle \partial_{\boldsymbol{n}} u_h, \varphi\rangle_{\partial\Omega} - \langle u_h - q_h, \partial_{\boldsymbol{n}}\varphi\rangle_{\partial\Omega} + \frac{\gamma}{h} \langle u_h - q_h, \varphi\rangle_{\partial\Omega} &= (f, \varphi)\,, \\ (\nabla z_h, \nabla\varphi) - \langle \partial_{\boldsymbol{n}} z_h, \varphi\rangle_{\partial\Omega} - \langle z_h, \partial_{\boldsymbol{n}}\varphi\rangle_{\partial\Omega} + \frac{\gamma}{h} \langle z_h, \varphi\rangle_{\partial\Omega} - (u_h, \varphi) &= -\,(\bar{u}, \varphi)\,, \\ \alpha \langle q_h, \rho\rangle_{\partial\Omega} - \langle \partial_{\boldsymbol{n}} z_h, \rho\rangle_{\partial\Omega} - \langle z_h, \partial_{\boldsymbol{n}}\rho\rangle_{\partial\Omega} + \frac{\gamma}{h} \langle z_h, \rho\rangle_{\partial\Omega} &= 0. \end{aligned}$$

This is almost the same optimality system as Becker obtained in [8] when he followed a discretise-then-optimise approach, where the PDE side condition was discretised with the help of Nitsche's approach. The only different term in the above system is

$$\langle z_h, \partial_{\boldsymbol{n}}\rho\rangle_{\partial\Omega}$$

in the control equation, which is not present in Beckers approach. However, the dual equation in the above system yields a discrete dual solution z_h which vanishes on the boundary. The test function ρ is a restriction of an element of the usual finite element space V_h (cf. Chapter 3.2) to the boundary. That means that the normal derivatives of this continuous function will stay bounded. Hence, the additional term in our formulation is vanishing. In this sense we can interpret our optimality system as equivalent to the one of Becker.

Remark 5.14 (Connection between Boundary Control Approaches).
We see that there is a close connection between the different presented ways of implementing Dirichlet boundary controls. The very weak formulation, which yields us the theoretical background, is closely connected to Robin-type boundary controls. Moreover, this Robin-type conditions can be treated on the numerical level by a stabilised implementation, which represents in the limit case Nitsche's technique of implementing weak boundary data.

Table 5.3 shows a calculation for Example 5.12 where Nitsche's implementation of Dirichlet boundary data was used. We see that it yields very good results and the expected quadratic order of convergence with respect to h.

Table 5.3. Results for Example 5.12 calculated with the stabilised bilinear form (5.19) for $\mu = 0$ and $\delta = \frac{h}{10}$ (that means Nitsche's method with $\gamma = 10$).

cells	$\|\hat{u} - u_{h,\mu}\|_{L^2(\Omega)}$	**(rate)**	$\|\hat{q} - q_{h,\mu}\|_{L^2(\Omega)}$	**(rate)**	$\|\hat{z} - z_{h,\mu}\|_{L^2(\Omega)}$	**(rate)**
64	5.5517e-2		7.4167e-1		9.4447e-4	
256	1.1222e-3	**(2.31)**	1.9473e-1	**(1.93)**	1.2533e-4	**(2.91)**
1024	2.2077e-3	**(2.35)**	5.0038e-2	**(1.96)**	1.6763e-5	**(2.90)**
4096	4.3912e-4	**(2.33)**	1.2696e-2	**(1.98)**	3.4947e-6	**(2.26)**
16384	9.0726e-5	**(2.28)**	3.1989e-3	**(1.99)**	9.6545e-7	**(1.86)**
65536	1.9737e-5	**(2.20)**	8.0297e-4	**(1.99)**	2.6353e-7	**(1.87)**
262144	4.5111e-6	**(2.13)**	2.0116e-4	**(2.00)**	6.9195e-8	**(1.93)**

5.1.3. Comparison of L^2- and $H^{\frac{1}{2}}$-Control

After the introduction of $H^{\frac{1}{2}}$- and L^2-control problems in the last two subsections we want to present a brief closing discussion of the differences and the connection between these approaches in this subsection.

Therefore we compare between the choice of the L^2-norm, the $H^{\frac{1}{2}}$-seminorm or the $H^{\frac{1}{2}}$-norm defined as

$$\|u\|^2_{H^{\frac{1}{2}}(\partial\Omega)} := \|u\|^2_{L^2(\partial\Omega)} + |u|_{H^{\frac{1}{2}}(\partial\Omega)}.$$

In terms of the operator A used in the introduction of this section, this may be expressed as

$$\begin{aligned} A &= I, && (L^2\text{-norm}),\\ A &= \mathcal{P}_{\mathrm{SP}}, && (H^{\frac{1}{2}}\text{-semi norm}),\\ A &= I + \mathcal{P}_{\mathrm{SP}}, && (H^{\frac{1}{2}}\text{-norm}). \end{aligned}$$

Remark 5.15 (Numerical Realisation).
We want to emphasise that we worked directly with the optimality system in case of the L^2-control ($A = I$) in the last subsection. The reason was that we simply substituted q by expressions of the dual solution z, due to the control equation.

This is changing when we work with the Steklov-Poincaré operator $\mathcal{P}_{SP}$ for realizing the $H^{\frac{1}{2}}$-control. The control equation then reads

$$\alpha \mathcal{P}_{SP}(q) - \partial_{\boldsymbol{n}} z = 0, \quad \text{on } \partial\Omega$$

in a strong form. Hence, we would have to invert this operator in some way.

However, this inversion can be avoided by working with the Newton-CG method. We remember the methodology described in Chapter 4.2.3. The essential part was to represent the first and second derivative of the reduced cost functional. In this representation the regularisation term $r(q, q)$ is involved directly.

In our particular situation the regularisation term has the concrete form

$$r(x, y) := \frac{\alpha}{2} \int_{\partial\Omega} \mathcal{P}_{SP}(x) y \, ds$$

for different x and y in $H^{\frac{1}{2}}(\partial\Omega)$. The expression

$$\mathcal{P}_{SP}(x)$$

is then evaluated by solving an additional problem

$$\begin{aligned} -\Delta\omega_x &= 0, && \text{in } \Omega,\\ \omega_x &= x, && \text{on } \partial\Omega \end{aligned} \tag{5.20}$$

and the setting $\mathcal{P}_{SP}(x) = \partial_{\boldsymbol{n}}\omega_x$.

Hence, to work with an $H^{\frac{1}{2}}$-control in a Newton-CG method requires the solution of two additional problems (5.20) for $x = q$, and $x = \delta q$ to evaluate the expressions needed

$$r(q, \delta q), \quad \text{and} \quad r(\delta q, \tau q),$$

and therefore essentially increases the computational costs.

For the following calculations we use the described approach to solve the $H^{\frac{1}{2}}$-control problem. At the end of this remark we want to emphasise that the described modification to treat $H^{\frac{1}{2}}$-Dirichlet controls is carrying easily over to the case of time-dependent equations. Then we have to solve additional equations of the above mentioned form in each time step.

As mentioned in the work of Of [82] for the example problem with

$$\bar{u} = \left(x^2 + y^2\right)^{-\frac{1}{3}} \quad \text{and} \quad f(x) = 0$$

we see very different behaviour for the solutions with respect to the mentioned choices of the control space. The left image of the upper row of Figure 5.2 shows the solution of the

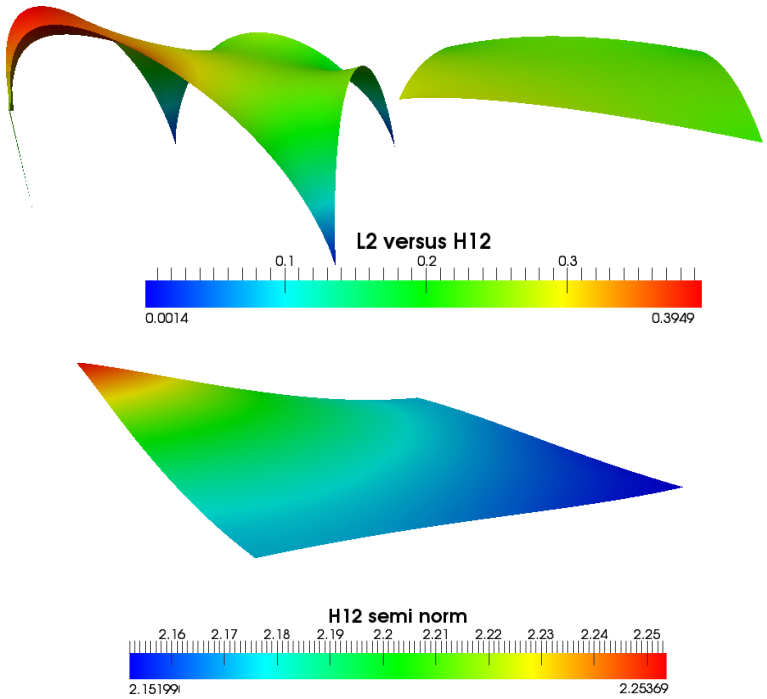

Figure 5.2. Calculation with $\alpha = 1$ Upper row: Left: L^2-control. Right: $H^{\frac{1}{2}}$-control. Lower row: $H^{\frac{1}{2}}$-seminorm control. The last image was a little bit rotated for a better visualisation.

L^2-control. Here the solution tends to zero in the corner points. This is due to the discrete control equation

$$\alpha \langle q_h, \rho \rangle_{\partial\Omega} - \langle \partial_{\boldsymbol{n}} z_h, \rho \rangle_{\partial\Omega} - \langle z_h, \partial_{\boldsymbol{n}} \rho \rangle_{\partial\Omega} + \frac{\gamma}{h} \langle z_h, \rho \rangle = 0$$

and the fact that it vanishes in the corner points of the boundary.

The right picture of the upper row of Figure 5.2 shows the result for the calculation with the full $H^{\frac{1}{2}}$-norm in the cost functional. It is directly comparable to the L^2-solution (left image) since we use the same color scale. Obviously the unnatural behaviour that the solution declines in the corner points is avoided, due to the appropriate mapping behaviour of the Steklov-Poincaré operator, although there is a slight curvature downwards in the corner points.

The image in the lower row of the figure shows the solution of the problem which uses only the seminorm part of the $H^{\frac{1}{2}}$-norm in the cost functional. It has larger values (see the

change of the color scale) due to the fact that there is a singularity in the corner point $(0, 0)$.

However, we also want to emphasise that this effect becomes more irrelevant as the control term tends to zero, due to the choice of a smaller α. This is also clear observing the control equation. The effect is documented in Figure 5.3. In the right image we see the L^2-solution, which represents the singularity in the corner $(0, 0)$ more appropriately, and shows only a slight decline in the corners.

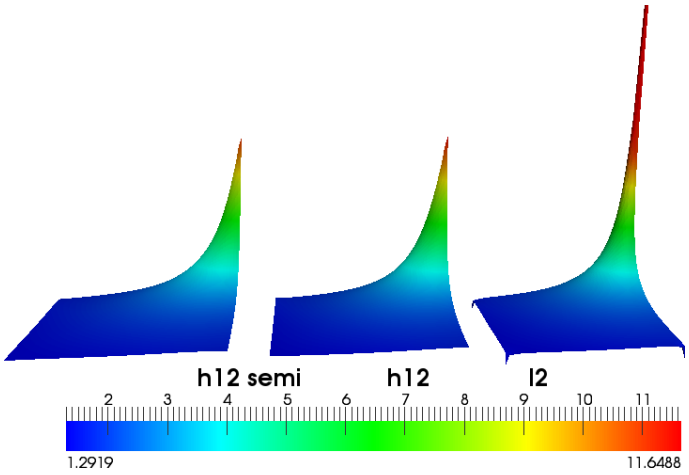

Figure 5.3. $\alpha = 0.001$. Left: $|\cdot|_{H^{\frac{1}{2}}(\partial\Omega)}$. Middle: $\|\cdot\|_{H^{\frac{1}{2}}(\partial\Omega)}$. Right: $\|\cdot\|_{L^2(\partial\Omega)}$. For better visibility we rotate all three images by about 180 degrees.

Conclusion

We want to sum up this section to fix ideas for our further considerations. We have seen that the theory of Dirichlet controls is a delicate matter due to the appropriate choice of function spaces. For the very weak formulation we find a good access to this topic, but from the numerical point of view the very weak formulation is not appropriate for implementations with bilinear finite elements.

Therefore, we searched for a theoretically justified approach to treat Dirichlet conditions, which is moreover very easy to implement. We found such an approach in the penalised Neumann method. The approach based on Robin-type control problems with a penalisation parameter μ. For varying μ we obatin a sequence, which converges for small values of μ to the desired solution of the very weak formulated Dirichlet-control problem.

Although this approach is reliable from a theoretical point of view the method gets troublesome from the numerical point of view, if we want to choose a very small penalisation parameter μ, since the appearing discrete systems are no longer appropriately solved. We can fix this issue by enhancing the boundary bilinear form by stabilizing terms described in Chapter 3.3 , where a stabilisation parameter δ is introduced.

Then we can even send μ to zero in the state equation and work with a Nitsche formulation for the implementation of the Dirichlet boundary data.

So it seems to be appropriate to deal with Dirichlet controls by weak implementation of boundary data, since this is easy to handle from the numerical point of view, and the control is entering the optimisation formulation in a "natural" way.

Finally we discussed the choice of the appropriate control space from the numerical point of view. We saw that for a huge influence of the control term steered by the regularisation parameter α we obtain very different solutions. Here the choice of an $H^{\frac{1}{2}}$-control, which can be realised by the Steklov-Poincaré operator, seems at first glance more natural, at least in the vicinity of corner points. The drawback is the increased computational effort for the numerical realisation. In the case of small values for α the effect becomes more and more negligible. Hence, in situations where the influence of the control costs (or the regularisation) becomes small or the resolution of corner points is negligible it seems more appropriate to work with an L^2-control.

5.2. Dirichlet Control for the Time-Dependent Convection-Diffusion Equation

The presented topics for the very simple elliptic equation mentioned in the section before will now be carried over to the time-dependent convection-diffusion equation.

Starting point is the minimisation of the cost functional

$$J(u,q) = \hat{j}_d(u) + \frac{\alpha}{2} \int_0^T \langle A(q-q^\star), q-q^\star \rangle dt \tag{5.21}$$

and as side condition we want to use the time-dependent convection-diffusion equation.

Written out, the strong formulation reads

$$\begin{aligned} \partial_t u - \nu \Delta u + \boldsymbol{\beta} \cdot \nabla u &= f, && \text{in } \Omega, \\ u &= q, && \text{on } \partial\Omega, \\ u(\boldsymbol{x}, 0) &= u^0, && \text{in } \Omega. \end{aligned} \tag{5.22}$$

For $\hat{j}_d(\cdot)$ we can choose an appropriate data term. Here we will work with

$$\hat{j}_d(u) := \frac{1}{2} \int_0^T \|u(t) - \bar{u}\|_2^2 \, dt,$$

where the target function $\bar{u} \in L^2(0,T;L^2(\Omega))$. Furthermore, we will set $q^\star = 0$ for the further theoretical discussion.

Moreover, we assume throughout the whole section that Ω is a convex polygon in $\mathbb{R}^2$.

The existence theory is again given by the results of Chapter 4.1.1, as long as we can define an appropriate solution operator

$$S : \mathcal{Q} \to \mathcal{X}, \qquad q \mapsto u = S(q).$$

This depends both on the structure of the transport field $\boldsymbol{\beta}(t)$ and again on the choice of the control space $\mathcal{Q}$. For the latter we have essentially the same possibilities as in the section before.

Remark 5.16 ($H^{\frac{1}{2}}$-Controls).
From the theoretical point of view it seems at first glance again more appropriate to work with $H^{\frac{1}{2}}$-controls since this is the appropriate space to achieve a meaningful formulation of the problem. Unfortunately the numerical effort becomes again expensive due to the fact that we have to solve an additional stationary Laplace problem in each time step to realise the mapping of the Steklov-Poincaré operator. However, the solution process can be performed in general as described in Remark 5.15 in the framework of the Newton-CG method by solving the necessary additional problems. Hence, in the case that the effort is justifiable (e. g. the number of system components n is essentially greater than the number of controls m ($n \gg m$)) it is easy to realise an $H^{\frac{1}{2}}$-control.

If each system component has a boundary control the numerical effort is doubled. Since this is the case in the following we skip a further discussion of $H^{\frac{1}{2}}$-controls and focus on Dirichlet and Robin controls with $q \in L^2(\partial\Omega)$. That means in particular that $A = I$.

Again we will argue with the help of the very weak formulation in the case of Dirichlet controls in $L^2(\partial\Omega)$ and discuss the existence and uniqueness of a solution. Afterwards, we use this to prove the existence of a unique solution of an optimisation problem, which involves the very weak formulation as side condition.

5.2.1. Very Weak Formulation

We follow Marusic-Paloka [74] and use very weak formulation:

Weak Formulation 5.17 (Very Weak Formulation).
A function $u \in L^2\left(0,T;L^2(\Omega)\right)$ is called a very weak solution if it fulfils

$$\int_0^T \Big\{ -\left(u(t), \partial_t\varphi(t)\right) - \nu\left(u(t), \Delta\varphi(t)\right) + \nu\left\langle q(t), \partial_{\boldsymbol{n}}\varphi(t)\right\rangle_{\partial\Omega} - \left(\boldsymbol{\beta}(t)\cdot\nabla\varphi(t), u(t)\right) \Big\} dt = \int_0^T \left(f(t),\varphi(t)\right)\, dt + \left(u^0, \varphi(0)\right)$$

for any test function

$$\varphi \in \tilde{\mathcal{X}} = \left\{ v \;:\; v \in L^2(0,T;\tilde{V}), \quad \text{and} \quad \partial_t v \in L^2(0,T;\tilde{V}') \right\},$$

with $\tilde{V} := H^2(\Omega) \cap H_0^1(\Omega)$. *Furthermore, we assume*

$$\begin{aligned} u^0 &\in L^2(\Omega), \\ f &\in L^2\left(0,T;L^2(\Omega)\right), \\ q &\in L^2\left(0,T;L^2(\partial\Omega)\right), \\ \boldsymbol{\beta} &\in L^2\left(0,T;H^1_{\mathrm{div}}(\Omega)^n\right) \cap L^\infty\left(0,T;L^\infty(\Omega)^n\right). \end{aligned}$$

Remark 5.18 (Initial Value u^0).
The space $\tilde{V}$ *is dense and continuously embedded in* $L^2(\Omega)$. *Hence it defines the Gelfand-Tripel (see Wloka [105])*

$$\tilde{V} \overset{d}{\hookrightarrow} L^2(\Omega) \overset{d}{\hookrightarrow} \tilde{V}'.$$

Like in Remark 2.3 we can argue that $\tilde{\mathcal{X}}$ *is continuously embedded in* $C\left([0,T];L^2(\Omega)\right)$. *In this sense the initial value is meaningful.*

Remark 5.19 (Solenoidal Transport Fields).
A simple calculation shows

$$-\left(\nabla\cdot\boldsymbol{\beta},u\varphi\right)+\left\langle(\boldsymbol{\beta}\cdot\boldsymbol{n})u,\varphi\right\rangle_{\partial\Omega}=\left(\boldsymbol{\beta}\cdot\nabla u,\varphi\right)+\left(\boldsymbol{\beta}\cdot\nabla\varphi,u\right).$$

Using the assumed solenoidal character of the transport field and $\varphi \in H^2(\Omega)\cap H_0^1(\Omega)$ *yields the identity*

$$\left(\boldsymbol{\beta}\cdot\nabla u,\varphi\right)=-\left(\boldsymbol{\beta}\cdot\nabla\varphi,u\right),$$

which was used in the very weak formulation. Moreover, we have for $\boldsymbol{\beta} \in H^1_{\mathrm{div}}(\Omega)$ *and* $u \in H^1(\Omega)$ *the relationship*

$$\left(\boldsymbol{\beta}\cdot\nabla u,u\right)=\frac{1}{2}\left\langle\left(\boldsymbol{\beta}\cdot\boldsymbol{n}\right)u,u\right\rangle_{\partial\Omega}. \tag{5.23}$$

The aim is now to prove the existence of a unique minimising pair $(\hat{u},\hat{q})$ of the following optimisation problem.

Optimisation Problem 5.20.
Find $(\hat{u},\hat{q}) \in L^2(\Omega)\times L^2(\partial\Omega)$ *so that the cost functional*

$$J(u,q)=\frac{1}{2}\int_0^T\|u(t)-\bar{u}\|_2^2\,dt+\frac{\alpha}{2}\int_0^T\|q(t)\|^2_{L^2(\partial\Omega)}\,dt$$

is minimised, under the condition that u *fulfils the (very) Weak Formulation 5.17.*

We will need the existence theory of the very weak solution $u \in L^2\left(0,T;L^2(\Omega)\right)$ for a given $q \in L^2\left(0,T;L^2(\partial\Omega)\right)$, which is given by the following theorem.

Theorem 5.21 (Existence of a Very Weak Solution).
The domain Ω is a convex polygon. For the diffusion coefficient we have $1 \geq \nu \geq \nu_0 > 0$, with $\nu_0 \in \mathbb{R} \setminus \{0\}$. Then there exists a unique solution $L^2\left(0,T;L^2(\Omega)\right)$ of the very weak formulation, under the assumption of appropriate regularity of the data (e. g. like Weak Formulation 5.17).

Proof. The proof works like the one for the heat equation in the article of Marusic-Paloka [74]. We will give a sketch of the basic steps.

1. We introduce an auxiliary problem by the following weak formulation:

   Weak Formulation 5.22 (Equation (5.22) with Robin-type Boundary).
   The data has the same regularity as in the Weak Formulation 5.17. We seek a function $u \in L^2\left(0,T;H^1(\Omega)\right)$ such that

   $$\int_0^T \Big\{ -\left(u(t),\partial_t\varphi(t)\right) + a(u(t),\varphi(t)) + b(q(t);u(t),\varphi(t)) \Big\}\, dt \\ -\Big(u^0,\varphi(0)\Big) = \int_0^T \left(f(t),\varphi(t)\right)\, dt$$

   for all $\varphi \in \mathcal{X} := \left\{ v : v \in L^2\left(0,T;H^1(\Omega)\right) \text{ and } \partial_t v \in L^2\left(0,T;\left(H^1(\Omega)\right)'\right)\right\}$, with the bilinear forms

   $$\begin{aligned} a(u,\varphi) &= \nu\left(\nabla u,\nabla\varphi\right) + \left(\boldsymbol{\beta}\cdot\nabla u,\varphi\right), \\ b(q;u,\varphi) &= \frac{1}{\mu}\left\langle u-q,\varphi\right\rangle_{\partial\Omega} - \frac{1}{2}\left\langle(\boldsymbol{\beta}\cdot\boldsymbol{n})u,\varphi\right\rangle_{\partial\Omega}, \quad \text{with } \mu\in(0,1]. \end{aligned}$$

2. By the standard Galerkin method (cf. Section 2.2.1) we can proof **existence** and **uniqueness** of solutions of the last equation. Therefore we need appropriate energy bounds, which are given by testing with the solution $u_\mu(t)$ itself. We obtain for almost every $t \in [0,T]$

   $$\underbrace{\frac{1}{2}\frac{d}{dt}\|u_\mu(t)\|_2^2 + \nu\|\nabla u_\mu(t)\|_2^2 + \frac{1}{\mu}\|u_\mu(t)\|_{L^2(\partial\Omega)}^2}_{=:\text{Lhs}} = \left(f(t),u_\mu(t)\right) + \frac{1}{\mu}\left\langle q(t),u_\mu(t)\right\rangle_{\partial\Omega}$$

   due to equation (5.23). By the modified Poincaré inequality already mentioned in formula (5.6) and Young's inequality we obtain

   $$\begin{aligned} \text{Lhs} &\leq C\|f(t)\|_2\left(\|\nabla u_\mu(t)\|_2 + \|u_\mu(t)\|_{L^2(\partial\Omega)}\right) + \frac{1}{\mu}\|q(t)\|_{L^2(\partial\Omega)}\|u_\mu(t)\|_{L^2(\partial\Omega)} \\ &\leq \frac{2C^2}{\nu}\|f(t)\|_2^2 + \frac{\nu}{8}\left(\|\nabla u_\mu(t)\|_2^2 + \|u_\mu(t)\|_{L^2(\partial\Omega)}\right)^2 + \frac{1}{\mu}\|q(t)\|_{L^2(\partial\Omega)}^2 \\ &\quad + \frac{1}{4\mu}\|u_\mu(t)\|_{L^2(\partial\Omega)}^2. \end{aligned}$$

Since we assumed $0 < \nu_0 \leq \nu \leq 1$ and $\mu \in (0, 1]$ we have also $\nu \leq \frac{1}{\mu}$. Moreover, by the inequality $(c+d)^2 \leq 2c^2 + 2d^2$ we can then derive by further estimation of the right hand side

$$\text{Lhs} \leq \frac{2C^2\|f(t)\|_2^2}{\nu_0} + \frac{1}{\mu}\|q(t)\|_{L^2(\partial\Omega)}^2 + \frac{\nu}{4}\|\nabla u_\mu(t)\|_2^2 + \frac{1}{2\mu}\|u_\mu(t)\|_{L^2(\partial\Omega)}$$

and finally after absorbing the terms involving u into the left hand side

$$\frac{1}{2}\frac{d}{dt}\|u_\mu(t)\|_2^2 + \frac{3\nu}{4}\|\nabla u_\mu(t)\|_2^2 + \frac{1}{2\mu}\|u_\mu(t)\|_{L^2(\partial\Omega)}^2 \leq \frac{2C^2}{\nu_0}\|f(t)\|_2^2 + \frac{1}{\mu}\|q(t)\|_{L^2(\partial\Omega)}^2. \tag{5.24}$$

Estimation of all necessary energy bounds follows by the same techniques we already presented in the first chapter of this work. Hence, we obtain the existence of a unique weak solution of the auxiliary problem in the Weak Formulation 5.22.

$$u_\mu \in L^2\left(0, T; H^1(\Omega)\right) \cap L^\infty\left(0, T; L^2(\Omega)\right).$$

Moreover, we directly obtain the estimates

$$\int_0^T \|u_\mu(t)\|_{L^2(\partial\Omega)}^2 \, dt \leq C, \qquad \text{and} \qquad \int_0^T \|\nabla u_\mu(t)\|_{L^2(\Omega)}^2 \, dt \leq C\frac{1}{\sqrt{\mu}}. \tag{5.25}$$

The uniqueness also follows from the energy bound (5.24) for the difference of two solutions u and v with the same data ν, f and q, since the convection-diffusion equation is linear.

3. We need a further estimation in $L^2(0, T; L^2(\Omega))$ for the sequence u_μ. We can generate such an estimate by using the following duality argument

$$\begin{aligned} -\partial_t\lambda(t) - \nu\Delta\lambda(t) - \boldsymbol{\beta}\cdot\nabla\lambda(t) &= u_\mu(t), \quad \text{in } (0,T]\times\Omega, \\ \lambda(\boldsymbol{x}, t) &= 0, \qquad \text{on } (0,T]\times\partial\Omega, \\ \lambda(\boldsymbol{x}, T) &= 0, \qquad \text{in } \Omega. \end{aligned}$$

Testing the last equation with u_μ and integrating over space and time yields after integration by parts and using the above boundary and initial conditions of λ

$$\begin{aligned} \int_0^T \|u_\mu(t)\|_2^2 \, dt = &\int_0^T \Big\{ -\left(\partial_t\lambda(t), u_\mu(t)\right) + \nu\left(\nabla\lambda(t), \nabla u_\mu(t)\right) + \left(\boldsymbol{\beta}\cdot\nabla u_\mu(t), \lambda(t)\right) \Big\} dt \\ &- \int_0^T \nu\left\langle \partial_{\boldsymbol{n}}\lambda(t), u_\mu(t)\right\rangle_{\partial\Omega} \, dt. \end{aligned}$$

Now we can use the Weak Formulation 5.22 and again that $\lambda(t)$ vanishes on the boundary

$$\int_0^T \|u_\mu(t)\|_2^2 \, dt = \int_0^T \Big\{ \left(f(t), \lambda(t)\right) - \nu\left\langle \partial_{\boldsymbol{n}}\lambda(t), u_\mu(t)\right\rangle_{\partial\Omega} \Big\} \, dt + \left(u^0, \lambda(0)\right).$$

With the first estimate in equation (5.25) and the estimate (2.3) from Theorem 2.6 we can now easily deduce the uniform bound

$$\int_0^T \|u_\mu(t)\|_2^2 \, dt \leq C. \tag{5.26}$$

Here we need the regularity assumptions on the domain (convex polygon) and that $\boldsymbol{\beta} \in L^\infty\left(0,T;L^\infty(\Omega)^2\right)$.

4. However, since the last mentioned bound is uniform with respect to μ, we have the weak convergence of a subsequence which we again denote by u_μ

$$u_\mu \rightharpoonup u \quad \text{weakly in } L^2(0,T;L^2(\Omega)). \tag{5.27}$$

Together with

$$u_\mu \rightharpoonup u \quad \text{weakly in } L^2(0,T;L^2(\partial\Omega)), \tag{5.28}$$

which we derived by the first estimate in (5.25), we can now show that u_μ converges to a solution of the very weak formulation (see Weak Formulation 5.17).

Therefore, we use the test space $L^2\left(0,T;H^2(\Omega)\cap H_0^1(\Omega)\right) \subset L^2\left(0,T;H^1(\Omega)\right)$ in the Weak Formulation 5.22. After spatial integration by parts we obtain

$$-\int_0^T \Big\{ \left(u_\mu(t),\partial_t\varphi(t)\right) + \nu\left(u_\mu(t),\Delta\varphi(t)\right) + \nu\left\langle u_\mu(t),\partial_{\boldsymbol{n}}\varphi(t)\right\rangle_{\partial\Omega} - \left(\boldsymbol{\beta}(t)\cdot\nabla\varphi(t),u_\mu(t)\right)\Big\}\, dt = \int_0^T \left(f(t),\varphi(t)\right)\, dt + \left(u^0,\varphi(0)\right).$$

All convergence processes in this equation can be treated by the properties (5.27) and (5.28), except the convergence to q on the boundary. However, this convergences can be proven in the following way.

By the Weak Formulation 5.22 we get after a few transformations with the help of the identities of Remark 5.19

$$\begin{aligned}\int_0^T \left\langle u_\mu(t)-q(t),\varphi(t)\right\rangle\, dt = \mu\int_0^T \Big\{ &\left(f(t),\varphi(t)\right) - \nu\left(\nabla u_\mu(t),\nabla\varphi(t)\right)\\ &-\frac{1}{2}\left(\boldsymbol{\beta}(t)\cdot\nabla u_\mu(t),\varphi(t)\right) + \frac{1}{2}\left(\boldsymbol{\beta}(t)\cdot\nabla\varphi(t),u_\mu(t)\right)\\ &+\left(u_\mu(t),\partial_t\varphi(t)\right)\Big\}\, dt - \mu\left(u^0,\varphi(0)\right),\end{aligned}$$

for all $\varphi \in L^2\left(0,T;H^1(\Omega)\right)$. Now we use again that $\boldsymbol{\beta} \in L^\infty\left(0,T;L^\infty(\Omega)\right)$, employ the general Poincaré inequality (5.6) and afterwards the inequalities in formula (5.25)

and $\mu \leq \sqrt{\mu}$ since $\mu \in (0,1]$ to obtain

$$\left| \int_0^T \langle u_\mu(t) - q(t), \varphi(t) \rangle \, dt \right| \leq \sqrt{\mu} C \to 0, \quad \text{for} \quad \mu \to 0, \quad \forall \varphi \in L^2\left(0,T; H^1(\Omega)\right).$$

Hence,

$$u_\mu\big|_{\partial\Omega} \rightharpoonup q \quad \text{weakly in } L^2(0,T;L^2(\partial\Omega)). \tag{5.29}$$

5. The **uniqueness** can also be obtained by generating an L^2 a-priori bound due to a duality argument very similar to the above presented technique. The course is the following:

   Consider the problem

$$\begin{aligned} -\partial_t \lambda(t) - \nu \Delta \lambda(t) - \boldsymbol{\beta} \cdot \nabla \lambda(t) &= u(t), \quad && \text{in } (0,T] \times \Omega, \\ \lambda(\boldsymbol{x}, t) &= 0, && \text{on } (0,T] \times \partial\Omega, \\ \lambda(\boldsymbol{x}, T) &= 0, && \boldsymbol{x} \in \Omega. \end{aligned}$$

   Since $u \in L^2\left(0,T;L^2(\Omega)\right)$ we have due to Theorem 2.6

$$\lambda \in L^2(0,T;H^2(\Omega)) \cap L^\infty(0,T;H_0^1(\Omega)), \quad \text{and} \quad \partial_t \lambda \in L^2(0,T;L^2(\Omega)).$$

   It is now easy to deduce the following a priori bound

$$\int_0^T \|u(t)\|_2^2 \, dt \leq \int_0^T C \left(\|q\|^2_{L^2(\partial\Omega)} + \|f\|_2^2 \right) \, dt \tag{5.30}$$

   by the techniques presented in this proof.

   If we now assume that we have two solutions u_1 and u_2 in $L^2(0,T;L^2(\Omega))$ of the very weak formulation for the same set of data the difference of these solutions $\omega = u_1 - u_2$ must solve the homogeneous problem. Hence by the estimate (5.30) we obtain the uniqueness, since

$$\int_0^T \|\omega(t)\|_2^2 \, dt = 0.$$

□

Remark 5.23 (Connection to the Penalised Neumann Method).
The auxiliary problem introduced by the Weak Formulation 5.22 was mentioned before as penalised Neumann method for the implementation of weakly imposed Dirichlet data (cf. Chapter 3.3). There we suggested a stabilised version of the boundary bilinear form, namely

$$\begin{aligned} b(q_D; u, \varphi) := &- \frac{\nu\delta}{\mu+\delta} \left(\langle \partial_{\boldsymbol{n}} u, \varphi \rangle_{\partial\Omega} + \langle u - q_D, \partial_{\boldsymbol{n}} \varphi \rangle_{\partial\Omega} \right) + \frac{1}{\mu+\delta} \langle u - q_D, \varphi \rangle_{\partial\Omega} \\ &- \frac{\nu\mu\delta}{\mu+\delta} \langle \partial_{\boldsymbol{n}} u, \partial_{\boldsymbol{n}} \varphi \rangle_{\partial\Omega} - \frac{\mu}{2(\mu+\delta)} \langle (\boldsymbol{\beta} \cdot \boldsymbol{n}) u, \varphi \rangle_{\partial\Omega} \\ &+ \frac{\delta\mu}{2(\mu+\delta)} \langle (\boldsymbol{\beta} \cdot \boldsymbol{n}) u, \partial_{\boldsymbol{n}} \varphi \rangle_{\partial\Omega} \end{aligned}$$

for the numerical approximation of Dirichlet data.

For the modified form we could even send μ to zero, as long as we choose an appropriate $\delta > 0$. The numerical method behind this is Nitsche's technique for the implementation of weakly imposed Dirichlet data.

In view of the above proof Nitsche's method seems somehow connected to the approximation of very weak solutions.

Now we are able to justify the following theorem, which provides us with the existence of a unique minimum of Optimisation Problem 5.20.

Theorem 5.24 (Existence of a Minimum).
There exists a unique minimum

$$(\hat{u}, \hat{q}) \in L^2\left(0, T; L^2(\Omega)\right) \times L^2\left(0, T; L^2(\partial\Omega)\right),$$

which minimises

$$J(u, q) = \frac{1}{2} \int_0^T \|u(t) - \bar{u}\|_2^2 \, dt + \frac{\alpha}{2} \int_0^T \|q(t)\|_{L^2(\partial\Omega)}^2 \, dt$$

subject to the Weak Formulation 5.17.

Proof. Theorem 5.21 yields the existence of a unique solution operator

$$S : L^2(\partial\Omega) \to L^2(\Omega), \qquad q \mapsto u = S(q).$$

This operator is linear and we can introduce the reduced cost functional

$$j(q) = \frac{1}{2} \int_0^T \|S(q(t)) - \bar{u}\|_2^2 \, dt + \frac{\alpha}{2} \int_0^T \|q(t)\|_{L^2(\partial\Omega)}^2 \, dt.$$

Since the cost functional has the same structure as in Example 4.8 we can apply Theorem 4.5 and Remark 4.7 and obtain directly the statement of this theorem. □

5.2.2. Penalised Neumann Approach

In the last section we saw that the penalised Neumann formulation for the convection-diffusion equation converges to a solution of the very Weak Formulation 5.17 with μ tending to zero. As in the case of the steady Poisson problem we want to formulate now an optimisation problem with the Weak Formulation 5.22 as side condition. After showing existence of a unique solution pair (u_μ, q_μ) of this problem we will investigate the question whether the sequence of minimising pairs in μ is converging to a solution of the Optimisation Problem 5.20 with the very weak formulation of the convection-diffusion equation as side condition.

We consider the following optimisation problem.

Optimisation Problem 5.25 (Robin-type Boundary).
Find $(u_\mu, q_\mu) \in L^2\left(0,T;H^1(\Omega)\right) \times L^2\left(0,T;L^2(\partial\Omega)\right)$ *such that the cost functional*

$$J(u_\mu, q_\mu) = \frac{1}{2}\int_0^T \|u_\mu(t) - \bar{u}\|_2^2 \, dt + \frac{\alpha}{2}\int_0^T \|q_\mu(t)\|_{L^2(\partial\Omega)}^2 \, dt$$

is minimised, under the condition that (u_μ, q_μ) *fulfils the Weak Formulation 5.22.*

For this problem we formulate the following theorem.

Theorem 5.26 (Minimum of the Robin-type Aproach).
For every μ*, with* $1 \geq \mu > 0$ *and* ν *with* $1 \geq \nu > 0$*, there exists a unique minimum*

$$(u_\mu, q_\mu) \in L^2\left(0,T;H^1(\Omega)\right) \times L^2\left(0,T;L^2(\partial\Omega)\right),$$

which minimises

$$J(u_\mu, q_\mu) = \frac{1}{2}\int_0^T \|u_\mu(t) - \bar{u}\|_2^2 \, dt + \frac{\alpha}{2}\int_0^T \|q_\mu(t)\|_{L^2(\partial\Omega)}^2 \, dt$$

subject to the Weak Formulation 5.22.

Proof. Since we have unique solvability (see the second point in the proof of Theorem 5.21), we can introduce a solution operator and argue as in Example 4.8 and Theorem 4.5. □

Remark 5.27 (Regularity of the Vector Field $\boldsymbol{\beta}$).
We want to emphasise that the high regularity requirements

$$\boldsymbol{\beta} \in L^2\left(0,T;H^1_{\mathrm{div}}(\Omega)^n\right) \cap L^\infty\left(0,T;L^\infty(\Omega)^n\right)$$

can be weakened in this case, since we need $L^\infty\left(0,T;L^\infty(\Omega)^n\right)$ *only for the duality arguments in the existence theory of the very weakly formulated Dirichlet problem. For the existence and uniqueness theory with the above described Robin boundary condition it is completely sufficient to require only*

$$\boldsymbol{\beta} \in L^2\left(0,T;H^1_{\mathrm{div}}(\Omega)^n\right).$$

Remark 5.28 (Advantage).
The big advantage of the above mentioned optimisation problem is, beside its simplicity from the theoretical point of view, that it is very easy to handle from the numerical point of view. We can directly use the Newton-CG algorithm formulated in Chapter 4.2.3. The arising PDEs have a similar structure and can be solved very efficiently with the implicit Euler or the Crank-Nicolson scheme in time and simple bilinear finite elements in space.

5.2.3. Convergence

We will now prove that the sequence $(u_\mu, q_\mu)_\mu$ of solutions of the Optimisation Problem 5.25 converges to a solution of the Optimisation Problem 5.20. That means we can use the penalised Neumann approach for an efficient calculation of an approximation of the Dirichlet control problem in Optimisation Problem 5.20.

We need therefore the optimality systems of the Optimisation problems 5.20 and 5.25.

Optimality System 5.29 (Optimality System of Optimisation Problem 5.20). *A solution $(\hat{u}, \hat{z}, \hat{q})$ of the following three equations characterises the minimum $(\hat{u}, \hat{q})$ of the Optimisation Problem 5.20.*

1. **State equation**: *Find $u \in L^2\left(0, T; L^2(\Omega)\right)$, which fulfils*

$$\int_0^T \Big\{ -(u, \partial_t \varphi) - \nu\,(u, \Delta\varphi) + \nu\,\langle q, \partial_{\boldsymbol{n}}\varphi\rangle_{\partial\Omega} - (\boldsymbol{\beta}\cdot\nabla\varphi, u) \Big\}\, dt \\ - \Big(u^0, \varphi(0)\Big) = \int_0^T (f, \varphi)\ dt$$

   for all $\varphi \in \tilde{\mathcal{X}}$.

2. **Dual Equation**: *Find $z \in \tilde{\mathcal{X}}$ such that*

$$\int_0^T \Big\{ (\hat{\varphi}, \partial_t z) + \nu\,(\hat{\varphi}, \Delta z) + (\boldsymbol{\beta}\cdot\nabla z, \hat{\varphi}) \Big\}\, dt = -\int_0^T (u - \bar{u}, \hat{\varphi})\ dt$$

   is fulfilled for all $\hat{\varphi} \in L^2(0, T; L^2(\Omega))$.

3. **Control Equation**:

$$\alpha \int_0^T \langle q, \rho\rangle_{\partial\Omega}\ dt = \nu \int_0^T \langle \partial_{\boldsymbol{n}} z, \rho\rangle_{\partial\Omega}\ dt, \qquad \forall \rho \in L^2(0, T; L^2(\partial\Omega)).$$

Optimality System 5.30 (Optimality System of Optimisation Problem 5.25). *A solution $(\hat{u}_\mu, \hat{z}_\mu, \hat{q}_\mu)$ of the following three equations characterises the minimum $(\hat{u}_\mu, \hat{q}_\mu)$ of the Optimisation Problem 5.25.*

1. **State equation**: *Find $u \in L^2\left(0, T; H^1(\Omega)\right)$, which fulfils*

$$\int_0^T \Big\{ -(u, \partial_t \varphi) + \nu\,(\nabla u, \nabla\varphi) + (\boldsymbol{\beta}\cdot\nabla u, \varphi) + \frac{1}{\mu}\langle u - q, \varphi\rangle_{\partial\Omega} \\ - \frac{1}{2}\langle (\boldsymbol{\beta}\cdot\boldsymbol{n})u, \varphi\rangle_{\partial\Omega} \Big\}\, dt - \Big(u^0, \varphi(0)\Big) = \int_0^T (f, \varphi)\ dt$$

   for all $\varphi \in \mathcal{X}$.

2. **Dual Equation**: *Find $z \in \mathcal{X}$ so that*

$$\int_0^T \Big\{ -(\partial_t z, \varphi) + \nu\,(\nabla z, \nabla\varphi) - (\boldsymbol{\beta}\cdot\nabla z, \varphi) + \frac{1}{\mu}\,\langle z, \varphi\rangle_{\partial\Omega} + \frac{1}{2}\,\langle(\boldsymbol{\beta}\cdot\boldsymbol{n})z, \varphi\rangle_{\partial\Omega} \Big\}\, dt = \int_0^T \big((u(t) - \bar{u}(t)), \varphi(T)\big)\; dt$$

is fulfilled for all $\varphi \in L^2(0,T;H^1(\Omega))$.

3. **Control Equation**:

$$\alpha \int_0^T \langle q, \rho\rangle_{\partial\Omega}\; dt = -\frac{1}{\mu}\int_0^T \langle z, \rho\rangle_{\partial\Omega}\; dt, \qquad \forall \rho \in L^2(0,T;L^2(\partial\Omega)).$$

We will show that the sequence of triplets $(u_\mu, z_\mu, q_\mu)_\mu$ converges to a solution (u,z,q) of the Optimality System 5.29 and therefore to a solution of the Optimisation Problem 5.20 for $\mu \to 0$. For this we need several convergence properties, which we prove in the next theorem.

Theorem 5.31 (Convergence of the Sequence (u_μ, z_μ, q_μ)).
With

$$(u_\mu, z_\mu, q_\mu) \in L^2(0,T;H^1(\Omega)) \times L^2(0,T;H^1(\Omega)) \times L^2(0,T;L^2(\partial\Omega))$$

we denote a solution of the Optimisation Problem 5.25 subject to the penalised Neumann formulation of the convection-diffusion equation by Theorem 5.26. The resulting sequence in μ has a convergent subsequence with

$$q_\mu \rightharpoonup \hat{q} \quad \textit{weakly in } L^2\left(0,T;L^2(\partial\Omega)\right), \tag{5.31}$$

$$u_\mu \rightharpoonup \hat{u} \quad \textit{weakly in } L^2\left(0,T;L^2(\Omega)\right), \tag{5.32}$$

$$u_\mu \rightharpoonup \hat{u} \quad \textit{weakly in } L^2\left(0,T;L^2(\partial\Omega)\right), \tag{5.33}$$

$$z_\mu \rightharpoonup \hat{z} \quad \textit{weakly in } L^2\left(0,T;H_0^1(\Omega)\right), \tag{5.34}$$

and

$$z_\mu \rightharpoonup \hat{z} \quad \textit{weakly-}\star \textit{ in } L^\infty\left(0,T;L^2(\Omega)\right). \tag{5.35}$$

Proof. We present the proof in four steps. In principle it is an extension of the proof of Theorem 5.9 to time-dependent problems.

1. To prove this we consider the state equation in the Optimality System 5.30 with $q = 0$. Thus we have the solution pair $(\tilde{u}, 0)$ which yields a functional value $J(\tilde{u}, 0)$ which is either equal to or greater than the one belonging to the minimising pair (u_μ, q_μ) of the optimisation problem mentioned in Theorem 5.26. That means

$$J(u_\mu, q_\mu) \leq J(\tilde{u}, 0)$$

or after the application of a view elementary estimates

$$\frac{1}{2}\int_0^T \|u_\mu(t)-\bar{u}(t)\|_2^2\,dt+\frac{\alpha}{2}\int_0^T \|q_\mu(t)\|_{L^2(\partial\Omega)}^2\,dt\le\int_0^T\|\tilde{u}(t)\|_2^2\,dt+\int_0^T\|\bar{u}\|_2^2\,dt. \quad (5.36)$$

Hence, we need an estimate for $\|\tilde{u}\|_{L^2\left(0,T;L^2(\Omega)\right)}$. We can easily deduce this inequality by testing with $\varphi(t)=\tilde{u}(t)$ in the Weak Formulation 5.22 of the state equation with $q(t)=0$. We obtain

$$\int_0^T\Big\{\frac{1}{2}\frac{d}{dt}\|\tilde{u}(t)\|_2^2+\nu\|\nabla\tilde{u}(t)\|_2^2+\frac{1}{\mu}\|\tilde{u}(t)\|_{L^2(\partial\Omega)}^2\Big\}\,dt=\int_0^T(f(t),\tilde{u}(t))\;dt \quad (5.37)$$

and estimate with the general Poincaré inequality (5.6)

$$\begin{aligned}\int_0^T(f(t),\tilde{u}(t))\;dt&\le\int_0^T\Big\{C\|f(t)\|_2\|\nabla\tilde{u}(t)\|_2+C\|f(t)\|_2\|\tilde{u}(t)\|_{L^2(\partial\Omega)}\Big\}\,dt\\&\le\int_0^T\Big\{\frac{C}{2\nu}\|f(t)\|_2^2+\frac{\nu}{2}\|\nabla\tilde{u}(t)\|_2^2+\frac{C}{2}\|f(t)\|_2^2+\frac{1}{2}\|\tilde{u}(t)\|_{L^2(\partial\Omega)}\Big\}\,dt.\end{aligned}$$

Since $\nu,\mu\in(0,1]$ we obtain

$$\int_0^T(f(t),\tilde{u}(t))\;dt\le\int_0^T\Big\{\frac{C}{\nu}\|f(t)\|_2^2+\frac{\nu}{2}\|\nabla\tilde{u}(t)\|_2^2+\frac{1}{2\mu}\|\tilde{u}(t)\|_{L^2(\partial\Omega)}\Big\}\,dt.$$

Thus we obtain for equation (5.37)

$$\int_0^T\frac{d}{dt}\|\tilde{u}(t)\|_2^2+\nu\|\nabla\tilde{u}(t)\|_2^2+\frac{1}{\mu}\|\tilde{u}(t)\|_{L^2(\partial\Omega)}^2\,dt\le\int_0^T\frac{C}{\nu}\|f(t)\|_2^2\,dt.$$

After integration of the first term and applying Poincaré s inequality (5.6) we then receive

$$\nu\int_0^T\|\tilde{u}(t)\|_2^2\,dt\le\int_0^T\Big\{\nu\|\nabla\tilde{u}(t)\|_2^2+\frac{1}{\mu}\|\tilde{u}(t)\|_{L^2(\partial\Omega)}^2\Big\}\,dt\le c\left(\|u^0\|_2^2+\int_0^T\frac{C}{\nu}\|f(t)\|_2^2\,dt\right). \quad (5.38)$$

Using the last inequality in formula (5.36) we find

$$\frac{\alpha}{2}\int_0^T\|q_\mu(t)\|_{L^2(\partial\Omega)}^2\le\frac{c_1}{\nu}\|u^0\|_2^2+\frac{c_2}{\nu^2}\int_0^T\|f(t)\|_2^2\,dt+\int_0^T\|\bar{u}(t)\|_2^2\,dt\le C_{u^0,f,\nu,\bar{u}}. \quad (5.39)$$

Since this bound is uniform with respect to μ we obtain the following weak convergence of a subsequence

$$q_\mu\rightharpoonup\hat{q}\;\text{ weakly in }\;L^2(0,T;L^2(\partial\Omega)).$$

2. Moreover, we have

$$\int_0^T \|u_\mu(t)\|_2^2 \, dt = \int_0^T \|u_\mu(t) - \bar{u}(t) + \bar{u}(t)\|_2^2 \, dt \leq 2 \left(\int_0^T \|u_\mu(t) - \bar{u}(t)\|_2^2 \, + \|\bar{u}(t)\|_2^2 \, dt \right).$$

Hence, we find with the inequalities in (5.36) and (5.38) the bound

$$\int_0^T \|u_\mu(t)\|_2^2 \, dt \leq C_{u^0,f,\nu,\bar{u}},$$

which is also uniform with respect to μ. That means we found the property (5.32).

3. Starting with the Weak Formulation 5.22 of the state equation we can obtain by a similar argumentation the following a priori bound

$$\begin{aligned} \int_0^T \Big\{ \frac{d}{dt}\|u_\mu(t)\|_2^2 + \frac{3\nu}{2}\|\nabla u_\mu(t)\|_2^2 + \frac{1}{\mu}\|u_\mu(t)\|_{L^2(\partial\Omega)}^2 \, dt \leq \quad & \frac{C_1}{\nu} \int_0^T \|f(t)\|_2^2 \Big\} \, dt \\ & + \frac{C_2}{\mu} \int_0^T \|q_\mu(t)\|_{L^2(\partial\Omega)}^2 \, dt. \end{aligned} \tag{5.40}$$

Here we can also bound the control term on the right hand side, due to formula (5.39) and obtain the bounds

$$\int_0^T \|u_\mu\|_{L^2(\partial\Omega)}^2 \, dt \leq C_{\alpha,\nu,f,\bar{u},u^0}, \quad \text{and} \quad \int_0^T \|\nabla u_\mu\|_2^2 \, dt \leq \frac{C_{\alpha,\nu,f,\bar{u},u^0}}{\mu}. \tag{5.41}$$

That means u_μ is uniformly bounded in the L^2-norm on the boundary and we have therefore

$$u_\mu \rightharpoonup \hat{u} \quad \text{weakly in} \quad L^2(0,T;L^2(\partial\Omega)).$$

4. Finally we discuss the uniform boundedness of the dual variable z_μ. Therefore, we test the dual equation in the Optimality System 5.30 with z_μ itself and use the identity (5.23). We get then

$$\begin{aligned} -\int_0^T \frac{1}{2}\frac{d}{dt}\|z_\mu(t)\|_2^2 \, dt + \nu \int_0^T \|\nabla z_\mu(t)\|_2^2 \, dt & \\ + \frac{1}{\mu}\int_0^T \|z_\mu(t)\|_{L^2(\partial\Omega)}^2 \, dt = \int_0^T \big(u_\mu(t) - \bar{u}(t), z_\mu(t)\big) \, dt & \\ \leq \int_0^T \|u_\mu(t) - \bar{u}(t)\|_2 \|z_\mu(t)\|_2 \, dt =: \text{Rhs}. & \end{aligned} \tag{5.42}$$

We use Youngs inequality for the right hand side and afterwards the Poincaré inequality (5.6)

$$\begin{aligned}\text{Rhs} &\leq \int_0^T \left\{ \frac{\kappa}{2} \|u_\mu(t) - \bar{u}(t)\|_2^2 + \frac{1}{2\kappa} \|z_\mu(t)\|_2^2 \right\} dt \\ &\leq \int_0^T \left\{ \frac{\kappa}{2} \|u_\mu(t) - \bar{u}(t)\|_2^2 + \frac{C}{2\kappa} \left(\|\nabla z_\mu(t)\|_2^2 + \|z_\mu(t)\|_{L^2(\partial\Omega)}^2 \right) \right\} dt.\end{aligned}$$

By choosing $\kappa = \frac{C}{\nu}$ we deduce

$$\text{Rhs} \leq \frac{C}{2\nu} \int_0^T \|u_\mu(t) - \bar{u}(t)\|_2^2 \, dt + \frac{\nu}{2} \int_0^T \|\nabla z_\mu(t)\|_2^2 \, dt + \frac{1}{2\mu} \int_0^T \|z_\mu(t)\|_{L^2(\partial\Omega)}^2 \, dt,$$

since $\nu \leq \frac{1}{\mu}$ for $\nu, \mu \in (0, 1]$. The first term on the right hand side is uniformly bounded with respect to μ due to the formulas (5.37) and (5.38). Using the last estimate for the right hand side in (5.42) we end up with

$$-\int_0^T \frac{d}{dt} \|z_\mu(t)\|_2^2 \, dt + \nu \int_0^T \|\nabla z_\mu(t)\|_2^2 \, dt + \frac{1}{\mu} \int_0^T \|z_\mu(t)\|_{L^2(\partial\Omega)}^2 \, dt \leq C_{\alpha,\nu,f,\bar{u},u^0}.$$

The first term of the left hand side yields

$$-\int_0^T \frac{d}{dt} \|z_\mu(t)\|_2^2 \, dt = -\|z_\mu(T)\|_2^2 + \|z(0)\|_2^2 = \|z(0)\|_2^2,$$

since the initial value for the backward integration is zero. Thus we have the following bounds:

$$\begin{aligned}&\int_0^T \|\nabla z_\mu(t)\|_2^2 \, dt \leq C_{f,\bar{u},u^0,\alpha,\nu}, \\ &\int_0^T \|z_\mu(t)\|_{L^2(\partial\Omega)}^2 \, dt \leq \mu C_{f,\bar{u},u^0,\alpha,\nu}, \\ &\|z_\mu(t)\|_2 \leq C_{f,\bar{u},u^0,\alpha,\nu}, \quad \text{(by a similar argumentation).}\end{aligned}$$

Since all these bounds are uniform we obtain the following convergence properties of subsequences

$$\left.\begin{aligned} z_\mu &\rightharpoonup \hat{z} \text{ weakly in} && L^2\left(0,T;H^1(\Omega)\right) \\ z_\mu &\to 0 \quad \text{in} && L^2\left(0,T;L^2(\partial\Omega)\right) \end{aligned}\right\} \Rightarrow z_\mu \rightharpoonup \hat{z} \;\text{ weakly in }\; L^2\left(0,T;H_0^1(\Omega)\right)$$

and

$$z_\mu \rightharpoonup \hat{z} \quad \text{weakly-}\star \text{ in } \left(L^1\left(0,T;L^2(\Omega)\right)\right)'. \qquad \square$$

Now we want to show that the sequence $(u_\mu, z_\mu, q_\mu)_\mu$ converges to a solution of the Optimality System 5.29 and therefore characterises a solution of the Optimisation Problem 5.20 with the very weak formulation of the convection-diffusion problem as side condition.

Theorem 5.32 (Passage to the Limit). *The unique solution triplet (u_μ, z_μ, q_μ) of the Optimality System 5.30 converges by the convergence properties of Theorem 5.31 to the solution of the Optimality System 5.29 for $\mu \to 0$.*

Proof. We discuss one after another the convergence in the state, dual and control equation.

1. The convergence of the state equation works like in step 4, in the proof of Theorem 5.24. Only the convergence to the control term needs a slight modification, since here q_μ depends on μ and is therefore also involved in the convergence process

$$\int_0^T \langle u_\mu - q, \varphi \rangle_{\partial\Omega} \; dt \leq \int_0^T \langle u_\mu - q_\mu, \varphi \rangle_{\partial\Omega} \; dt + \int_0^T \langle q_\mu - q, \varphi \rangle_{\partial\Omega} \; dt.$$

   By the convergence property in (5.31) the second term on the right hand side vanishes. By analogous estimates as in step 4 of the above mentioned proof we derive

$$\left| \int_0^T \langle u_\mu - q_\mu, \varphi \rangle_{\partial\Omega} \; dt \right| \leq \sqrt{\mu} C \to 0 \quad \text{for} \quad \mu \to 0,$$

   and finally

$$\int_0^T \langle u_\mu, \varphi \rangle_{\partial\Omega} \; dt \to \int_0^T \langle q, \varphi \rangle_{\partial\Omega} \; dt, \qquad \forall \varphi \in H^1(\Omega).$$

2. For the convergence in the dual equation we start with the weak formulation

$$\int_0^T \Big\{ -(\partial_t z_\mu, \varphi) + \nu (\nabla z_\mu, \nabla \varphi) - (\boldsymbol{\beta} \cdot \nabla z_\mu, \varphi) + \frac{1}{\mu} \langle z_\mu, \varphi \rangle_{\partial\Omega} + \frac{1}{2} \langle (\boldsymbol{\beta} \cdot \boldsymbol{n}) z_\mu, \varphi \rangle_{\partial\Omega} \Big\} \; dt = \int_0^T (u_\mu - \bar{u}, \varphi) \; dt$$

   for all $\varphi \in L^2\left(0, T; H^1(\Omega)\right)$. Now we choose the test functions from the subspace

$$\mathcal{X}^\star \subset L^2\left(0, T; H^1(\Omega)\right)$$

   with

$$\mathcal{X}^\star := \Big\{ v : v \in L^2\left(0, T; H_0^1(\Omega)\right) \text{ and } \partial_t v \in L^2\left(0, T; L^2(\Omega)\right) \Big\}.$$

   That means we find

$$\int_0^T \Big\{ -(\partial_t z_\mu, \varphi) + \nu (\nabla z_\mu, \nabla \varphi) - (\boldsymbol{\beta} \cdot \nabla z_\mu, \varphi) \Big\} \; dt = \int_0^T (u_\mu - \bar{u}, \varphi) \; dt.$$

Since the equation is linear passing to the limit is standard. We use the properties in (5.34) and (5.35) to pass to the limit on the left hand side (remember $\boldsymbol{\beta} \in L^\infty(0,T;L^\infty(\Omega))$). The convergence on the right hand side can be treated by formula (5.32). We find

$$\int_0^T \Big\{ -(\partial_t \hat{z}, \varphi) + \nu\,(\nabla \hat{z}, \nabla \varphi) - (\boldsymbol{\beta} \cdot \nabla \hat{z}, \varphi) \Big\}\, dt = \int_0^T (\hat{u} - \bar{u}, \varphi)\; dt. \tag{5.43}$$

This formulation is equivalent to the classical formulation

$$\begin{aligned} -\partial_t \hat{z}(t) - \Delta \hat{z}(t) - \boldsymbol{\beta}(t) \cdot \nabla \hat{z}(t) &= \hat{u}(t) - \bar{u}(t), && \text{in } \Omega \times (0,T], \\ z(t) &= 0, && \text{on } \partial\Omega \times (0,T], \\ z(T) &= 0, && \text{in } \Omega \end{aligned} \tag{5.44}$$

due to the usual regularity theory for parabolic operators, since in this particular case $z(T)$ is zero and $\hat{u} - \bar{u}$ is in $L^2\left(0,T;L^2(\Omega)\right)$. That means we have the results of Theorem 2.6 and obtain the higher regularity

$$\hat{z} \in L^2\left(0,T;H^2(\Omega) \cap H_0^1(\Omega)\right) \quad \text{and} \quad \partial_t \hat{z} \in L^2(0,T;L^2(\Omega)),$$

and the estimate

$$\operatorname*{ess\,sup}_{0 \le t \le T} \|\hat{z}(t)\|_{H^1(\Omega)} + \int_0^T \left\{ \|\hat{z}(t)\|^2_{H^2(\Omega)} + \|\partial_t \hat{z}(t)\|_2^2 \right\} dt \le C \int_0^T \|u(t) - \bar{u}(t)\|_2^2\, dt.$$

To sum up, we found

$$\hat{z} \in L^2\left(0,T;H^2(\Omega) \cap H_0^1(\Omega)\right), \text{ and } \partial_t \hat{z} \in L^2\left(0,T;L^2(\Omega)\right) \subset L^2\left(0,T;\tilde{V}'\right),$$

with the dual space $\tilde{V}'$ of the space $\tilde{V} = H^2(\Omega) \cap H_0^1(\Omega)$. Hence, $\hat{z}$ is in $\tilde{X}$ and the weak formulation of the dual equation in the Optimality System 5.29 is equivalent to the one in equation (5.43). Thus $\hat{z}$ must be the unique solution of the dual equation in the Optimality System 5.29.

3. Now the convergence in the control equation remains. We start with the weak formulation of the perturbed problem

$$\alpha \int_0^T \langle q_\mu, \rho \rangle_{\partial\Omega}\; dt = -\frac{1}{\mu} \int_0^T \langle z_\mu, \rho \rangle_{\partial\Omega}\; dt, \quad \forall \rho \in L^2\left(0,T;L^2(\partial\Omega)\right).$$

The convergence on the left hand side can be obtained by the property (5.31).

For the right hand side we wish to show

$$\left| \int_0^T \left\langle \partial_{\boldsymbol{n}} \hat{z} - \left(-\frac{1}{\mu} z_\mu \right), \rho \right\rangle_{\partial\Omega} dt \right| \to 0, \quad \forall \rho \in L^2\left(0,T;L^2(\partial\Omega)\right).$$

We multiply the classical equation (5.44) with an arbitrary function of the subset $L^2(0,T;H^1(\Omega))$ of $L^2(0,T;L^2(\Omega))$ and obtain after integration by parts

$$-\int_0^T \left\{ (\partial_t \hat{z}, \varphi) + \nu\,(\nabla\hat{z}, \nabla\varphi) - \langle \partial_{\boldsymbol{n}}\hat{z}, \varphi\rangle_{\partial\Omega} - (\boldsymbol{\beta}\cdot\nabla\hat{z}, \varphi) \right\} dt = \int_0^T (\hat{u}-\bar{u}, \varphi)\ dt.$$

By this equation and the dual equation in Optimality System 5.30 we find

$$\begin{aligned}\left|\int_0^T \left\langle \partial_{\boldsymbol{n}}\hat{z} + \frac{z_\mu}{\mu}, \varphi \right\rangle_{\partial\Omega} dt\right| \leq\ & \left|\int_0^T (\partial_t(\hat{z}-z_\mu), \varphi)\ dt\right| + \left|\int_0^T (\nabla(z_\mu-\hat{z}), \nabla\varphi)\ dt\right| \\ &+ \left|\int_0^T (\boldsymbol{\beta}\cdot\nabla(z_\mu-\hat{z}), \nabla\varphi)\ dt\right| \\ &+ \left|\int_0^T (\hat{u}(t)-u_\mu(t), \varphi(t))\ dt\right| \\ &+ \left|\frac{1}{2}\int_0^T \langle(\boldsymbol{\beta}\cdot\boldsymbol{n})z_\mu, \varphi\rangle_{\partial\Omega}\ dt\right|.\end{aligned}$$

It is easy to verify the convergence to zero of the first four terms on the right hand side by the properties of Theorem 5.31. The last term converges to zero since $\boldsymbol{\beta}$ is in $L^\infty\left(0,T;L^\infty(\Omega)\right)$ and z_μ converges weakly to zero in $L^2(0,T;L^2(\partial\Omega))$. Hence, we have

$$\int_0^T \frac{1}{\mu}\langle z_\mu, \rho\rangle_{\partial\Omega}\ dt \to \int_0^T \langle \partial_{\boldsymbol{n}} z, \rho\rangle_{\partial\Omega}\ dt,$$

with a test function $\rho = \varphi|_{\partial\Omega}$ in $L^2\left(0,T;L^2(\partial\Omega)\right)$. □

Since the triplets (u_μ, z_μ, q_μ) and (u,z,q) characterise unique solutions (u_μ, q_μ) and (u,q) of the perturbed Optimisation Problem 5.25 and the Optimisation Problem 5.20 we can state that the solution pair (u_μ, q_μ) converges to a solution of the Optimisation Problem 5.20 with the very Weak Formulation 5.17 as PDE side condition. That means that also in this case we can use the perturbed approach to approximate Dirichlet controls in the sense of the very weak formulation.

After a short numerical example we will discuss a few modifications of the problem and their influence on the presented theory.

Test Example

We present a numerical example for the convection-diffusion equation which is based on the Example 5.12. We obtain the right hand side f and the target function $\bar{u}(t)$ by choosing

the solution

$$\begin{aligned}\hat{q} &= -\frac{t(t-1)}{\alpha}\left(x(1-x)+y(1-y)\right),\\ \hat{u} &= -\frac{t(t-1)}{\alpha}\left(x(1-x)+y(1-y)\right),\\ \hat{z} &= t(t-1)xy(1-x)(1-y)\end{aligned}$$

and we evaluate the equivalent classical formulation of the Optimality System 5.29 for the further assumptions

$$\nu = 1, \qquad \boldsymbol{\beta} = (y-0.5, 0.5-x)^T, \qquad \alpha = 0.1$$

on the data. The computational domain Ω is the unit square $(0,1)\times(0,1)$ and the time interval $[0,1]$.

Table 5.4. Results for a calculation with $\mu = h^2$ on different meshes. The norms are evaluated at the midpoint of the time interval $t^\star = 0.5$.

cells	$\|u_h(t^\star) - \bar{u}(t^\star)\|_2$	**(rate)**	$\|z_h(t^\star) - \bar{z}(t^\star)\|_2$	**(rate)**	$\|q_h(t^\star) - \bar{q}(t^\star)\|_{L^2(\partial\Omega)}$	**(rate)**
4	$1.62\cdot10^{-1}$		$4.01\cdot10^{-3}$		$7.56\cdot10^{-1}$	
16	$3.69\cdot10^{-2}$	**(2.1)**	$1.18\cdot10^{-3}$	**(1.8)**	$1.92\cdot10^{-1}$	**(2.0)**
64	$9.39\cdot10^{-3}$	**(2.0)**	$4.36\cdot10^{-4}$	**(1.4)**	$4.82\cdot10^{-2}$	**(2.0)**
256	$2.37\cdot10^{-3}$	**(2.0)**	$1.68\cdot10^{-4}$	**(1.4)**	$1.21\cdot10^{-2}$	**(2.0)**
1024	$6.05\cdot10^{-4}$	**(2.0)**	$1.02\cdot10^{-4}$	**(0.7)**	$3.19\cdot10^{-3}$	**(1.9)**
4096	$1.57\cdot10^{-4}$	**(2.0)**	$8.75\cdot10^{-5}$	**(0.2)**	$8.63\cdot10^{-4}$	**(1.9)**

We calculate the solution with the Newton-CG method presented in Chapter 4.2. The occurring boundary bilinear form is given by the Robin-type approach

$$b(q;u;\varphi) = \frac{1}{\mu}\langle u-q,\varphi\rangle_{\partial\Omega} - \frac{1}{2}\langle(\boldsymbol{\beta}\cdot\boldsymbol{n})u,\varphi\rangle_{\partial\Omega}$$

to realise the discussed methodology of the section before. For the first numerical study we use the parameter choice $\mu = h^2$. Moreover, we use the Crank-Nicolson scheme with a time step size $k = 0.005$ for the temporal discretisation.

The development of the numerical error for this configuration is given in the Table 5.4. The example indicates that the error development under mesh refinement is analogous to the case of the time-independent Laplace problem. Furthermore, we visualise the state variable and dual variable for different time points in the Figures 5.4 and 5.5.

We want to emphasise that the problem becomes troublesome from a numerical point of view, when μ becomes too small. This is reflected by an increasing number of Newton-steps in the optimisation process to obtain a certain tolerance for the Newton residual. A remedy for this is to use the bilinear form given in Remark 5.23 to stabilise the numerical scheme.

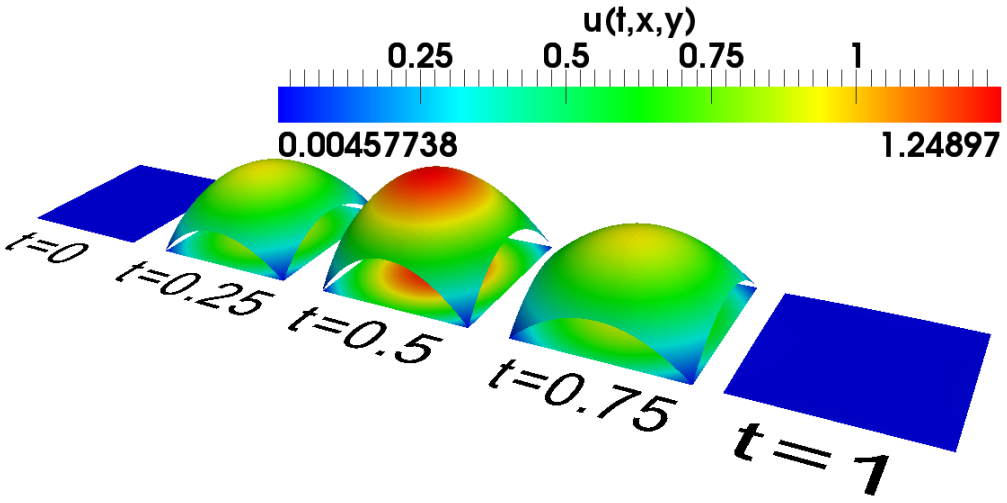

Figure 5.4. Calculated state u_h at five different time points.

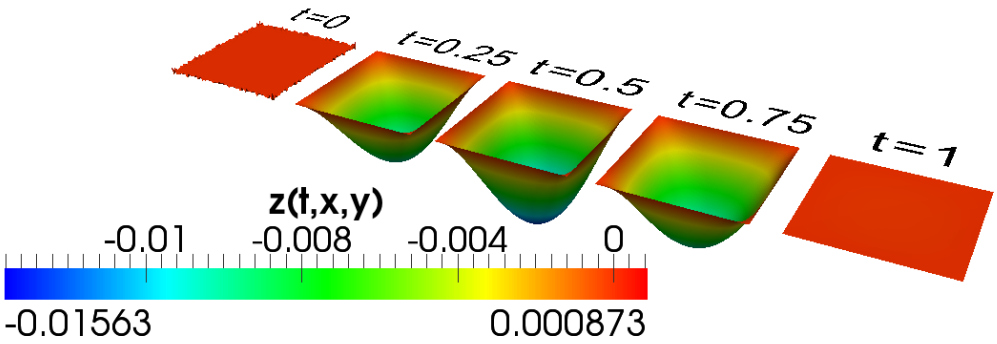

Figure 5.5. Calculated dual solution z_h at five different time points.

Setting $\mu = 0$ and $\delta = \tilde{\delta}_h$ we obtain a Nitsche-type weak implementation of the Dirichlet control.

In Table 5.5 we document the error development under mesh refinement for this parameter choice and observe also the expected properties.

At first glance an exception to this seems to be the dual solution for both parameter choices. However, the errors in the dual solution are small and we apparently observe here the temporal discretisation error.

Table 5.5. Results for a calculation with $\delta = \frac{h}{100}$ on different meshes. The norms are evaluated at the midpoint of the time interval $t^\star = 0.5$.

cells	$\|u_h(t^\star) - \bar{u}(t^\star)\|_2$	**(rate)**	$\|z_h(t^\star) - \bar{z}(t^\star)\|_2$	**(rate)**	$\|q_h(t^\star) - \bar{q}(t^\star)\|_{L^2(\partial\Omega)}$	**(rate)**
4	$2.52 \cdot 10^{-2}$		$4.28 \cdot 10^{-4}$		$9.00 \cdot 10^{-2}$	
16	$7.96 \cdot 10^{-3}$	**(1.7)**	$1.17 \cdot 10^{-4}$	**(1.9)**	$2.82 \cdot 10^{-2}$	**(1.7)**
64	$2.00 \cdot 10^{-3}$	**(2.0)**	$6.78 \cdot 10^{-5}$	**(0.8)**	$8.07 \cdot 10^{-3}$	**(1.8)**
256	$4.89 \cdot 10^{-4}$	**(2.0)**	$7.41 \cdot 10^{-5}$	**(−)**	$2.16 \cdot 10^{-3}$	**(1.9)**
1024	$1.17 \cdot 10^{-4}$	**(2.1)**	$8.02 \cdot 10^{-5}$	**(−)**	$5.40 \cdot 10^{-4}$	**(2.0)**
4096	$2.81 \cdot 10^{-5}$	**(2.1)**	$8.23 \cdot 10^{-5}$	**(−)**	$1.61 \cdot 10^{-4}$	**(1.8)**

Remarks on other Data Terms

The proof of the above mentioned results depends essentially on the structure of the cost functional and therefore also on the type of the data term. In the following we are mainly interested in comparing the state function to measurements given in a finite number of time points

$$\sum_{k=1}^{N} \|u(t_k) - \bar{u}_k\|_2^2.$$

Hence we want to discuss briefly the theoretical background of this case.

To get started we concentrate on the case of two given measurements $\bar{u}_0$ and $\bar{u}_1$, and the aim is to minimise the cost functional

$$J(u,q) = \frac{1}{2}\|u(T) - \bar{u}_1\|_2^2 + \frac{\alpha}{2}\int_0^T \|q(t)\|_{L^2(\partial\Omega)}^2 \, dt \tag{5.45}$$

subject to an appropriate formulation of the convection-diffusion equation with the initial value $u(t_0) = \bar{u}_0$ in $L^2(\Omega)$.

Remark 5.33 (Boundary Identification).
The interpretation of this problem is two- fold. On the one hand we can say that we control by α the influence of the time dependent-boundary function to obtain a function $u(\boldsymbol{x}, t)$ which is as close as possible to the second measurement.

On the other hand we can also interpret this as a boundary identification problem. The aim is to minimise the data term and to send α to zero to neglect the influence of the control. However, without the control term this is an ill-posed problem. So the control term is very important since it acts as regularisation term and is necessary for a well-posed formulation of the problem. In this sense we are not controlling anymore, since the task switches to the evaluation of a good regularisation parameter which allows for a very good fit in the data term.

Obviously Theorems 5.24 with the very weak formulation of the convection-diffusion equation and Theorem 5.26 with the penalised Neumann approach are still valid after a switch to the cost functional in equation (5.45) (this was discussed in Example 4.8). Hence, we have also the existence of a unique $(u, q) \in L^2(0, T; L^2(\Omega)) \times L^2(0, T; L^2(\partial\Omega))$ of the Optimisation Problem 5.20 and $(u_\mu, q_\mu) \in L^2(0, T; H^1(\Omega)) \times L^2(0, T; L^2(\partial\Omega))$ of the Optimisation Problem 5.25, when we change the cost functional to the one in formula (5.45).

We would again prefer to work with Robin-type conditions, since it is simple to handle. The first question is whether the above stated results of convergence of the sequence (u_μ, q_μ) is still valid if we modify the cost functional in the mentioned way. Thus, we have to be careful, since the cost functional influences the argumentation in the proof.

However, the question becomes more or less obsolete for the discussion since we change our optimisation paradigm as we mentioned in Remark 5.33. The aim is now to identify boundary conditions in such a way that we find a function $u(t)$ which fits the target at the end time point as good as possible. Hence, we are not limited to Dirichlet control problems and can tackle this problems directly with the presented Robin-type control problems regardless whether the result converges to an appropriate Dirichlet control problem or not.

Nevertheless we will now briefly discuss the changes for the convergence proof to see that both formulations are closly connected also for the choice of the cost functional in equation (5.45).

First we observe that we lose the estimate

$$\int_0^T \|u(t)\|_2^2 \, dt \leq C_{u^0, f, \nu, \bar{u}},$$

which we obtained only by the good structure of the L^2-tracking type term in space and time. Fortunately by a duality argument like in Step 3. in the proof of Theorem 5.21 we can find an analogous estimate independent of the use of the data term.

Moreover, all estimates for the dual equation stay valid since we can bound the term

$$\left(u_\mu(T) - \bar{u}_1, \varphi(T)\right)$$

in terms of

$$\|u_\mu(T) - \bar{u}_1\|_2^2,$$

which can be controlled following the argumentation in Step 1. in the proof of Theorem 5.31.

Thus, all convergence properties of Theorem 5.31 are conserved.

To show that the limit triplet $(\hat{u}, \hat{z}, \hat{q})$ is a solution of the Optimality System 5.29 of the very weakly formulated optimisation problem we used the parabolic regularity theory for the adjoint equation to show the convergence of the dual equation and the control equation. This was possible since $\hat{u}(t) - \bar{u}(t)$ was in $L^2(\Omega)$ and $\hat{z}(T) = 0$. Now we lose these properties since the initial value for the backward integration of the dual equation $\hat{u}(T) - \bar{u}$ is not necessarily in $H^1(\Omega)$.

However, as long as we have higher regularity of the whole system we will obtain also a good approximation of the Dirichlet control problem with the penalised Neumann technique.

Remarks on Pure Transport Problems

Finally we want to remark on the linear transport equation as side condition, since this equation is essential for image processing purposes. Due to $\nu = 0$ we obtain the bilinear forms

$$\begin{aligned} a(u, \varphi) &= (\boldsymbol{\beta} \cdot \nabla u, \varphi)\,, \\ b(q; u, \varphi) &= -\left\langle (\boldsymbol{\beta} \cdot \boldsymbol{n})\,(u - q)\,, \varphi \right\rangle_{\Gamma_{\mathrm{In}}} \end{aligned} \tag{5.46}$$

when we work with the state equation given in formula (3.11) (cf. Remark 3.9).

That means especially that we are able to control only the inflow. Thus, we may change the regularisation term to

$$\frac{\alpha}{2} \int_0^T \|q(t)\|^2_{L^2(\Gamma_{\mathrm{In}})}\, dt.$$

Then we obtain the optimisation problem

Optimisation Problem 5.34 (Image Interpolation across the Boudnary).
Find $(u, q) \in L^2\left(0, T; H^1(\Omega)\right) \times L^2\left(0, T; L^2(\Gamma_{In})\right)$ *so that*

$$J(u, q) = \frac{1}{2}\|u(T) - \bar{u}\|_2^2 + \frac{\alpha}{2} \int_0^T \|q(t)\|^2_{L^2(\Gamma_{In})}\, dt$$

is minimised subject to

$$\left(\partial_t u(t), \varphi\right) + a(u(t), \varphi) + b(q(t); u(t), \varphi) = \left(f(t), \varphi\right), \quad \forall \varphi \in H^1(\Omega),$$

with the bilinear forms given in (5.46) in almost every $t \in (0,1]$, with an initial value $u(0) = u^0$ in $L^2(\Omega)$.

Remark 5.35 (Existence of Solutions).
We want to emphasise that we cannot prove existence of a unique minimum for this Robin-type control problem (see Optimisation Problem 5.34) for the choice of the above spaces for the state and the control and the initial value.

The starting point would be to formulate the problem with artificial diffusion

$$\nu \left(\nabla u, \nabla \varphi \right).$$

For this equation we obtain for a fixed μ a unique

$$(u_\nu, q_\nu) \in L^2\left(0,T; H^1(\Omega)\right) \times L^2\left(0,T; L^2(\Gamma_{In})\right).$$

Then for this sequence in ν we have to show convergence, which is not trivial since the parameter ν will usually occur in the denominator of the bound and thus we have no uniform boundedness with respect to ν. With further assumptions on the data $\boldsymbol{\beta}$, u^0 and $\bar{u}$ it should be possible to show existence results.

However, we will mostly work with a small amount of diffusion in our numerical schemes for stabilisation issues. Moreover, the usual equation we have to deal with in physics-based optical flow estimation is the equation

$$\partial_t I(\boldsymbol{x},t) + \boldsymbol{u}(\boldsymbol{x},t) \cdot \nabla I(\boldsymbol{x},t) = \varepsilon \Delta I(\boldsymbol{x},t),$$

which is covered by the theory presented in the preceding sections as long as $\boldsymbol{u}$ has appropriate regularity conditions. We skip a further theoretical discussion of the pure transport equation and present two examples to show that the numerical method is also working for this configuration.

5.2.4. Numerical Examples

Given are two functions $\mathcal{I}_i(\boldsymbol{x}, t_i) : \Omega \to \mathbb{R}^+$ (see Figure 5.6) at different time points $t_0 = 0$ and $t_1 = T$. The initial function $\mathcal{I}_1(\boldsymbol{x}, t)$ is transported by the vector field $\boldsymbol{\beta} = (1,0)^T$ into $\mathcal{I}_2(\boldsymbol{x}, t)$ by the linear transport equation

$$\begin{aligned} \partial_t u(\boldsymbol{x},t) + \boldsymbol{\beta}(\boldsymbol{x},t) \cdot \nabla u(\boldsymbol{x},t) &= 0, && \text{in } \Omega \times (0,T], \\ u(\boldsymbol{x},t) &= q(\boldsymbol{x},t), && \text{on } \Gamma_{\text{In}} \times (0,T], \\ u(\boldsymbol{x},0) &= \mathcal{I}_1(\boldsymbol{x}), && \text{in } \Omega. \end{aligned} \tag{5.47}$$

Remark 5.36 (Connection to Image Processing).
We can interpret $\mathcal{I}_i$ as grey value distributions. The linear transport equation is then the model for the grey value transport in the two dimensional image domain, which is referred to as optical flow equation (cf. Chapter 1.2.1). The task to identify the intermediate images between the two given ones is called image interpolation.

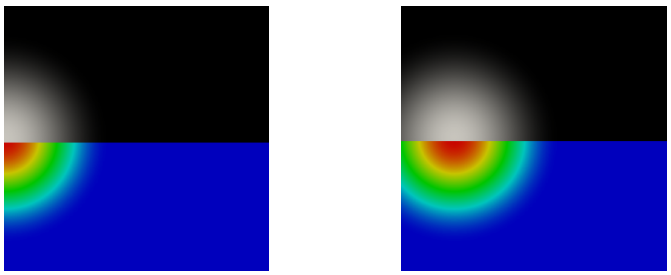

Figure 5.6. Image sequence of two intensity funtions $(\mathcal{I}_k)_{k=1}^2$. Left: $\mathcal{I}_1$. Right: $\mathcal{I}_2$. The lower half of the images shows a heat map (Red: Highest value. Blue: Lowest value.). The upper half shows an interpretation as grey value distribution.

As long as we have a concrete boundary function $q(\boldsymbol{x}, t)$ describing the inflow of $I(\boldsymbol{x}, t)$ for all $t \in (0, T]$ we can easily obtain the evolution of the grey value distribution by a simple forward calculation. Unfortunately we have no knowledge of such a function in general. A forward calculation with simply setting $q(\boldsymbol{x}, t) = 0$ or $q(\boldsymbol{x}, t) = \mathcal{I}_0(\boldsymbol{x})|_{\partial\Omega}$ representing this lacking knowledge of $q(\boldsymbol{x}, t)$ is given in Figure 5.7. We see that these approaches produce grey value distributions, which do not fit to the expected functions.

Remark 5.37 (Regularisation Parameter α).
The aim is to identify an appropriate boundary function by using the Optimisation Problem 5.34. Therefore we need an appropriate choice of the regularisation parameter α. Choosing such a parameter is a delicate matter, since we want to choose on the one hand a very small parameter to obtain the best possible fit in the data term. On the other hand we need enough regularisation to be able to calculate a solution. We postpone the discussion of heuristic parameter choice rules for α to the next chapter and work here with the fixed value of $\alpha = 10^{-3}$, since this yields significant results for the current presentation of transport dominant optimal control problems.

Figure 5.8 shows the results of a calculation of the above mentioned optimisation problem. Hereby we used a grid hierarchy to achieve a good initial value for a calculation on a 65×65 node spatial grid. Furthermore we used 80 equidistant implicit Euler steps on the time interval $[0, 0.2]$. We want to remark that we avoid to work with a transport stabilisation technique, due to the smooth character of the assumed solution and the transport field. We see here that the calculated discrete grey value distribution $I_h(\boldsymbol{x}, t)$ is a good approximation of the expected function $\hat{I}(\boldsymbol{x}, t)$.

To emphasise the connection to image processing problems (see Remark 5.36) and the necessity of stabilisation techniques in the case of general grey value distributions $I(\boldsymbol{x}, t)$ we discuss another configuration in the next example.

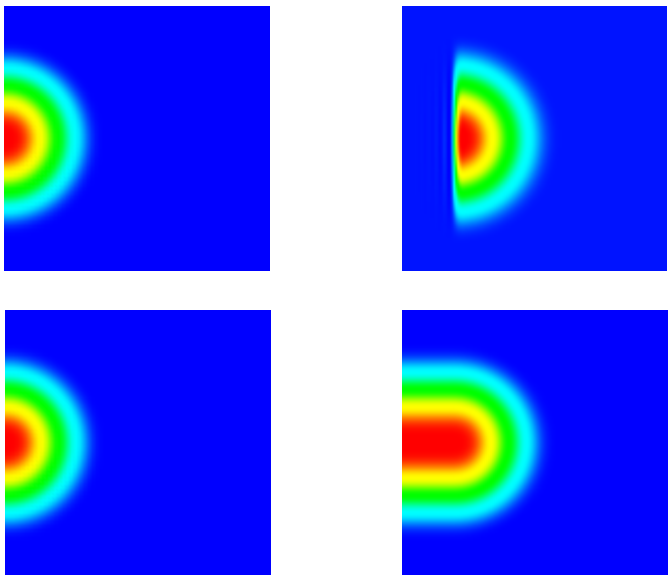

Figure 5.7. First row: Forward calculation with $I(\boldsymbol{x}, t) = 0$ on $\partial\Omega$. Left: Initial function. Right: Result at end time T. Second row: The same with $I(\boldsymbol{x}, t) = \mathcal{I}_0(\boldsymbol{x})|_{\partial\Omega}$ for all $t \in [0, T]$.

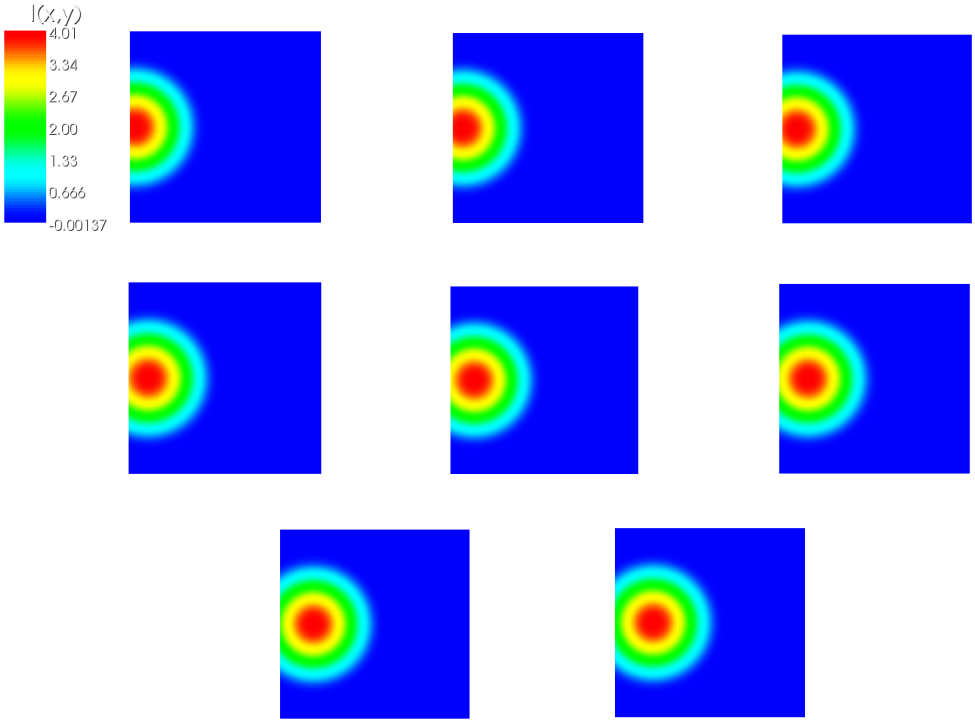

Figure 5.8. Results of the boundary identification for $\alpha = 10^{-3}$. From first row to third row, left to right: $\frac{iT}{8}$ with $i = 1, \ldots, 8$. The error: $\|I_h - \hat{I}\|_{L^2(Q)} = 4.99 \cdot 10^{-4}$.

Figure 5.9. Yoshimi-Example: Left: $\mathcal{I}_1$. Right: $\mathcal{I}_2$.

Numerical Example: Image Interpolation Across Boundaries

We have taken a picture of the authors cat Yoshimi by a modern digital camera. The image was directly converted to an grey value image by the camera. Afterwards, we take two apertures $\mathcal{I}_1^c$ and $\mathcal{I}_2^c$ of the grey value image. The two choosen apertures fit to the flow field

$$\boldsymbol{\beta} = (1, 0)^T$$

for a fixed time interval $[0, T]$.

Figure 5.9 shows the two available grey value images $\mathcal{I}_1$ and $\mathcal{I}_2$. We will now proceed with the same techniques presented in the last section to calculate intermediate images of the two given images.

The result of a calculation with the Crank-Nicolson scheme on the time interval $[0, 0.2]$ with 160 time steps is given in Figure 5.10. The left picture is the one we expect, while the right one is calculated. We see that there are wave perturbations next to the chair, the ear of the cat and in the background. This effect results from transport instabilities, which can be suppressed by using the techniques presented in Chapter 3. Figure 5.11 shows an LP stabilised version of the example on a 257×257 node grid. Qualitatively the result looks much better than the one in Figure 5.10, but we still have some oscillations in the neighborhood of sharp edges (e. g. chair). However, by the introduction of the stabilisation we smooth out sharp fronts in the function $I(t, \boldsymbol{x})$ which leads to a blurring effect in the image as we can see if we compare the bottom right image in Figure 5.11 to the expected image at the end time point (the right one in Figure 5.9). That means that the stabilisation represents a trade off between high oscillations on sharp structures in the image and blurring the image. Both aspects lead to a misfit between the original second image $\mathcal{I}_2$ and the grey value distribution at the end time $I(T)$. We observe this also by the L^2-errors in Table 5.6 and suppose that the major amount of the error was influenced by a insufficient stabilisation.

Figure 5.10. Left: Expected solution at $\frac{T}{2}$. Right: Interpolated solution by the presented optimisation process. The calculation was done on a 257×257 grid, without any further stabilisation techniques.

Figure 5.11. 257×257 grid with LP-stabilisation: $\delta = 0.1\frac{h}{|\boldsymbol{\beta}|_2^2}$.Upper left: $\frac{T}{4}$. Upper right: $\frac{T}{2}$. Lower left: $\frac{3T}{4}$. Lower right: T.

Nevertheless, it is a remarkable result that we are able to reconstruct the image up to 5 % in each time step without further tuning of the parameters α for the regularisation and δ for the stabilisation. Thus, we conjecture that it is possible to obtain even better results by working out sophisticated strategies for choosing α, δ or working with a another stabilisation technique.

Table 5.6. Difference between the calculated solution I_{h_8} on a 257×257 spatial grid and the expected solution. The table shows the L^2-norm difference and the relative difference in percent at four different time points. The four corresponding calculated images are given in Figure 5.11.

t	$\|I_{h_8}(t) - \bar{I}(t)\|_2$	$\|\bar{I}(t)\|_2$	%
$\frac{T}{4}$	$3.08 \cdot 10^{-2}$	$4.77 \cdot 10^{-1}$	4.2
$\frac{T}{2}$	$3.43 \cdot 10^{-2}$	$4.86 \cdot 10^{-1}$	5
$\frac{3T}{4}$	$3.53 \cdot 10^{-2}$	$4.85 \cdot 10^{-1}$	5.3
T	$3.54 \cdot 10^{-2}$	$4.80 \cdot 10^{-1}$	5.4

5.3. Dirichlet Control for the Time-Dependent (Navier-) Stokes Equations

We first state the optimisation problem for a general solenoidal vector field $\boldsymbol{\beta}$.

Optimisation Problem 5.38 (Dirichlet Control for the Oseen System). *Minimise*

$$J(\boldsymbol{u}, \boldsymbol{q}) = \hat{j}_d(\boldsymbol{u}) + \frac{\alpha}{2} \int_{t_0}^{T} \|\boldsymbol{q}(t)\|_{\mathcal{Q}}^2 dt, \tag{5.48}$$

with respect to $\boldsymbol{u} \in \mathcal{V}$ and $\boldsymbol{q} \in \mathcal{Q}$, subject to an appropriate weak formulation of the Oseen equations

$$\begin{aligned} \partial_t \boldsymbol{u}(t) - \nu \Delta \boldsymbol{u}(t) + \boldsymbol{\beta}(t) \cdot \nabla \boldsymbol{u}(t) + \nabla p(t) &= 0, && \text{in } \Omega \times (0,T], \\ \nabla \cdot \boldsymbol{u}(t) &= 0, && \text{in } \Omega \times (0,T], \\ \boldsymbol{u}(t) &= \boldsymbol{q}(t), && \text{on } \partial\Omega \times (0,T], \\ \boldsymbol{u}(\cdot, t_0) &= \boldsymbol{u}^0, && \text{in } \Omega. \end{aligned} \tag{5.49}$$

We will only discuss the following choice

$$\hat{j}_d(\boldsymbol{u}) = \frac{1}{2} \int_0^T \|\boldsymbol{u}(t) - \bar{\boldsymbol{u}}(t)\|_2^2 \, dt$$

of the data term and comment on other choices in form of remarks.

The theoretical background is widely discussed in the literature. Exemplarily we want to mention the article of Fursikov et al. [38] and the literature cited therein.

As in the sections before we consider the possibility of approximating a L^2-Dirichlet control problem by a sequence of solutions of Robin-type control problems. Thus, we discuss the access to the topic by the very weak formulation, to be able to work with $L^2(\partial\Omega)$ as control space. We start by introducing the following very weak formulation on the basis of the discussion in Chapter 2 in Farwig et al. [34].

Weak Formulation 5.39 (Very Weak Formulation).
A function

$$\boldsymbol{u} \in L^2\left(0, T; L^2(\Omega)\right)$$

is called a very weak solution if it fulfils

$$\int_0^T \Big\{ -(\boldsymbol{u}, \partial_t \boldsymbol{\varphi}) - \nu\,(\boldsymbol{u}, \Delta\boldsymbol{\varphi}) + \langle \boldsymbol{q}, \partial_{\boldsymbol{n}} \boldsymbol{\varphi} \rangle_{\partial\Omega} - (\boldsymbol{\beta} \cdot \nabla \boldsymbol{\varphi}, \boldsymbol{u}) \Big\} \, dt = \left(\boldsymbol{u}^0, \boldsymbol{\varphi}(0)\right) - \int_0^T (\boldsymbol{f}, \boldsymbol{\varphi}) \, dt$$

for any $\boldsymbol{\varphi}$ with

$$\boldsymbol{\varphi} \in L^2\left([0,T); H^2(\Omega) \cap H^1_{0,\mathrm{div}}(\Omega)\right) \quad \text{and} \quad \partial_t \boldsymbol{\varphi} \in L^2\left([0,T); \left(H^2(\Omega) \cap H^1_{0,\mathrm{div}}(\Omega)\right)'\right)$$

and

$$\int_0^T (\boldsymbol{u}(t), \nabla \xi(t)) - \langle \boldsymbol{q}(t) \cdot \boldsymbol{n}, \xi(t) \rangle_{\partial\Omega} \, dt = 0,$$

for $\xi \in L^2(0,T;\mathcal{H})$ with $\mathcal{H} := \{v \in H^1(\Omega); \int_\Omega v \, d\boldsymbol{x} = 0\}$. Here, the data is assumed to be in the following spaces

$$\begin{aligned}
&\boldsymbol{q} \in L^2\left(0, T; L^2(\partial\Omega)^n\right), \\
&\boldsymbol{f} \in L^2\left(0, T; H^1(\Omega)^n\right), \\
&\boldsymbol{\beta} \in L^\infty\left(0, T; H^1_{\mathrm{div}}(\Omega)^n\right) \cap L^\infty\left(0, T; L^\infty(\Omega)^n\right)
\end{aligned}$$

and $\boldsymbol{u}^0$ is in $L^2(\Omega)^2$.

Remark 5.40 (Wrong Formulation for Fully Nonlinear Navier-Stokes).
The above very weak formulation is not valid for the choice

$$\boldsymbol{\beta}(t) = \boldsymbol{u}(t),$$

since $\boldsymbol{u}(t) \in L^2(\Omega)^n$ *and therefore the term*

$$\int_0^T (\boldsymbol{u}(t) \cdot \nabla \boldsymbol{\varphi}, \boldsymbol{u}(t)) \; dt$$

cannot be defined unless we choose $\boldsymbol{\varphi} \in W^{1,\infty}(\Omega)^n$*, or in two dimensions* $H^3(\Omega)^2$*, due to embedding properties (see for example Adams et al. [1]).*

A well defined very weak formulation for the fully nonlinear Navier-Stokes equations is given in Marusic-Paloka [75]. Hereby

$$\boldsymbol{u}(t) \in L^{\frac{2n}{n-1}}(\Omega)^n$$

and therefore in $L^4(\Omega)^2$ *for two and* $L^3(\Omega)^3$ *for three space dimensions.*

Further theoretical insight to very weak formulations for the fully nonlinear Navier-Stokes equations can be found in Farwig et al. [34].

Hence, for an L^2*-fitting term in the cost functional the access by the very weak formulation is not given.*

In the following we distinguish between the linear case and the nonlinear case.

5.3.1. The Linear Case ($\beta \neq u$)

In Farwig et al. [34] also the existence and uniqueness theory for very weak formulations is discussed. It based essentially on a duality argument. Here we want to present again an approach working by penalised Neumann approach like in the case of the convection-diffusion equation to show the connection between the L^2-Dirichlet control approach with the very weak formulation of the Oseen problem as side condition and the Robin-type control approach.

We start with the following weak formulation

Weak Formulation 5.41.
We seek a function $u \in L^2\left(0, T; H^1_{div}(\Omega)^2\right)$ *such that*

$$\int_0^T \Big\{ -(\boldsymbol{u}(t), \partial_t \boldsymbol{\varphi}(t)) + a(\boldsymbol{u}(t), \boldsymbol{\varphi}(t)) + b(\boldsymbol{q}(t); \boldsymbol{u}(t), \boldsymbol{\varphi}(t)) \Big\} \, dt = \int_0^T (\boldsymbol{f}(t), \boldsymbol{\varphi}(t)) \; dt + \left(\boldsymbol{u}^0, \boldsymbol{\varphi}(0)\right)$$

is fulfilled for all

$$\boldsymbol{\varphi} \in \mathcal{X} := \left\{ \boldsymbol{v} : \boldsymbol{v} \in L^2\left(0,T; H^1_{div}(\Omega)^2\right) \text{ and } \partial_t \boldsymbol{v} \in L^2\left(0,T; \left(H^1_{\mathrm{div}}(\Omega)^2\right)'\right) \right\},$$

with the following bilinear forms

$$\begin{aligned} a(\boldsymbol{u},\boldsymbol{\varphi}) &= \nu\left(\nabla \boldsymbol{u}, \nabla \boldsymbol{\varphi}\right) + \left(\boldsymbol{\beta}\cdot\nabla \boldsymbol{u}, \boldsymbol{\varphi}\right), \\ b(\boldsymbol{q};\boldsymbol{u},\boldsymbol{\varphi}) &= \frac{1}{\mu}\left\langle \boldsymbol{u}-\boldsymbol{q}, \boldsymbol{\varphi}\right\rangle_{\partial\Omega} - \frac{1}{2}\left\langle (\boldsymbol{\beta}\cdot\boldsymbol{n})\boldsymbol{u}, \boldsymbol{\varphi}\right\rangle_{\partial\Omega}. \end{aligned}$$

We are able to prove the following existence theorem for this Weak Formulation.

Theorem 5.42.
For $\mu \in (0,1]$ and $\boldsymbol{q}$, $\boldsymbol{f}$ given as before and

$$\boldsymbol{\beta} \in L^2\left(0,T; H^1_{\mathrm{div}}(\Omega)^2\right)$$

there exists a unique solution $\boldsymbol{u} \in L^2(0,T; H^1_{\mathrm{div}}(\Omega)^2)$ of the Weak Formulation 5.41.

Proof. We test with the solution itself and gather

$$\begin{aligned} \int_0^T \left\{ \frac{1}{2}\frac{d}{dt}\|\boldsymbol{u}(t)\|_2^2 + \nu\|\nabla\boldsymbol{u}(t)\|_2^2 + \frac{1}{\mu}\|\boldsymbol{u}(t)\|^2_{L^2(\partial\Omega)^2}\right\} dt \leq & \int_0^T \|\boldsymbol{f}(t)\|_2\|\boldsymbol{u}(t)\|_2\, dt \\ & + \frac{1}{\mu}\int_0^T \|\boldsymbol{q}(t)\|_{L^2(\partial\Omega)^2}\|\boldsymbol{u}(t)\|_{L^2(\partial\Omega)^2}\, dt. \end{aligned} \tag{5.50}$$

Using the same techniques as in the proof of Theorem 5.21 (Hölder, Young and Poincaré inequality in formula (5.6)) we find after absorbing the $\boldsymbol{u}$-dependent terms on the right hand side into the left hand side

$$\begin{aligned} \|\boldsymbol{u}(T)\|_2^2 + \nu\int_0^T \|\nabla\boldsymbol{u}(t)\|_2^2\, dt + \frac{1}{\mu}\int_0^T \|\boldsymbol{u}(t)\|^2_{L^2(\partial\Omega)^2}\, dt & \\ \leq c_1\|u^0\|_2^2 + c_2\int_0^T \|\boldsymbol{f}(t)\|_2^2\, dt + \frac{1}{\mu}\int_0^T \|\boldsymbol{q}(t)\|^2_{L^2(\partial\Omega)^2}\, dt. & \end{aligned} \tag{5.51}$$

Now the existence and uniqueness for a fixed $\mu \in (0,1]$ is again obtained by the standard Galerkin technique (cf. Temam [99]). □

This means we can find a unique $u_\mu \in L^2\left(0,T; H^1_{\mathrm{div}}(\Omega)^2\right)$. Moreover, we can find a pressure function $p_\mu \in L^2(\Omega)$ which is unique up to an additive constant.

Remark 5.43 (Associating a Pressure Function).
Subtracting the right hand side from the left hand side in the Weak Formulation 5.41, it is easy to show (cf. Remark 2.13) that we gather a functional $\boldsymbol{l} \in H^{-1}(\Omega)$ *which fulfils*

$$\boldsymbol{l}(\boldsymbol{\varphi}) = 0, \qquad \forall \boldsymbol{\varphi} \in H^1_{0,\mathrm{div}}(\Omega)^2$$

for the subset $H^1_{0,\mathrm{div}}(\Omega)^2 \subset H^1_{\mathrm{div}}(\Omega)^2$ *(cf. equation (2.9)). Hence, we can associate an appropriate pressure* $p \in L^2(\Omega)$ *with* $\int_\Omega p(\boldsymbol{x})\, d\boldsymbol{x} = 0$ *by Lemma 2.12.*

Hence, the Weak Formulation 5.41 is equivalent to the following weak formulation.

Weak Formulation 5.44.
Find a pair $(\boldsymbol{u}, p) \in L^2\left(0,T; H^1(\Omega)^2\right) \times L^2\left(0,T; L^2(\Omega)\right)$ *so that*

$$\begin{aligned}\int_0^T \Big\{ \left(\partial_t \boldsymbol{u}(t), \boldsymbol{\varphi}(t)\right) + \nu \left(\nabla \boldsymbol{u}(t), \nabla \boldsymbol{\varphi}(t)\right) - \left(p(t), \nabla \cdot \boldsymbol{\varphi}(t)\right) + \frac{1}{\mu} \left\langle \boldsymbol{u}(t) - \boldsymbol{q}(t), \boldsymbol{\varphi}(t)\right\rangle_{\partial\Omega} \\ - \frac{1}{2} \left\langle (\boldsymbol{\beta}(t) \cdot \boldsymbol{n}) \boldsymbol{u}(t), \boldsymbol{\varphi}(t)\right\rangle_{\partial\Omega} \\ + \left(\boldsymbol{\beta}(t) \cdot \nabla \boldsymbol{u}(t), \boldsymbol{\varphi}(t)\right)\, dt = \int_0^T \left(\boldsymbol{f}(t), \boldsymbol{\varphi}(t)\right) \Big\}\, dt, \\ \int_0^T \left(\xi(t), \nabla \cdot u(t)\right)\, dt = 0\end{aligned}$$

is fulfilled for all $\varphi \in L^2\left(0,T; H^1(\Omega)^2\right)$ *and* $\xi \in L^2\left(0,T; L^2(\Omega)\right)$.

Furthermore, we obtain by the estimate (5.50) for a fixed $\boldsymbol{q} \in L^2\left(0,T; L^2(\partial\Omega)^2\right)$ a uniform bound for $\boldsymbol{u}_\mu$ on the boundary. Thus, we have

$$\boldsymbol{u}_\mu \rightharpoonup \tilde{\boldsymbol{u}} \quad \text{weakly in } L^2\left(0,T; L^2(\partial\Omega)^2\right).$$

In order to prove the connection between the weakly formulated problem and the very weakly formulated problem we need a further uniform bound for $\boldsymbol{u}_\mu$ in $L^2\left(0,T; L^2(\Omega)^2\right)$. We can achieve this estimate by a duality argument like in the case of the convection-diffusion equation. We have the classical formulation

$$\begin{aligned} -\partial_t \boldsymbol{\lambda}(t) - \nu \Delta \boldsymbol{\lambda}(t) - \boldsymbol{\beta}(t) \cdot \nabla \boldsymbol{\lambda}(t) + \nabla r(t) &= \boldsymbol{u}_\mu, && \text{in } \Omega \times [0,T), \\ \nabla \cdot \boldsymbol{\lambda}(t) &= 0, && \text{in } \Omega \times [0,T), \\ \boldsymbol{\lambda}(t) &= 0, && \text{on } \partial\Omega \times [0,T), \\ \boldsymbol{\lambda}(T) &= 0, && \text{in } \Omega. \end{aligned}$$

For this formulation we have analogous regularity results as in the parabolic regularity theory as long as we assume a sufficiently regular vector field $\boldsymbol{\beta}(t)$ and appropriate regularity

of the domain. For example in the Stokes case ($\boldsymbol{\beta} = 0$) or for $\boldsymbol{\beta} \in L^\infty\left(0,T;L^\infty(\Omega)^2\right)$ this can easily be obtained (cf. Temam [99, Proposition 3.1.2. and Chapter 3.5.1.]). Then, we find

$$\int_0^T \|\boldsymbol{\lambda}(t)\|^2_{H^2(\Omega)^2}\,dt \le C\int_0^T \|\boldsymbol{u}_\mu\|_2^2\,dt \quad \text{and} \quad \|\boldsymbol{\lambda}(0)\|_2^2 \le C\int_0^T \|\boldsymbol{u}_\mu\|_2^2\,dt.$$

Testing the classical formulation above with $\boldsymbol{u}_\mu$ and integrating over time yields after a few transformations

$$\int_0^T \|\boldsymbol{u}_\mu\|_2^2\,dt = (\boldsymbol{\lambda}(0),\boldsymbol{u}^0) + \int_0^T \Big\{\,(\boldsymbol{f}(t),\boldsymbol{\lambda}(t)) - \nu\,\langle \partial_{\boldsymbol{n}}\boldsymbol{\lambda}(t),\boldsymbol{u}_\mu(t)\rangle_{\partial\Omega}\,\Big\}dt.$$

With

$$\begin{aligned}\|\boldsymbol{\lambda}(t)\|_2 &\le C\|\boldsymbol{\lambda}(t)\|_{H^2(\Omega)^2},\\ \|\partial_{\boldsymbol{n}}\boldsymbol{\lambda}(t)\|_{L^2(\partial\Omega)^2} &\le C\|\boldsymbol{\lambda}(t)\|_{H^2(\Omega)^2}\end{aligned}$$

we gather

$$\int_0^T \|\boldsymbol{u}_\mu(t)\|_2^2\,dt \le \|\boldsymbol{\lambda}(0)\|_2\|\boldsymbol{u}^0\|_2 + \int_0^T \left(\|\boldsymbol{f}(t)\|_2 + \|\boldsymbol{u}_\mu\|_{L^2(\partial\Omega)^2}\right)\|\boldsymbol{\lambda}(t)\|_{H^2(\Omega)^2}\,dt.$$

Using Young's inequality with a clever choice of the parameter and the above mentioned regularity results we find

$$\begin{aligned}\int_0^T \|\boldsymbol{u}_\mu(t)\|_2^2\,dt \le\ & \frac{1}{4}\int_0^T \|\boldsymbol{u}_\mu(t)\|_2^2\,dt\\ &+ c_1\|\boldsymbol{u}^0\|_2^2 + c_2\int_0^T \left(\|\boldsymbol{f}(t)\|_2^2 + \|\boldsymbol{u}_\mu\|^2_{L^2(\partial\Omega)^2}\right)\,dt + \frac{1}{4}\int_0^T \|\boldsymbol{u}_\mu(t)\|_2^2\,dt.\end{aligned}$$

Absorbing the $\boldsymbol{u}$-dependent L^2-domain terms into the left hand side and using that $\boldsymbol{u}_\mu$ stays uniformly bounded on the boundary we end up with

$$\int_0^T \|\boldsymbol{u}_\mu(t)\|_2^2\,dt \le C_{\boldsymbol{f},\boldsymbol{u}^0,\boldsymbol{q},\nu}$$

and therefore

$$\boldsymbol{u}_\mu \rightharpoonup \tilde{\boldsymbol{u}} \quad \text{weakly in } L^2\left(0,T;L^2(\Omega)^2\right). \tag{5.52}$$

To prove that $\tilde{\boldsymbol{u}}$ is a solution of the (very) Weak Formulation 5.39 works now in the same way as in the case of the convection-diffusion equation. Also the convergence property

$$\int_0^T \langle \boldsymbol{u}_\mu(t) - \boldsymbol{q}(t),\boldsymbol{\rho}(t)\rangle_{\partial\Omega} \to 0, \quad \text{for } \mu\to 0 \text{ and for all } \boldsymbol{\rho} \in L^2\left(0,T;L^2(\partial\Omega)^2\right) \tag{5.53}$$

can easily be deduced in the Oseen case in the same fashion as in the convection-diffusion equation. We discuss only the divergence equation. Since $\boldsymbol{u}_\mu \in L^2\left(0,T;H^1_{\mathrm{div}}(\Omega)^2\right)$ we have

$$\int_0^T \left(\nabla\cdot\boldsymbol{u}_\mu(t),\xi(t)\right)\,dt = 0, \qquad \forall \xi \in L^2\left(0,T;\mathcal{H}\right).$$

Integration by parts yields

$$\int_0^T -\left(\boldsymbol{u}_\mu(t),\nabla\xi(t)\right) + \left\langle \boldsymbol{u}_\mu(t)\cdot\boldsymbol{n},\xi(t)\right\rangle_{\partial\Omega}\,dt = 0. \tag{5.54}$$

The convergence in the first term is clear due formula (5.52) since $\nabla\xi(t) \in L^2\left(0,T;L^2(\Omega)\right)$ and the second term converges due to property (5.53). This is obvious after resorting the terms in the second integral

$$\int_0^T \int_\Omega \boldsymbol{u}_\mu\cdot\left(\xi(t)\boldsymbol{n}\right)\,d\boldsymbol{x}\,dt$$

and realising that $\xi(t)\boldsymbol{n} \in L^2\left(0,T;L^2(\partial\Omega)^2\right)$ due to

$$\int_0^T \|\xi(t)\boldsymbol{n}\|^2_{L^2(\partial\Omega)^2}\,dt \le \int_0^T \|\xi(t)\|^2_{L^2(\partial\Omega)}\,dt \le C\int_0^T \|\xi(t)\|^2_{H^1(\Omega)}\,dt.$$

Combined we have the convergence of equation (5.54) to the second property in the very Weak Formulation 5.39

$$\int_0^T \left(\boldsymbol{u}(t),\nabla\xi(t)\right) - \left\langle \boldsymbol{q}(t)\cdot\boldsymbol{n},\xi(t)\right\rangle_{\partial\Omega}\,dt = 0, \quad \forall \xi \in L^2\left(0,T;\mathcal{H}\right).$$

Thus, we can formulate the following Theorem

Theorem 5.45.
Assuming Ω is bounded with a sufficiently regular boundary and the vector field $\boldsymbol{\beta}$ has sufficient regularity. Then, there exists a unique very weak solution

$$\boldsymbol{u} \in L^2\left(0,T;L^2(\Omega)^2\right)$$

of the (very) Weak Formulation 5.39.

Remark 5.46 (Convergence in the Oseen-Case).
The technique we chose to prove the existence theorem shows that we can use the Robin-type Oseen equation to approximate solutions of the very weak formulated Oseen equation for L^2-boundary data.

After proving the unique existence of solutions of the Robin-type formulation and the very weak formulation, we can use Theorem 4.5 and Remark 4.7 to justify the following two theorems, since the Oseen system is linear.

Theorem 5.47 (Optimisation Problem with the Very Weak Formulation).
For $0 < \nu_0 \leq \nu \leq 1$ there exists a unique minimum

$$(\boldsymbol{u}, \boldsymbol{q}) \in L^2\left(0, T; L^2(\Omega)^2\right) \times L^2\left(0, T; L^2(\partial\Omega)^2\right),$$

which minimises the cost functional

$$J(\boldsymbol{u}, \boldsymbol{q}) = \frac{1}{2} \int_0^T \|\boldsymbol{u}(t) - \bar{\boldsymbol{u}}(t)\|_2^2 \, dt + \frac{\alpha}{2} \int_0^T \|\boldsymbol{q}(t)\|_{L^2(\partial\Omega)^2}^2 \, dt$$

subject to the (very) Weak Formulation 5.39.

Theorem 5.48 (Optimisation Problem with the Robin Formulation).
For every $0 < \mu \leq 1$ and $0 < \nu_0 \leq \nu \leq 1$ there exists a unique minimum

$$(\boldsymbol{u}_\mu, \boldsymbol{q}_\mu) \in L^2\left(0, T; H^1_{\mathrm{div}}(\Omega)^2\right) \times L^2\left(0, T; L^2(\partial\Omega)^2\right)$$

which minimises the cost functional

$$J(\boldsymbol{u}, \boldsymbol{q}) = \frac{1}{2} \int_0^T \|\boldsymbol{u}(t) - \bar{\boldsymbol{u}}(t)\|_2^2 \, dt + \frac{\alpha}{2} \int_0^T \|\boldsymbol{q}(t)\|_{L^2(\partial\Omega)^2}^2 \, dt$$

subject to the penalised Neumann approach stated in the Weak Formulation 5.41.

Remark 5.49 (Convergence of the Sequence $(\boldsymbol{u}_\mu, \boldsymbol{q}_\mu)$).
It should be possible to argue analogously by the optimality systems as in the case of the convection-diffusion equation to prove the convergence of the sequence $(\boldsymbol{u}_\mu, \boldsymbol{q}_\mu)$ to a solution $(\hat{\boldsymbol{u}}, \hat{\boldsymbol{q}})$ of the optimisation problem mentioned in the Theorem 5.47 for the very weak formulated Oseen equation. Thus, the Robin formulation should also exhibit the possibility to approximate Dirichlet controls for the Oseen system.

However, the proof is rather technical. We skip the details here due to the following reasons: The first one is that in general we will work with the fully nonlinear Navier-Stokes system instead of the Oseen equations, where we have no appropriate very weak formulation. The second reason is that we will work with Robin-type controls in the final application chapter, since the numerical example at the end of this chapter indicates that this approach is working very well for L^2-boundary controls.

5.3.2. The Nonlinear Case ($\boldsymbol{\beta} = \boldsymbol{u}$)

If we consider the case $\boldsymbol{\beta} = \boldsymbol{u}$ everything becomes more complicated, since the nonlinearity influences intensively the whole theory. For example we are no longer able to prove

existence of a minimum by Theorem 4.5. Hence we have to prove the existence of a minimum separately.

Furthermore, the whole framework of working with very weak formulations and L^2-controls is not working as before, since we need a different function space for the state variable (cf. Remark 5.40).

However, there are widely discussed approaches for the treatment of Dirichlet controls in the Navier-Stokes case in the literature. For example in the time-dependent case the work of Fursikov et al. [38, 39] or in the steady case Gunzburger et al. [45] and the literature cited therein.

Especially we want to mention the work of Hou et al. [55, 56], where a penalised Neumann approach for the approximation of Dirichlet controls in the steady Navier-Stokes case is considered. The authors are able to show that the limit of the sequence $\left(\{\boldsymbol{u}_\mu, p_\mu\}, \boldsymbol{q}_\mu\right)$ for μ tending to zero is both, a suboptimal solution of a Dirichlet control problem without data restrictions and an optimal solution of the Dirichlet control problem with data restrictions. Their argumentation's based on a specific choice of the cost functional, namely the minimisation of the vorticity of a flow, to obtain (weak) convergence results. Thus, also in the Navier-Stokes case there seems to be a connection between Robin and Dirichlet control problems.

We will briefly discuss the theory of a Robin control problem for the fully nonlinear Navier-Stokes system with a tracking type cost functional. Starting point is the modification of the Weak Formulation 5.41 for the nonlinear case:

Weak Formulation 5.50.
We seek a function $\boldsymbol{u} \in L^2\left(0,T; H^1_{\mathrm{div}}(\Omega)^2\right)$ *so that*

$$\int_0^T \Big\{ -\left(\boldsymbol{u}(t), \partial_t \boldsymbol{\varphi}(t)\right) + a\left(\boldsymbol{u}(t)\right)(\boldsymbol{\varphi}(t)) + b\left(\boldsymbol{q}(t); \boldsymbol{u}(t)\right)(\boldsymbol{\varphi}(t))\Big)\ dt = \int_0^T \left(\boldsymbol{f}(t), \boldsymbol{\varphi}(t)\right) \Big\}\, dt + \left(\boldsymbol{u}^0, \boldsymbol{\varphi}(0)\right)$$

is fulfilled for all

$$\boldsymbol{\varphi} \in \mathcal{X} := \left\{ \boldsymbol{v} : \boldsymbol{v} \in L^2\left(0,T; H^1_{\mathrm{div}}(\Omega)^2\right) \ \textit{and} \ \ \partial_t \boldsymbol{v} \in L^2\left(0,T; \left(H^1_{\mathrm{div}}(\Omega)^2\right)'\right) \right\}$$

with the following semilinear forms

$$\begin{aligned} a(\boldsymbol{u})(\boldsymbol{\varphi}) &= \nu\left(\nabla \boldsymbol{u}, \nabla \boldsymbol{\varphi}\right) + \left(\boldsymbol{u} \cdot \nabla \boldsymbol{u}, \boldsymbol{\varphi}\right), \\ b(\boldsymbol{q}; \boldsymbol{u})(\boldsymbol{\varphi}) &= \frac{1}{\mu}\left\langle \boldsymbol{u} - \boldsymbol{q}, \boldsymbol{\varphi}\right\rangle_{\partial\Omega} - \frac{1}{2}\left\langle (\boldsymbol{u}\cdot\boldsymbol{n})\boldsymbol{u}, \boldsymbol{\varphi}\right\rangle_{\partial\Omega}. \end{aligned}$$

First we observe that Theorem 5.42 is still valid in the nonlinear case:

Theorem 5.51.
For $\mu \in (0,1]$ and $\boldsymbol{q}, \boldsymbol{f}$ given as before we find the existence of a unique solution $\boldsymbol{u} \in L^2\left(0,T; H^1_{\mathrm{div}}(\Omega)^2\right)$ of the Weak Formulation 5.50.

Proof. We discuss the differences in proving this result. For abbreviation we will sometimes omit to write the time variable in the following discussion.

- For the above described Robin boundary data the term

$$-\frac{1}{2}\left\langle(\boldsymbol{\beta}\cdot\boldsymbol{n})\boldsymbol{u},\boldsymbol{u}\right\rangle_{\partial\Omega} + (\boldsymbol{\beta}\cdot\nabla\boldsymbol{u},\boldsymbol{u}) = 0$$

  is obviously vanishing due to the test with the solution itself. Therefore the existence theory is working also in the nonlinear case

$$\boldsymbol{\beta} = \boldsymbol{u}.$$

  as before by the standard theory (cf. Temam [99]).

- The uniqueness cannot be obtained that easily, since here the same problems occur that we already mentioned in Section 2.3.

  Fortunately the two-dimensional uniqueness can be achieved like in the standard case of Theorem 2.15, due to the following estimation:

  As usual we assume we have two different solutions $\boldsymbol{u}, \boldsymbol{v}$ of the Weak Formulation 5.50 for the same data $\boldsymbol{f}$ and $\boldsymbol{q}$. Building the difference of the two equations and testing with the difference $\boldsymbol{w} = \boldsymbol{u} - \boldsymbol{v}$ yields

$$\begin{aligned}\frac{1}{2}\frac{d}{dt}\|\boldsymbol{w}\|_2^2 + \nu\|\nabla\boldsymbol{w}\|_2^2 + \frac{1}{\mu}\|\boldsymbol{w}\|^2_{L^2(\partial\Omega)^2} = \quad & \frac{1}{2}\left\langle(\boldsymbol{w}\cdot\boldsymbol{n})\boldsymbol{u},\boldsymbol{w}\right\rangle_{\partial\Omega} - (\boldsymbol{w}\cdot\nabla\boldsymbol{u},\boldsymbol{w}) \\ & + \frac{1}{2}\left\langle(\boldsymbol{v}\cdot\boldsymbol{n})\boldsymbol{w},\boldsymbol{w}\right\rangle_{\partial\Omega} - (\boldsymbol{v}\cdot\nabla\boldsymbol{w},\boldsymbol{w}).\end{aligned}$$

  The last two terms on the right hand side cancel each other out (see Remark 5.19). Reformulation of the boundary integral as domain integrals gives us

$$-\frac{1}{2}(\boldsymbol{w}\cdot\nabla\boldsymbol{u},\boldsymbol{w}) + \frac{1}{2}(\boldsymbol{w}\cdot\nabla\boldsymbol{w},\boldsymbol{u})$$

  on the right hand side. We present now only the basic steps, since a detailed argumentation can be found in the work of Klinger [66, Proof of Satz 4.19] for an analogous problem.

  By the interpolation estimate (cf. Galdi [41, Chapter II.2, Lemma 2.2 and Exercise 2.9])

$$\|\boldsymbol{w}\|_{L^4(\Omega)^2} \le c\|\boldsymbol{w}\|_2^{\frac{1}{2}}\|\boldsymbol{w}\|^{\frac{1}{2}}_{H^1(\Omega)^2}$$

  we can treat the two domain integrals. We obtain

$$|-(\boldsymbol{w}\cdot\nabla\boldsymbol{u},\boldsymbol{w})| \le c\|\boldsymbol{w}\|_2\|\boldsymbol{w}\|_{H^1(\Omega)^2}\|\boldsymbol{u}\|_{H^1(\Omega)^2}$$

and

$$|\,(\boldsymbol{w}\cdot\nabla\boldsymbol{w},\boldsymbol{u})\,| \le c\|\boldsymbol{u}\|_2^{\frac{1}{2}}\|\boldsymbol{u}\|_{H^1(\Omega)^2}^{\frac{1}{2}}\|\boldsymbol{w}\|_2^{\frac{1}{2}}\|\boldsymbol{w}\|_{H^1(\Omega)^2}^{\frac{3}{2}}.$$

Using Youngs inequality with $p=q=2$ and $\tilde{p}=4$ and $\tilde{q}=\frac{4}{3}$ yields

$$\|\boldsymbol{w}\|_2\|\boldsymbol{w}\|_{H^1(\Omega)^2}\|\boldsymbol{u}\|_{H^1(\Omega)^2} \le \frac{\kappa\|\boldsymbol{w}\|_2^2\|\boldsymbol{u}\|_{H^1(\Omega)^2}^2}{2} + \frac{\|\boldsymbol{w}\|_{H^1(\Omega)^2}^2}{2\kappa},$$
$$\|\boldsymbol{u}\|_2^{\frac{1}{2}}\|\boldsymbol{u}\|_{H^1(\Omega)^2}^{\frac{1}{2}}\|\boldsymbol{w}\|_2^{\frac{1}{2}}\|\boldsymbol{w}\|_{H^1(\Omega)^2}^{\frac{3}{2}} \le \frac{\tilde{\kappa}\|\boldsymbol{u}\|_2^2\|\boldsymbol{u}\|_{H^1(\Omega)^2}^2\|\boldsymbol{w}\|_2^2}{4} + \frac{3\|\boldsymbol{w}\|_{H^1(\Omega)^2}^2}{4\tilde{\kappa}}.$$

Hence, we have

$$|-(\boldsymbol{w}\cdot\nabla\boldsymbol{u},\boldsymbol{w})| + |\,(\boldsymbol{w}\cdot\nabla\boldsymbol{w},\boldsymbol{u})\,| \le \underbrace{\left(c(\kappa)\|\boldsymbol{u}\|_{H^1(\Omega)^2}^2 + c(\tilde{\kappa})\|\boldsymbol{u}\|_2^2\|\boldsymbol{u}\|_{H^1(\Omega)^2}^2\right)}_{=:\beta}\|\boldsymbol{w}\|_2^2 + \left(\frac{1}{2\kappa}+\frac{3}{4\tilde{\kappa}}\right)\|\boldsymbol{w}\|_{H^1(\Omega)^2}^2.$$

Now we use the general Poincaré inequality

$$\|\boldsymbol{w}\|_{H^1(\Omega)^2}^2 \le c\left(\|\nabla\boldsymbol{w}\|_2^2 + \|\boldsymbol{w}\|_{L^2(\partial\Omega)^2}^2\right)$$

for the second term on the right hand side. Furthermore, we use $1\le\frac{1}{\mu}$ and choose the parameters κ and $\tilde{\kappa}$ so that we are able to absorb the terms $\frac{\nu}{2}\|\nabla\boldsymbol{w}\|^2$ and $\frac{1}{2\mu}\|\boldsymbol{w}\|_{L^2(\partial\Omega)}^2$ into the left hand side. Finally, we get the inequality

$$\frac{d}{dt}\|\boldsymbol{w}\|_2^2 \le c(\nu)\beta(t)\|\boldsymbol{w}(t)\|_2^2.$$

Since

$$\int_0^t \beta(s)\,ds \le c_1\int_0^t \|\boldsymbol{u}(s)\|_{H^1(\Omega)^2}^2\,ds + c_2\operatorname*{ess\,sup}_{s\in[0,t]}\|\boldsymbol{u}(s)\|_2^2\int_0^t\|\boldsymbol{u}(s)\|_{H^1(\Omega)^2}^2\,ds$$

is bounded due to the a-priori bounds, we can apply Gronwall's inequality. The fact that $\boldsymbol{w}(\boldsymbol{x},0)=0$ yields the uniqueness. □

Now we consider an optimisation problem involving the Weak Formulation 5.50.

Theorem 5.52 (Optimisation Problem for the Navier-Stokes equations). *For every $0<\mu\le 1$ and $0<\nu_0\le\nu\le 1$ there exists at least one minimum*

$$(\boldsymbol{u}_\mu,\boldsymbol{q}_\mu)\in L^2\left(0,T;H^1_{\mathrm{div}}(\Omega)^2\right)\times L^2\left(0,T;L^2(\partial\Omega)^2\right),$$

which minimises the cost functional

$$J(\boldsymbol{u},\boldsymbol{q}) = \frac{1}{2}\int_0^T\|\boldsymbol{u}(t)-\bar{\boldsymbol{u}}(t)\|_2^2\,dt + \frac{\alpha}{2}\int_0^T\|\boldsymbol{q}(t)\|_{L^2(\partial\Omega)^2}^2\,dt$$

subject to the Robin-type approach for the fully nonlinear Navier-Stokes equation in the Weak Formulation 5.50.

Proof. We follow the proof of Hou et al. [55], which considered an optimisation problem with the steady Navier-Stokes systems as PDE constraint. In general we have to consider the following steps:

1. Choosing a minimising sequence $\{\boldsymbol{u}^{(k)}, \boldsymbol{q}^{(k)}\}$.
2. Showing uniform boundedness of the sequence in appropriate norms.
3. By usual compactness and embedding results choosing converging subsequence.
4. Showing for the limit of the convergent subsequence:
   a) That it fulfils the state equation.
   b) That it is indeed a minimum of the cost functional.

Thanks to Theorem 5.51 we have the existence of a unique solution $\boldsymbol{u}_\mu$ in $L^2\left(0,T;H^1_{\mathrm{div}}(\Omega)^2\right)$ for a given $q_\mu \in L^2\left(0,T;L^2(\Omega)^2\right)$. That means especially that the set $\mathcal{F}_{\mathrm{ad}}$ of admissible minimisers is not empty.

We choose a minimising sequence $\{\boldsymbol{u}_\mu^{(k)}, \boldsymbol{q}_\mu^{(k)}\}$ in k which fulfils the Navier-Stokes equation with Robin boundary conditions (Weak Formulation 5.50):

$$\lim_{k\to\infty} J(\boldsymbol{u}_\mu^{(k)}, \boldsymbol{q}_\mu^{(k)}) = \inf_{\{\boldsymbol{u},\boldsymbol{q}\}\in\mathcal{F}_{ad}} J(\boldsymbol{u},\boldsymbol{q}) =: \theta.$$

By Young's inequality we have again the coercivity

$$J(\boldsymbol{u},\boldsymbol{q}) \geq \frac{\alpha}{2}\int_0^T \|\boldsymbol{q}\|^2_{L^2(\partial\Omega)^2}\,dt \geq \alpha\left(\left(\int_0^T \|\boldsymbol{q}(t)\|^2_{L^2(\partial\Omega)^2}\,dt\right)^{\frac{1}{2}} - \frac{1}{2}\right).$$

Then we are able to bound the control on the boundary

$$\|\boldsymbol{q}_\mu^{(k)}\|_{L^2\left(0,T;L^2(\partial\Omega)^2\right)} \leq \frac{1}{\alpha} J(\boldsymbol{u}_\mu^{(k)}, \boldsymbol{q}_\mu^{(k)}) + \frac{1}{2} \leq B$$

with a k-independent constant B.

Via the usual a priori estimate from the existence theory we obtain the uniform bounds

$$\int_0^T \|\nabla \boldsymbol{u}_\mu^{(k)}\|_2^2\,dt \leq C_1,$$

$$\int_0^T \|\boldsymbol{u}_\mu^{(k)}\|^2_{L^2(\partial\Omega)^2}\,dt \leq C_2.$$

Hence, by the general Poincaré inequality (5.6) we obtain that $(u_\mu^{(k)})_{k\in\mathbb{N}}$ is uniformly bounded in $L^2\left(0,T;H^1_{\mathrm{div}}(\Omega)^2\right)$.

Furthermore, we get also from the same a priori estimates that the sequence is uniformly bounded in the space $L^\infty(0,T;L^2(\Omega)^2)$.

Moreover, we receive by compact embedding properties the strong convergence property

$$\int_0^T \|u_\mu^{(k)}(t) - u_\mu(t)\|_2^2 \, dt \to 0, \quad (k \to \infty)$$

for a subsequence.

These bounds yield the (weak) convergence of a subsequence. It is then standard to pass to the limit in the Weak Formulation 5.50. We gather

$$\begin{aligned}(\partial_t \boldsymbol{u}_\mu(t), \boldsymbol{\varphi}) + \nu \left(\nabla \boldsymbol{u}_\mu(t), \nabla \boldsymbol{\varphi}\right) + \frac{1}{\mu} \left\langle \boldsymbol{u}_\mu(t) - \boldsymbol{q}_\mu(t), \boldsymbol{\varphi} \right\rangle_{\partial\Omega} \\ - \frac{1}{2} \left\langle (\boldsymbol{u}_\mu(t) \cdot \boldsymbol{n}) \boldsymbol{u}_\mu(t), \boldsymbol{\varphi} \right\rangle_{\partial\Omega} + \left(\boldsymbol{u}_\mu(t) \cdot \nabla \boldsymbol{u}_\mu(t), \boldsymbol{\varphi}\right) = \left(\boldsymbol{f}(t), \boldsymbol{\varphi}\right).\end{aligned}$$

Now we have to show that the solution pair $\{\boldsymbol{u}_\mu, \boldsymbol{q}_\mu\}$ is optimal.

At first we use the convergence properties from above and obtain

$$\begin{aligned}\theta &= \lim_{k\to\infty} J(\boldsymbol{u}_\mu^{(k)}, \boldsymbol{q}_\mu^{(k)}) = \lim_{k\to\infty} \frac{1}{2} \int_0^T \|\boldsymbol{u}_\mu^{(k)}(t) - \bar{\boldsymbol{u}}(t)\|_2^2 \, dt + \lim_{k\to\infty} \frac{\alpha}{2} \int_0^T \|\boldsymbol{q}_\mu^{(k)}\|_{L^2(\partial\Omega)^2}^2 \, dt \\ &= \frac{1}{2} \int_0^T \|\boldsymbol{u}_\mu(t) - \bar{\boldsymbol{u}}(t)\|_2^2 \, dt + \liminf_{k\to\infty} \frac{\alpha}{2} \int_0^T \|\boldsymbol{q}_\mu^{(k)}\|_{L^2(\partial\Omega)^2}^2 \, dt.\end{aligned}$$

Since the norm $\|\cdot\|_{L^2(0,T;L^2(\partial\Omega)^2)}$ is continuous and convex we obtain by a standard argument (see the end of the proof of Theorem 4.5 in Section 4.1) that the norm is also weakly lower semicontinuous and we have

$$\theta \geq \int_0^T \|\boldsymbol{u}_\mu(t) - \bar{\boldsymbol{u}}(t)\|_2^2 \, dt + \frac{\alpha}{2} \int_0^T \|\boldsymbol{q}_\mu\|_{L^2(\partial\Omega)^2}^2 \, dt = J(\boldsymbol{u}_\mu, \boldsymbol{q}_\mu).$$

Thus, we obtain the optimality of $\boldsymbol{u}_\mu$ and $\boldsymbol{q}_\mu$. □

Remark 5.53 (Convergence to a Solution of a Dirichlet Control Problem).
In dependence of μ we gather again a sequence of solutions of this Robin-type optimisation problem. The question is now whether the limit of the sequence for $\mu \to 0$ is in some sense again a solution of a Dirichlet control problem.

The problem is that the pair of the L^2-tracking type and the L^2-regularisation term on the boundary is not appropriate for a meaningful statement of a Dirichlet control problem for the Navier-Stokes equation.

On the other hand we can only generate convergent subsequences in $L^2\left(0,T;L^2(\Omega)^2\right)$ and $L^2\left(0,T;L^2(\partial\Omega)^2\right)$ as in the Oseen case.

That means we are not able to prove any convergence result for the sequence $(\boldsymbol{u}_\mu, \boldsymbol{q}_\mu)$ *in our setting.*

Only by changing the cost functional we are perhaps able to prove a connection between the penalised Neumann control and the Dirichlet control problem (cf. Hou et al. [55] in the steady case).

5.3.3. Numerical Example

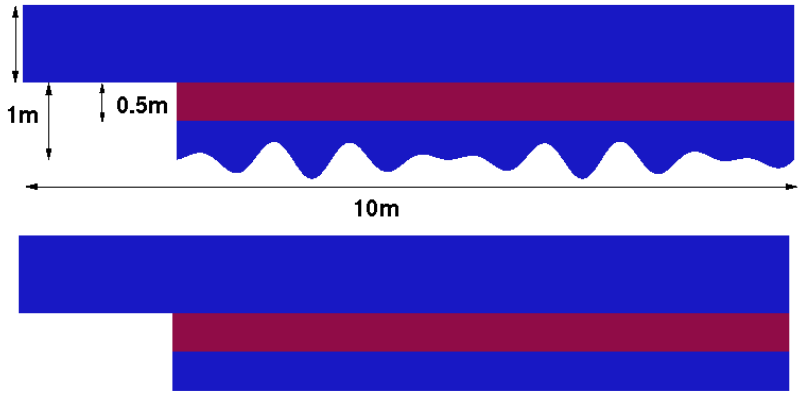

Figure 5.12. Top: Original domain with a rough lower boundary $\hat{\Omega}$. Bottom: Almost the same domain Ω with a lower boundary which is flat. The red area marks the observation domain Ω_{Obs} which is used in the data term of the optimisation problem.

In this subsection we want to present a numerical example for the above discussed boundary control problems in the case of the two dimensional unsteady Navier-Stokes system.

At first we will describe the setting. Starting point is a backward facing step channel as computational domain. Many numerical calculations in the case of Navier-Stokes boundary control considering the backward facing step in the literature, see for example in Choi et al. [47], or Ito et al. [58] or Becker [8] to mention a few of them. But mostly the authors are interested in the reduction of vorticity in these cases.

We present another interesting example which is also motivated by a physical application, namely the flow in a backward facing step with an unknown roughness of the lower wall (see Figure 5.12). A related example for the standard benchmark channel with rough walls for the identification of finitely many parameters was given by Vexler [102]. The difference is that we want to identify a distributed quantity by the mentioned optimisation problems with either a Robin control or a Nitsche-type Dirichlet control.

Given is for a example a velocity field $\bar{\boldsymbol{u}}$ in the red area Ω_{Obs} of the rough channel (upper picture in Figure 5.12) for a known inflow on the left side of the channel and a free outflow boundary on the right side of the channel, while the flow field is zero on all other walls of the domain, including the rough lower part of the boundary. The aim is now to reconstruct an appropriate flow field $\boldsymbol{u}$ in a channel with a smooth and flat lower boundary, which fits $\bar{\boldsymbol{u}}$ as good as possible in the observation domain Ω_{Obs}. The background is that we have in real world applications measurements of flows in channels with rough walls, where the structure of the roughness is in general unavailable. The proposed method is able to reconstruct a reliable flow field out of the measurements under the assumption that the walls are flat.

Remark 5.54 (Connection to Real World Application).
The estimation of so-called effective boundary conditions on an auxiliary boundary chosen above an unknown boundary structure is also discussed in the literature, e. g. Friedmann [37]. In connection to available velocity data in certain areas of the flow domain, the described technique should be able to recovery such effective boundary conditions. The flow data could be obtained for example by so-called particle image velocimetry (PIV) or hot-wire statistics, e. g. Dróżdż et al. [30]. Later on we will present examples, where we connect the image data directly to the flow on an artificial truncated domain to estimate reliable flow informations, which are only indirectly described by the movement of a passive tracer. We will use schlieren images of the tracer instead of particle images.

We want to use our Robin-type boundary control problem from Theorem 5.52 for the mentioned problem. Here we modify the cost functional in the following way

$$J(\boldsymbol{u}, \boldsymbol{q}) = \frac{1}{2} \int_0^T \|\boldsymbol{u}(t) - \bar{\boldsymbol{u}}(t)\|^2_{2,\Omega_{\text{Obs}}} \, dt + \frac{\alpha}{2} \int_0^T \|\boldsymbol{q}(t)\|^2_{L^2(\Gamma_{\text{Bottom}})^2} \, dt,$$

with Γ_{Bottom} denoting the flat lower boundary of the channel. To obtain a reliable $\bar{\boldsymbol{u}}$ for a test case we performed a forward calculation in a rough channel, where the roughness was described by the function

$$y(x) = -\frac{1}{4} \sin(2\pi x) \cos\left(\frac{17}{20}\pi x\right) m.$$

Furthermore, we chose as time step size $k = 0.01s$ on the time interval $[0, 2s]$ and a spatial discretisation with 18817 nodes, that means an average spatial resolution of $h = 0.03125m$. For the inflow on the boundary part $\{0\} \times (1m, 2m)$ we took the function

$$\boldsymbol{g}_{\text{In}} = -24t(2-t)(y-2)(y-1)\frac{m}{s}$$

and the viscosity parameter $\nu = 1\frac{m^2}{s}$. Hence we have a Reynolds-number $\text{Re} \in [1, 10]$.

The solution process for the optimisation was again performed by the Newton-CG method from Chapter 4, where we used the techniques mentioned in Chapter 3 for the solution of

the PDE subproblems. However, we want to discuss the choice of the parameter and some other specific features.

We want to choose a relatively small regularisation parameter $\alpha = 10^{-4}$. Unfortunately the CG-method is not converging very well for this choice. Hence, we resign solving the linear system up to a certain accuracy in the overall Newton process for the optimisation and only perform a fixed amount of CG steps. The result is a Quasi-Newton method (cf. Remark 4.13). This Quasi-Newton method is applied to a mesh evolution and after each refinement we use the calculated control of the preceding grid as given information $\boldsymbol{q}^\star$ in the regularisation term

$$\frac{\alpha}{2} \int_0^T \|\boldsymbol{q}(t) - \boldsymbol{q}^\star(t)\|^2_{L^2(\Gamma_{\text{Bottom})^2}} \, dt.$$

Hence, the information of the control for a certain regularisation parameter α is kept for the process by the function $\boldsymbol{q}^\star$ and it is even possible to increase the parameter α after each refinement step to guarantee that the Newton residual drops below a prescribed tolerance.

However, we performed three grid refinements for the choice of $\alpha = 10^{-4}$ and stopped the process when the method achieved a Newton residual within the range 10^{-6} to 10^{-5}.

Remark 5.55 (Choice of the Regularisation Parameter).
Here we fix the parameter α since for this example we still stay in the context of optimal control. If we interpret the presented example as an identification problem the question arises how to choose a suitable α to achieve a good trade-off between the fitting of the data term and an appropriate boundary function in the regularisation. We will discuss this question in the next chapter within the scope of the application mentioned in the introduction.

Now we make last statements on the computation of the PDE subproblems. Instead of the boundary semi-linear form $b(\boldsymbol{q};\boldsymbol{u})(\boldsymbol{\varphi})$ in the Weak Formulation 5.50 we will use the stabilised semi-linear form $b^\delta_\mu(\boldsymbol{q};\boldsymbol{u})(\boldsymbol{\varphi})$ from equation (3.24) in Chapter 3.5.1 to even allow very small choices of μ without getting any trouble in the numerical calculation of the PDE subproblems.

The results for a calculation with $\delta = \frac{h}{100}$ and $\mu = 0$ (Nitsche-type formulation) are given in Figures 5.15 and 5.16 for the time points $t = 1$ and $t = 2$. We also performed a Robin control with the parameter setting $\delta = 0$ and $\mu = 0.01$. The results for this setting look almost like in the Nitsche case as we can see in Figure 5.14.

Remark 5.56 (Robin Approach Versus Nitsche Approach).
As we mentioned before the Nitsche approach is a realisation of a Dirichlet control, where $\boldsymbol{q}$ fits $\boldsymbol{u}|_{\Gamma_{Bottom}}$, while in the Robin approach the control function $\boldsymbol{q}$ differs from the restriction of the state solution $\boldsymbol{u}$ on the boundary Γ_{Bottom}, since we have

$$\partial_{\boldsymbol{n}}\boldsymbol{u} - p\boldsymbol{n} = \frac{1}{10^{-2}}(\boldsymbol{q} - \boldsymbol{u}) + \frac{1}{2}(\boldsymbol{u}\cdot\boldsymbol{n})\,\boldsymbol{u}$$

on this boundary part. We visualise this difference in Figure 5.13.

Nevertheless, the state solutions of both approaches are almost equal to each other

$$\frac{\|\boldsymbol{u}_{Robin} - \boldsymbol{u}_{Nitsche}\|_2^2}{\|\boldsymbol{u}_{Nitsche}\|_2^2} \approx 7.4 \cdot 10^{-3}, \qquad \textit{(relative error)}$$

for the particular choice of a small regularisation parameter $\alpha = 10^{-4}$ *(see Figure 5.13). Hence, in the context of identification problems, where we want to minimise the data term*

$$\|S(\boldsymbol{q}) - \boldsymbol{u}\|_{\mathcal{X}}^2$$

by reducing the influence of the regularisation

$$\frac{\alpha}{2}\|\boldsymbol{q} - \boldsymbol{q}^\star\|_{\mathcal{Q}}^2,$$

i. e. by choosing small α*'s, it seems to be more appropriate to work directly with a Robin control formulation, since we obtain almost the same state solution as in the Dirichlet case. Furthermore, we have in this context besides an easy implementation technique also a satisfying theoretical justification of the optimisation problem (see Theorem 5.52).*

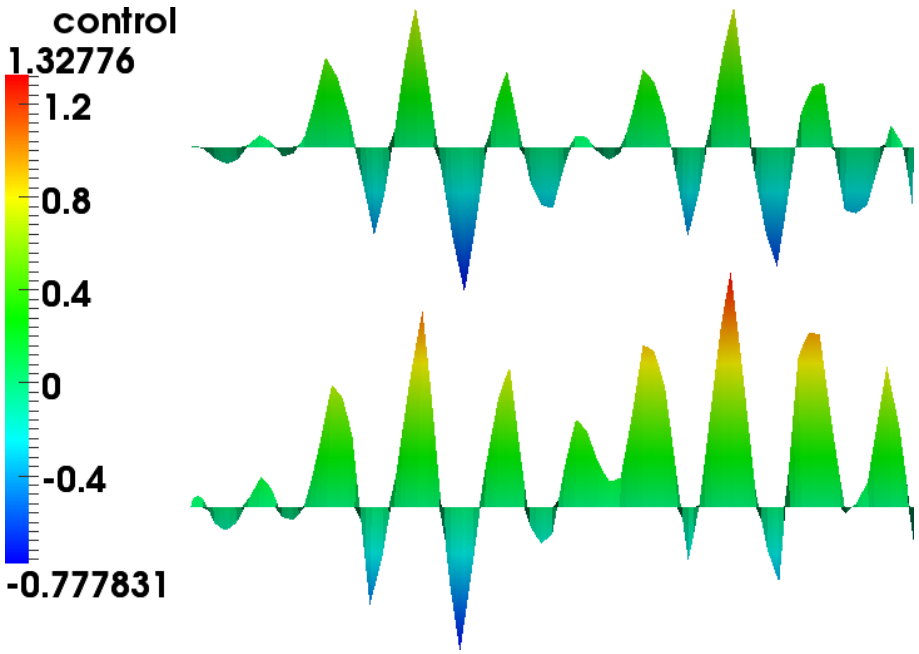

Figure 5.13. The controls on the boundary Γ_{Bottom} at the time point $t = 1$. Upper row: Nitsche control $\boldsymbol{q}_{\text{Nitsche}}$ ($\delta = \frac{h}{100}$ and $\mu = 0$). Lower row: Robin control $\boldsymbol{q}_{\text{Robin}}$ ($\delta = 0$ and $\mu = 10^{-2}$). We see that both controls show clear differences, although the corresponding state solutions looks alike (see Figure 5.14).

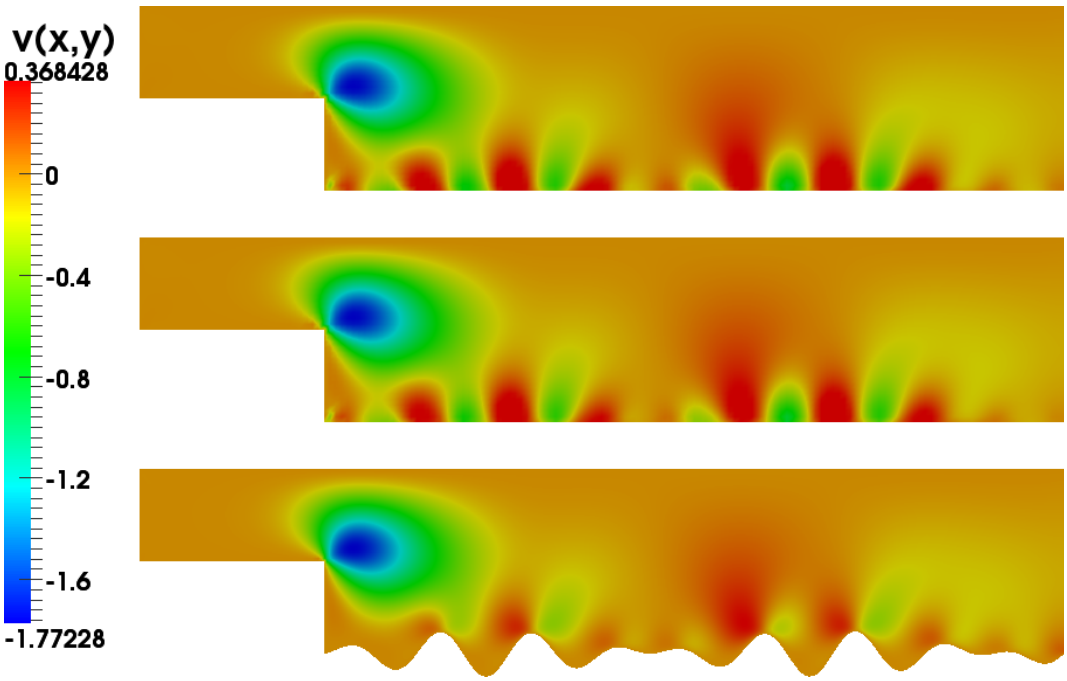

Figure 5.14. Second component of the state solution $\boldsymbol{u}(t, \boldsymbol{x})$ at the time point $t = 1$. Upper row: Approximation $v_h(1, \boldsymbol{x})$ with the the Nitsche control configuration $\delta = \frac{h}{100}$ and $\mu = 0$. Middle row: Approximation with the Robin control configuration $\delta = 0$ and $\mu = 10^{-2}$. Lower row: Second component of the original flow configuration.

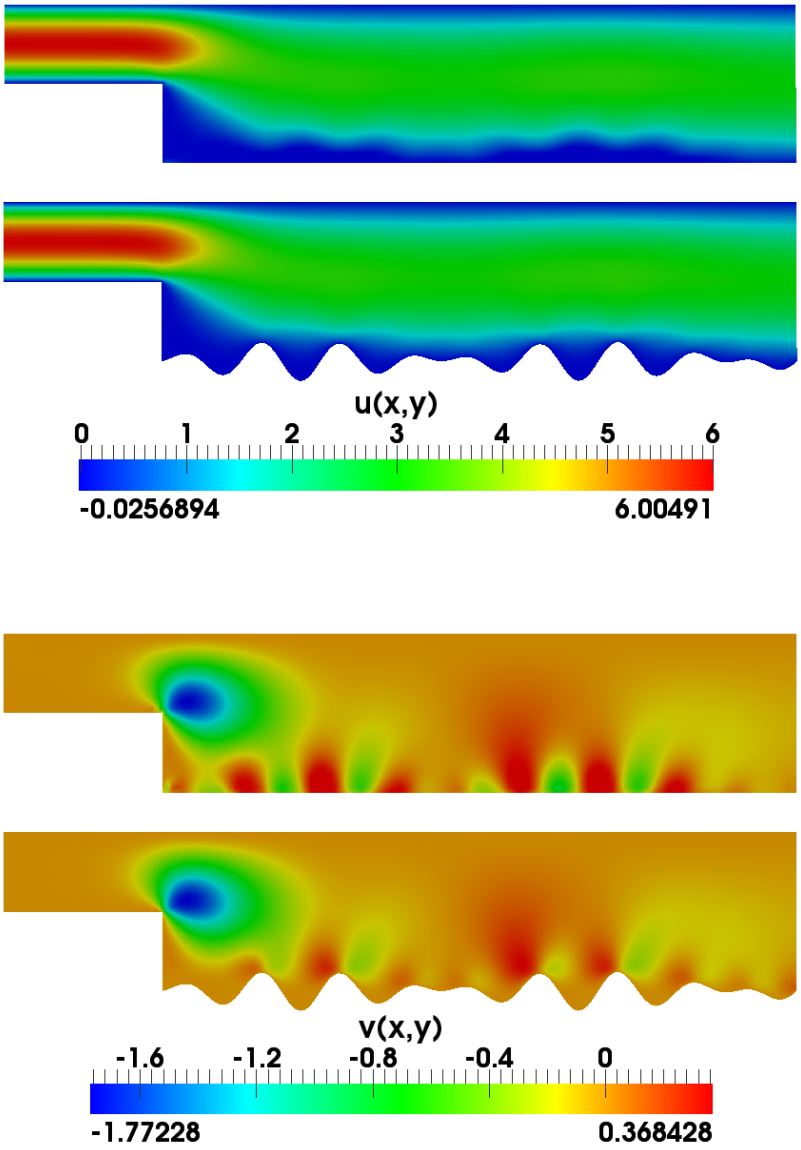

Figure 5.15. Comparison between the boundary control on an even wall to the original configuration at $t = 1$. Nitsche-type control problem $\delta = \frac{h}{100}$ and $\mu = 0$. Upper couple of images: Visualised approximation of the x-component $u(1, \boldsymbol{x})$ of the velocity field $\boldsymbol{u} = (u, v)^T$ (top) versus the original solution in the rough channel (bottom). Lower couple: Same presentation for the y-component of the velocity field.

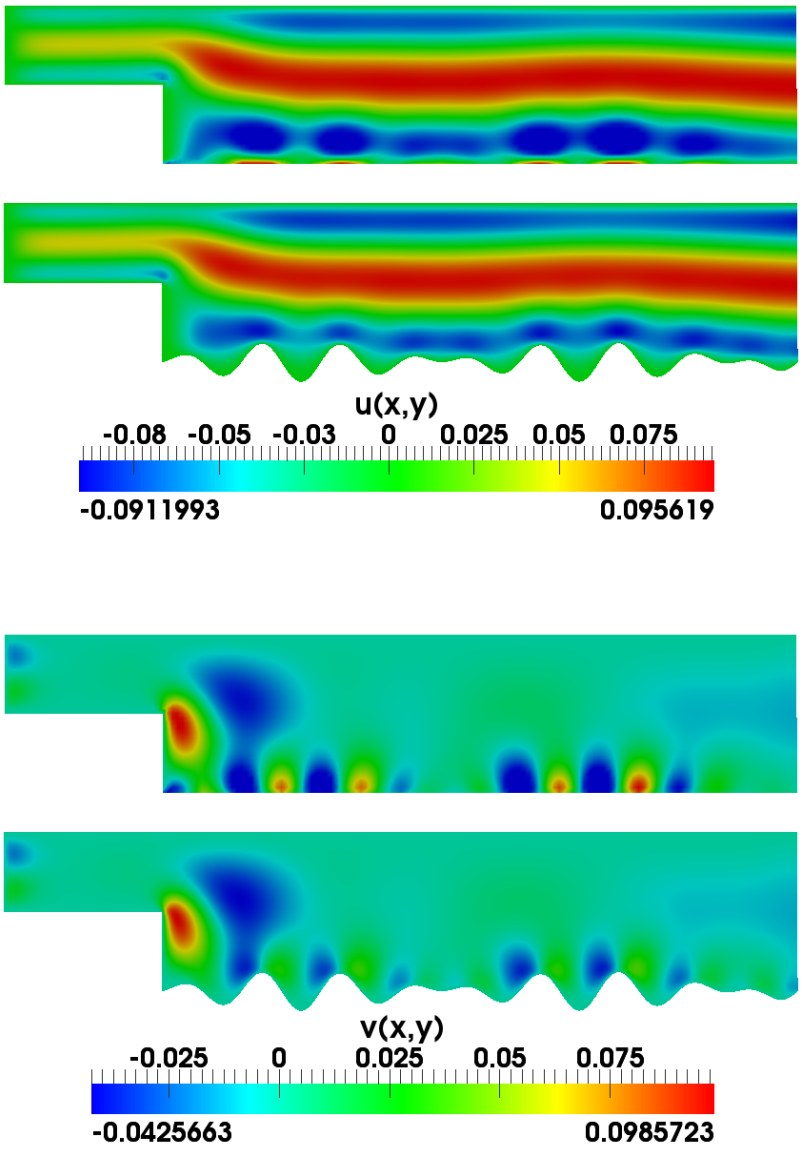

Figure 5.16. Same configuration and presentation as in Figure 5.15 for the time point $t = 2$

6. Boundary Identification for the Observation of a Passive Tracer

All the numerical examples of the last chapter consider a feedback function $\bar{\boldsymbol{u}}$ for the transport field in the data term $\|\boldsymbol{u} - \bar{\boldsymbol{u}}\|_2^2$, which was always assumed to be available by given measurements or simulation data. In this section we will enhance the presented techniques to the complex situation mentioned in the introduction (see Chapter 1) of this thesis.
Available are now only indirect measurements of the fluid flow by information of the behaviour of a passive tracer, which is transported by the unknown flow field. The aim is to recover appropriate boundary conditions which drive the flow that causes the observed distribution of the passive tracer.
In mind we have the application from Chapter 1.2.3, which we want to solve with the approach presented in Optimisation Problem 1.7 in the introduction. In the first section we concretise the mathematical problem by using Robin-type boundary conditions and classify the problem as an inverse problem which is regularised by the boundary control formulation. Afterwards, we formulate the problem weakly and choose appropriate vector spaces. In the third section we present theoretical results, which are also summarised in an article by Klinger [68]. We present then a simple numerical test example for a solution of the developed optimisation problem.
In a further step, we will discuss the choice of the regularisation to be able to cope with a synthetical example. For the investigation of the dependence of the method on the regularisation parameter we restrict the example to a time-independent version.
For this time-independent example we present a heuristic to stop a homotopy method in the regularisation parameter for an appropriate choice of the parameter, which leads to good reconstructions. In this context we can furthermore investigate the influence of the fluid model parameter ν, which is indirect proportional to the Reynolds number describing the fluid flow. We will show that it is possible to estimate this parameter in addition to the boundary identification in a segregation process. Finally we use the developed techniques to solve the time-dependent version of the example and discuss the results.

6.1. Robin-type Boundary Control Problem

We recall the system (1.2):

$$\begin{aligned} \partial_t I - \varepsilon \Delta I + \boldsymbol{u} \cdot \nabla I &= 0, \\ \partial_t \boldsymbol{u} - \nu \Delta \boldsymbol{u} + \boldsymbol{u} \cdot \nabla \boldsymbol{u} + \nabla p &= 0, \qquad \text{in } \ \Omega \times (0,T], \\ \nabla \cdot \boldsymbol{u} &= 0, \end{aligned} \tag{6.1}$$

with the initial conditions

$$I(\boldsymbol{x},0) = I^0(\boldsymbol{x}) \qquad \text{and} \qquad \boldsymbol{u}(\boldsymbol{x},0) = \boldsymbol{u}^0(\boldsymbol{x}), \qquad \text{in } \ \Omega.$$

We assume that no external forces influence the fluid and thus the flow is described only by stating appropriate boundary conditions. In view of the observations of the previous chapters we decided to work directly with Robin-type boundary conditions instead of Dirichlet boundary conditions

$$\begin{aligned} \varepsilon \partial_{\boldsymbol{n}} I &= \frac{1}{\mu_I}\left(q_I - I\right) - \frac{1}{2}\left(\boldsymbol{u}\cdot\boldsymbol{n}\right) I, \qquad \text{on } \ \partial\Omega \times (0,T], \\ \nu \partial_{\boldsymbol{n}} \boldsymbol{u} - p\boldsymbol{n} &= \frac{1}{\mu_{\boldsymbol{u}}}\left(\boldsymbol{q}_{\boldsymbol{u}} - \boldsymbol{u}\right) - \frac{1}{2}\left(\boldsymbol{u}\cdot\boldsymbol{n}\right)\boldsymbol{u}, \qquad \text{on } \ \partial\Omega \times (0,T]. \end{aligned} \tag{6.2}$$

Remember that, for small parameters μ_I and $\mu_{\boldsymbol{u}}$, this represents in principle Dirichlet conditions.

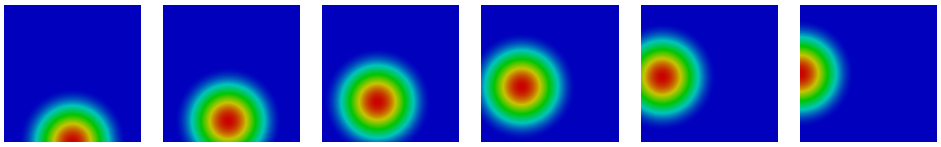

Figure 6.1. Image sequence: $\hat{I} = (\mathcal{I}_k)_{k=1}^6$ for $t_k = 0.04(k-1)$ with $k = 1,\dots,6$ and $T = 0.2$ from left to right.

In the identification problem, which will be considered in the following, we assume that we have temporally discrete brightness intensity functions $\hat{I}$ of a passive tracer. The model for the temporal evolution of the tracer in the fluid is given by the system (6.1). We want to emphasise that we assume that no information of the fluid flow vector field $\boldsymbol{u}$ is available for the identification process.

Example 6.1 (Examples for $\hat{I}$).
We present two examples for intensity functions. In Figure 6.1 we see a bulb function

$$\mathcal{I}_0(\boldsymbol{x}) = \begin{cases} 2\left(1 + \cos\left(\frac{\pi}{r}\right)\sqrt{(x-x_0)^2 + (y-y_0)^2}\right), & \text{for } \sqrt{(x-x_0)^2 + (y-y_0)^2} \le r, \\ 0, & \text{else}, \end{cases} \tag{6.3}$$

which is moved by a solution of the Stokes system, namely

$$\boldsymbol{u} = \kappa\,(-y, x)^T\,, \qquad \text{with } \kappa = \frac{5}{2}\pi.$$

The presented domain shows only the aperture $(0,1) \times (0,1)$*. Hence in- and outflow of the bulb function through the domain boundaries are essential in this example.*

The second example in Figure 6.2 shows the flow of a passive tracer in a benchmark channel with a rough lower boundary as we have mentioned it in Chapter 1.2.3. The geometry for the example is given as in the example in Chapter 3.6, except for a unknown roughness of the lower boundary. The light red area in the pictures represents the observation (or image) domain Ω_O*, which is an aperture of the original domain.*

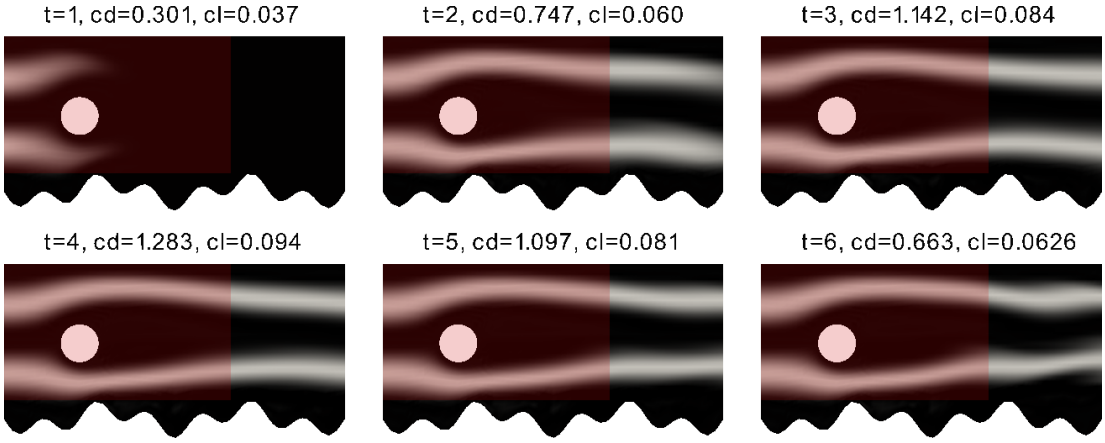

Figure 6.2. Intensity function $\hat{I} := I(\boldsymbol{x}, t)$ of a tracer in a channel with rough lower boundary Ω at the times $t = 1, 2, 3, 4, 5, 6$. The light red colored box is an example for an observation domain Ω_O of the tracer, where nearly no obvious differences in the intensity function can be observed. Thus ambiguities are possible and therefore the boundary identification problem becomes an ill-posed inverse problem.

By $\mathcal{S}$ we denote now the nonlinear solution operator which has the following mapping behaviour:

$$\mathcal{S} : \mathcal{Q}_I \times \mathcal{Q}_{\boldsymbol{u}} \to V_I \qquad \text{and} \qquad \mathcal{S}\,(q_I, \boldsymbol{q_u}) = I(t).$$

Our goal is then to find appropriate q_I and $\boldsymbol{q_u}$ such that $I(t)$ fits to the given data $\hat{I}$. Thus, we will minimise the following data term

$$\|\mathcal{C}\,(q_I, \boldsymbol{q_u}) - \hat{I}\|_M^2,$$

where $\mathcal{C} = \mathcal{M} \circ \mathcal{S}$ with the measurement operator $\mathcal{M} : V_I \to M$, with a vector space M, which has to be specified.

In general this problem is ill-posed, due to the lack of uniqueness or continuous dependence on the data of the solution. Consider therefore the second example illustrated in Figure

6.2, with the observation domain Ω_{O}. The available intensity function $I(t)$ in Ω_{O} is at different time points almost identical, although the flow is drastically changing during the time evolution (see $I(t)$, drag and lift coefficients at $t = 2$, $t = 3$ and $t = 4$). Assuming no knowledge of the functions on the boundary of Ω_{O} it is impossible to reconstruct the correct flow configuration in a unique way. Thus we have to prescribe additional knowledge in form of known boundary conditions (e. g. the rigid walls in the benchmark channel) or estimates or measurements of the functions on the boundary (e. g. $\hat{\boldsymbol{q}}_{\boldsymbol{u}}$).

Even in the case that a unique pair $(q_I, \boldsymbol{q}_{\boldsymbol{u}})$ exists the identification of boundary functions is an inverse problem (see Engl et al. [31]) due to the lack of continuous dependence on the data and we have to regularise the problem in any case. The task is thus:

$$\text{Minimise} \qquad \left\|\mathcal{C}\left(q_I, \boldsymbol{q}_{\boldsymbol{u}}\right) - \hat{I}\right\|_M^2 + \mathcal{R}_\alpha\left(q_I, \boldsymbol{q}_{\boldsymbol{u}}\right), \qquad \text{with respect to } q_I \text{ and } \boldsymbol{q}_{\boldsymbol{u}}.$$

For the theoretical consideration in the next subsections, we concretise this abstract setting. As data term we simply assume a functional of tracking type in the L^2-norm at discrete time points as already mentioned in the introduction. The reason for this choice is the subsequent use of the method for data in form of image sequences, which we assume to have a high spatial and a sparse temporal resolution. For the regularisation we use the famous Tikhonov technique for the distributed boundary functions. We end up with the minimisation of the following cost functional:

$$\begin{aligned} J(I, q_I, \boldsymbol{q}_{\boldsymbol{u}}) = \frac{\zeta}{2} \sum_{j=1}^{N} \|I(t_j) - \mathcal{I}_j\|_2^2 + \frac{\alpha_1}{2} \int_0^T \|q_I(t) - \hat{q}_I(t)\|_{L^2(\partial\Omega)}^2 \, dt \\ + \frac{\alpha_2}{2} \int_0^T \|\boldsymbol{q}_{\boldsymbol{u}}(t) - \hat{\boldsymbol{q}}_{\boldsymbol{u}}(t)\|_{L^2(\partial\Omega)}^2 \, dt, \end{aligned}$$

under the side condition that the functions $I, \boldsymbol{u}$ and p fulfil an appropriate weak formulation of equation (6.1) and (6.2).

6.2. Mathematical Formulation

To discuss the mathematical theory for the problem presented in the last section, we need a concrete mathematical setting, which we formulate now. We define the optimisation problem and the needed spaces and weak formulations.

Optimisation Problem 6.2.
Find

$$\{I, \boldsymbol{u}\} \in L^2\left(0, T; H^1(\Omega)\right) \times L^2\left(0, T; H^1_{\mathrm{div}}(\Omega)^2\right)$$

and

$$\tilde{\boldsymbol{q}} = \{q_I, \boldsymbol{q}_{\boldsymbol{u}}\} \in \mathcal{Q} = \left\{L^2\left(0, T; L^2(\partial\Omega)\right) \times L^2\left(0, T; L^2(\partial\Omega)^2\right)\right\}$$

such that for $\alpha = \alpha_1 = \alpha_2$

$$J(I, \boldsymbol{q}) = \frac{\zeta}{2} \sum_{j=1}^{N} \|I(t_j) - \mathcal{I}_j\|_2^2 + \frac{\alpha}{2} \int_0^T \|\tilde{\boldsymbol{q}}(t)\|_{\mathcal{Q}}^2 \, dt$$

becomes minimal under the side condition that the following weak formulation is fulfilled.

Weak Formulation 6.3.
Find a pair $(I, \boldsymbol{u}) \in L^2\left(0, T; H^1(\Omega)\right) \times L^2\left(0, T; H^1_{\mathrm{div}}(\Omega)^2\right)$ *such that*

$$\int_0^T -\left(I(t), \partial_t \psi(t)\right) + a_I\left(\boldsymbol{u}(t); I(t), \psi(t)\right) + b_I\left(\boldsymbol{u}(t); q_I(t); I(t), \psi(t)\right) \, dt = \left(I^0, \psi(0)\right),$$

$$\int_0^T -\left(\boldsymbol{u}(t), \partial_t \boldsymbol{\varphi}(t)\right) + a_{\boldsymbol{u}}\left(\boldsymbol{u}(t)\right)\left(\boldsymbol{\varphi}(t)\right) + b_{\boldsymbol{u}}\left(\boldsymbol{q}_{\boldsymbol{u}}(t); \boldsymbol{u}(t)\right)\left(\boldsymbol{\varphi}(t)\right) \, dt = \left(\boldsymbol{u}^0, \boldsymbol{\varphi}(0)\right)$$

is fulfilled for all

$$\psi \in \mathcal{X}_I := \left\{ \psi : \psi \in L^2\left(0, T; H^1(\Omega)\right) \text{ and } \partial_t \psi \in L^2\left(0, T; \left(H^1(\Omega)\right)'\right) \right\},$$

$$\boldsymbol{\varphi} \in \mathcal{X}_{\boldsymbol{u}} := \left\{ \boldsymbol{\varphi} : \boldsymbol{\varphi} \in L^2\left(0, T; H^1_{\mathrm{div}}(\Omega)^2\right) \text{ and } \partial_t \boldsymbol{\varphi} \in L^2\left(0, T; \left(H^1_{\mathrm{div}}(\Omega)^2\right)'\right) \right\}$$

and with the semi- and bilinear forms

$$\begin{aligned}
a_I(\boldsymbol{u}; I, \psi) &:= \varepsilon\left(\nabla I, \nabla \psi\right) + \left(\boldsymbol{u} \cdot \nabla I, \psi\right), \\
a_{\boldsymbol{u}}\left(\boldsymbol{u}\right)\left(\boldsymbol{\varphi}\right) &:= \nu\left(\nabla \boldsymbol{u}, \nabla \boldsymbol{\varphi}\right) + \left(\boldsymbol{u} \cdot \nabla \boldsymbol{u}, \boldsymbol{\varphi}\right), \\
b_I(\boldsymbol{u}; q_I; I, \psi) &:= \frac{1}{\mu_I} \left\langle I - q_I, \psi \right\rangle_{\partial\Omega} - \frac{1}{2} \left\langle \left(\boldsymbol{u} \cdot \boldsymbol{n}\right) I, \psi \right\rangle_{\partial\Omega}, \\
b_{\boldsymbol{u}}(\boldsymbol{q}_{\boldsymbol{u}}; \boldsymbol{u})(\boldsymbol{\varphi}) &:= \frac{1}{\mu_{\boldsymbol{u}}} \left\langle \boldsymbol{u} - \boldsymbol{q}_{\boldsymbol{u}}, \boldsymbol{\varphi} \right\rangle_{\partial\Omega} - \frac{1}{2} \left\langle \left(\boldsymbol{u} \cdot \boldsymbol{n}\right) \boldsymbol{u}, \boldsymbol{\varphi} \right\rangle_{\partial\Omega}.
\end{aligned}$$

6.3. Theoretical Results

In this section we will prove the existence of solutions of the presented optimisation problem. We will proceed in two steps. First, we prove existence of unique solutions of the Weak Formulation 6.3. In a second step we can by the existence of solutions of the system prove the existence of minimisers of the optimisation problem. We following the argumentation presented in Klinger [68].

Theorem 6.4 (Existence and Uniqueness (Weak Formulation 6.3)).
For fixed parameters μ_I *and* $\mu_{\boldsymbol{u}}$ *in* $(0, 1]$ *and given boundary functions* q_I *and* $\boldsymbol{q}_{\boldsymbol{u}}$ *with the above required regularity there exists a unique solution pair*

$$\{I_{\mu_I}, \boldsymbol{u}_{\mu_{\boldsymbol{u}}}\} \in L^2(0, T; H^1(\Omega)) \times L^2(0, T; H^1_{\mathrm{div}}(\Omega)^2).$$

Proof. The following proof is a combination of the techniques in the proofs of Theorem 2.20 in Chapter 2.4 and Theorem 5.42 in Chapter 5.3.

By Theorem 5.42 we have the existence of a unique solution

$$\boldsymbol{u}_{\mu_{\boldsymbol{u}}} \in L^2(0,T;H^1_{\mathrm{div}}(\Omega)^2).$$

In the first lines of the proof of Theorem 5.21 we argue that for such a solenoidal transport field (see Remark 5.19) the convection-diffusion equation with a Robin boundary condition admits also a unique solution

$$I_{\mu_I} \in L^2(0,T;H^1(\Omega)) \cap L^\infty(0,T;L^2(\Omega))$$

by the standard Galerkin technique. We skip now the indices μ_I and $\mu_{\boldsymbol{u}}$ for abbreviation. To sum up we have shown the existence of at least one solution pair $\{I,\boldsymbol{u}\}$, since the system is nonlinear, due to the dependence of the function I on the velocity field $\boldsymbol{u}$.

We have to prove that $\{I,\boldsymbol{u}\}$ is the only solution pair. Therefore we assume as usual the existence of two possible solutions $\{I,\boldsymbol{u}\}$ and $\{\tilde{I},\tilde{\boldsymbol{u}}\}$ for the same data $\varepsilon,\nu,\mu_I,\mu_{\boldsymbol{u}},q_I$ and $\boldsymbol{q}_{\boldsymbol{u}}$. The difference of these solutions is denoted by the variables $\boldsymbol{w}=\boldsymbol{u}-\tilde{\boldsymbol{u}}$ and $K=I-\tilde{I}$.

Since the Navier-Stokes part of the system is completely independent of the intensity function, we can argue as in the proof of Theorem 5.51 and obtain that $\boldsymbol{w}$ is almost everywhere equal to zero. Thus $\boldsymbol{u}=\tilde{\boldsymbol{u}}$ almost everywhere and the difference of the first part of the system is

$$(\partial_t K,\psi)+\varepsilon\,(\nabla K,\nabla\psi)+\frac{1}{\mu_I}\,\langle K,\psi\rangle_{\partial\Omega}+(\boldsymbol{u}\cdot\nabla K,\psi)=0.$$

The uniqueness follows then directly by testing with $\psi=K$ and using Remark 5.19. □

Now we are able to prove the existence of a solution of the optimization problem. Therefore we assume for brevity $\mu := \mu_I = \mu_{\boldsymbol{u}}$. However, the proof is also working in the general case.

Theorem 6.5 (Solution of Optimisation Problem 6.2).
For a fixed $\mu\in(0,1]$ we have the existence of at least one minimiser

$$\begin{aligned}
I_\mu &\in L^2\left(0,T;H^1(\Omega)\right),\\
\boldsymbol{u}_\mu &\in L^2\left(0,T;H^1_{\mathrm{div}}(\Omega)^2\right),\\
q_{I,\mu} &\in L^2\left(0,T;L^2(\partial\Omega)\right),\\
\boldsymbol{q}_{\vec{u},\mu} &\in L^2\left(0,T;L^2(\partial\Omega)^2\right)
\end{aligned}$$

of Optimisation Problem 6.2.

Proof. The proof works analogously to the one of Theorem 5.52. Thanks to the last theorem of this section we have the existence of solutions of the state equation and therefore the admissible set is not empty.

We skip the index μ for abbreviation, set $\boldsymbol{q} = \{q_I, \boldsymbol{q_u}\}$ and choose then a minimising sequence

$$\{I^{(k)}, \boldsymbol{u}^{(k)}, \boldsymbol{q}^{(k)}\}$$

in the admissible set with the property

$$\lim_{k\to\infty} J(I^{(k)}, \boldsymbol{q}^{(k)}) = \inf_{\{I,\boldsymbol{u},\boldsymbol{q}\}} J(I, \boldsymbol{q}) =: \theta.$$

By the same arguments as in the mentioned proof of Theorem 5.52 we can find a uniform bound of the form

$$\|\boldsymbol{q}^{(k)}\|_{L^2(0,T;L^2(\partial\Omega)^3)} \leq B.$$

Hence, the control components are bounded in $L^2\left(0,T;L^2(\partial\Omega)\right)$ and by the energy estimates (5.24) and (5.51) we receive all necessary uniform bounds for $I^{(k)}$ and $\boldsymbol{u}^{(k)}$:

$$\begin{aligned} I^{(k)} &\in L^\infty(0,T;L^2(\Omega)) \cap L^2(0,T;H^1(\Omega)) \cap L^2(0,T;L^2(\partial\Omega)),\\ \boldsymbol{u}^{(k)} &\in L^\infty(0,T;L^2(\Omega)^2) \cap L^2(0,T;H^1_{\mathrm{div}}(\Omega)^2) \cap L^2(0,T;L^2(\partial\Omega)^2). \end{aligned}$$

We can then extract the following subsequences

$$\begin{aligned} I^{(k')} &\rightharpoonup I \quad \text{weakly in } L^2(0,T;H^1(\Omega)), \quad \text{weakly-}\star \text{ in } L^\infty(0,T;L^2(\Omega)) \quad \text{as } k'\to\infty,\\ &\qquad \text{weakly in } L^2(0,T;L^2(\partial\Omega)),\\ \boldsymbol{u}^{(k')} &\rightharpoonup \boldsymbol{u} \quad \text{weakly in } L^2(0,T;H^1_{\mathrm{div}}(\Omega)^2), \quad \text{weakly-}\star \text{ in } L^\infty(0,T;L^2(\Omega)^2) \quad \text{as } k'\to\infty,\\ &\qquad \text{weakly in } L^2(0,T;L^2(\partial\Omega)^2). \end{aligned}$$

By compactness results we obtain again the strong convergence

$$I^{(k')} \to I \quad \text{in } L^2(0,T;L^2(\Omega)), \quad \boldsymbol{u}^{(k')} \to \boldsymbol{u} \quad \text{in } L^2(0,T;L^2(\Omega)^2)$$

of a subsequence.

Passing to the limit in the state equation is then a standard task. The only thing that remains to be shown is the optimality, which is obtained as in the proof of Theorem 5.42, due to the convergence properties and the fact that the regularisation term is again convex and continuous and therefore weakly lower semicontinuous. □

Remark 6.6 (Connection to Dirichlet-Controls for $\mu \to 0$).
In the last chapter we discussed how the Robin-type controls are connected to Dirichlet controls in the case of convection-diffusion equations or the Navier-Stokes system. The access to this connection was always that we were able to formulate an appropriate very weak problem. In the above example such a very weak formulation is hard to find, since we know that a solution $\boldsymbol{u}(t)$ of the very weakly formulated Navier-Stokes equations is only in $L^4(\Omega)^2$ (see Remark 5.40). However, this regularity for the velocity field is far

too weak to formulate the convection-diffusion equation very weakly in the sense of the Weak Formulation 5.17. Since for the following boundary identification problems it is not necessary to work with a Dirichlet-control formulation, we postpone a further theoretical investigation of the connection between the mentioned approach and Dirichlet-controls to future work.

Example 6.7 (Simple Test Case for low Reynolds-Numbers).
We will at first consider a very simple example, which will not accommodate to the inherent dynamic behaviour of the Navier-Stokes system, but emphasise that the method is able to reconstruct the transport of a signal across the boundary.

Therefore, we recall the sequence of brightness functions in Figure 6.1 of Example 6.1. The computational and observation domain is $\Omega = [0,1] \times [0,1]$. *The time interval is given by* $(0, 0.2]$. *Furthermore, we choose*

$$\hat{q}_I = 0, \qquad \hat{\boldsymbol{q}}_{\boldsymbol{u}} = (0,0)^T, \qquad \zeta = 1, \qquad \varepsilon = 10^{-10}, \qquad \nu = 1$$

for the state equations.

The sequence $\mathcal{I}_k(\boldsymbol{x})$ *of intensity functions documents the movement of a bulb signal by a given analytic solenoidal function. It was generated by setting*

$$\mathcal{I}_k = \hat{I}(t_k), \qquad t_k = 0.04(k-1), \qquad \text{for } k = 1, \dots, 6$$

of a solution $\hat{I}$ *of the equation*

$$\begin{aligned} \partial_t \hat{I} + \boldsymbol{\beta} \cdot \nabla \hat{I} &= 0, && \text{in } [0,1]^2 \times (0, 0.2], \\ \hat{I}(\boldsymbol{x}, 0) &= I_0(\boldsymbol{x}), && \text{in } [0,1]^2, \end{aligned}$$

with $\boldsymbol{\beta} = \frac{5}{2}\pi(-y, x)^T$ *and appropriate boundary conditions.*

For the reconstruction we solved the Optimisation Problem 6.2 with the Newton-CG method presented in Chapter 4. Since the CG method is not converging very well for small parameters α we apply an inexact Newton method (cf. Remark 4.13), by performing only a bunch of CG steps. We stop the Newton-type method if the residual drops below 10^{-5}.

Furthermore, we start the computation with setting the initial transport field $\boldsymbol{u}^0 = (-2, 2)^T$, since we observe by the image sequence that the signal is moving from the center of the bottom boundary to the center of the left boundary.

For further stabilisation reasons we perform moreover a homotopy method in α. We start with a large α and solve the optimisation problem. Afterwards we use the solution as an initial value for a further solve of the optimisation problem with a reduced α. We loop this procedure a few times (3-5 steps) until $\alpha \approx 10^{-3}$. Essential for the process is the choice of the parameters μ_I and $\mu_{\boldsymbol{u}}$ for the Robin-type boundary conditions. However, we also want

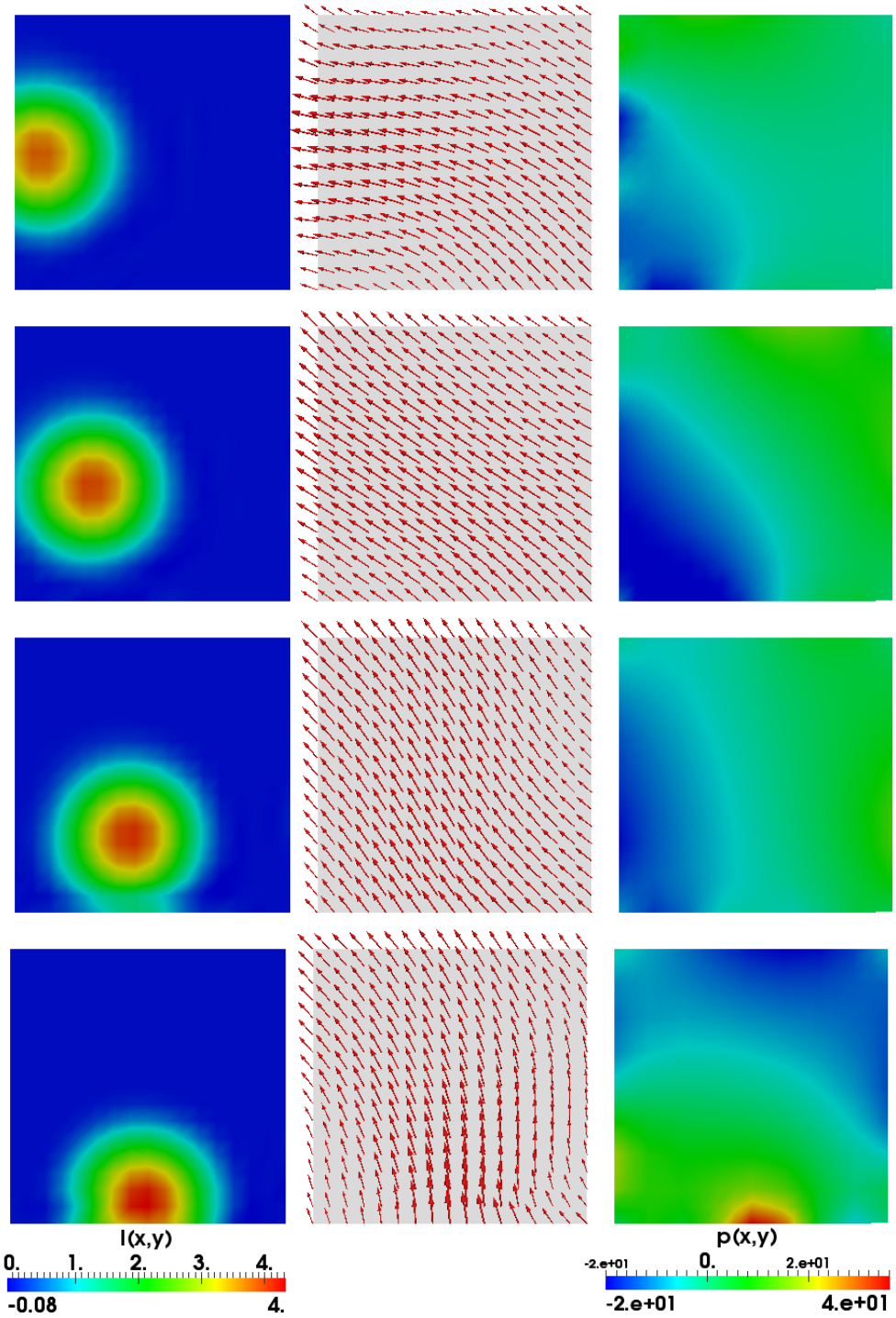

Figure 6.3. Calculated Solution for $\alpha \approx 10^{-3}$. Left column: From bottom to top: $I(\vec{x}, t_k)$ with $t_k = \frac{kT}{8}$ and $k = 1, 3, 5, 7$. Middle column: Corresponding transport field. Right column: Corresponding pressure function.

Table 6.1. Error: $e_{h,k} := \|I - I_{h,k}\|^2_{L^2(\Omega\times[0,2])}$. The expected brightness function has the following norm $g := \|I\|^2_{L^2(\Omega\times[0,2])} = 2.454 \cdot 10^{-1}$.

Case	$e_{h,k}$	Rel. Error ($\frac{e_{h,k}}{g}$)
1	$1.735 \cdot 10^{-3}$	0.71%
2	$7.976 \cdot 10^{-4}$	0.33%
3	$6.205 \cdot 10^{-4}$	0.25%
4	$5.616 \cdot 10^{-4}$	0.23%
5	$5.346 \cdot 10^{-4}$	0.22%

to investigate the connection to Dirichlet controls. Therefore, we use the boundary forms developed in Chapter 3.3

$$\begin{aligned} b(q_I; I, \psi) := &- \frac{\varepsilon\delta_I}{\mu_I + \delta_I} \left(\langle \partial_{\boldsymbol{n}} I, \psi \rangle_{\partial\Omega} + \langle I - q_I, \partial_{\boldsymbol{n}}\psi \rangle_{\partial\Omega} \right) + \frac{1}{\mu_I + \delta_I} \langle I - q_I, \psi \rangle_{\partial\Omega} \\ &- \frac{\varepsilon\mu_I\delta_I}{\mu_I + \delta_I} \langle \partial_{\boldsymbol{n}} I, \partial_{\boldsymbol{n}}\psi \rangle_{\partial\Omega} - \frac{\mu_I}{2(\mu_I + \delta_I)} \langle (\boldsymbol{u}\cdot\boldsymbol{n}) I, \psi \rangle_{\partial\Omega} \\ &+ \frac{\delta_I\mu_I}{2(\mu_I + \delta_I)} \langle (\boldsymbol{u}\cdot\boldsymbol{n}) I, \partial_{\boldsymbol{n}}\psi \rangle_{\partial\Omega} \end{aligned}$$

for the convection-diffusion part of system (6.1) and from Chapter 3.5.1

$$\begin{aligned} b(\boldsymbol{q_u}; \boldsymbol{u})(\boldsymbol{\varphi}) := &- \frac{\delta_{\boldsymbol{u}}}{\mu_{\boldsymbol{u}} + \delta_{\boldsymbol{u}}} \left(\langle \nu\partial_{\boldsymbol{n}}\boldsymbol{u} - p\boldsymbol{n}, \boldsymbol{\varphi} \rangle_{\partial\Omega} + \langle \boldsymbol{u} - \boldsymbol{q_u}, \nu\partial_{\boldsymbol{n}}\boldsymbol{\varphi} + \xi\boldsymbol{n} \rangle_{\partial\Omega} \right) \\ &+ \frac{1}{\mu_{\boldsymbol{u}} + \delta_{\boldsymbol{u}}} \langle \boldsymbol{u} - \boldsymbol{q_u}, \boldsymbol{\varphi} \rangle_{\partial\Omega} - \frac{\mu_{\boldsymbol{u}}}{2(\mu_{\boldsymbol{u}} + \delta_{\boldsymbol{u}})} \langle (\boldsymbol{u}\cdot\boldsymbol{n})\boldsymbol{u}, \boldsymbol{\varphi} \rangle_{\partial\Omega} \\ &- \frac{\delta_{\boldsymbol{u}}\mu_{\boldsymbol{u}}}{\delta_{\boldsymbol{u}} + \mu_{\boldsymbol{u}}} \langle \nu\partial_{\boldsymbol{n}}\boldsymbol{u} - p\boldsymbol{n}, \nu\partial_{\boldsymbol{n}}\boldsymbol{\varphi} + \xi\boldsymbol{n} \rangle_{\partial\Omega} \\ &+ \frac{\delta_{\boldsymbol{u}}\mu_{\boldsymbol{u}}}{2(\delta_{\boldsymbol{u}} + \mu_{\boldsymbol{u}})} \langle (\boldsymbol{u}\cdot\boldsymbol{n})\boldsymbol{u}, \nu\boldsymbol{\varphi} + \xi\boldsymbol{n} \rangle_{\partial\Omega} \end{aligned}$$

for the Navier-Stokes part. We compare then the cases:

$$\begin{aligned} &\delta_I = \delta_{\boldsymbol{u}} = 0, && \mu_I = \mu_{\boldsymbol{u}} = 1, && \text{(Case 1)}, \\ &\delta_I = \delta_{\boldsymbol{u}} = 0, && \mu_I = \mu_{\boldsymbol{u}} = 0.1, && \text{(Case 2)}, \\ &\delta_I = \delta_{\boldsymbol{u}} = 0, && \mu_I = \mu_{\boldsymbol{u}} = h, && \text{(Case 3)}, \\ &\delta_I = \begin{cases} -\frac{1}{(\boldsymbol{u}\cdot\boldsymbol{n})}, & \boldsymbol{u}\cdot\boldsymbol{n} < 0 \\ 0, & \boldsymbol{u}\cdot\boldsymbol{n} \geq 0 \end{cases}, \delta_{\boldsymbol{u}} = \frac{h}{5}, && \mu_I = \mu_{\boldsymbol{u}} = 0, && \text{(Case 4)}, \\ &\delta_I = \begin{cases} -\frac{1}{(\boldsymbol{u}\cdot\boldsymbol{n})}, & \boldsymbol{u}\cdot\boldsymbol{n} < 0 \\ 0, & \boldsymbol{u}\cdot\boldsymbol{n} \geq 0 \end{cases}, \delta_{\boldsymbol{u}} = 0, && \mu_I = 0,\ \mu_{\boldsymbol{u}} = h, && \text{(Case 5)} \end{aligned}$$

in Table 6.1.

The first three cases are Robin-type conditions, which fits to the Weak Formulation 6.3. Thus the theory developed in the last section is applicable. The fourth case considers weakly imposed Dirichlet data in the sense of equation (3.9) for the convection-diffusion part and equation (3.24) for the Navier-Stokes part of the system (see Chapter 3). We want to emphasise that we have no theoretical justification for this method. The fifth case is a combination of the cases before.

The result of the calculation for Case 3 is visualised in Figure 6.3. We see that the method is able to recover the movement of the signal.

As Table 6.1 indicates all parameter choices lead to a good interpolation of the original signal transport. We have for larger μ a bigger error, since we observe several artefacts of the signal on the inflow boundary as the signal enters the computational domain (see Cases 1-3). This is for small choice of μ_I and $\mu_{\boldsymbol{u}}$ or the Dirichlet boundaries (Case 4) not the case.

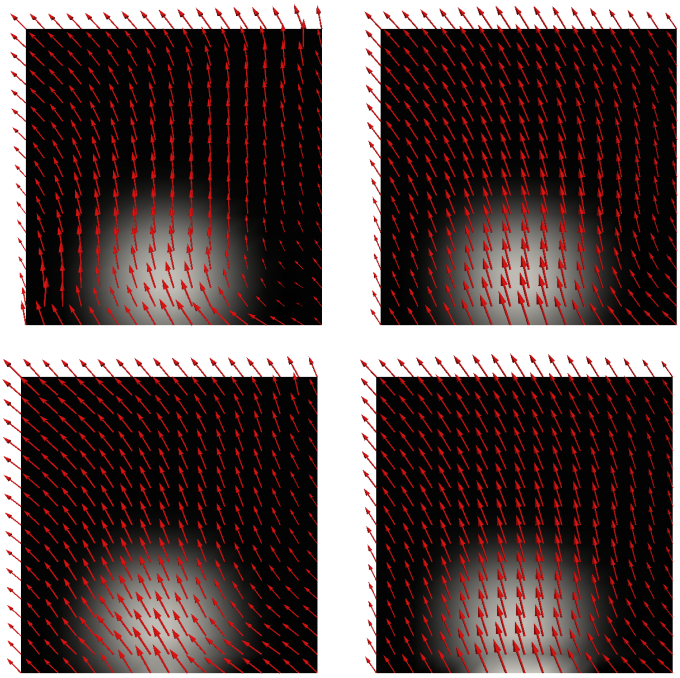

Figure 6.4. Top: $t = 0.04$. Bottom: $t = 0.0425$. Left Column: Transport field for the weak Dirichlet boundary control. Right Column: Transport field for the Robin-type control approach with $\mu_1 = \mu_2 = 0.1$. The left transport field is immediately changing and has therefore a kink in the time variable.

However, in the Dirichlet case (Case 4) we observe kinks of the transport field in the time points, where image information is available as Figure 6.4 indicates for $t_1 = 0.004$. The left

column shows two consecutive time steps (from top to bottom) for the transport vector field in the Dirichlet case and the right column shows the same for Robin-type boundary controls with $\mu_I = \mu_{\boldsymbol{u}} = 0.1$.

This effect can be avoided by using for the Navier-Stokes part of the coupled system the Robin-type prescription of the boundary controls (e. g. with $\mu_{\boldsymbol{u}} = h$) and for the transport equation we use the weakly imposed Dirichlet conditions (see Case 5).

Remark 6.8 (Dynamic Behaviour).
The presented example does not need the fully nonlinear Navier-Stokes equation in our coupled system, since the dynamic which is usually introduced by the nonlinear term has no effect on the presented flow scenarios. Nevertheless, we choose them as a proof of concept for the possibility of the coupled estimation of the flow field boundaries and the boundary conditions of the intensity function.

In a next step we will investigate flows with higher Reynolds numbers, where the use of the fully nonlinear Navier-Stokes system has an effect to the process. Before doing so, we will shortly comment on a few algorithmic aspects, especially on the choice of the regularisation parameter in the context of boundary identification.

6.4. Algorithmic Aspects: Brief Overview of Parameter Choice Techniques

The presented examples of the last subsection are problematic in that they can hardly be calculated for small regularisation parameters α, due to the ill-posed character of the boundary identification problem. Even if we use a homotopy method in α we need a growing amount of Newton-type steps to reduce the residual below a given tolerance, as we decrease α. Our aim is therefore to present in this subsection heuristic techniques for the choice of appropriate regularisation parameters.

Thus, we start by recalling the abstract setting of the Optimisation Problem 6.2

$$\min_{\tilde{\boldsymbol{q}} \in \mathcal{Q}} \left(\|\mathcal{S}(\tilde{\boldsymbol{q}}) - \hat{I}\|_M^2 + \alpha \|\tilde{\boldsymbol{q}} - \hat{\boldsymbol{q}}\|_{\mathcal{Q}}^2 \right), \tag{6.4}$$

with the solution operator S and two norms defined as

$$\|I\|_M^2 := \frac{\zeta}{2} \sum_{j=1}^{N} \|I(t_j)\|_2^2 \qquad \text{and} \quad \|q\|_{\mathcal{Q}}^2 := \frac{1}{2} \int_0^T \|\boldsymbol{q}\|_{L^2(\partial\Omega)^2}^2 \, dt.$$

The problem (6.4) is the Tikhonov regularisation of the nonlinear inverse problem

$$\mathcal{S}(\tilde{q}) = \hat{I}.$$

In our particular case the ill-posed character comes from two sources:

1. Uniqueness: For example assume the two intensity functions

$$I_1(\boldsymbol{x},0) = \begin{cases} 2\left(1+\cos\left(\frac{\pi}{0.2}\right)\bar{a}\right), & \text{for } \bar{a} := \sqrt{(x-0.5)^2+(y-0.25)^2} \leq 0.2, \\ 0, & \text{else}, \end{cases}$$

$$I_2(\boldsymbol{x},1) = \begin{cases} 2\left(1+\cos\left(\frac{\pi}{0.2}\right)\bar{b}\right), & \text{for } \bar{b} := \sqrt{(x-0.5)^2+(y-0.75)^2} \leq 0.2, \\ 0, & \text{else}. \end{cases}$$

We set $\varepsilon = 0$ and $\nu = 1$ in system (6.1). For the boundary conditions we choose

$$I(\boldsymbol{x},t) = 0, \qquad \boldsymbol{u}(\boldsymbol{x},t) = (2n-1)\pi\,(0.5-y, x-0.5)^T, \qquad \text{on } \partial\Omega.$$

The Navier-Stokes part of the system has the (analytic) solutions

$$u(\boldsymbol{x},t) = (2n-1)\pi(0.5-y, x-0.5)^T,$$
$$p(\boldsymbol{x},t) = -\frac{(2n-1)^2\pi^2}{2}\left(x-x^2+y-y^2-\frac{1}{3}\right),$$

assuming that the initial conditions u^0 is choosen appropriate and the pressure is normalised by $\int_\Omega p(\boldsymbol{x},t)\,d\boldsymbol{x} = 0$ for all $t \in [0,T]$.

This solution transports the initial brightness function $I_1(\boldsymbol{x},0)$ for any $n \in \mathbb{N}$ to the final signal $I_2(\boldsymbol{x},T)$ by the linear transport equation in system (6.1). That means that on the mere basis of the two intensity functions, we cannot find a unique vector field which transported the intensity signal in the observation domain.

Remark 6.9 (Selecting a Solution).
Although we are able to calculate a solution for the Optimisation Problem 6.2 (see Example 6.7) we have to be very careful trusting our results. Without further prior knowledge it is always doubtful that the estimated flow field represents the vector field which transported the signal originally.

As mentioned for example in Engl et al. [31] one can use further information for $\hat{\boldsymbol{q}}$ to select a certain solution out of a variety of different solutions. Furthermore, we may restrict the number of possible solutions by using more information, if available, about the domain geometry. If further informations of the flow field itself for example in an aperture of the observation domain is available they can also be used to achieve a better approximation of the "real" flow field.

2. The solution does not depend continuously on the data, which means that the numerical method for the solution process becomes unstable.

The structure of problem (6.4) accommodates this fact. For increasing α the regularisation dominates and makes the numerical process stable, but the minimisation process leads to

$$\|\tilde{\boldsymbol{q}} - \hat{\boldsymbol{q}}\|_{\mathcal{Q}}^2 \to 0 \qquad \Rightarrow \qquad \tilde{\boldsymbol{q}} \approx \hat{\boldsymbol{q}}.$$

However, the approximation of a solution could be bad in terms of the data term

$$\|\mathcal{S}(\hat{\boldsymbol{q}}) - \hat{I}\|_M^2 =: \mathrm{err}(\hat{\boldsymbol{q}}),$$

with an error $\mathrm{err}(\hat{\boldsymbol{q}})$, which is maybye very big.

Decreasing α makes the method more unstable, while the fitting term is much smaller, and thus the approximation error for noise free data $\hat{I}$ tends to zero. Hence α deals as a knob to adjust a good trade-off between the opposed proposition of approximation accuracy and stability of the numerical process (see also Engl et al. [31]).

A first step for stabilising the numerical solution of the optimisation problem was mentioned in Example 6.7, where we used a homotopy method in α. However, in many applications $\hat{I}$ is not given as an analytic function. We have to take into account errors introduced by approximations or interpolations of possibly even defective measurement data. In the literature these error sources are collected by the term "noise" and the noise level is denoted by δ. We have for the disturbed measurement function $\hat{I}^\delta$ then the relation

$$\|\hat{I} - \hat{I}^\delta\|_\Sigma \leq \delta$$

in a norm which has to be specified.

As mentioned in the second point, the choice of α is crucial for calculating good approximations for inverse problems. Due to this fact it is no suprise that it is a very attractive topic in modern inverse problem literature. It is beyond the scope of this thesis to present all possible directions and developments. We will only give a brief prospect of possible directions for investigations and available techniques. Two fundamental directions are a-priori and a-posteriori choice rules. The latter is often based on the Mozorov discrepancy principle

$$\|\mathcal{S}(\boldsymbol{q}_\alpha^\delta) - \hat{I}^\delta\|_M = \tau\delta, \qquad \text{with} \quad \tau \geq 1, \tag{6.5}$$

which can then be used to calculate α. In the case of PDE constrained optimisation this was done for example by Griesbaum et al. [43] and for nonlinear problems by Kaltenbacher et al. [64]. They use a Newton method to solve the root finding problem in equation (6.5).

The discrepancy principle can furthermore be used as stopping criterion for iterated Tikhonov methods. The iterated Tikhonov method for nonlinear inverse problems is for example described in Scherzer [95]. In this method we calculate at first a regularised solution $\tilde{\boldsymbol{q}}_\alpha^1 := \tilde{\boldsymbol{q}}$, and afterwards we compute successively the n-th iterate $\tilde{\boldsymbol{q}}_\alpha^n$ by

$$\tilde{\boldsymbol{q}}_\alpha^n = \operatorname*{argmin}_{\tilde{\boldsymbol{q}} \in \mathcal{Q}} \left(\|\mathcal{S}(\tilde{\boldsymbol{q}}) - \hat{I}\|_M^2 + \alpha \|\tilde{\boldsymbol{q}} - \tilde{\boldsymbol{q}}_\alpha^{n-1}\|_{\mathcal{Q}}^2 \right).$$

The method stops if equation (6.5) is in some sense fulfilled. The method represents a stable way of estimating as good as possible a solution as long as the noise level δ is available. We want to emphasise that this method is different to the mentioned homotopy method for the Example 6.7, since the old control function is here entering the cost functional directly in the regularisation term.

All these iterative methods suffer of course from the fact that the optimisation problem must be solved in each iteration. Especially in the case of PDE constrained optimisation with a time-dependent nonlinear and coupled PDE system as constraint like the one in equation (6.1) this procedure is very expensive, as long as the convergence rate in α is too small.

A suggestion for accelerating the convergence process is the non-stationary iterated Tikhonov method, which adapts the regularisation parameter in each iteration of the iterated Tikhonov method. Here the functional reads

$$\tilde{\boldsymbol{q}}_\alpha^n = \underset{\tilde{\boldsymbol{q}}\in\mathcal{Q}}{\operatorname{argmin}} \|\mathcal{S}(\tilde{\boldsymbol{q}}^{n-1}) - \hat{I}^\delta + \mathcal{S}'(\tilde{\boldsymbol{q}}^{n-1})\left(\tilde{\boldsymbol{q}} - \tilde{\boldsymbol{q}}^{n-1}\right)\|_M^2 + \alpha_n \|\tilde{\boldsymbol{q}} - \tilde{\boldsymbol{q}}^{n-1}\|_{\mathcal{Q}}^2$$

and is also known as Levenberg-Marquardt method. For example Hanke [48] describes how the method can be applied to nonlinear PDE based inverse problems.

Calculating the sensitivity $\mathcal{S}'(\boldsymbol{q})$ can be done by solving additional PDE problems. The method therefore possibly increases the number of PDE solves and it is not clear if the reduction of iterations by the acceleration really reduces the number of overall PDE solves drastically. Furthermore, the approach has no proper stopping criterion if the noise level is uncertain.

Our aim is to use a homotopy method in α to stabilise the solution process even for small choices of α. Therefore we want to use a heuristic technique for reducing α to an appropriately small value on the one hand and stopping the algorithmic routine as early as possible. In our situation we assume that we have no knowledge of the noise level. Thus all methodologies basing directly on Mozorovs discrepancy principle are not appropriate for us. However, there are examples for so-called "heuristic parameter choice rules" for linear or nonlinear inverse problems described in the literature (c.f. Engl et al. [31, Chapter 4.5], Clason et al. [24], Ito et al. [59] and Jin et al. [61]).

Investigating heuristics has always an experimental character. Thus we need to solve a large amount of optimisation problems. Especially for the PDE constrained optimisation problem presented in this chapter this is not convenient, since the time-dependent problems need a huge amount of computational time. Thus, we introduce an analogous time-independent example and discuss heuristic parameter choice rules in this context. Later on we will use our experiences also for the time-dependent case.

6.5. Time-Independent Numerical Example

First we describe the numerical example and discuss in remarks the differences to the time-dependent case. Afterwards, we present first results, which prove the ability of the suggested method to estimate quantities which are not directly observed by the given data. Finally we discuss a heuristic technique for automatically running the identification process.

6.5.1. Estimation of Drag and Lift in a Benchmark Channel

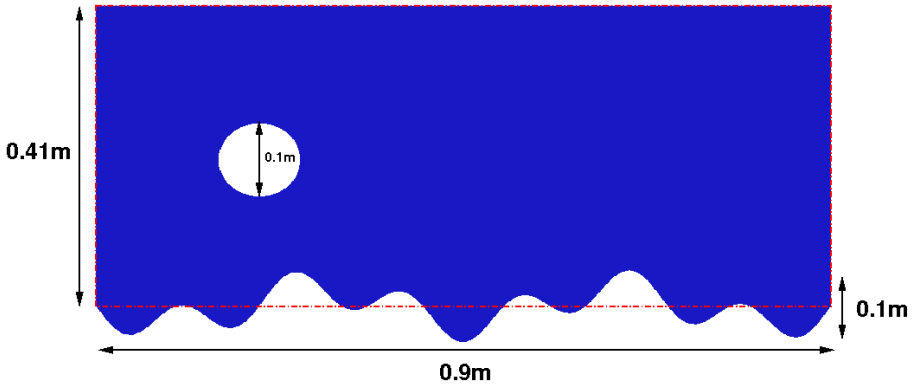

Figure 6.5. Computational domain with rough lower boundary Ω_R. Due to the unknown roughness, we perform a boundary identification problem on the domain Ω, which is indicated by the red dotted lines.

The test case we have in mind is a combination of the examples in Chapter 3.6 and at the end of Chapter 5.3.

The data I_{R} for our test case is constructed by solving the system

$$\begin{aligned} -\varepsilon \Delta I_R(\boldsymbol{x}) + \boldsymbol{u}_R(\boldsymbol{x}) \cdot \nabla I_R(\boldsymbol{x}) &= 0, && \text{in } \Omega_R, \\ -\nu \Delta \boldsymbol{u}_R(\boldsymbol{x}) + \boldsymbol{u}_R(\boldsymbol{x}) \cdot \nabla \boldsymbol{u}_R(\boldsymbol{x}) + \nabla p_R(\boldsymbol{x}) &= 0, && \text{in } \Omega_R, \\ \nabla \cdot \boldsymbol{u}_R(\boldsymbol{x}) &= 0, && \text{in } \Omega_R \end{aligned} \tag{6.6}$$

for the boundary data

$$\begin{aligned} \boldsymbol{u}_R(\boldsymbol{x}) &= 4u_{\max} y(0.41 - y), && \text{on } \Gamma_{\mathrm{In}} := \{0\} \times [0, 0.41], \\ \nu \partial_{\boldsymbol{n}} \boldsymbol{u}_R(\boldsymbol{x}) - p(\boldsymbol{x}) \boldsymbol{n}(\boldsymbol{x}) &= 0, && \text{on } \Gamma_{\mathrm{Out}} := \{0.9\} \times [0, 0.41], \\ \boldsymbol{u}_R(\boldsymbol{x}) &= 0, && \text{on } \Gamma_{\mathrm{D}} = \partial\Omega \setminus (\Gamma_{\mathrm{In}} \cup \Gamma_{\mathrm{Out}}) \end{aligned}$$

and

$$\begin{aligned} I_R(\boldsymbol{x}) &= \begin{cases} 0.075 \left(1 + \cos\left(\frac{\pi}{r}\sqrt{(y - y_i)}\right)\right), & \forall y \in B_r(y_i), \\ 0, & \text{else}, \end{cases} && \text{on } \Gamma_{\mathrm{In}}, \\ \varepsilon \partial_{\boldsymbol{n}} I_R(\boldsymbol{x}) &= 0, && \text{on } \Gamma_{\mathrm{Out}}, \\ I_R(\boldsymbol{x}) &= 0, && \text{on } \Gamma_{\mathrm{D}}, \end{aligned}$$

with $\nu = 10^{-3} \frac{\mathrm{m}^2}{\mathrm{s}}$, $\rho = 1 \frac{\mathrm{kg}}{\mathrm{s}}$, $\varepsilon = 10^{-5}$ and $u_{\max} = 1.8 \frac{\mathrm{m}}{\mathrm{s}}$ in the computational domain Ω_R, which is visualised in Figure 6.5.

For the intensity boundary condition we set $y_1 = 0.12\mathrm{m}$, $y_2 = 0.3\mathrm{m}$ and $r = 0.075\mathrm{m}$.

The roughness of the lower boundary is given by the function

$$y(x) = -0.05 \cos\left(\frac{9}{2}\pi x\right) \sin\left(10\pi x\right) \mathrm{m}.$$

The resulting flow situation, which is presented in Figure 6.6, can furthermore be characterised by two common quantities, namely the drag and the lift coefficients (see for example Schäfer [93])

$$c_{\mathrm{D}} = \frac{2}{\rho \bar{u}^2 D} F_{\mathrm{D}}, \qquad c_{\mathrm{L}} = \frac{2}{\rho \bar{u}^2 D} F_{\mathrm{L}},$$

where ρ denotes the fluid density, which we assumed to be $1\frac{\mathrm{kg}}{\mathrm{m}^3}$, $D = 0.1\mathrm{m}$ is a characteristic length and the mean velocity is given by $\bar{u} = \frac{2}{3}\max|u_1(\boldsymbol{x})| = 0.2\frac{\mathrm{m}}{\mathrm{s}}$. Furthermore the vector

$$(F_{\mathrm{D}}, F_{\mathrm{L}})^T = \int_C \hat{\eta}\boldsymbol{n}\, ds$$

defines the drag and lift forces, with

$$\hat{\eta} := \nu \nabla \boldsymbol{u} - pI.$$

We calculated the values on a globally refined mesh with 2696 nodes:

$$c_{\mathrm{L}} = 0.6717, \qquad c_{\mathrm{D}} = 6.2529$$

and remark that we used the equal order Finite Element element approach with LP stabilisation for pressure and transport dominance as it was presented in Chapter 3.

Now we assume that the function which describes the roughness on the lower boundary is not available. Hence, we assume that the lower boundary is smooth and flat, what essentially influences the solution. See therefore Figure 6.6 and the drag and lift coefficient:

$$\tilde{c}_{\mathrm{L}} = 0.0110 \qquad \left(\frac{|\tilde{c}_{\mathrm{L}} - c_{\mathrm{L}}|}{|c_{\mathrm{L}}|} \approx 98.4\%\right), \qquad \tilde{c}_{\mathrm{D}} = 5.2888 \qquad \left(\frac{|\tilde{c}_{\mathrm{D}} - c_{\mathrm{D}}|}{|c_{\mathrm{D}}|} \approx 15.4\%\right).$$

As mentioned above, we assume that the function $I(\boldsymbol{x})$ represents the transport of a passive tracer, which can be directly observed. Thus the function $I(\boldsymbol{x})$ is also available in this scenario and we will use this information to estimate appropriate boundary conditions for the flow on the lower boundary.

The aim is then to minimise

$$J(I, \boldsymbol{q}) = \frac{\zeta}{2}\|I - I_R\|^2_{L^2(\Omega_{\mathrm{Obs}})} + \frac{\alpha}{2}\|\boldsymbol{q}\|^2_{L^2(\Gamma_B)^2} \tag{6.7}$$

subject to the system (6.6) but this time for the domain $\Omega = [0, 0.9] \times [0, 0.41]$ instead of the domain Ω_R described before (the red box in Figure 6.5). We choose moreover for the cost functional an observation domain $\Omega_{\mathrm{Obs}} = [0, 0.9] \times [0.05, 0.41]$, assuming that the

data in this area is trustworthy. Furthermore Γ_B indicates the bottom boundary where we prescribe the Robin-type condition

$$\nu \partial_{\boldsymbol{n}} \boldsymbol{u} - p\boldsymbol{n} = \frac{1}{\mu_{\boldsymbol{u}}} (\boldsymbol{q} - \boldsymbol{u}) + \frac{1}{2} (\boldsymbol{u} \cdot \boldsymbol{n}) \boldsymbol{u}, \qquad \text{on } \Gamma_B = [0, 0.9] \times \{0\}$$

for the velocity vector field. The intensity function has homogeneous Dirichlet data on this boundary. For all following numerical calculations we choose the parameter $\mu_{\boldsymbol{u}} = h^2$.

Remark 6.10 (Remarks on the Solution Theory).
The problem is a time-independent version of the problem formulated at the beginning of the chapter. A main ingredient of the used model is the Navier-Stokes system. For this system we know that there are differences in the uniqueness theory for the time-dependent and time-independent case. For the time-independent case we know that only for "sufficiently small" data the solution is unique (cf. Temam [99, Chapter 2, Theorem 1.3]), while we have in the time-dependent case no restrictions on the data.

Thus, we have to modify Theorem 6.4. Nevertheless we conjecture that we can guarantee the existence of a solution of the optimisation problem with the time-independent PDE side condition. The result can analogously be proved by the same techniques presented throughout this thesis, since Theorem 6.5 requires only the existence of a solution of the PDE side condition.

However, the statement of optimality conditions in terms of the Lagrangian or the reformulation of the problem by a reduced cost functional to formulate a Newton-type method needs the existence of appropriate Lagrange parameters (existence of an adjoint state) or the existence of a unique solution operator. Since this cannot be guaranteed for the Navier-Stokes equations we have also no chance to obtain this for our coupled model. Then we have to restrict ourselves to smallness assumptions on the data. For the Navier-Stokes equations we find discussions of this issues for example in the works of De los Reyes et al. [87], Gunzburger et al. [46], Roubíček et al. [89] and Tröltzsch et al. [101].

We skip a further discussion, since our main focus lays on the time-dependent case, and we only need the time-independent case for the investigation of the regularisation parameter.

6.5.2. A Heuristic Stopping Rule for a Homotopy-Type Method

For the above presented example we can make a parameter study for the regularisation parameter α. We consider therefore the parameter sequence

$$\alpha_i = \frac{\hat{\alpha}}{2^i} \qquad \text{for } i = 0, \dots, 25 \qquad \text{and } \hat{\alpha} = 1000.$$

To stabilise the optimisation process for small choices of α_i we use the solution for the previous parameter α_{i-1} as initial solution for the optimisation algorithm (the homotopy method mentioned in the sections before).

Again we use only a fixed amount of CG steps and perform then Newton steps (inexact Newton method) until the Newton-residual drops below a threshold of 10^{-5}.

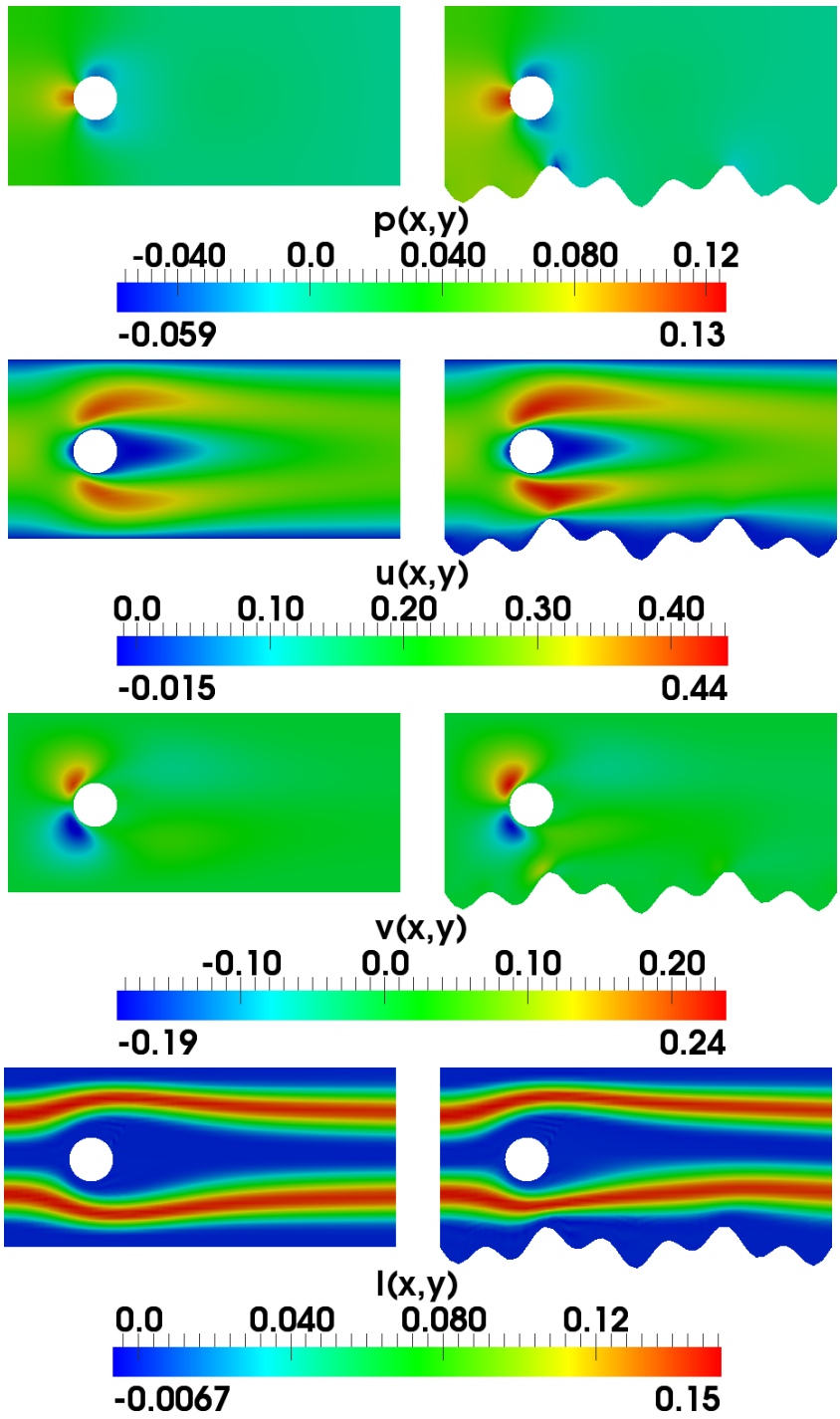

Figure 6.6. Channel Flow (Re = 20). From top to bottom: Pressure, Velocity in x direction and y direction and the intensity function. Left: Results without identification: $\boldsymbol{q}|_{\Gamma_B} = 0$. Right: Original flow in the domain with rough bottom boundary. Compare the graphs to the results of the flow with an identified boundary condition on the bottom wall in Figure 6.7.

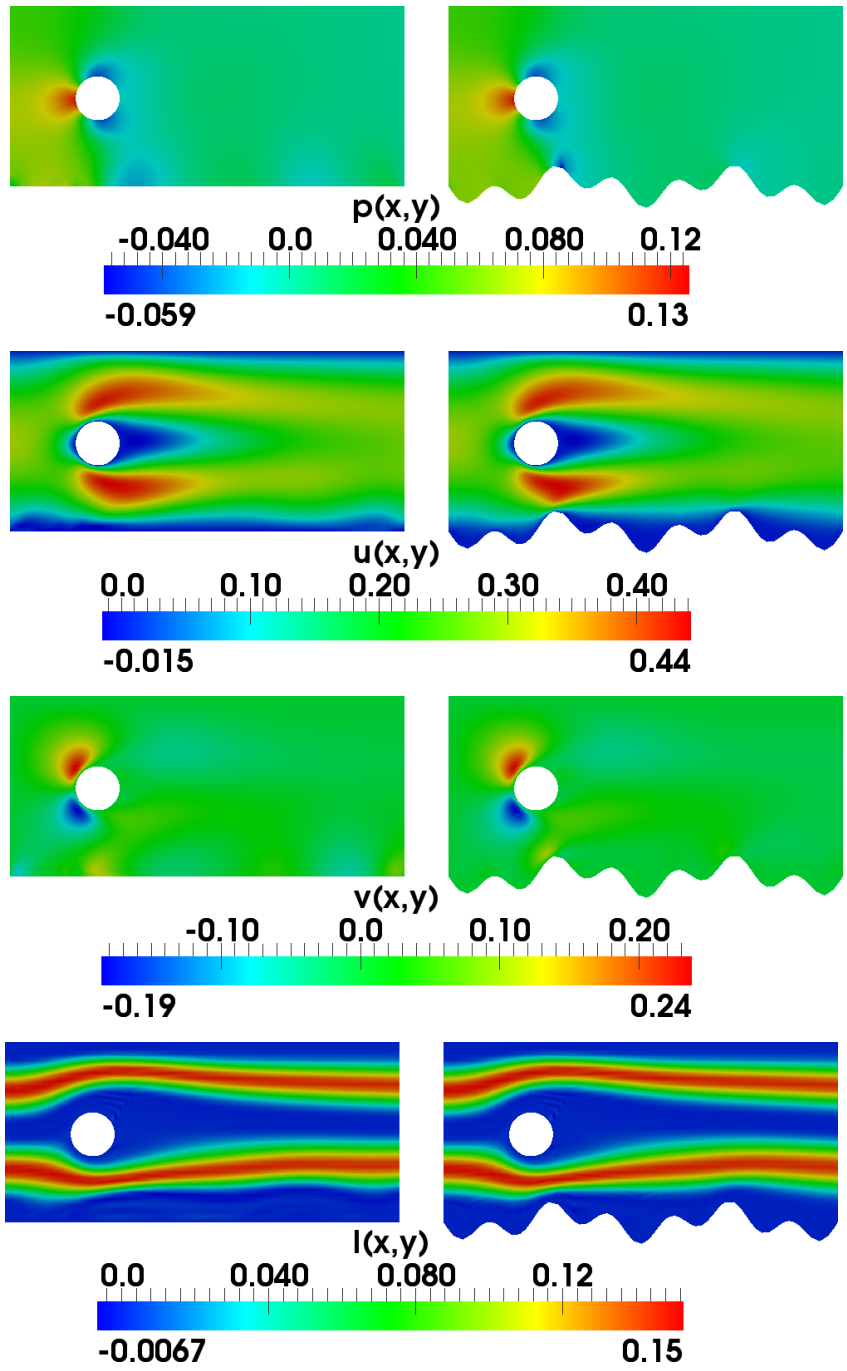

Figure 6.7. Channel Flow (Re = 20). From top to bottom: Pressure, Velocity in x direction and y direction and the intensity function. Left: Estimation with boundary identification on the bottom boundary for the choice $\alpha = 2$ of the regularisation parameter. Right: Original flow in the domain with rough bottom boundary. Compare the graphs to the results of the flow with zero boundary conditions on the bottom wall in Figure 6.6.

The results of the calculation are given in Figure 6.8. The dotted curves in the bottom plot show the data term and regularisation term

$$d(\alpha) := \frac{\zeta}{2}\|I(\alpha) - \hat{I}\|_2^2 \quad \text{(green)}, \qquad r(\alpha) := \frac{1}{2}\|\boldsymbol{q}(\alpha)\|^2_{L^2(\Gamma_{\text{Bottom}})^2} \quad \text{(red)}$$

and the overall functional value $J_\alpha(I, \boldsymbol{q})$ (blue). Furthermore, we visualise the relative error of the α-dependent drag and lift coefficient in the top figure

$$\text{err}_D(\alpha) := \frac{|c_D(\alpha) - \hat{c}_D|}{|\hat{c}_D|} \quad \text{(green)}, \qquad \text{err}_L(\alpha) := \frac{|c_L(\alpha) - \hat{c}_L|}{|\hat{c}_L|} \quad \text{(blue)}$$

by the connected curves.

Due to the magnitude of the data function $\hat{I}$ we choose the scaling parameter $\zeta = 1000$ to guarantee that the data term for the uncontrolled case is not too small. Usually we have $\frac{\zeta}{2}\|I(\alpha) - \hat{I}\|_2^2 \in [0.1, 1]$.

At first we observe that the lift coefficient stays for small α clearly below 10% relative error. In comparison to the 98% relative error in the channel with zero boundary conditions on the bottom wall this is a remarkable result. The same can be observed for the drag error function $\text{err}_D(\alpha)$ where the value stays for small α at approximately 2% which is also impressive in comparison to the 15% relative error in the drag estimation in the channel with homogeneous boundary conditions on a flat bottom wall. For the concrete choice $\alpha \approx 2$ we find actually the optimal values

$$\hat{c}_\text{L} = 0.6599 \qquad \left(\frac{|\hat{c}_\text{L} - c_\text{L}|}{|c_\text{L}|} \approx 1.8\%\right), \qquad \hat{c}_\text{D} = 6.3034 \qquad \left(\frac{|\hat{c}_\text{D} - c_\text{D}|}{|c_\text{D}|} \approx 0.81\%\right).$$

Figure 6.7 shows a comparison between the estimated pressure, x-velocity, y-velocity and intensity function on the left side to the original ones on the right side for the best parameter $\alpha \approx 2$.

We see from the top plot in Figure 6.8 that the drag and lift coefficient is for $\alpha \approx 4$ already estimated with the same magnitude of accuracy as for smaller values of α. Since the numerical method becomes more unstable for small α in terms of a higher amount of needed steps for the inexact Newton method to achieve the prescribed tolerance for the Newton residual, we should therefore choose α as big as possible. The aim is now to establish a criterion to find automatically an appropriate α.

Ideas in this direction are presented in the articles of Kunisch et al. [69] for linear inverse problems and Ito et al. [57] for nonlinear inverse problems, especially for problems in the context of PDE constrained optimisation. Here they introduce the "optimal value function"

$$j(\alpha) := \min_{\alpha>0} \left\{ J(u(\alpha), q(\alpha)) \text{ subject to } \mathcal{P}(u(\alpha), q(\alpha)) = 0 \right\},$$

where J represents the cost functional and $\mathcal{P}(\cdot,\cdot)$ the PDE constraint. On the basis of $j(\alpha)$ the authors developed an ordinary differential equation for the function $j(\cdot)$, which is then approximated by a model function $m(\alpha)$. By solving the optimisation problem for different

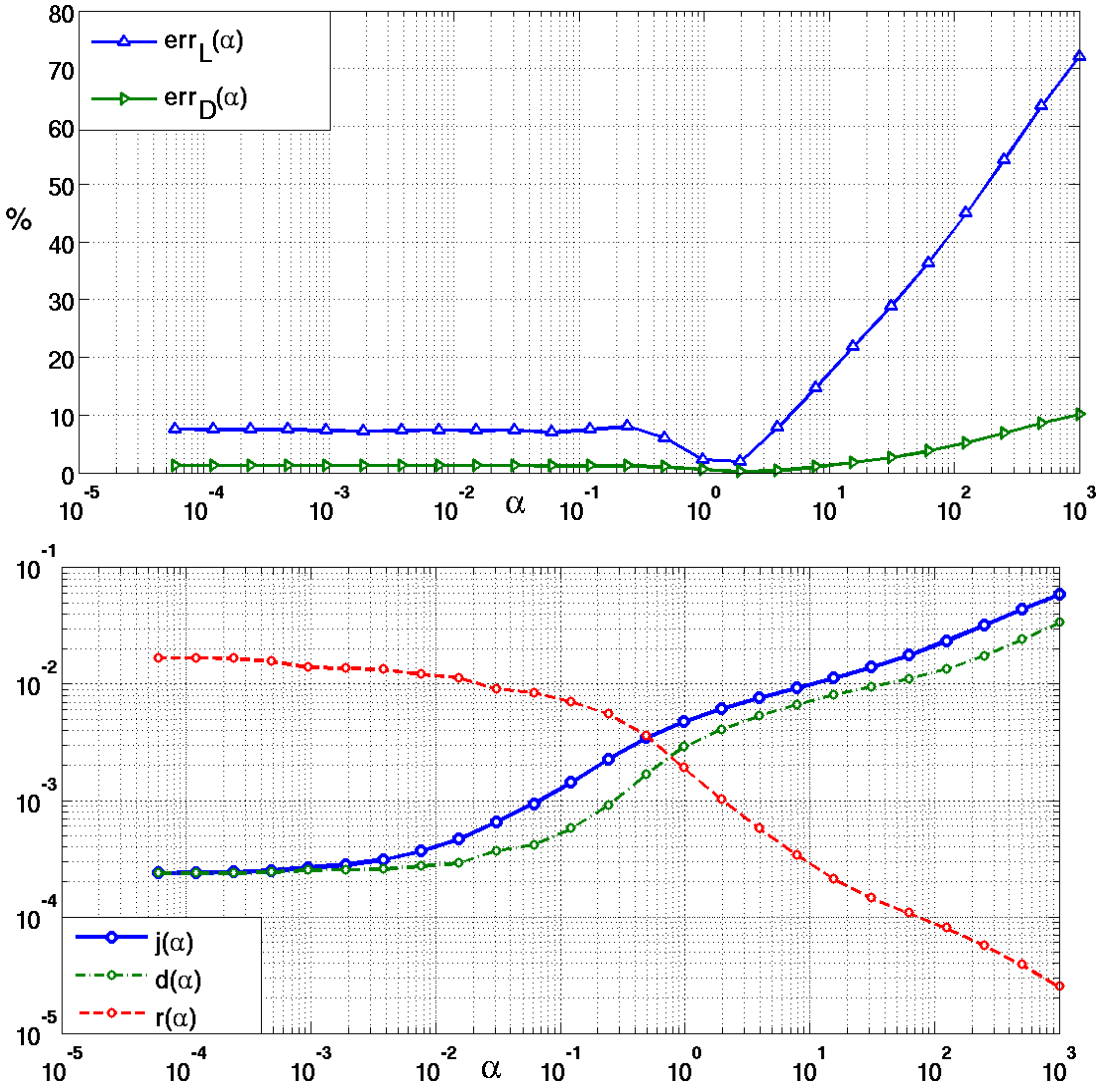

Figure 6.8. Dependence on the regularisation parameter α. Top: Relative error of the drag coefficient $\mathrm{err}_D(\alpha)$ (green) and lift coefficient $\mathrm{err}_L(\alpha)$ (blue). Bottom: The functional value in dependence of α: $j(\alpha)$ (blue). The data term $d(\alpha) := \frac{1000}{2}\|I(\alpha) - I_R\|_2^2$ (green). The regularisation term: $r(\alpha) := \frac{1}{2}\|\boldsymbol{q}(\alpha)\|^2_{L^2(\Gamma_B)^2}$ (red).

α they are able to compute the coefficients of the model function. Afterwards, they use the value $m(0)$ as estimation for the unknown noise level δ. This noise level approximation can then be used to calculate with a Newton or Newton-type method a root α for the so called damped Mozorov principle

$$j(\alpha) + (\alpha^\gamma - \alpha)j'(\alpha) = \frac{1}{2}\delta^2, \qquad \text{with} \quad \gamma \in [1, \infty].$$

Our experiences with a Newton-type method, where we approximate the higher derivatives

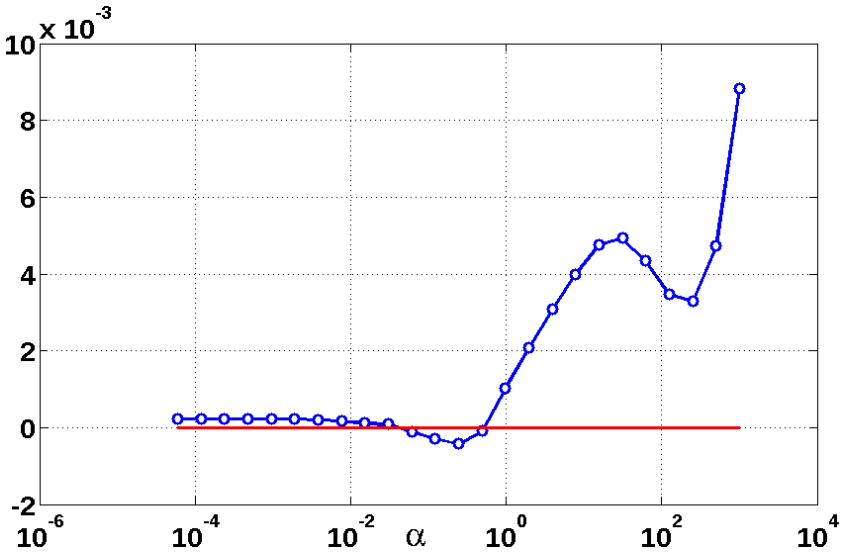

Figure 6.9. The function $g(\alpha) = d(\alpha) - \alpha r(\alpha)$. In the zeros of the function the data term and the penalty term are balanced.

of $j(\alpha)$, showed that this methodology for our example leads to α-values in the range $[10^{-3}, 10^{-2}]$, which is in our particular example far to small in our opinion, since values in the range $[0.3, 3]$ show the best results.

That is why we use another heuristic technique, which for example Clason et al. [24] used for linear inverse problems with L^1-data fitting terms. The idea is to find an appropriate α by balancing the data $d(\alpha)$ and the penalty term $\alpha r(\alpha)$. The heuristic procedure has also the name "zero-crossing" method. We consider therefore

$$g(\alpha) = d(\alpha) - \alpha r(\alpha),$$

which we plotted for our problem in Figure 6.9. The task is now to find the biggest root of the function $g(\alpha)$.

Again we like to apply a Newton-type method. We used a secant method to avoid the calculation of the derivative $g'(\alpha)$, since we need again a representation of this derivative by solutions of PDE problems.

However, both methods converge only for initial values in a certain neighborhood of the root we wish to find. For different choices of starting values we were not able to produce a

converging iteration, since this neighborhood seems to be very small. Geometrically this is clear, when we consider the special structure of the function. The function values for $\alpha < 0.1$ are very small and the curve is parallel to the abscissa, while for bigger values the function has a winding structure. The iterations of the method always jump between values bigger then 1 and smaller as 0.1, but are not able to localise the desired root in the interval $[0.1, 1]$. Thus we have to globalise the convergence area somehow.

We tried at first to work with line search strategies, also known as damped Newton-method. However, we stopped our attempts if we exceed more then 100 steps, since this meant to solve also the optimisation problem more then a hundred times, which seems unattractive, due to the resulting huge computational costs.

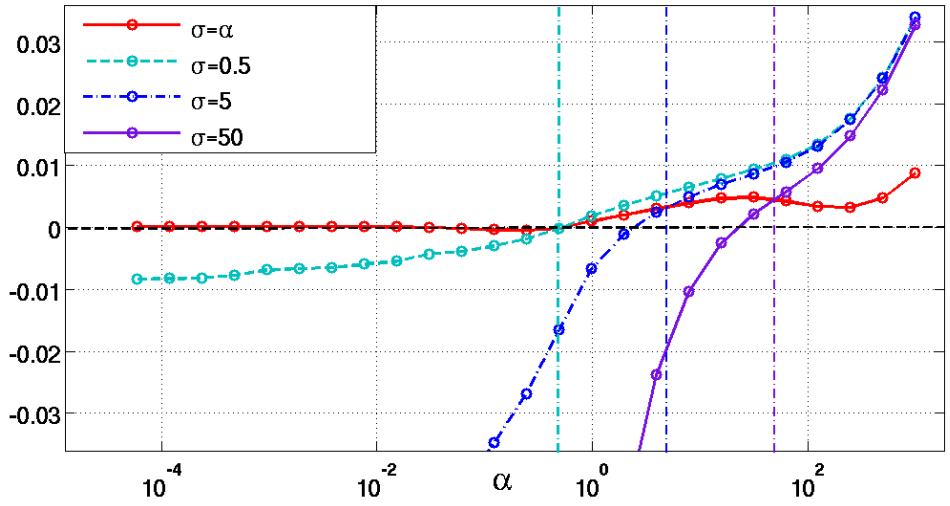

Figure 6.10. The family of functions $g_\sigma(\alpha)$ for the values $\sigma = \alpha$ (red), $\sigma = 0.5$ (cyan), $\sigma = 5$ (blue) and $\sigma = 50$ (purple). The vertical lines in the different colours represent the respective values for σ. We see that if the root $\alpha^\star$ is close to σ we found a good approximation of the original zero-crossing method.

We suggest thus a modified balancing strategy, due to the following observation. We introduce the function

$$g_\sigma(\alpha) = d(\alpha) - \sigma r(\alpha),$$

with $\sigma > 0$. This function is clearly a monotonically increasing function, since

$$\begin{aligned} d(\alpha_1) \leq d(\alpha_2), \qquad & \text{for} \quad \alpha_1 \leq \alpha_2, \qquad && \text{(monotonically increasing)}, \\ r(\alpha_1) \geq r(\alpha_2), \qquad & \text{for} \quad \alpha_1 \leq \alpha_2, \qquad && \text{(monotonically decreasing)}. \end{aligned}$$

The latter can be easily deduced by the minimising property of the optimisation problem (see for example Ito et al. [59]). Thus the function has in general only one root (see the

examples in Figure 6.10) and due to its monotonical structure it is possible to achieve by a secant method very easily a good estimation of the root of the function $g_\sigma(\alpha)$. The only thing we have to care about is to damp the method, with respect to negative values for α, which are not allowed for the optimisation problems. The Algorithm 6.1 describes the procedure. The algorithm can also be suited with further line search techniques to globalise the convergence of the method. However, in all our experiments this was not necessary.

Algorithm 6.1. Newton-type method for $g_\sigma(\cdot)$ with a damping strategy for providing positivity of α.

1. Choose an initial $\boldsymbol{q}^0$, set $k = 0$ and set $\alpha_k = \alpha_{\mathtt{Ini}}$ and $\alpha_{k+1} = \frac{\alpha_k}{2}$
2. Minimise the cost functional in equation (6.7) subject to the system (6.6) for α_k and α_{k+1}.
   $\Rightarrow$ $\boldsymbol{q}^k$, $\boldsymbol{q}^{k+1}$, $d(\alpha_k)$, $d(\alpha_{k+1})$, $r(\alpha_k)$ and $r(\alpha_{k+1})$.
3. Increment k and set $\lambda = 1$.
4. While $\frac{|\alpha_k - \alpha_{k-1}|}{|\alpha_{k-1}|} > \mathtt{Tol}_1$
   4.1 Calculate $\alpha_{k+1} = \alpha_k - \lambda \frac{d(\alpha_k) - \sigma r(\alpha_k)}{d'(\alpha_k) - \sigma r'(\alpha_k)}$ with the approximations:
   $$d'(\alpha_k) \approx \frac{d(\alpha_k) - d(\alpha_{k-1})}{\alpha_k - \alpha_{k-1}} \text{ and } r'(\alpha_k) \approx \frac{r(\alpha_k) - r(\alpha_{k-1})}{\alpha_k - \alpha_{k-1}} \text{ (secant method)}$$
   4.2 While $\alpha_{k+1} \leq 0$
   4.2.1 $\lambda \leftarrow 0.5\lambda$
   4.2.2 $\alpha_{k+1} = \alpha_k - \lambda \frac{d(\alpha_k) - \sigma r(\alpha_k)}{d'(\alpha_k) - \sigma r'(\alpha_k)}$
   4.3 Minimise the cost functional in equation (6.7) subject to the system (6.6) for α_{k+1} $\Rightarrow$ $\boldsymbol{q}^{k+1}$, $d(\alpha_{k+1})$ and $r(\alpha_{k+1})$.
   4.4 Increment k and set $\lambda = 1$.

We compute the difference of both functions

$$g(\alpha) - g_\sigma(\alpha) = (\sigma - \alpha) r(\alpha).$$

and observe that $\alpha = \sigma$ yields $g(\sigma) = g_\sigma(\sigma)$. Thus the function $g_{\alpha^\star}(\alpha)$ has the same root $\alpha^\star$ as $g(\alpha)$.

Furthermore for $\sigma > \alpha^\star$ the root of $g_\sigma(\alpha)$ is in the interval $(\alpha^\star, \sigma)$, as long as we consider the biggest root $\alpha^\star$ of $g(\alpha)$ and $g(\alpha) > 0$ for all $\alpha > \alpha^\star$. The reason is that

$$\underbrace{g(\alpha^\star)}_{=0} - g_\sigma(\alpha^\star) = \underbrace{(\sigma - \alpha^\star)}_{>0} r(\alpha^\star) > 0 \qquad \Rightarrow \qquad g_\sigma(\alpha^\star) < 0$$

and on the other hand

$$g_\sigma(\sigma) = g(\sigma) > 0, \qquad \text{due to } \ \sigma > \alpha^\star.$$

Algorithm 6.2. Strategy to find a root of $g(\alpha) = d(\alpha) - \alpha r(\alpha)$ based on the Newton-type method in Algorithm 6.1.

1. Choose an initial $\boldsymbol{q}^0$, set $l = 0$ and set α_{Ini}. Furthermore choose $\sigma_l = \sigma_{\text{Ini}}$.
2. Apply Algorithm 6.1 $\Rightarrow \alpha_l$
3. Increment l and set $\sigma_l = \alpha_{l-1}$.
4. While $\frac{|\sigma_l - \sigma_{l-1}|}{|\sigma_{l-1}|} > \text{Tol}_2$
   4.1 Set $\alpha_{\text{Ini}} = 2\alpha_{l-1}$ and apply Algorithm 6.1.
   $\Rightarrow \alpha_l$.
   4.2 Increment l and set $\sigma_l = \alpha_{l-1}$.

Since g_σ is a combination of continuous functions, it is continuous as well and therefore has its root in the interval $(\alpha^\star, \sigma)$.

Hence, if we already have a good estimate $\hat{\alpha}$ for $\alpha^\star$, we can use Algorithm 6.1 for the function $g_{\hat{\alpha}}(\alpha)$ to obtain a better estimation of $\alpha^\star$ of the function $g(\alpha)$. The quality of the approximation of $\hat{\alpha}$ can be evaluated by calculating the value $g_{\hat{\alpha}}(\hat{\alpha})$. A small value indicates that the equation $g(\hat{\alpha}) \approx 0$ is well approximated, which was the required condition of the zero crossing method.

The mentioned consideration leads to the following strategy. Since in general we also lack information on a good choice for σ we could start with a big σ_0 and estimate roughly the root α_0 of $g_{\sigma_0}(\alpha)$. Afterwards, we check if the estimated root α_0 is close to σ_0 by checking $\frac{|\alpha_0 - \sigma_0|}{|\sigma_0|} < \text{Tol}$ with a certain tolerance Tol. If this is not the case we take α_0 as σ_1 and repeat the process. In consideration of the fact that a broader range of α values leads to qualitatively equal results in terms of the drag and lift reconstruction (see Figure 6.8) we can choose a relatively big tolerance. Thus a few steps of this heuristic should be sufficient to find an α with a good reconstruction property. We summarise the procedure in Algorithm 6.2.

Remark 6.11 (Other Root-Finding Techniques). *We want to emphasise that there exist global converging root finding techniques to calculate the zero of*

$$g(\alpha) = d(\alpha) - \alpha d(\alpha)$$

like for example the Dekker-Brent method (see Quarteroni [84]). However, these methods involve usually the bisection method, which we want to avoid in this context, since α influences the computation of the PDE constrained optimisation problem.

Table 6.2. Algorithm 6.1 for the first test case with the initial values $\sigma = 1$ and $\alpha = 1000$. As tolerance for the stopping criteria $s_\alpha := \frac{|\alpha_n - \alpha_{n-1}|}{|\alpha_{n-1}|}$ in α we choose 0.01 and for $s_\sigma := \frac{|\sigma_n - \sigma_{n-1}|}{|\sigma_{n-1}|}$ we choose 0.1.

n	σ	α	$\lvert\alpha_n - \alpha_{n-1}\rvert$	$\lvert d(\alpha) - \sigma r(\alpha)\rvert$
1	1	1000		$3.405 \cdot 10^{-2}$
2	1	500	500	$2.424 \cdot 10^{-2}$
3	1	191.12	308.88	$1.577 \cdot 10^{-2}$
4	1	47.24	143.89	$1.027 \cdot 10^{-2}$
5	1	13.66	33.57	$7.557 \cdot 10^{-3}$
6	1	1.98	11.68	$3.105 \cdot 10^{-3}$
7	1	0.96	1.02	$9.880 \cdot 10^{-4}$
8	1	0.49	0.48	$1.882 \cdot 10^{-3}$
9	1	0.80	0.31	$4.423 \cdot 10^{-5}$
		0.81	0.008	$(s_\alpha < 0.01)$
10	0.81	1.61		$2.774 \cdot 10^{-3}$
11	0.81	0.81	0.81	$8.124 \cdot 10^{-4}$
12	0.81	0.47	0.33	$1.754 \cdot 10^{-3}$
13	0.81	0.70	0.22	$1.295 \cdot 10^{-4}$
14	0.81	0.72	0.02	$4.131 \cdot 10^{-5}$
		0.71	0.004	$(s_\alpha < 0.01)$
15	0.71	1.43		$2.586 \cdot 10^{-3}$
16	0.71	0.71	0.71	$6.082 \cdot 10^{-4}$
17	0.71	0.49	0.22	$9.466 \cdot 10^{-4}$
18	0.71	0.63	0.13	$3.170 \cdot 10^{-4}$
19	0.71	0.70	0.07	$1.632 \cdot 10^{-5}$
		0.69	0.003	$(s_\alpha < 0.01)$
	0.71	0.69		$(s_\sigma < 0.1)$

For a very small choice of α we can perhaps not even solve the optimisation problem, unless we apply a homotopy method in α, as mentioned in the sections before.

Our proposed heuristic technique has the advantage that in the beginning the iterations α_k are permanently decreased (see Table 6.2 $n = 1, \ldots, 7$) unless the magnitude of the sought $\alpha^\star$ is reached. Using the solution of the optimisation for α_{k-1} as initial values for the solution with α_k, we can combine the homotopy method with the α-strategy and thus stabilise the numerical solution process for the optimisation problems.

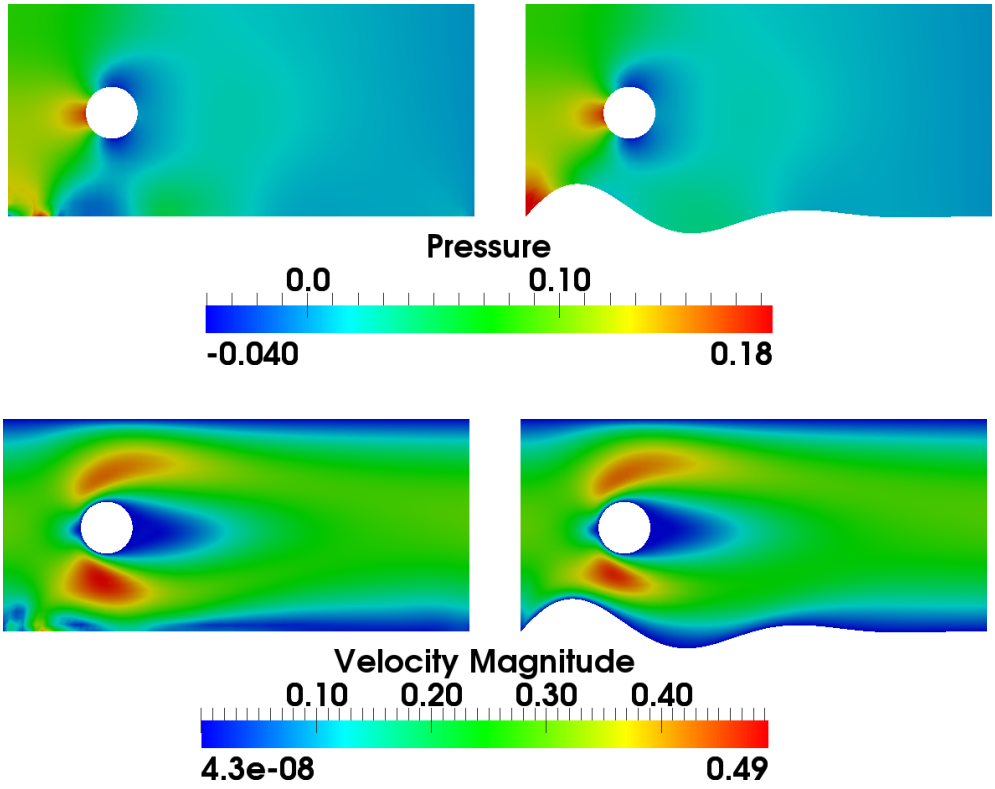

Figure 6.11. Second Test Case ($\nu = 2 \cdot 10^{-3} \frac{m^2}{s}$, Re $= 10$). Left: Estimated. Right: Original. Top: Pressure function. Bottom: Magnitude of the velocity components. Regularisation parameter: $\alpha = 1.07$. The estimated values are $\hat{c}_D = 9.167$ (Rel. error: 0.1%) and $\hat{c}_L = 0.267$ (Rel. error: 9.3%). In comparison: For $\boldsymbol{q}|_{\Gamma_B} = 0$ we have $\tilde{c}_D = 8.142$ (Rel. error: 11.3%) and $\tilde{c}_L = 0.078$ (Rel. error: 73.4%).

The algorithmic behaviour for our particular example is presented in the Table 6.2. We choose a relative tolerance of 1% for the root finding process with Algorithm 6.1 and if σ_i has a relative difference of 10% to σ_{i-1} we accept the root $\alpha^\star$ of this function $g_{\sigma_i}(\cdot)$ as a reliable α for the optimisation process. The evaluated $\alpha = 0.69$ is close to the expected value, but the process still needs many steps to obtain α.

However, we want to demonstrate the functionality of the suggested identification technique for three other test configurations with unknown boundary roughness. We present the results in Table 6.3. In the upper part of the table the expected values c_D and c_L are compared to the estimations $\hat{c}_D$ and $\hat{c}_L$ with the above described strategy. The lower part of the table shows the results for $\sigma = 1$ fixed. The process needs then of course a lower amount of steps and therefore solves of the optimisation process. The relative errors

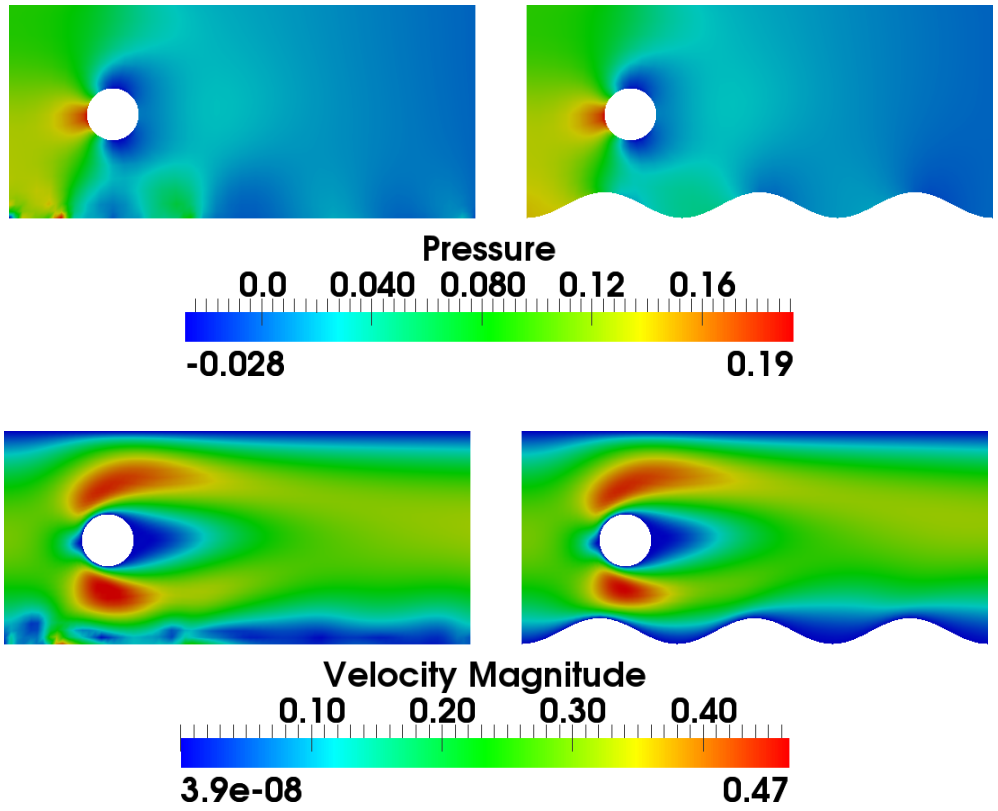

Figure 6.12. Third Test Case ($\nu = 2 \cdot 10^{-3} \frac{m^2}{s}$, Re $= 10$). Left: Estimated. Right: Original. Top: Pressure function. Bottom: Magnitude of the velocity components. Regularisation parameter: $\alpha = 0.66$. The estimated values are $\hat{c}_D = 9.797$ (Rel. error: 0.2%) and $\hat{c}_L = 0.86$ (Rel. error: 9.6%). In comparison: For $\boldsymbol{q}|_{\Gamma_B} = 0$ we have $\tilde{c}_D = 8.142$ (Rel. error: 16.8%) and $\tilde{c}_L = 0.078$ (Rel. error: 91.8%).

between these two techniques show only marginal differences so that it seems advisable to choose $\sigma = 1$ for this concrete problem class of identification problems. The Figures 6.11, 6.12 and 6.13 show the results of the second to the fourth test case. The upper image pair always visualises a comparison between the expected pressure (right) and the estimated one (left). The lower image pair visualises a comparison between the velocity magnitude of the estimated flow (left) and the expected one (right). We want to emphasise that, beside the boundary roughness, we also changed the viscosity parameter ν to demonstrate that

the procedure is also working for different flow configurations.

Remark 6.12 (Final Remark - Advantage of the Presented Heuristic).
Finally we want to emphasise that the presented technique relies on pure heuristics and thus it is possibly not transferable to more complex geometries and configurations. However, the technique had for us the big advantage that we could use it as some kind of automatic stopping rule for our homotopy type method in α, which we needed to solve the problem appropriately.

We observed that the special structure of $g_\sigma(\alpha)$ as monotone increasing function in α leads to sequences of α_k which in the beginning decreases, which could perfectly used in the homotopy technique to produce in each step good initial values for the optimisation process.

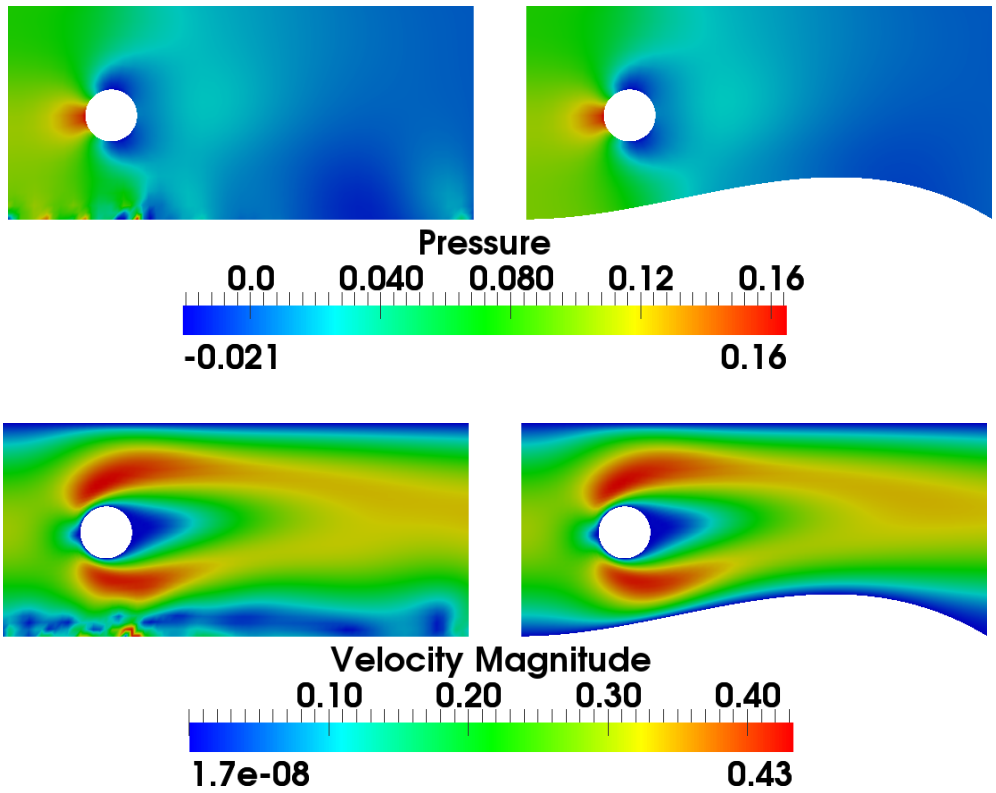

Figure 6.13. Fourth Test Case ($\nu = 1.5 \cdot 10^{-3} \frac{m^2}{s}$, Re ≈ 13.3). Left: Estimated. Right: Original. Top: Pressure function. Bottom: Magnitude of the velocity components. Regularisation parameter: $\alpha = 0.24$. The estimated values are $\hat{c}_D = 7.989$ (Rel. error: 1%) and $\hat{c}_L = 0.933$ (Rel. error: 6.3%). In comparison: For $\boldsymbol{q}|_{\Gamma_B} = 0$ we have $\tilde{c}_D = 6.710$ (Rel. error: 14.6%) and $\tilde{c}_L = 0.039$ (Rel. error: 95.5%).

Moreover, we want to emphasise that we are not certain that the application of the "zero-crossing" method for our problem really leads to a reliable choice of the regularisation

parameter in terms of the quality of the reconstruction of the flow. We merely observed that we are able to stop the homotopy method by this approach automatically for an regularisation parameter, which yields to a comparatively good reconstruction of the drag and lift coefficient.

Table 6.3. Boundary identification for four test cases with different rough boundaries and viscosities. Upper half: The described strategy in the Algorithm 6.2 for a tolerance of 10% relative difference in σ_i and 1% in each root evaluation of $g_{\sigma_i}(\alpha)$. Lower half: Estimation of α by Algorithm 6.1 with fixed $\sigma = 1$. Original values: c_D and c_L. Estimated values: $\hat{c}_D$ and $\hat{c}_L$. The number n indicates the number of evaluated optimisation problems to obtain an appropriate α.

Test	c_D	c_L	α-Strategy (Total n)	$\hat{c}_D$		$\hat{c}_L$	
1.	6.253	0.672	0.69 (19)	6.345	(1.5%)	0.706	(5.0%)
2.	9.178	0.293	1.07 (8)	9.167	(0.1%)	0.266	(9.3%)
3.	9.782	0.952	0.66 (23)	9.798	(0.2%)	0.860	(9.6%)
4.	7.907	0.878	0.24 (46)	7.989	(1.0%)	0.933	(6.3%)
Test	c_D	c_L	α for $\sigma = 1$ (n)	$\hat{c}_D$		$\hat{c}_L$	
1.	6.253	0.672	0.81 (8)	6.338	(1.4%)	0.697	(3.8%)
2.	9.178	0.293	1.07 (8)	9.167	(0.1%)	0.266	(9.3%)
3.	9.782	0.952	0.79 (12)	9.786	(<0.1%)	0.854	(10.3%)
4.	7.907	0.878	0.49 (12)	7.989	(1.0%)	0.929	(5.8%)

6.5.3. Dependence on the Model Parameter (Reynolds-Number)

As we mentioned in the last subsection, the time-independent setting decreases computational costs and enables us to experiment with the regularisation parameter. Furthermore, we can use this example to investigate the dependence of the reconstruction on model uncertainties. We will create these uncertainties by the Reynolds number Re, which characterises the fluid flow. We recall the definition of the Reynolds number

$$\mathrm{Re} = \frac{\boldsymbol{u}^c d}{\nu},$$

with the characteristic velocity $\boldsymbol{u}^c$, diameter d and the fluid viscosity ν. For our specific situation the diameter $d = 0.1\mathrm{m}$ is always given by the diameter of the obstacle. The characteristic velocity is also always given by the mean inflow $\bar{u} = 0.2\frac{m}{s}$. Thus the Reynolds number is indirectly proportional to the viscosity parameter ν

$$\mathrm{Re} = 0.2\frac{m^2}{s}\nu^{-1}.$$

In the following experiments we will use the intensity functions of the First Test Case and the Fourth Test Case of the last subsections, which were calculated for a certain fixed viscosity ν. We will assume that for the identification process only a vague knowledge of the viscosity ν^δ is available. The size of the deviation will be given by the following formula

$$\nu^\delta = \nu + \delta\nu,$$

with a percentage δ, to investigate the influence of the model parameter ν.

Table 6.4. First example. Boundary identification for the First Test Case with different deviation levels δ of the viscosity ν and the corresponding drag and lift estimation. In parentheses the relative error related to the expected values for the drag and lift is given.

δ	c_D		c_L	
1%	6.372	(1.3%)	0.702	(4.3%)
5%	6.507	(3.5%)	0.721	(7.1%)
10%	6.679	(6.2%)	0.749	(11.3%)
20%	7.007	(11.4%)	0.792	(17.7%)
50%	7.997	(27.2%)	0.942	(40.0%)
100%	9.583	(52.4%)	1.148	(70.6%)

We present the results of the First Test Case ($\nu = 10^{-3}\frac{\mathrm{m}^2}{\mathrm{s}}$) in Figure 6.14 and Table 6.4 and for the Fourth Test Case ($\nu = 1.5 \cdot 10^{-3}\frac{m^2}{s}$) in Figure 6.15 and Table 6.5. All combinations were calculated with the same strategy for choosing the regularisation parameter as in the last subsection.

We see that for small perturbations of the viscosity parameter we still achieve good approximations of the drag and lift coefficients. If the uncertainty is too large ($> 50\%$) the flow situation is clearly different to the original one. To make sure that this is not an effect of an early stopping of the parameter strategy we present in Table 6.6 the estimates of the coefficients also for very small regularisation parameters for a fixed amount of deviation $\delta = 50\%$ of the viscosity parameter. We see that for small α the estimates have the same relative errors so that we can draw the conclusion that the modeling error is dominant in this case. Thus we can conclude that the boundary identification process is not able to adjust the lack of model information, so that reliable model information is fundamental for the presented boundary identification technique.

Remark 6.13 (Real World Applications).
Due to the observation for the time-independent examples in this chapter it becomes clear that model information is essential for a good identification process. Obviously the coefficients c_D and c_L are directly influenced by the change of the viscosity. We conjecture

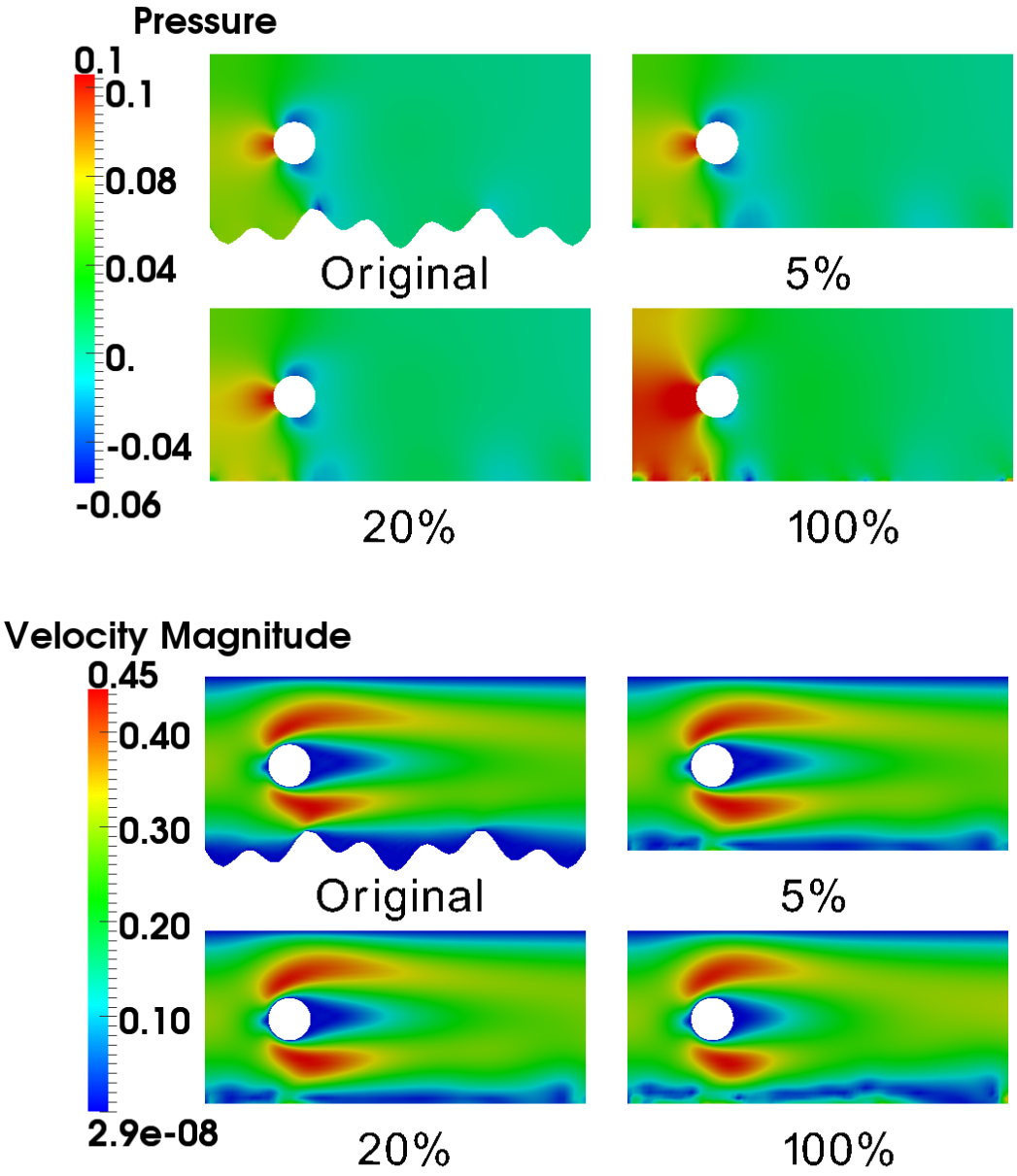

Figure 6.14. First Test Case. Top group: Pressure function for the original flow configuration (top left), identification with 5% deviation of the viscosity parameter ν (top right), 20% deviation (bottom left) and 100% deviation (bottom right). Bottom group: Same as the top group for the velocity magnitude.

therefore that in analogous real world flow situations accurate model knowledge will be crucial for a good identification process.

However, at the moment we cannot make any statements for flow situation like the one presented in the Third Example of Chapter 1.2.3. In this prototypical example no obstacle influence the flow. Thus it is not clear if the boundary identification for a different flow model is able to generate a qualitatively good reconstruction of the flow features. We will investigate this topic in the next chapter.

Table 6.5. Second example. Boundary identification for the Fourth Test Case with different deviation levels δ of the viscosity ν.

δ	c_D		c_L	
1%	8.0393	(1.7%)	0.9402	(7.1%)
5%	8.2256	(4.0%)	0.9658	(10.0%)
10%	8.3740	(5.9%)	0.9915	(12.9%)
20%	8.9286	(12.9%)	1.0749	(22.4%)
50%	10.4698	(32.4%)	1.3205	(50.4%)
100%	12.6055	(59.4%)	1.6590	(89.0%)

Table 6.6. Influence of the modeling error related to the regularisation parameter investigated by the boundary identification problem for the First Test Case with a fixed deviation level of $\delta = 50\%$ for different regularisation parameters α. In parentheses the relative error related to the expected values for the drag and lift is given.

α	c_D		c_L	
10^3	7.104	(13.0%)	0.246	(63.5%)
10^2	7.507	(19.1%)	0.490	(27.2%)
10^1	7.797	(24.0%)	0.715	(6.2%)
10^0	7.960	(26.6%)	0.899	(33.5%)
10^{-1}	8.018	(27.5%)	0.959	(42.4%)
10^{-2}	8.014	(27.5%)	0.951	(41.3%)
10^{-3}	8.022	(27.6%)	0.959	(42.4%)
10^{-4}	8.018	(27.5%)	0.956	(41.9%)
10^{-5}	8.016	(27.5%)	0.953	(41.6%)
10^{-6}	8.018	(27.5%)	0.956	(41.9%)

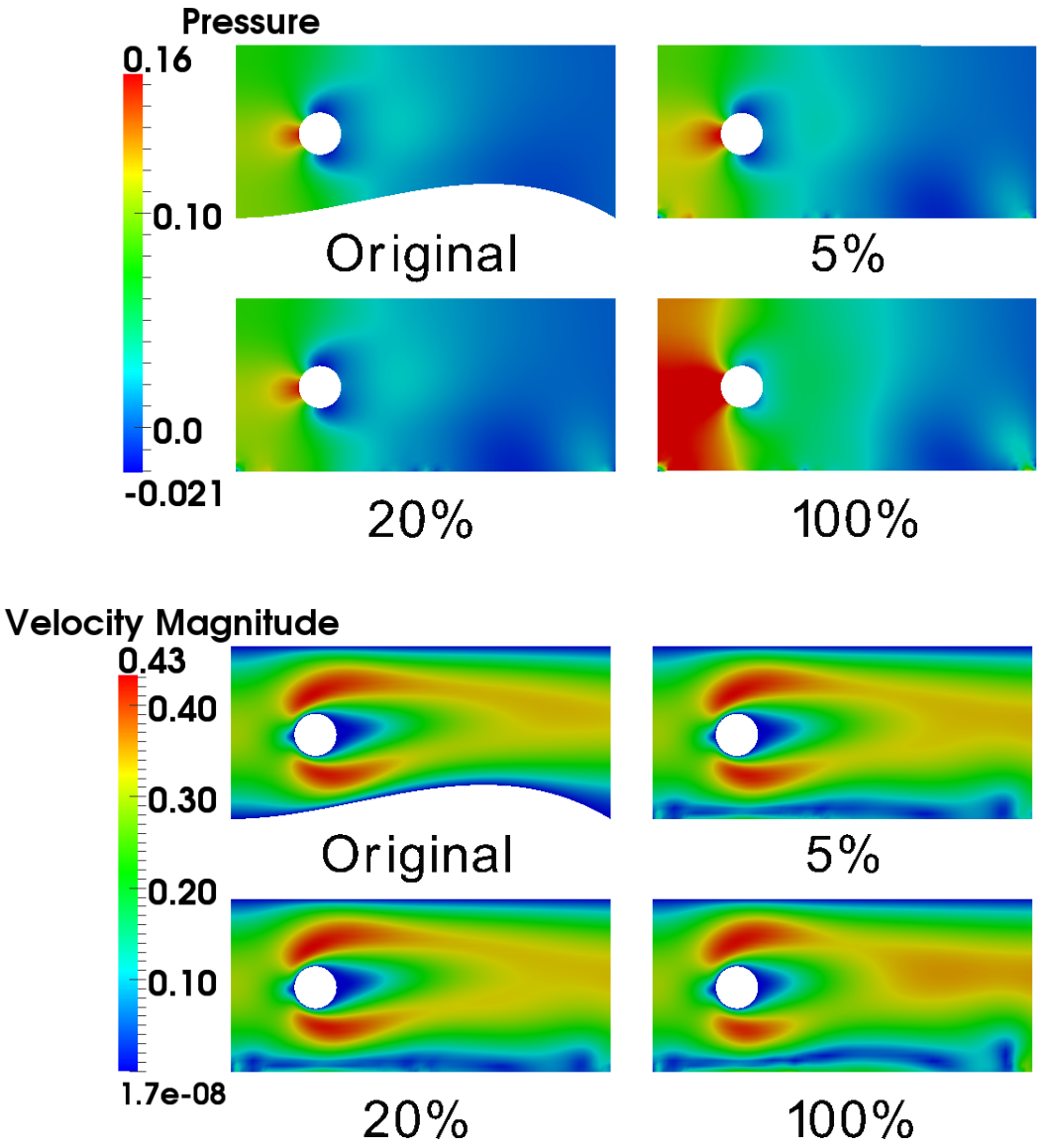

Figure 6.15. Fourth Test Case. Top group: Pressure function for the original flow configuration (top left), identification with 5% deviation of the viscosity parameter ν (top right), 20% deviation (bottom left) and 100% deviation (bottom right). Bottom group: Same as the top group for the velocity magnitude.

6.5.4. Heuristic Algorithm for Boundary Estimation and Parameter Adjustment

The last subsection demonstrates that the viscosity as model parameter drastically influences the behaviour of the fluid flow. In general we will also have only a vague notion of this the parameter. Thus, the question arose if it is possible to estimate also the viscosity and to combine this process with the identification of the boundary function.

We will discuss in this subsection a heuristic procedure for the considered time-independent example. Starting point is the following observation. Figure 6.16 shows a plot of the functional value

$$j(\nu) := \frac{\zeta}{2}\|I(\nu) - \hat{I}\|^2_{L^2(\Omega_{\text{Obs}})}$$

in dependence on the varying viscosity parameter ν in the system (6.6). We want to remark that the functional is not vanishing for the exact viscosity parameter ν, since the data function $\hat{I}$ was interpolated on the observation domain Ω_{Obs} and has therefore an interpolation error. Furthermore, the roughness was chosen as in the First Test Case (see Figure 6.5) and the function $\hat{I}$ was generated by a forward calculation with the viscosity parameter $\nu = 10^{-3}$. Figure 6.5 indicates that the minimum of the graph is $\log(10^{-3}) \approx -6.91$, which marks almost the accurate value for the viscosity on a logarithmic scale. Thus, in case the computational domain is known, we should be able to identify the viscosity parameter pretty well.

Such parameter identification problems and their numerical treatment are extensively discussed in Vexler ([102]). However, we will in the following rely on a heuristic technique for derivative free minimisation in the case of one-dimensional functions which is known as successive parabolic minimisation. It is described for example in Heath [50]. We present the procedure in Algorithm 6.3. By the values $\kappa_{\max}$ and $\kappa_{\min}$ we can prescribe the interval in which we are looking for a reliable viscosity parameter $\nu = \exp(x)$ with $x \in [\kappa_{\min}, \kappa_{\max}]$. Thereby, we looking for the minima on the logarithmic scale, since the choice $\nu = \exp(x)$ guarantees that the viscosity stays positive.

A huge drawback of the method is that it is not necessarily converging to a minimum, since it can also calculate a maximum. However, we can check the curvature of the parabola by the leading coefficient of the polynomial and adjust the triplet (x_0, x_1, x_2).

In order to find an appropriate triplet we worked with the following initial setting in all examples of this subsection: We calculated the functional values at five equidistant points $\tilde{x}_i$ between $\kappa_{\min} = -9$ and $\kappa_{\max} = 0$. Then we checked which of the three triplets $(\tilde{x}_0, \tilde{x}_1, \tilde{x}_2)$, $(\tilde{x}_1, \tilde{x}_2, \tilde{x}_3)$ or $(\tilde{x}_2, \tilde{x}_3, \tilde{x}_4)$ fullfils the condition in Step 3. of the Algorithm 6.3 and has the minimum functional value in the middle point. For the resulting triplet we perform Algorithm 6.3.

Applying Algorithm 6.3 to the above example leads to an estimation of $\nu \approx 9.951 \cdot 10^{-3}$, which is a 0.5% relative error to the expected value. The reason for the difference is the noise in the data due to the interpolation error. For this estimation we needed overall 14 evaluations of the state equation (Tol $= 10^{-3}$).

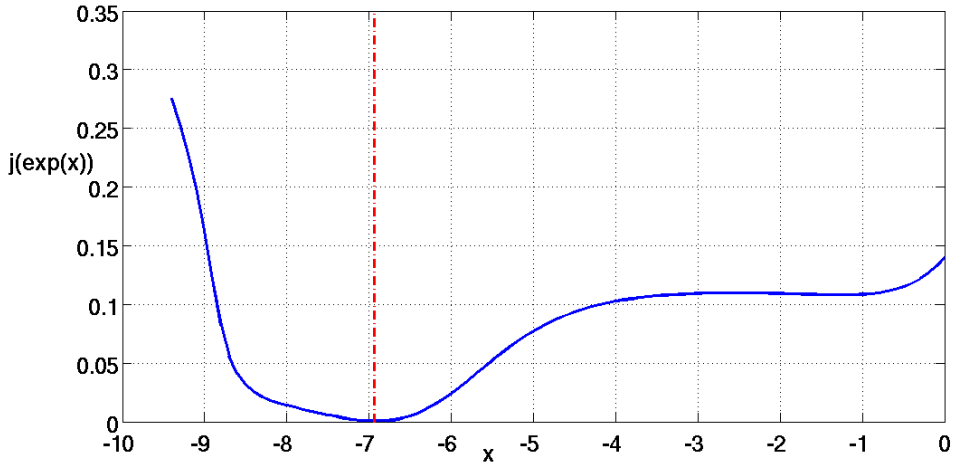

Figure 6.16. The functional value $j(\nu)$ for $\nu = \exp(x)$ for varying x. The minimum is marked by the red dotted line at $x \approx -6.9$, which is almost the desired ν.

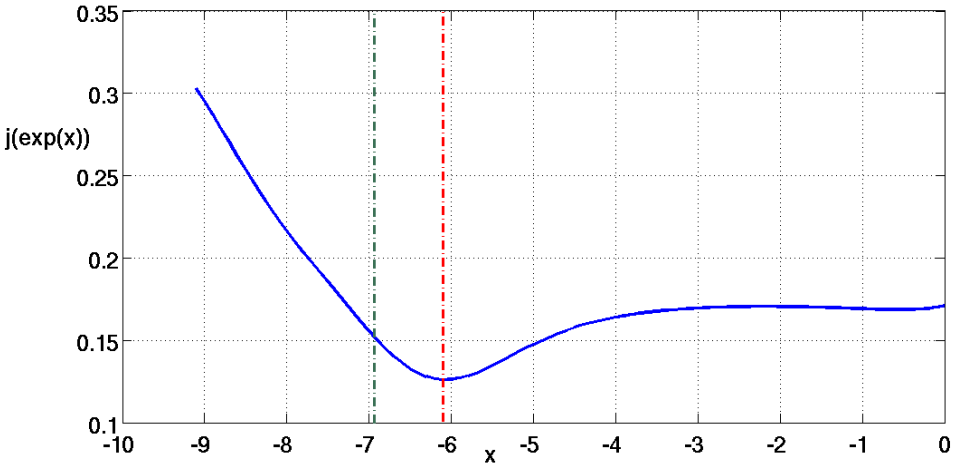

Figure 6.17. The functional value $j(\nu)$ for $\nu = \exp(x)$ for varying x if the rough lower boundary is substituted by a smooth and flat wall with homogeneous Dirichlet data. The minimum is marked by the red dotted line at $x \approx -6.1$. The green dotted line marks the value of the expected viscosity parameter.

Algorithm 6.3. Successive Parabolic Minimisation

1. Choose $\kappa_{\max} \geq x_0 > x_1 > x_2 \geq \kappa_{\min}$
2. Solve system (6.6) for $\nu_i = \exp(x_i)$ and calculate $j_i \leftarrow j(\nu_i)$.
3. If $j_0 > j_1$ and $j_2 > j_1$ accept x_i. Otherwise return to Step 1. and choose new points.
4. Calculate the coefficients a_0, a_1 and a_2 of the interpolation polynomial, e. g. in Newton representation

$$p(x) = a_0 + a_1(x - x_0) + a_2(x - x_0)(x - x_1)$$

5. $x_{\text{new}} = \frac{1}{2}\left((x_0 + x_1) - \frac{a_1}{a_2}\right)$ and solve system (6.6) for $\nu_{\text{new}} = \exp(x_{\text{new}})$. Calculate $j_{\text{new}} \leftarrow j(\nu_{\text{new}})$.
6. If $x_{\text{new}} < x_1$

   If $j_{\text{new}} < j_1$: $x_2 \leftarrow x_1$, $x_1 \leftarrow x_{\text{new}}$, $j_2 \leftarrow j_1$ and $j_1 \leftarrow j_{\text{new}}$.

   else: $x_0 \leftarrow x_{\text{new}}$ and $j_0 \leftarrow j_{\text{new}}$.

   else

   If $j_{\text{new}} < j_1$: $x_0 \leftarrow x_1$, $x_1 \leftarrow x_{\text{new}}$, $j_0 \leftarrow j_1$ and $j_1 \leftarrow j_{\text{new}}$.

   else: $x_2 \leftarrow x_{\text{new}}$ and $j_2 \leftarrow j_{\text{new}}$.
7. If $|x_0 - x_1| < \text{Tol}$ or $|x_1 - x_2| < \text{Tol}$ stop the program and accept $\exp(x_1)$ as approximation of ν. Otherwise return to Step 4.

As mentioned troughout the whole section the roughness of the channel is assumed to be not available. Thus, the first question that arose is how the choice of an smooth and flat boundary on the lower wall influence the curve of $j(\nu)$. The answer is given in Figure 6.17. We see that the minimum of the curve is now shifted in comparison to the original situation. If we use the successive parabolic minimisation in Algorithm 6.3 to estimate the value of the parameter we derive a value of $\nu \approx 2.305 \cdot 10^{-3}$ (rel. error $> 100\%$). Although the value has the same magnitude as the expected one and is thus certainly a better choice than using an arbritary value, an appropriate identification of the drag and lift coefficient will not work as Table 6.5 in the last subsection indicates.

The next thing we want to investigate is how the functional value behaves in dependence on the viscosity parameter if the lower boundary is smooth, but a suitable boundary function is prescribed. Thus, we will use the boundary function we estimated for the exact viscosity 10^{-3} in the second last subsection. The curve for $j(\nu)$ of this setting was plotted in Figure 6.18. Although the graph looks different to the setting where the roughness was known (compare Figure 6.16 and Figure 6.18) the minimiser lies at almost the same point $x \approx -6.9$ and the behaviour of the curve around the minimiser is also very similar. By Algorithm 6.3 we calculated $\nu \approx 9.87 \cdot 10^{-4}$, which is a relative error of 1.3% in comparison to the expected viscosity parameter.

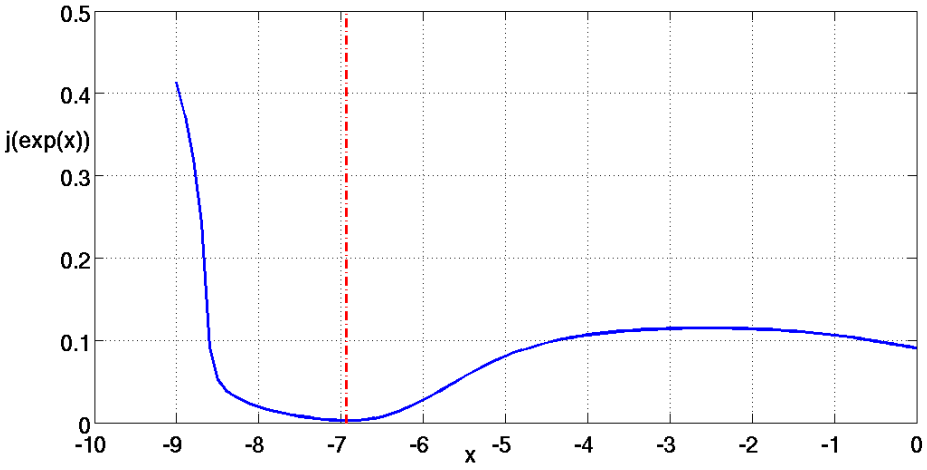

Figure 6.18. The functional value $j(\nu)$ for $\nu = \exp(x)$ for varying x if the rough lower boundary is subsituted by a smooth wall and an estimated boundary function for $\nu = 10^{-3}$ is prescribed on this boundary. The minimum is marked by the red dotted line at $x \approx -6.92$.

This observation suggests a heuristic, which makes it possible to adjust also the viscosity parameter, while the boundary function is estimated. We try to segregrate both processes and loop over them until a sufficient minimum is found. The rough structure of the procedure is sketched in Algorithm 6.4.

In the beginning the suggested segregation loop is very expensive due to the repeated

use of Algorithm 6.1, which involves probably a big ammount of Newton-type steps for the root finding problem $g_\sigma(\alpha) = d(\alpha) - \sigma r(\alpha) = 0$. Remind that each Newton-type step requires the solution of a PDE-constrained optimisation problem with an inexact Newton-CG method from Chapter 4. For each solving of these optimisation problems we need to solve up to 140 PDE's. However, at the end of the process when ν is pretty good adjusted α is also not changing very much and is therefore estimated in a few Newton-type steps. Due to this observation we suggest a second segregation loop, which integrates Algorithm 6.3 into Algorithm 6.1. The procedure is described in Algorithm 6.5 and can also be interpreted in the way that we perform only one Newton-type step of Algorithm 6.1 for the root finding of $g(\alpha)$ in Algorithm 6.4.

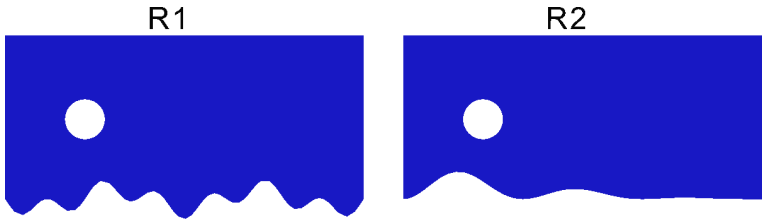

Figure 6.19. Channels for the forward calculations in this subsection to obtain the data function $\hat{I}$. Right: R1 was also used for the first test case in Section 6.5.4. Left: R2 was also used for the second test case in the mentioned section.

Remark 6.14 (Remark on Algorithm 6.5).
We use Algorithm 6.3 in Step 2.4 of Algorithm 6.5, which requires to find a triplet $tri := (x_0, x_1, x_2)$ *with* $x_0 > x_1 > x_2$ *and* $j_0 > j_1$ *and* $j_2 > j_1$, *where* $j_i \leftarrow j(\nu_i)$ *with* $\nu_i = \exp(x_i)$. *We always use in the* k*th iteration the triplet of the old iteration* $tri^{(k-1)} := (x_0^{(k-1)}, x_1^{(k-1)}, x_2^{(k-1)})$ *and check if one of the following triplets*

$$
\begin{aligned}
tri_1 &:= (x_0^{(k-1)}, \frac{x_0^{(k-1)} + x_1^{(k-1)}}{2}, x_1^{(k-1)}),\\
tri_2 &:= (\frac{x_0^{(k-1)} + x_1^{(k-1)}}{2}, x_1^{(k-1)}, \frac{x_1^{(k-1)} + x_2^{(k-1)}}{2}),\\
tri_3 &:= (x_1^{(k-1)}, \frac{x_1^{(k-1)} + x_2^{(k-1)}}{2}, x_2^{(k-1)})
\end{aligned}
$$

fulfils the condition and which has the minimal functional value in case that more than one triplet fulfils the condition. The rsulting triplet $tri^{(k)}$ *is used for the current calculation. If none of the triplets fulfils the conditons, we decrease the smallest value and increase the biggest value of the triplet unless we find a new triplet* $tri^{(k)}$ *which satisfies the condition.*

By this technique we can guarantee that we have always a triplet for Algorithm 6.3, which has a length $|x_0 - x_2|$ *which is in general decreasing. The later issue explains why we need in the end of the overall Algorithm 6.5 less inner iterations of Algorithm 6.3 (see the example in Table 6.8).*

Algorithm 6.4. Segregation loop I.

1. Set $\boldsymbol{q}^{(0)} = 0$, $\alpha^{(0)} = 10^3$, $\nu^{(0)} = 10$ and $k = 1$
2. Use $\boldsymbol{q}^{(0)}$ and apply Algorithm 6.3 $\rightarrow \nu^{(1)}$
3. Use $\alpha^{(0)}$ and $\nu^{(1)}$ and perform Algorithm 6.1 $\rightarrow \boldsymbol{q}^{(1)}$ and $\alpha^{(1)}$
4. While $\max\{|\nu^{(k)} - \nu^{(k-1)}|, \|\boldsymbol{q}^{(k)} - \boldsymbol{q}^{(k-1)}\|^2_{L^2(\Gamma_B)^2}\} >$ Tol
   - 4.1 Increment k.
   - 4.2 Use $\boldsymbol{q}^{(k-1)}$ and apply Algorithm 6.3 $\rightarrow \nu^{(k)}$
   - 4.3 Use $\alpha^{(k-1)}$ and $\nu^{(k)}$ and perform Algorithm 6.1 $\rightarrow \boldsymbol{q}^{(k)}$ and $\alpha^{(k)}$

Algorithm 6.5. Segregation loop II.

1. Assume $\nu^{(k-1)}, \nu^{(k)}, \alpha_{k-1}, \alpha_k$ and $\boldsymbol{q}^k$ are already calculated.
2. While $\max\left\{\frac{|\nu^{(k)}-\nu^{(k-1)}|}{|\nu^{(k-1)}|}, \frac{|\alpha_k-\alpha_{k-1}|}{|\alpha_{k-1}|}\right\} >$ Tol
   - a) Calculate $\alpha_{k+1} = \alpha_k - \lambda_k \frac{\alpha_k-\alpha_{k-1}}{g(\alpha_k)-g(\alpha_{k-1})} g(\alpha_k)$ with $g(\alpha) = d(\alpha) - r(\alpha)$ and $\lambda_k := 1$.
   - b) In case $\alpha_{k+1} \leq 0$ perform damping by decreasing λ_k until $\alpha_{k+1} > 0$.
   - c) Minimise the functional (6.7) subject to the system (6.6) with $\nu^{(k)}$ for the evaluated $\alpha_{k+1} \Rightarrow \boldsymbol{q}^{(k+1)}, d(\alpha_{k+1})$ and $r(\alpha_{k+1})$.
   - d) Use $\boldsymbol{q}^{(k+1)}$ in Algorithm 6.3 $\Rightarrow \nu^{(k+1)}$.
   - e) Increment k.

Table 6.7. Numerical results for eight different Cases. Upper table **R1**: Data function $\hat{I}$ was obtained by a forward calculation with the left geometry in Figure 6.19 for $\nu = 1.5 \cdot 10^{-3}, \nu = 1.2 \cdot 10^{-3}, \nu = 1 \cdot 10^{-3}$ and $\nu = 8.6 \cdot 10^{-4}$. The values for the forward calculation are given by ν, c_D and c_L. The estimations obtained by using Algorithm 6.5 are given by the values $\hat{\nu}$, $\hat{c}_D$ and $\hat{c}_L$. The values $\tilde{c}_D$ and $\tilde{c}_L$ show the results for a calculation in a channel with smooth lower boundary for the exact viscosities and the values $\bar{\nu}$, $\bar{c}_D$ and $\bar{c}_L$ are obtained after estimating the viscosity in an smooth channel by Algorithm 6.3. Lower table **R2**: The same calculations for an intensity function, which was obtained by a forward calculation in a channel with the right geometry in Figure 6.19.

R1

Re	ν	c_D	c_L	$\hat{\nu}$	$\hat{c}_D$	$\hat{c}_L$
≈ 13.3	$1.5 \cdot 10^{-3}$	7.906	0.948	$1.41 \cdot 10^{-3}$ (5.7%)	7.689 (2.7%)	0.930 (1.9%)
≈ 16.6	$1.2 \cdot 10^{-3}$	6.922	0.780	$1.16 \cdot 10^{-3}$ (3.0%)	6.858 (0.9%)	0.793 (1.7%)
20	$1.0 \cdot 10^{-3}$	6.253	0.672	$9.95 \cdot 10^{-4}$ (0.5%)	6.285 (0.5%)	0.696 (3.7%)
≈ 23.3	$8.6 \cdot 10^{-4}$	5.774	0.596	$8.76 \cdot 10^{-4}$ (1.8%)	5.878 (1.8%)	0.636 (6.6%)

Re	$\tilde{c}_D$	$\tilde{c}_L$	$\bar{\nu}$	$\bar{c}_D$	$\bar{c}_L$
≈ 13.3	6.710 (15.1%)	0.039 (95.8%)	$2.95 \cdot 10^{-3}$	10.713 (35.5%)	0.174 (81.2%)
≈ 16.6	5.865 (15.3%)	0.021 (97.3%)	$2.56 \cdot 10^{-3}$	9.644 (39.3%)	0.132 (83.1%)
20	5.289 (15.4%)	0.011 (98.4%)	$2.30 \cdot 10^{-3}$	8.936 (42.9%)	0.105 (84.3%)
≈ 23.3	4.875 (15.6%)	0.005 (99.2%)	$2.14 \cdot 10^{-3}$	8.492 (47.1%)	0.090 (84.9%)

R2

Re	ν	c_D	c_L	$\hat{\nu}$	$\hat{c}_D$	$\hat{c}_L$
≈ 13.3	$1.5 \cdot 10^{-3}$	8.556	0.895	$1.42 \cdot 10^{-3}$ (5.3%)	8.366 (2.2%)	0.924 (3.2%)
≈ 16.6	$1.2 \cdot 10^{-3}$	7.416	0.738	$1.19 \cdot 10^{-3}$ (0.6%)	7.472 (0.8%)	0.827 (12.0%)
20	$1.0 \cdot 10^{-3}$	6.648	0.659	$1.05 \cdot 10^{-3}$ (1.5%)	6.883 (3.5%)	0.747 (13.3%)
≈ 23.3	$8.6 \cdot 10^{-4}$	6.103	0.610	$9.22 \cdot 10^{-4}$ (7.2%)	6.396 (4.8%)	0.697 (14.4%)

Re	$\tilde{c}_D$	$\tilde{c}_L$	$\bar{\nu}$	$\bar{c}_D$	$\bar{c}_L$
≈ 13.3	6.710 (21.6%)	0.039 (95.6%)	$2.24 \cdot 10^{-3}$	8.766 (2.5%)	0.100 (88.9%)
≈ 16.6	5.865 (20.9%)	0.021 (97.1%)	$1.77 \cdot 10^{-3}$	7.467 (0.7%)	0.059 (93.0%)
20	5.289 (19.9%)	0.011 (98.3%)	$1.45 \cdot 10^{-3}$	6.579 (1.0%)	0.036 (94.5%)
≈ 23.3	4.875 (30.1%)	0.005 (99.2%)	$1.22 \cdot 10^{-3}$	5.936 (2.7%)	0.023 (96.3%)

In the end we want to emphasise that the presented algorithms are only heuristics and have no theoretical justification. However, we will present a bunch of test cases to exemplify the functionality of the presented technique. Thus, we consider two channels with a different roughness for a different set of Reynolds numbers and present numerical results.

In Figure 6.19 we visualise the two different geometries, which are denoted by R1 and R2. For these channels we consider the Reynolds numbers $13.3, 16.6, 20$ and 23.3, which corespond to the viscosities $1.5 \cdot 10^{-3}, 1.2 \cdot 10^{-3}, 1.0 \cdot 10^{-3}$ and $8.6 \cdot 10^{-4}$ and produce by solving the state equation the observation $\hat{I}(\boldsymbol{x})$, which we use as data function in the cost functional of the optimisation problem. Afterwards, we applied Algorithm 6.5 to evaluate both the viscosity parameter and a boundary function on the lower boundary. As tolerance we used $\mathrm{Tol} = 10^{-3}$ in the algorithm. The results of all calculations are presented in Table 6.7.

Table 6.8. Algorithm 6.5 applied to the test data function $\hat{I}$ for the configuration R1 (see Figure 6.19) and $\nu = 1 \cdot 10^{-3}$. The procedure stoped after step 13 as $\frac{|\alpha_k - \alpha_{k-1}|}{|\alpha_{k-1}|}$ droped below the tolerance of 10^{-3}.

k	$\nu^{(k)}$ (No. It.)	$\frac{\lvert\nu^{(k)}-\nu^{(k-1)}\rvert}{\lvert\nu^{(k-1)}\rvert}$	α_k	$\frac{\lvert\alpha_k-\alpha_{k-1}\rvert}{\lvert\alpha_k\rvert}$
1	$2.3046 \cdot 10^{-3}$ (18)	–	$1.0000 \cdot 10^{3}$	–
2	$1.3310 \cdot 10^{-3}$ (15)	$4.22 \cdot 10^{-1}$	$5.0000 \cdot 10^{2}$	$5.00 \cdot 10^{-1}$
3	$1.0608 \cdot 10^{-3}$ (11)	$2.03 \cdot 10^{-1}$	$2.2054 \cdot 10^{2}$	$5.59 \cdot 10^{-1}$
4	$9.5933 \cdot 10^{-4}$ (11)	$9.56 \cdot 10^{-2}$	$1.0406 \cdot 10^{2}$	$5.28 \cdot 10^{-1}$
5	$9.2965 \cdot 10^{-4}$ (14)	$3.09 \cdot 10^{-2}$	$2.2511 \cdot 10^{1}$	$7.84 \cdot 10^{-1}$
6	$9.3085 \cdot 10^{-4}$ (5)	$1.28 \cdot 10^{-3}$	$7.3675 \cdot 10^{-1}$	$9.67 \cdot 10^{-1}$
7	$9.8488 \cdot 10^{-4}$ (9)	$5.80 \cdot 10^{-2}$	$2.1205 \cdot 10^{-1}$	$7.12 \cdot 10^{-1}$
8	$1.0050 \cdot 10^{-3}$ (13)	$2.04 \cdot 10^{-2}$	$7.1430 \cdot 10^{-1}$	$2.37 \cdot 10^{0}$
9	$9.9817 \cdot 10^{-4}$ (3)	$6.77 \cdot 10^{-3}$	$7.7008 \cdot 10^{-1}$	$7.81 \cdot 10^{-2}$
10	$9.9567 \cdot 10^{-4}$ (1)	$2.51 \cdot 10^{-3}$	$7.7881 \cdot 10^{-1}$	$1.13 \cdot 10^{-2}$
11	$9.9378 \cdot 10^{-4}$ (2)	$1.89 \cdot 10^{-3}$	$7.7595 \cdot 10^{-1}$	$3.67 \cdot 10^{-3}$
12	$9.9452 \cdot 10^{-4}$ (6)	$7.39 \cdot 10^{-4}$	$7.7260 \cdot 10^{-1}$	$4.32 \cdot 10^{-3}$
13	$9.9452 \cdot 10^{-4}$ (8)	$< 1 \cdot 10^{-4}$	$7.7392 \cdot 10^{-1}$	$1.71 \cdot 10^{-3}$

Compared to the values $\tilde{c}_D$, $\tilde{c}_L$, $\bar{nu}$, $\bar{c}_D$ and $\bar{c}_L$ the Algorithm 6.5 yield with the values $\hat{\nu}$, $\hat{c}_D$ and $\hat{c}_L$ good estimations. Thus the algorithm performs very well in consideration of the fact that we have used minimal information for the fluid flow model (inflow boundary, homogeneuous Dirichlet conditions on the top wall and the obstacle). Finally we present in Table 6.8 the behaviour of Algorithm 6.5 for the case R1 and $\nu = 10^{-3}$.

6.6. Numerical Example for the Time-Dependent Case

Finally we want to apply the presented techniques for a time-dependent example. However, the computational cost increases drastically so that we avoid the estimation of the viscosity parameter and assume that this parameter is already known. We concentrate on the identification process of the boundary functions on the lower boundary. To choose α appropriately small we use the homotopy method with the heuristic automatic stopping rule from the time-independent example.

We will at first describe the forward calculation, which we use to generate the intensity function for the identification process. Starting point is again the benchmark channel in Figure 6.5 with a rough bottom boundary. The equations for the forward calculation are now given by the time-dependent system in equation (6.1). The initial functions for the intensity $I^0(\boldsymbol{x})$ and the transport field $\boldsymbol{u}^0(\boldsymbol{x})$ will both be zero. The boundary conditions are given by

$$\begin{aligned}
\boldsymbol{u}(\boldsymbol{x},t) &= 4u_{\max}y(0.41-y)\sin\left(\frac{\pi t}{8}\right), && \text{on } \Gamma_{\text{In}} := \{0\}\times[0,0.41],\\
\nu\partial_{\boldsymbol{n}}\boldsymbol{u}(\boldsymbol{x},t) - p(\boldsymbol{x},t)\boldsymbol{n}(\boldsymbol{x}) &= 0, && \text{on } \Gamma_{\text{Out}} := \{0.9\}\times[0,0.41],\\
\boldsymbol{u}(\boldsymbol{x},t) &= 0, && \text{on } \Gamma_{\text{D}} := \partial\Omega\setminus(\Gamma_{\text{In}}\cup\Gamma_{\text{Out}})
\end{aligned}$$

for the transport field and

$$\begin{aligned}
I(\boldsymbol{x},t) &= \begin{cases} 0.075\min(t,1)\left(1+\cos\left(\frac{\pi}{r}\sqrt{y-y_i}\right)\right), & \forall y\in B_r(y_i),\\ 0, & \text{else,}\end{cases} && \text{on } \Gamma_{\text{In}},\\
\varepsilon\partial_{\boldsymbol{n}}I(\boldsymbol{x},t) &= 0, && \text{on } \Gamma_{\text{Out}},\\
I(\boldsymbol{x},t) &= 0, && \text{on } \Gamma_{\text{D}},
\end{aligned}$$

for the intensity function. The parameters in this setting are chosen as follows:

$$\nu = 10^{-3}\frac{\text{m}^2}{\text{s}},\ \rho = 1\frac{\text{kg}}{\text{s}},\ \varepsilon = 10^{-5} \qquad \text{and} \quad u_{\max} = 8.9\frac{\text{m}}{\text{s}}.$$

Thus the Reynolds number calculated with the mean velocity $\bar{u} = \frac{2}{3}\max|u_1(\boldsymbol{x},t)| \approx 1$ is approximately 100. For the intensity boundary condition we have $i = 1,2$ and set $y_1 = 0.12\text{m}$, $y_2 = 0.3\text{m}$ and $r = 0.075\text{m}$.

For the numerical realisation we use the implicit Euler method for the time discretisation of the time interval $[0,8]$ with 1600 time steps to resolve the dynamics of the problem. For the spatial discretisation we use bilinear finite elements for all four components $p(\boldsymbol{x},\boldsymbol{t}), \boldsymbol{u}(\boldsymbol{x},t)$ and $I(\boldsymbol{x},t)$ with LP stabilisation for the convection dominance and to ensure inf-sup stability.

We calculate again on a mesh with 2696 nodes. In the right columns of the Figures 6.20 and 6.21 we visualise the velocity magnitude and the intensity function at four different time points $t = 2,4,6,8$.

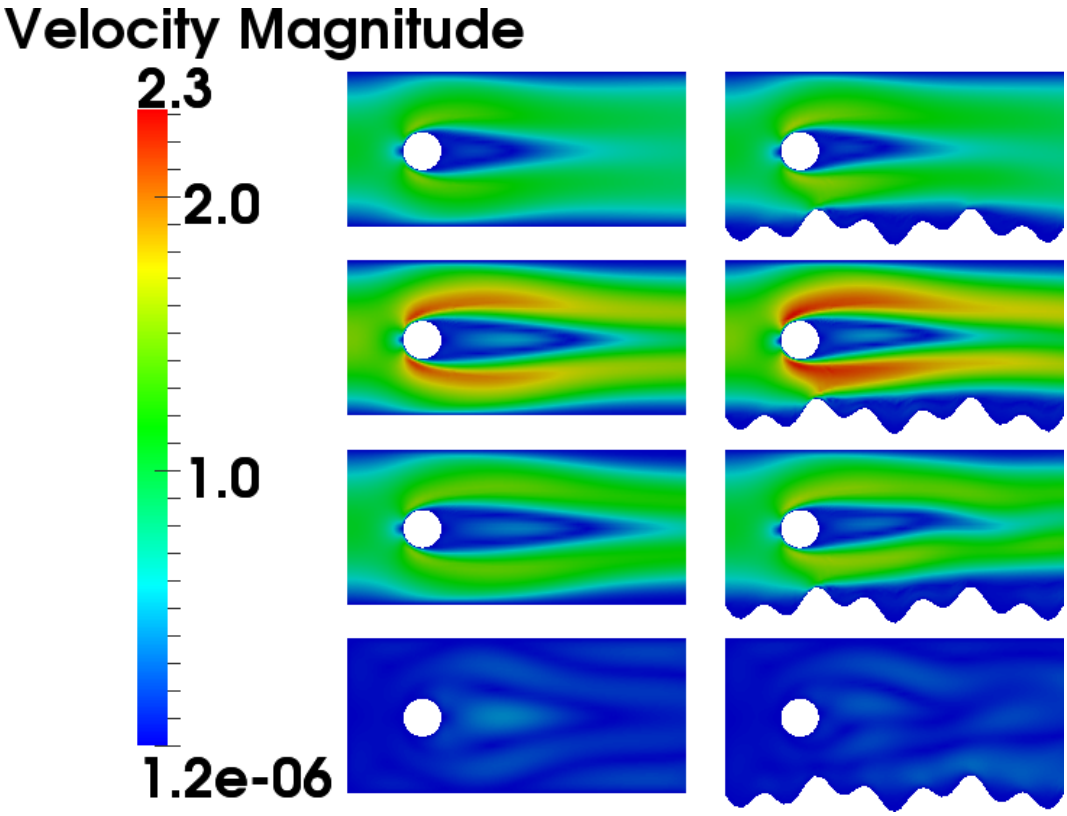

Figure 6.20. Velocity magnitude ($\mathrm{Re} \approx 100$). Left Column: Result of a forward calculation with homogeneous Dirichlet conditions on the bottom boundary (implicit Euler with 80 time steps). Right Column: Results for a forward calculation with the roughness on the lower boundary (implicit Euler with 1600 time steps). From top to bottom four different time points $t = 2, 4, 6, 8$.

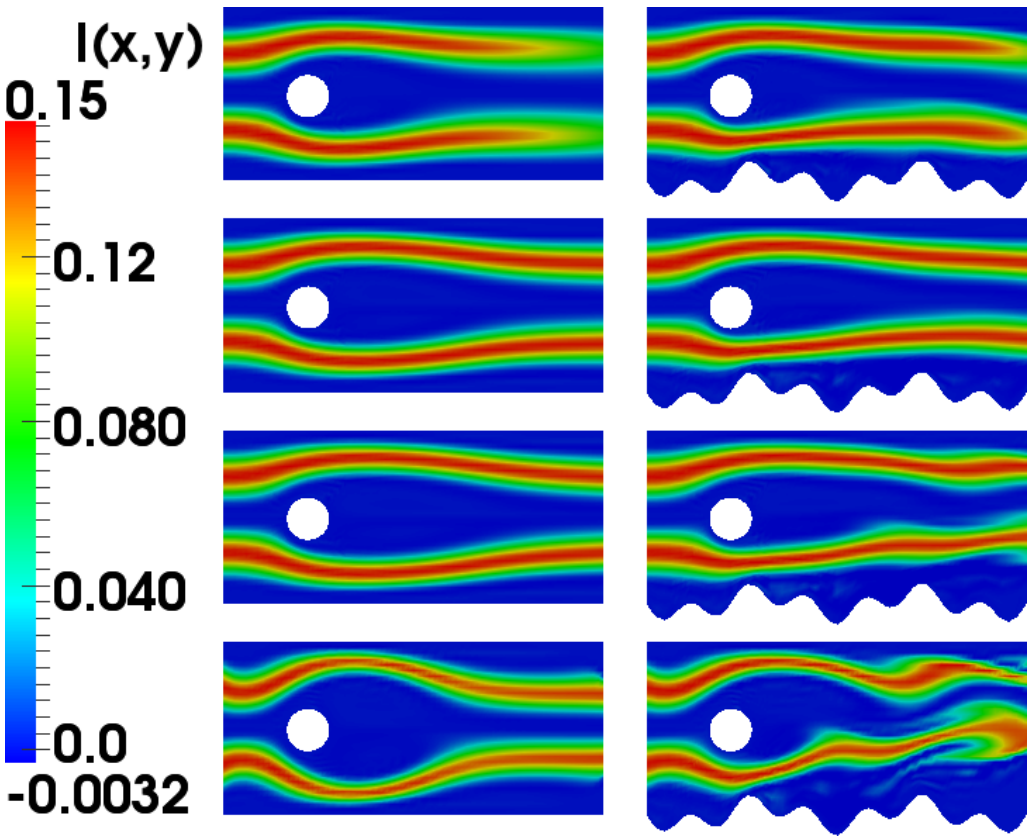

Figure 6.21. Intensity function $I(\boldsymbol{x}, t)$ (Re $\approx$ 100). Left Column: Result of a forward calculation with homogeneous Dirichlet conditions on the bottom boundary (implicit Euler with 80 time steps). Right Column: Results for a forward calculation with the roughness on the lower boundary (implicit Euler with 1600 time steps). From top to bottom four different time points $t = 2, 4, 6, 8$.

Our aim is again to identify appropriate boundary conditions on the bottom wall, which yield a good approximation of the flow scenario only by taking the information on the intensity function into account. Moreover, we assume that the intensity function is only given on a sparse time grid, that means we have only a sequence

$$\hat{I}_k(\boldsymbol{x}) := I(\boldsymbol{x}, t_k), \qquad \text{with} \quad k = 1, \dots, 80, \qquad \text{and} \quad t_k - t_{k-1} = 0.1$$

as given data.

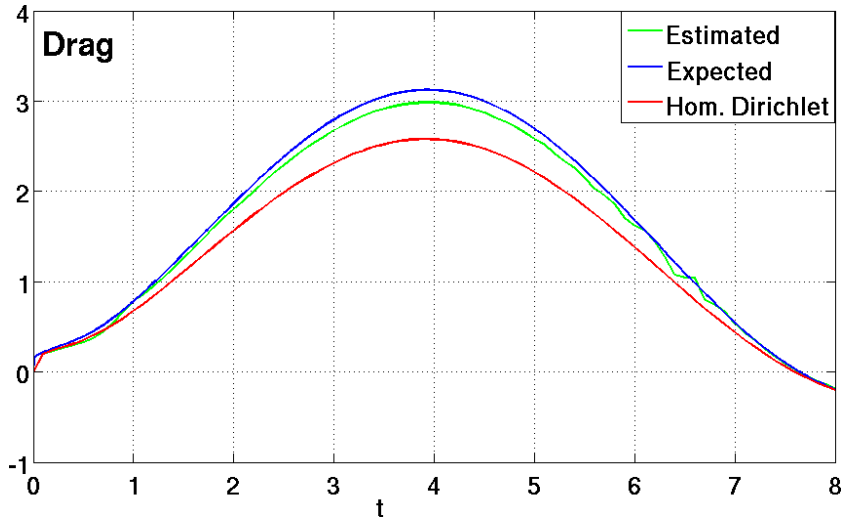

Figure 6.22. Drag coefficient: Original flow in the rough channel (blue curve, time steps: 1600). Estimated flow by the boundary identification process (green curve, time steps: 80) for $\alpha = 0.497$ (obtained by the α-strategy in Algorithm 6.1). Flow in a channel with homogeneous Dirichlet boundary on the bottom wall (red curve, time steps: 80).

The boundary identification is then performed by solving the Optimisation Problem 6.2 with an inexact Newton-CG method, where we only performed a few CG-steps in each Newton step and several Newton steps until we drop below a threshold of 10^{-4} for the Newton residual.

We set $\zeta = 100$ to scale the data term and avoid to control the intensity function on the boundary, since we assume that there is no essential transport of the signal across the bottom boundary. To find an appropriate α we use the strategy we used in the time-independent case. Due to repeated solving of the optimisation problem and the larger amount of Newton steps the computation becomes very time intensive and expensive (compare Chapter 4.2) as long as we calculate on the same temporal discretisation as for the forward calculation. We will therefore choose a temporal discretisation with a time step size of the same quantity as for the given intensity sequence $\hat{I}_k$ ($dt = 0.1$).

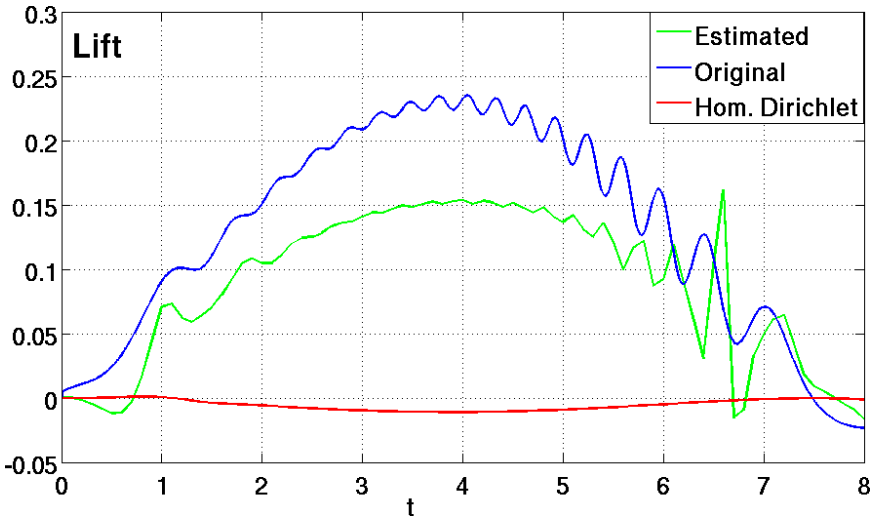

Figure 6.23. Lift coefficient: Original flow in the rough channel (blue curve, time steps: 1600). Estimated flow by the boundary identification process (green curve, time steps: 80) for $\alpha = 0.497$ (obtained by the α-strategy in Algorithm 6.1). Flow in a channel with homogeneous Dirichlet boundary on the bottom wall (red curve, time steps: 80).

For the mentioned time discretisation a forward calculation with homogeneous Dirichlet boundary conditions on an flat bottom boundary is visualised in the left columns of Figures 6.20 and 6.21. Especially for the intensity function, we see essential differences to the given data in the right column (see Figure 6.21).

In comparison to this Figures 6.24 and 6.25 show the results of our identification process (right columns of the figures). Although we see still differences compared to the expected solution, the solution seems better fitted than the one with a zero Dirichlet boundary condition on the bottom boundary. The quality of our identification is again documented by the drag and lift coefficient, which are visualised in Figures 6.22 and 6.23. The blue curves indicate in these figures the expected values, while the green curves indicate the estimate and the red curves the drag and lift coefficient for the benchmark channel with a smooth and flat boundary and prescribed homogenuous Dirichlet conditions. We see a significant improvement by the boundary identification process. Nevertheless the result is not as satisfactory as in the time-independent case.

One reason could be that the α-strategy fails. The α-strategy is presented in Table 6.9 and seems to be working fine. To make sure that the chosen parameter is reliable we calculated the solution also for $\alpha = 10^{-3}$ and visualised the estimated drag and lift coefficients in Figures 6.26 and 6.27. We see that in some areas the green curve fits the original drag and lift curve better. However, spurious oscillations are introduced in the initial phase and in the second half of the time interval for our solution. The reason for the oscillations is that in this particular example the boundary identification must also absorb the discretisation

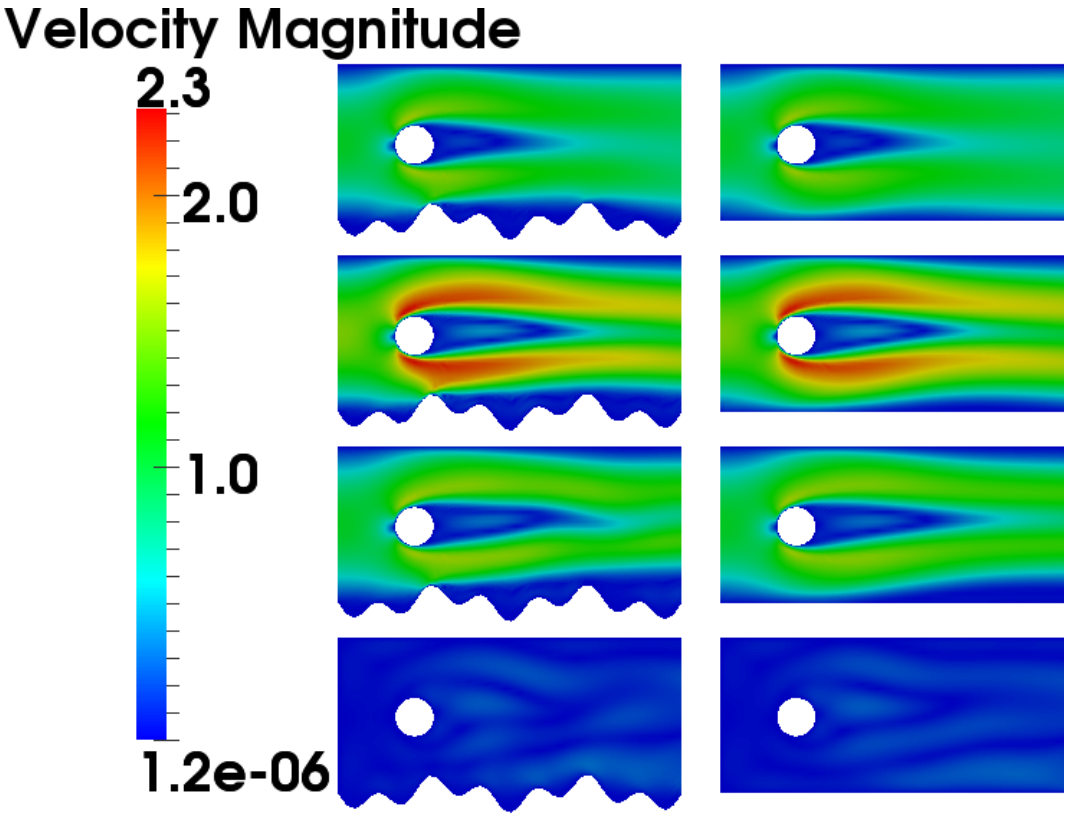

Figure 6.24. Velocity magnitude (Re $\approx$ 100). Left Column: Results for a forward calculation with the roughness on the lower boundary (implicit Euler with 1600 time steps). Right Column: Results of the Boundary Identification Process with $\alpha = 0.497$ obtained by the α-strategy from Algorithm 6.1. From top to bottom four different time points $t = 2, 4, 6, 8$.

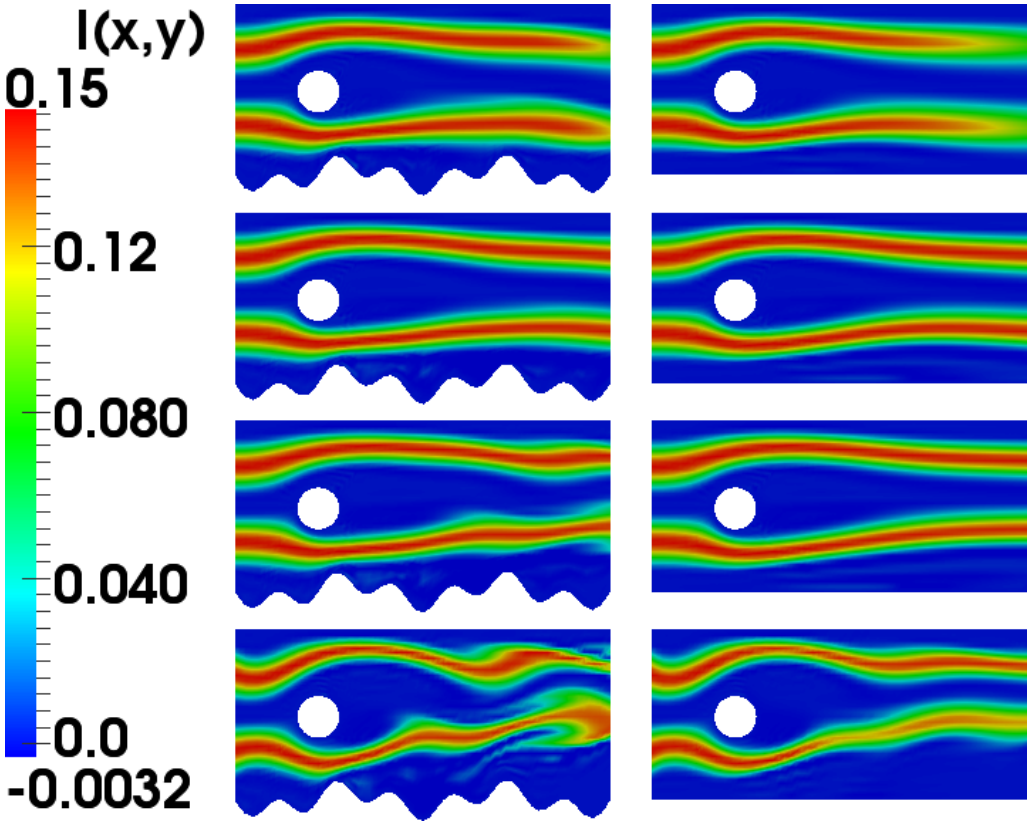

Figure 6.25. Intensity function $I(\boldsymbol{x}, t)(\mathrm{Re} \approx 100)$. Left Column: Results for a forward calculation with the roughness on the lower boundary (implicit Euler with 1600 time steps). Right Column: Results of the Boundary Identification Process with $\alpha = 0.497$ obtained by the α-strategy from Algorithm 6.1. From top to bottom four different time points $t = 2, 4, 6, 8$.

error, which results from choosing a large time step size $dt = 0.1$ in the numerical scheme in contrast to the time step size $dt = 0.005$ for the forward calculation. The chosen time step size for the optimisation problem is not able to resolve the dynamic behaviour. Thus the dynamics of the flow is introduced by the identified boundary condition $\boldsymbol{q}$. We see this effect mainly in the time period $[6, 8]$ in the lift coefficient (cf. Figures 6.23 and 6.27). However, the choice of a large α suppresses the fitting of the discretisation error and in this sense our α-strategy is reliable. Nevertheless, an interesting topic for future work would be to work with a time-dependent α, which is smaller in the laminar starting phase and becomes larger in phases where the identification process starts to fit the discretisation error.

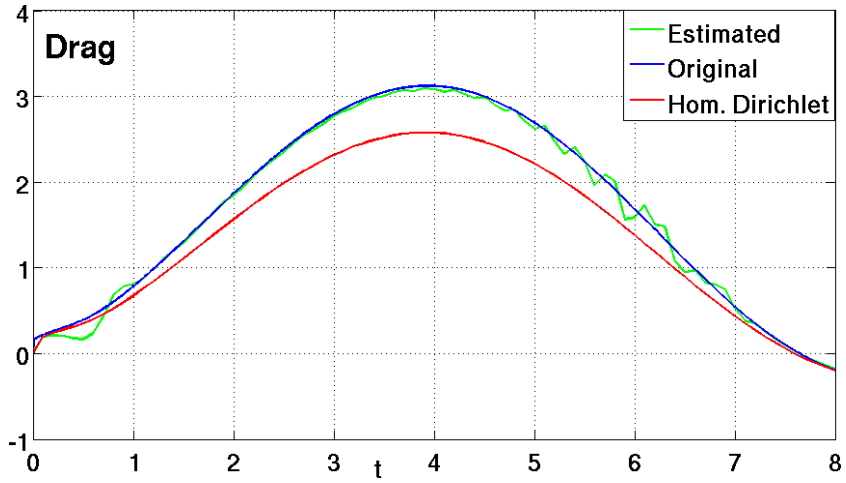

Figure 6.26. Drag coefficient: Original flow in the rough channel (blue line, time steps: 1600). Estimated flow by the boundary identification process (green line, time steps: 80) for $\alpha = 10^{-3}$. Flow in a channel with homogeneous Dirichlet boundary on the bottom wall (red line, time steps: 80).

Another possibility to reduce the influence of the discretisation error is to choose a smaller time step size, which on the other hand increases the already large computational effort of the solution process.

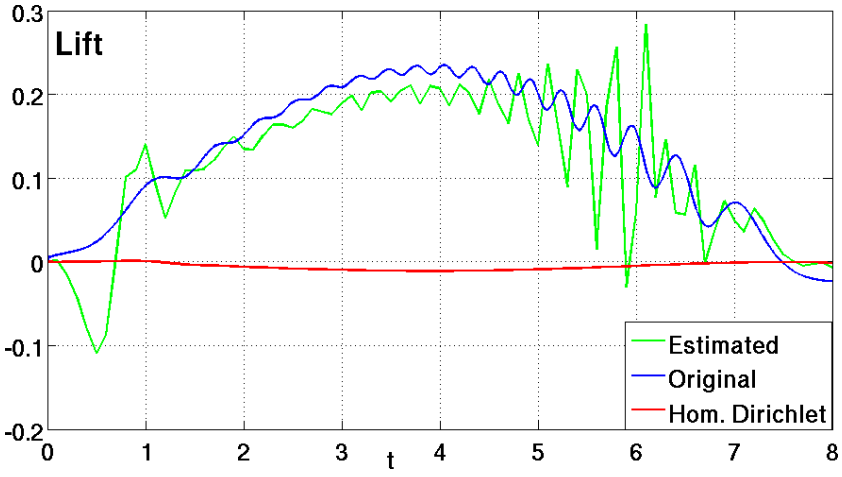

Figure 6.27. Lift coefficient: Original flow in the rough channel (blue line, time steps: 1600). Estimated flow by the boundary identification process (green line, time steps: 80) for $\alpha = 10^{-3}$. Flow in a channel with homogeneous Dirichlet boundary on the bottom wall (red line, time steps: 80).

Table 6.9. Algorithm 6.1 for the time-dependent boundary identification problem with initial value $\alpha = 1000$. As tolerance for the stopping criterion $s_\alpha := \frac{|\alpha_n - \alpha_{n-1}|}{|\alpha_{n-1}|}$ in α we choose 0.01.

n	α	$\lvert\alpha_n - \alpha_{n-1}\rvert$	$\lvert d(\alpha) - r(\alpha)\rvert$
1	1000		$1.598 \cdot 10^{-1}$
2	500	500	$1.434 \cdot 10^{-1}$
3	225.894	274.106	$1.191 \cdot 10^{-1}$
4	58.003	167.891	$7.232 \cdot 10^{-2}$
5	25.564	32.439	$4.974 \cdot 10^{-2}$
6	7.703	17.861	$2.725 \cdot 10^{-2}$
7	2.291	5.411	$1.170 \cdot 10^{-2}$
8	0.256	2.036	$3.702 \cdot 10^{-3}$
9	0.745	0.489	$2.690 \cdot 10^{-3}$
10	0.539	0.206	$6.138 \cdot 10^{-4}$
11	0.478	0.061	$1.960 \cdot 10^{-4}$
12	0.493	0.015	$5.627 \cdot 10^{-5}$
13	0.499	0.006	$2.710 \cdot 10^{-5}$
14	0.497	0.002	$4.206 \cdot 10^{-6}$

7. Prototypical Application: Monitoring Pollutants in the Atmosphere

This final chapter is devoted to demonstrate the ability of the developed techniques to solve complex problems, which we have to face when we consider real world applications. Our main objective is to demonstrate that using the modeling knowledge leads to more reliable results and thus the increased computational cost of the method is justified. Essential for these investigations is that we have comparable quantities. These quantities are not always available for real world applications. Moreover, real world data is in general disturbed by model uncertainties and unknown measurement errors, which influences the optimisation problem drastically. Thus the validation process should be performed in a framework where certain informations are available. Nevertheless, the emphasis should rely on a complex application, which is oriented at a real world scenario. That is the reason why we will use a synthetic prototypical application, which has an environmental physics background and was already motivated in the introduction of this thesis (Chapter 1.2.3, 3rd Example).
More precisely the motivating application is to reconstruct the wind flow in the lower atmosphere by using a sequence of satellite images observing the movement of dust plumes in the desert. The dust plumes act as an observable passive tracer in the ground based horizontal atmospheric flow. Accurate knowledge of the wind field is needed since it describes also the movement and distribution of harmful and possibly not observable substances. As quantity of interest we consider the mean value of the concentration of such a substance in a certain subdomain of the computational domain. The question is then if it is possible to compute the temporal evolution of this quantity by means of a reconstructed flow field, which we obtain by the use of our method.
We will proceed as follows. At first we will motivate the background of the prototypical application, explain the complications and describe the simplification which leads to the example. Furthermore, we will make simplifications and describe how we achieve comparable data by a forward calculation. Afterwards, we will use our methodology to solve the problem and compare our result to the expected values. The next step is to discuss the influence of the used fluid flow model. We will compare the original fluid flow model to simplified models (Stokes system and heat equation). We will show that the quality of the reconstruction is definitely increased by using as much model knowledge as possible.

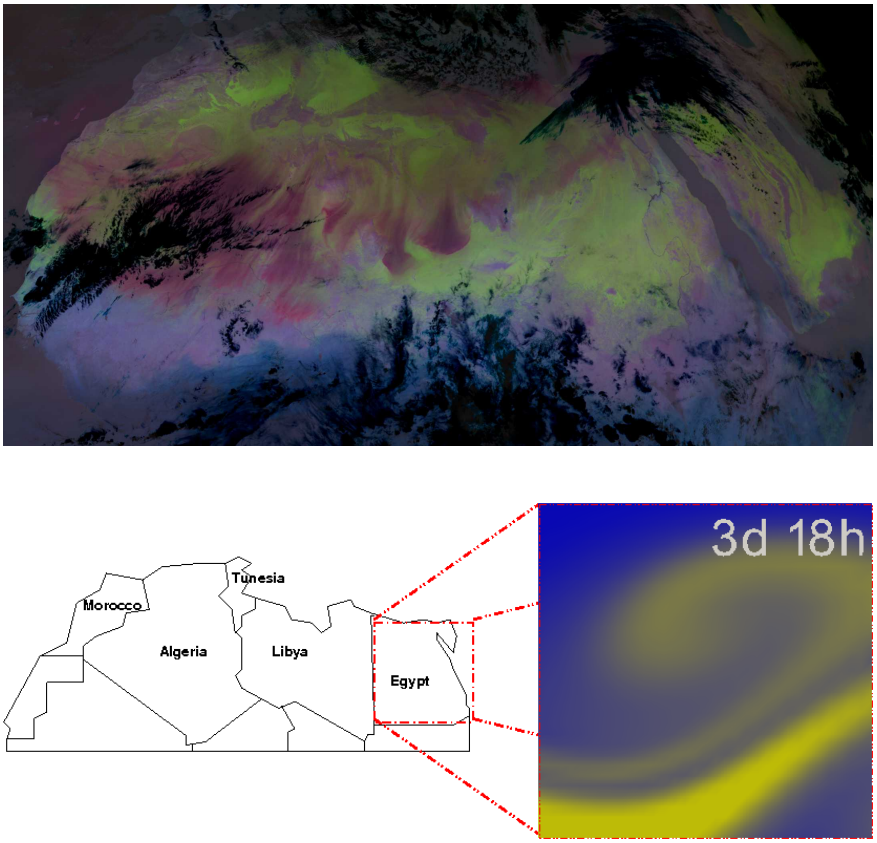

Figure 7.1. Top: False colour image taken by a geostationary satellite. Black coloured structures indicate water clouds. Sand dust plumes are coloured in magenta. Bottom: Schematical image of the northern African countries. The red coloured box indicates the computational domain Ω. The right hand side indicates the intensity functions on this domain. It is clear that we have movement across the boundaries of this domain.

7.1. Problem Description

The motivation for our prototypical example is the following scenario in environmental physics. We consider the Sahara desert, which is the biggest desert on earth. While we have very good measurements of the wind system in densely populated areas at the boundary of the desert, we have nearly no information about the wind in the interior, due to a lack of measurement stations. However, by satellite remote sensing we can observe the wind system due to the movement of water clouds, desert dust and other visible aerosols. See therefore the top image in Figure 7.1 which shows an image of the northern part of the African continent. Black coloured structures indicate water clouds and magenta coloured structures mark dust plumes. We can interpret the dust aerosols as a passive tracer of the wind system in the desert and we can use optical flow estimation techniques to gather informations of the optical flow field in a sequence of these satellite images. In a more statistical framework this was done by Bachl et al. [3], [4].
However, in the context of atmospheric flows especially physics-based optical flow techniques are of high importance, if we assume that this optical flow field represents an approximation of the underlying physical flow. Then we could use the approximated flow field to evaluate further quantities, which cannot be directly observed. As an example we think of a source of a harmful pollutant in the middle of the desert. The substance will be transported by the wind system. We want to estimate the amount of this substance entering populated areas.

To fix ideas we state the problem in a concrete context. We choose as computational domain a quadrilateral aperture of north east Africa, which contains almost the whole area of Egypt (see bottom picture in Figure 7.1). In the North at the coast and around the Nil river the region is densely populated and we assume that on the upper and the right boundary distributed measurements for the wind field are available. However, the artificial boundaries of the computational domain in the west and in the south run directly through the desert and we assume that no or only sparse measurements of the ground-based wind system are available. Our developed method fits now perfectly to reconstruct reliable boundary conditions, which yield an approximation of the flow. Furthermore, information about the wind system could be of interest to judge the consequences of intensifying agriculture in the desert. Industrial agriculture is a source for air pollution (pesticides, fertilisers etc.) and the pollutants are distributed by the wind system. Moreover, we can assume that several of these substances cannot be directly observed by satellite remote sensing and therefore information about their temporal evolution could be of high interest.

However, we face a lot of difficulties, if we want to consider this highly sophisticated real world example:

- The most important aspect is that to the authors knowledge there exists not correlation between a measured brightness pattern by a camera and the mean density of the dust in the vertical column observed by the brightness pattern. Thus, the intensity function is no physical meaningful quantity in connection to the dust plumes and therefore also the connection to the underlying physical flow field is not clear.

- Even if a physical meaningful model for the dust transport would be available, the satellite images are not constantly illuminated due to the changing altitude of the sun. Thus, the physics-based optical flow equation is certainly not valid and needs a reliable modification.
- Moreover, increasing wind speed raises dust, while slow speeds lead to a deposition of sand. Both effects influence the intensity function and have to be introduced to the model.
- The Navier-Stokes system is only a part of a more complex weather model (introducing also temperature, humidity etc.) describing the wind system.
- The satellite data is disturbed by measurement errors.
- The data is also polluted by errors introduced due to post-processing of the data (e. g. taking out the background or filling in the gaps in the data, due to water clouds).

A competitive method for this real world application must be adapted to all these difficulties. This adaption process requires also a validation of several steps related to the mentioned issues. However, this is beyond the scope of this thesis and we will concentrate on validating our methodology for a prototypical example, where we generate the data and thus have the information on the underlying flow field and the transported tracers. Furthermore, we know the physical model for certain and can assume a direct connection between optical flow and underlying physical flow. Our scenario focuses on the following aspects:

- The images define our computational domain. They represent only an aperture of the original flow domain. Thus our method must be able to reconstruct:
  - The fluid flow field across the computational domain boundaries. Therefore we have to estimate appropriate boundary conditions for the function $\boldsymbol{u}(\boldsymbol{x}, t)$.
  - The transport of intensity signals across the boundary. Again this is realised by estimating an appropriate boundary condition for $I(\boldsymbol{x}, t)$ in space and time.
- Furthermore, we want to be able to decouple the sampling rate of the satellite images and the time step size of our numerical calculation to be able to cope with image sequences which have a sparse temporal structure.
- Finally we want to introduce as much knowledge about the fluid model as possible.

7.1.1. Setting and Forward Calculation

As mentioned before we will consider a domain

$$\Omega = (0, a) \times (0, a)$$

with $a = 800km$, which represents a quadrilateral aperture of almost the area of Egypt. Nearly the entire country is part of the desert ($> 95\%$). The only exception is the Nil valley in the east and Nil delta in the north of the country. We assume in our example

that the right boundary represents the river Nil and the top boundary the coast line. Later on we will prescribe boundary conditions on these boundaries, while we assume that we lack such dense wind field information on the left and the bottom boundaries.
Oriented on the realistic application our scenario needs a time-dependent flow across all boundaries. Thus, we perform a forward calculation on a bigger computational domain Ω_{For}, which contains Ω.

At first we assume that the ground-based wind field is described by the two-dimensional Navier-Stokes equations. Furthermore, we assume a straightforward relation to the intensity function documenting the movement of dust in Ω_{For}. To generate dynamical behaviour we design a domain for the forward calculation by means of the examples we presented in the last chapter. Figure 7.2 indicates the domain Ω_{For} by the green colour. The red coloured box indicates our aperture Ω, where we consider the flow later on for the reconstruction. We prescribe an inflow profile on the left magenta boundary part

$$\boldsymbol{u}(\boldsymbol{x},t) = \left(\bar{u}\min(t,1)\max\left(0, \frac{1}{0.25^2}(y-0.5)(1-y)\right), 0\right)^T, \qquad \text{with } \bar{u} = 2.813\frac{a}{d}$$

and the "do nothing" outflow condition on the right side of the channel. On all other boundaries we prescribe homogeneous Dirichlet conditions. The curved shape of the lower boundary was chosen to generate more dynamical structures of the flow. It is given by the function

$$y(x) = 0.3\sin\left(\frac{\pi}{2}x\right)\cos\left(\frac{20}{19}\pi x\right).$$

We prescribe two kinds of sources for the intensity function $I(\boldsymbol{x},t)$. Firstly, the "west

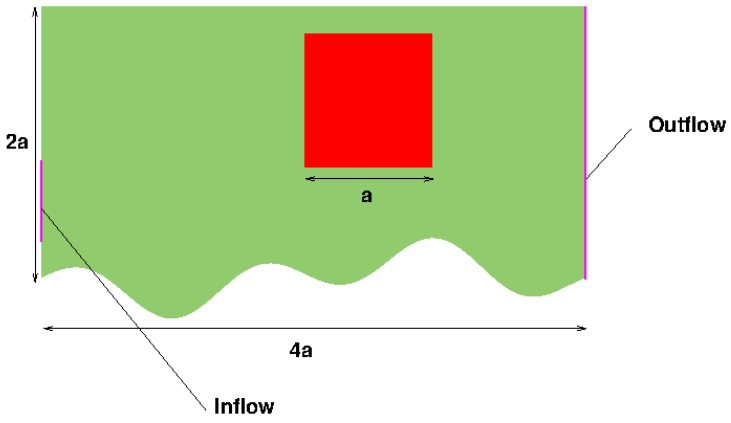

Figure 7.2. Computational domain Ω_{For} for the forward calculation (green) and aperture Ω for the estimation (red). The left magenta boundary is the inflow boundary and the right boundary is the outflow boundary.

wind" transports signals into Ω_{For} by the boundary function

$$I(\boldsymbol{x},t) = \begin{cases} 2\max\left(\sin\left(\pi t - \frac{\pi}{2}\right) + 1, 0\right)\left(1 + \cos\left(\frac{\pi}{r}|y - 0.75|\right)\right), & |y - 0.75| < 0.25, \\ 0, & \text{else.} \end{cases}$$

Secondly, we introduce a source term into the convection-diffusion equation by the right hand side function:

$$f(\boldsymbol{x},t) = \begin{cases} 320\min(t,1)(y-1)(1.5-y)(x-1)(1.5-x), & \text{for } |x - 1.25| < 0.25, \\ & \text{and } |y - 1.25| < 0.25, \\ 0, & \text{else.} \end{cases}$$

Moreover we choose the following parameters in the equations. For the diffusive term in the convection-diffusion equation we choose

$$\varepsilon = 0.001.$$

We will briefly discuss the choice of the viscosity in the Navier-Stokes part of the system. Since we assume no temperature influences in our simplified model we consider the kinematic viscosity of air at $15°C$, which is $1.48 \cdot 10^{-5}\frac{m^2}{s}$. We have to convert this quantity to our unit system, which results in the value

$$\nu = 8.183 \cdot 10^{-9}\frac{a}{d}.$$

The value is comparably small and thus we work actually with a convection stabilised version (see the LP stabilisation in Chapter 3.4.2) of the Euler system.

Figure 7.3 shows the result of this forward calculation for two different time steps. Figure 7.4 shows a discrete sequence of the intensity distribution $I(\boldsymbol{x},t)$ for the aperture $x \in (2,3)$ and $y \in (0.8, 1.8)$.

7.1.2. Reconstruction of the Distribution of a Pollutant

In this subsection we formulate a prototypical problem, which we want to solve. Starting point is the temporal sequence $(\mathcal{I}_k)_{k=1}^N$ of spatial intensity distributions in Ω documenting the movement of a passive tracer (transported dust plumes), which we constructed by the forward calculation in the last subsection.
We assume that we have no knowledge of the underlying flow field, except for the boundary data at the right and top boundaries of Ω.

The objective is now to evaluate the temporal and spatial distribution of a second, not directly observable passive tracer, which is described by the equation

$$\partial_t c(\boldsymbol{x},t) - \eta\Delta c(\boldsymbol{x},t) + \boldsymbol{u}(\boldsymbol{x},t)\cdot\nabla c(\boldsymbol{x},t) = f(\boldsymbol{x},t), \qquad \text{in } \Omega \times [t_0, T].$$

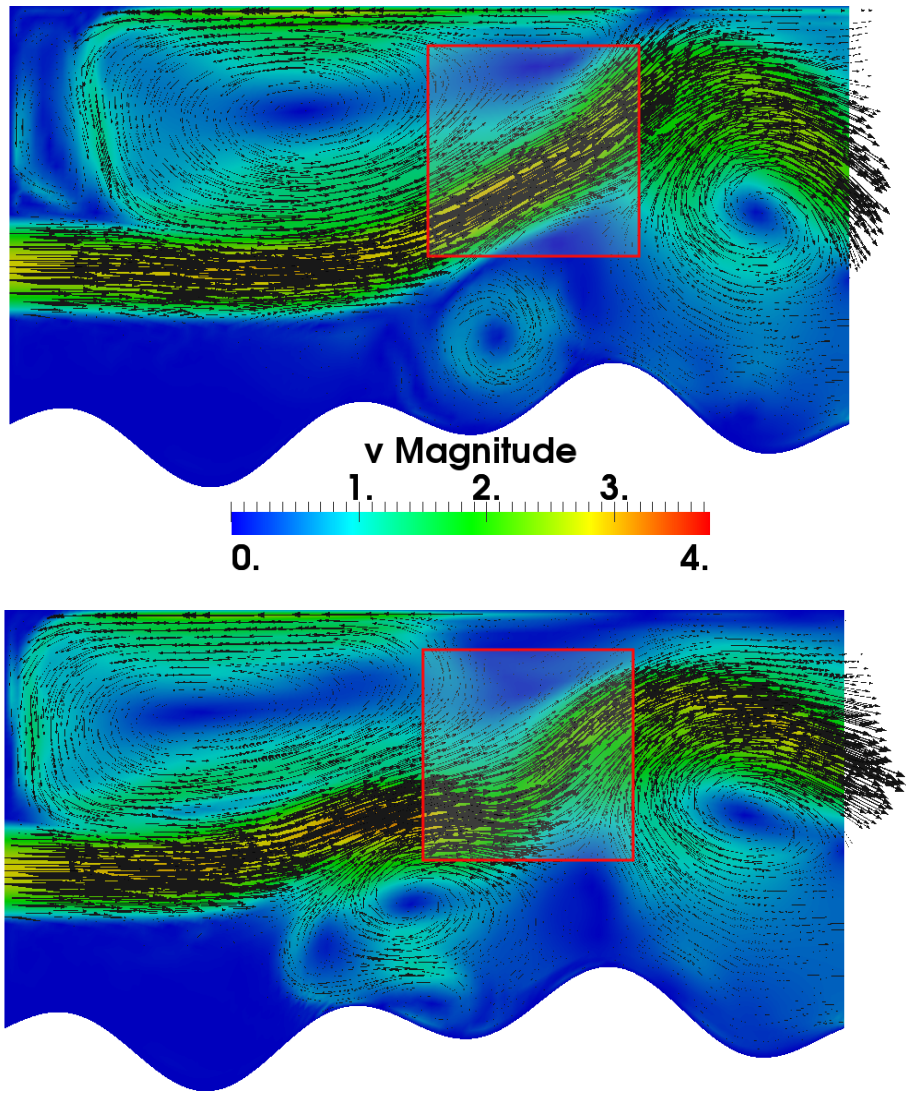

Figure 7.3. Results of the forward calculation visualised by a coloured magnitude map and vectors. Top: $t = 25d$. Bottom: $t = 28d$. The red quadrilateral indicates the aperture we will later on consider for the reconstruction.

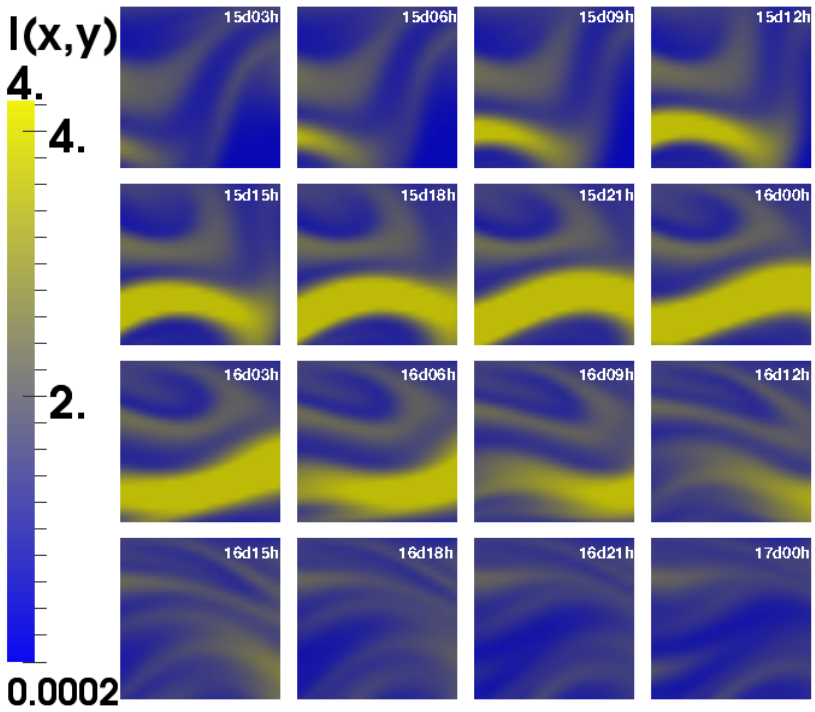

Figure 7.4. Example for an intensity function sequence $\mathcal{I}$ documenting the movement of the passive tracer in the domain Ω from $t_1 = 15d03h$ to $t_f = 17d$ with $\delta t = 3h$. We see a highly dynamical movement of the tracer. The tracer is sparsely distributed in space and we want to emphasise that the tracer is transported across the boundaries.

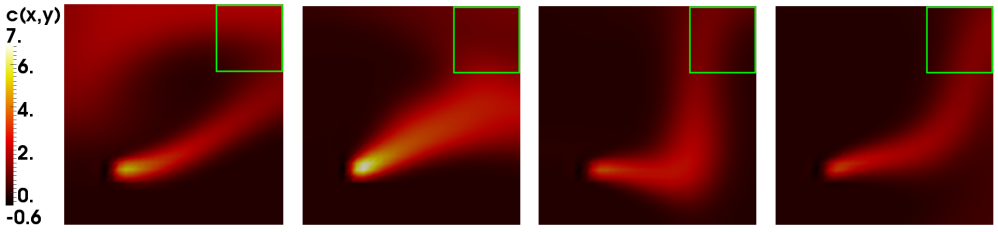

Figure 7.5. A second passive tracer, a pollutant, with source in the lower left corner of Ω, which is transported through the domain by the solution of the forward calculation on Ω. The green box indicates the area of interest Ω_{Det} where we want to evaluate the mean concentration of the pollutant.

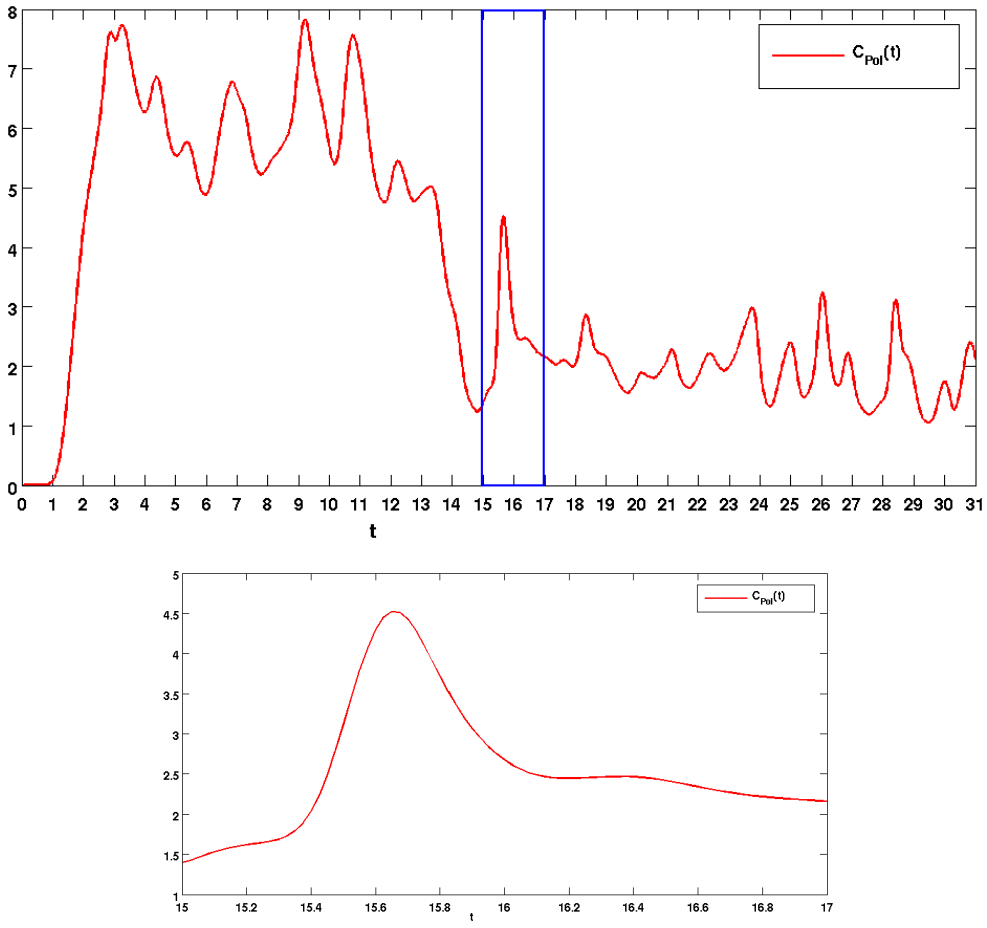

Figure 7.6. The mean $C_{\mathrm{Pol}}(t)$ of the concentration $c(\boldsymbol{x}, t)$ of the pollutant in the domain Ω_{Det} depending on the time variable t. Top: For the whole time horizon of the forward calculation. Bottom: For the time interval $t = [15d, 17d]$.

We assume $c(\boldsymbol{x}, t)$ to be the concentration of a harmful pollutant. The source $f(\boldsymbol{x}, t)$ of the pollutant is known (e. g. area with intensive industrial agriculture in the desert). To evaluate a reliable distribution of the pollutant, we need a good approximation of the transport vector field $\boldsymbol{u}(\boldsymbol{x}, t)$. However, the transport vector field is the same field that transports the observable passive tracer, which is documented by our sequence $(\mathcal{I}_k)_{k=1}^N$.

Thus we have to estimate appropriate boundary functions of $\boldsymbol{u}(\boldsymbol{x}, t)$ on the left and the lower boundary and for the intensity function $I(\boldsymbol{x}, t)$ on all boundaries. We will employ our method to obtain this information by using only the intensity function sequence.

To show that our reconstruction is reliable we define a quantity of interest, which is the spatial mean of the pollutant concentration in a certain detection area Ω_{Det} at a fixed time point

$$C_{\text{Pol}}(t) = \frac{1}{|\Omega_{\text{Det}}|} \int_{\Omega_{\text{Det}}} c(\boldsymbol{x}, t)\, d\boldsymbol{x}.$$

The domain Ω_{Det} could be interpreted as a densely populated area, where we want to figure out how big the amount of the transported pollutant is.

Figure 7.6 shows the function $C_{\text{Pol}}(t)$ for the wind field obtained by the forward calculation.

Our objective is now to recover C_{Pol}, by identifying appropriate boundary conditions on the left and lower boundaries with our physics-based flow estimation technique.

7.2. Numerical Results

We divide this results section into two parts. In the first subsection we will illustrate the ability of our method to recover the flow, even with sparse given data. In the second subsection we concentrate on the influence of the fluid model.

7.2.1. Reconstruction by Boundary Identification

As mentioned before the objective is to reconstruct the flow on a certain time interval by the methodology developed throughout this thesis. We will concretise the setting of the PDE constrained optimisation framework for this special problem.

The computational domain is given by $\Omega = (0, a) \times (0, a)$. For the control boundary, the left and the lower part of the boundary, we set

$$\Gamma_{\text{Con}} = \{0\} \times (0, a) \cup (0, a) \times \{0\}.$$

As time interval we choose $[15d, 17d]$. The time discretisation is given by $k = 0.025d$. The spatial mesh consists of 1089 equidistantly distributed nodes.

We wish to find a minimum of the functional

$$J(\boldsymbol{u}, I) = \frac{\sigma}{2} \sum_{k=1}^{N} \|I(t_k) - \mathcal{I}_k\|^2_{L^2(\Omega)} + \frac{\alpha}{2} \int_{t_0}^{T} \|\boldsymbol{q_u}(t)\|^2_{L^2(\Gamma_{\text{Con}})}\, dt + \frac{\beta}{2} \int_{t_0}^{T} \|q_I(t)\|^2_{L^2(\partial\Omega)^2}\, dt,$$

with $\sigma = 100$ subject to an appropriate weak formulation of the system

$$\begin{aligned} \partial_t I - \varepsilon \Delta I + \boldsymbol{u} \cdot \nabla I = 0, &\qquad \text{in } \Omega \times (t_0, T], \\ \partial_t \boldsymbol{u} - \nu \Delta \boldsymbol{u} + \boldsymbol{u} \cdot \nabla \boldsymbol{u} + \nabla p = 0, &\qquad \text{in } \Omega \times (t_0, T], \\ \nabla \cdot \boldsymbol{u} = 0, &\qquad \text{in } \Omega \times (t_0, T]. \end{aligned}$$

The boundary conditions for this system are given in the following strong formulation for almost every time point t

$$\begin{aligned} \varepsilon \partial_{\boldsymbol{n}} I(t) &= \frac{1}{\mu_I} \left(q_I(t) - I(t)\right) - \frac{1}{2} \left(\boldsymbol{u}(t) \cdot \boldsymbol{n}\right) I(t), && \text{on } \partial\Omega, \\ \nu \partial_{\boldsymbol{n}} \boldsymbol{u}(t) - p(t)\boldsymbol{n} &= \frac{1}{\mu_{\boldsymbol{u},1}} \left(\hat{\boldsymbol{u}}(t) - \boldsymbol{u}(t)\right) - \frac{1}{2} \left(\boldsymbol{u}(t) \cdot \boldsymbol{n}\right) \boldsymbol{u}(t), && \text{on } \partial\Omega \setminus \Gamma_{\text{Con}}, \\ \nu \partial_{\boldsymbol{n}} \boldsymbol{u}(t) - p(t)\boldsymbol{n} &= \frac{1}{\mu_{\boldsymbol{u},2}} \left(\left(\boldsymbol{u}^0 + \boldsymbol{q}(t)\right) - \boldsymbol{u}(t)\right) - \frac{1}{2} \left(\boldsymbol{u}(t) \cdot \boldsymbol{n}\right) \boldsymbol{u}(t), && \text{on } \Gamma_{\text{Con}}, \end{aligned}$$

where $\hat{\boldsymbol{u}}$ denotes measurements of the flow field at the right and upper boundaries, which are assumed to be accurate. Furthermore, we have the initial conditions

$$I(\boldsymbol{x}, 0) = \mathcal{I}_0(\boldsymbol{x}) \qquad \text{and} \quad \boldsymbol{u}(\boldsymbol{x}, 0) = \boldsymbol{u}^0(\boldsymbol{x}), \qquad \text{in } \Omega,$$

which are also assumed to be given. The boundary conditions of the initial value $\boldsymbol{u}^0$ at the boundary part Γ_{Con} are used to set boundary conditions for the left and lower boundaries for the whole time horizon to stabilise the computational process. However, the control $\boldsymbol{q_u}$ has to adapt to the temporal change of the boundary conditions on Γ_{Con}.

The parameters are chosen as follows

$$\varepsilon = 10^{-3}, \qquad \nu = 8.18 \cdot 10^{-9}, \qquad \mu_{\boldsymbol{u},1} = h^2 \qquad \text{and} \quad \mu_{\boldsymbol{u},2} = h.$$

For the realisation of the control in the convection-diffusion part of the system we want to set $\mu = 0$ and use therefore a Nitsche-type formulation (Chapter 3.3, equation (3.15))

$$-\varepsilon \left(\langle \partial_{\boldsymbol{n}} I, \varphi \rangle_{\partial\Omega} + \langle I - q_D, \partial_{\boldsymbol{n}} \varphi \rangle_{\partial\Omega}\right) + \frac{1}{\delta} \langle I - q_D, \varphi \rangle_{\partial\Omega},$$

with

$$\delta = \begin{cases} -\boldsymbol{u} \cdot \boldsymbol{n}, & \text{if } \boldsymbol{u} \cdot \boldsymbol{n} < 0, \\ 0, & \text{else.} \end{cases}$$

All following computations are based on the weak formulation of the problem, which is achieved in the same manner as in Chapter 6.2.

Now we have to specify the choice of the regularisation parameters α and β. In comparison to the example in Chapter 6 it is somehow complicated to define an appropriate criterion for an automatic stopping rule consisting of three terms in the cost functional. However, we still need a homotopy type method to stabilise the solution process. We decided to start with $\alpha = 10^3$ and $\beta = 10^3$ and reduce β by 0.1 after each step until $\beta = 10^{-2}$. Afterwards, we reduce α in the same manner until we reach a threshold of $\alpha = 10^{-3}$. It would be an interesting topic for future work to adjust both parameters in this context automatically.

After discussing the whole setting of the optimisation problem we will now consider two different intensity function sequences. The first one is coupled to the time step size k. That means we have in each time point an observation of the intensity distribution

$$\left(\mathcal{I}_k^{(1)}\right)_{k=0}^{80}.$$

The second sequence consists of 17 observations, which are equidistantly distributed over the interval $[15d, 17d]$ ($k = 1, \ldots, 16$ are illustrated in Figure 7.4):

$$\left(\mathcal{I}_k^{(2)}\right)_{k=0}^{16}.$$

The results of our computations for the sequence $\mathcal{I}^{(2)}$ are visualised in Figures 7.7 and 7.8. Figure 7.7 shows from left to right the intensity functions $I(\boldsymbol{x}, t)$ for the original function, for a forward calculation without control and the reconstructed flow problem. From top to bottom the time points $t_1 = 15.4$, $t_2 = 15.8$, $t_3 = 16.2$, $t_4 = 16.6$ and $t_5 = 17$ are visualised. Figure 7.8 visualises the magnitude of $\boldsymbol{u}(\boldsymbol{x}, t)$ for the same arrangement of methods and time points as before. We see that our PDE-based optimisation process is able to reconstruct the inflow of the intensity signals. Therefore also the boundary conditions of the transport field are qualitatively well adapted.

However, we also want to compare the results of the transport reconstruction more quantitatively in the context of the transport of the non-observable pollutant. Therefore, we visualise the quantity $C_{\mathrm{Pol}}(t)$ in Figure 7.9. The graphs indicate the temporal evolution of the mean value of the concentration in Ω_{Det}. Green indicates the expected evolution. Blue is the result of a forward calculation without the reconstruction process. The orange curve indicates the reconstruction with the decoupling of sampling rate and time step size (sequence $\mathcal{I}^{(2)}$) and the pink line shows the result if in every time step intensity function informations are available (sequence $\mathcal{I}^{(1)}$).

We observe immediately that the reconstructed curve yields a progression almost as accurate as the expected curve. Thus we were able, by use of our methodology, to gather enough information of the flow field to reconstruct the distribution of the pollutant in the chosen time interval. We even showed that we are not determined to couple time step size to sampling rate by using sequence $\mathcal{I}^{(2)}$. The results of the reconstruction for the two sequences $\mathcal{I}^{(1)}$ and $\mathcal{I}^{(2)}$ are almost the same. This indicates on the one hand that the sampling rate for $\mathcal{I}^{(2)}$ can be chosen even bigger. On the other hand we see that the differences to the expected curve must have another source. A further look on the left

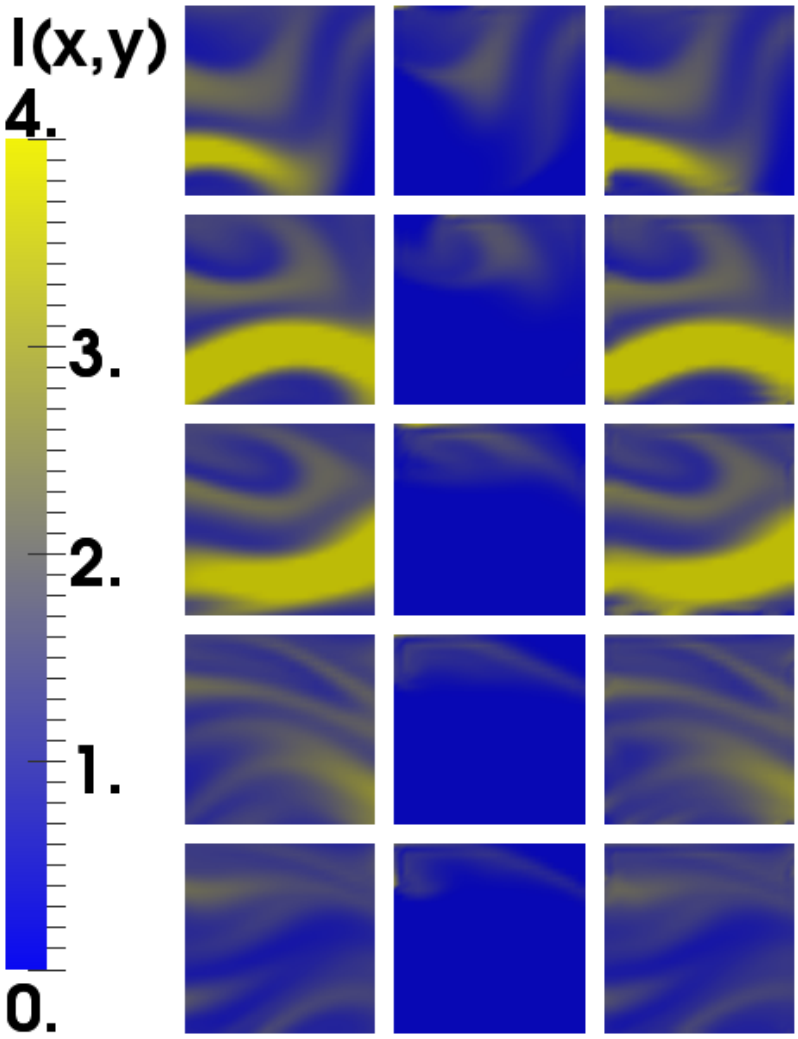

Figure 7.7. Visualisation of the spatial intensity distribution $I(\boldsymbol{x}, t_k)$ at different time points t_k. Rows: From top to bottom $t_k = 15d + k0.4d$ with $k = 1, \ldots, 5$. Columns: Left: Expected Distribution. Middle: Forward calculation without reconstruction. Right: Reconstruction by boundary identification problem.

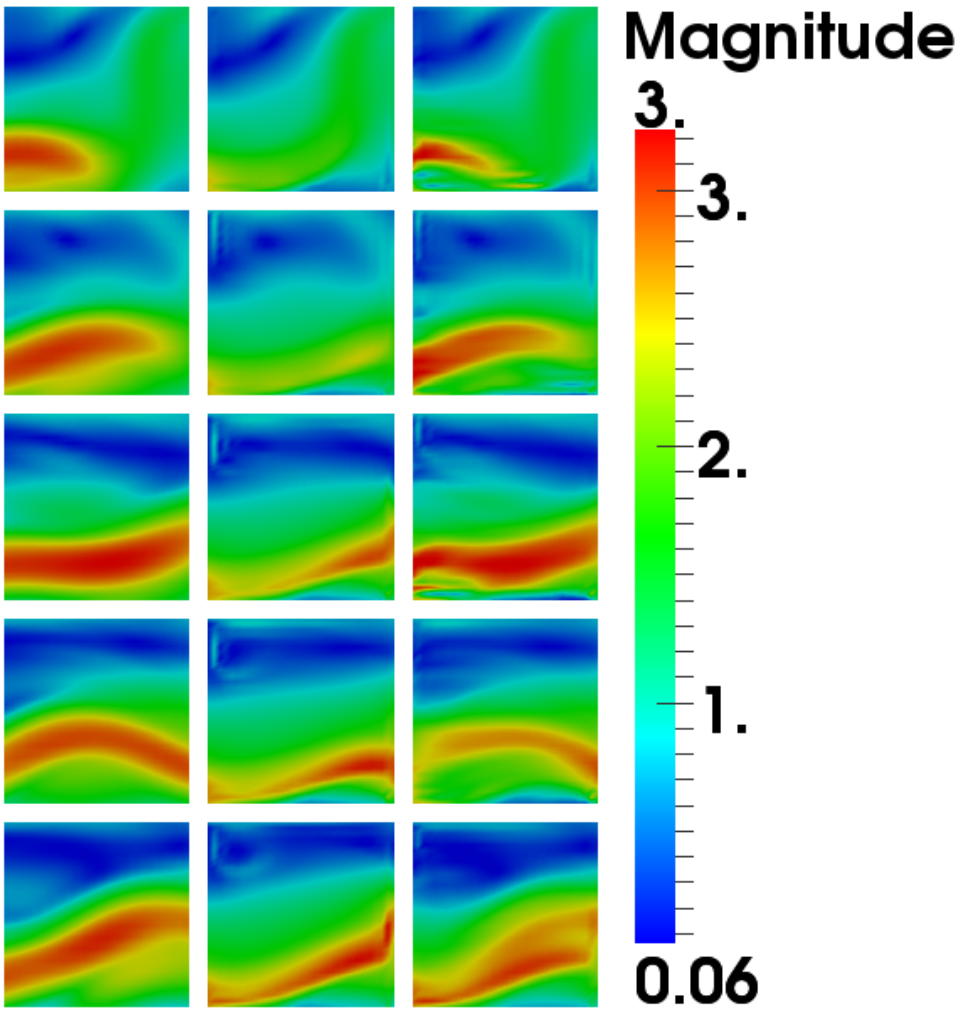

Figure 7.8. Visualisation of the magnitude of the vector field $\boldsymbol{u}(\boldsymbol{x}, t)$ at different time points t_k. Rows: From top to bottom $t_k = 15d + k0.4d$ with $k = 1, \ldots, 5$.Columns: Left: Expected Distribution. Middle: Forward calculation without reconstruction. Right: Reconstruction by boundary identification problem.

column of the expected intensity distributions in Figure 7.7 gives us the answer. The differences result from the spatial sparsity of the intensity function signal. At some time points bigger areas of the computational domain have almost no intensity informations (indicated by the blue background). In these areas the reconstruction of the flow field suffers, which explains the difference in the temporal evolution of $C_{\mathrm{Pol}}(t)$.

The results of this subsection show that the method is working appropriately. However the approach is very sophisticated from the numerical point of view, since our flow model includes the fully nonlinear term

$$\boldsymbol{u} \cdot \nabla \boldsymbol{u},$$

which has to be treated by a Newton-type method in the forward calculation. Moreover, the flow is solenoidal

$$\nabla \cdot \boldsymbol{u},$$

which means that we have to deal with a saddle point problem. A first indicator that

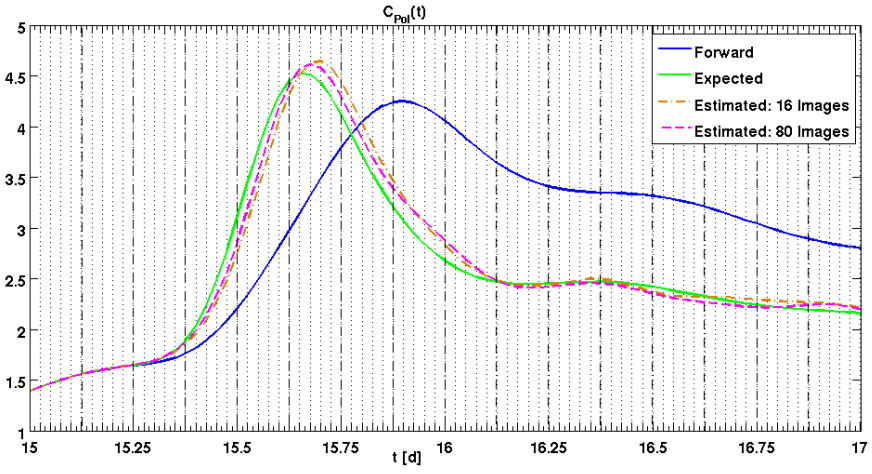

Figure 7.9. Recovery of the quantity of interest $C_{\mathrm{Pol}}(t)$. The green curve indicates the expected curvature. The blue curve shows the progression if we perform a forward calculation without reconstruction. The dashed orange curve shows the result if the flow field is identified by the boundary identification problem, with intensity informations only every fifth time step (sequence $\mathcal{I}^{(2)}$). The dashed pink curve shows the reconstruction, when intensity information in every time point of the time discretisation is available (sequence $\mathcal{I}^{(1)}$).

the flow model has probably a high influence on the reconstruction can be obtained by performing forward calculations with the original boundary conditions for varying viscosity parameters ν. Figure 7.10 visualises the results of these computations. The graphs show the percentage of the relative error

$$\mathrm{err}_{\nu}(t) := \frac{|C_{\mathrm{Pol}}^{(\nu)}(t) - C_{\mathrm{Pol}}(t)|}{|C_{\mathrm{Pol}}(t)|} \tag{7.1}$$

for the temporal evolution of $C_{\mathrm{Pol}}^{(\nu)}(t)$ for different ν.

The right graph shows the curves for three values of ν smaller than 10^{-4}. Here we see almost no difference, since the diffusive part of the system has a smaller influence than the artificial diffusion introduced by our convection-stabilisation technique (LPS, Chapter 3.4.2). The left graph in Figure 7.10 shows the curves for $\nu = 10^{-2}$, $\nu = 10^{-3}$ and $\nu = 10^{-4}$. Here we see that the evolution of the quantity of interest is violated up to 4%, which indicates that the flow field clearly changes. However, this example does not completely

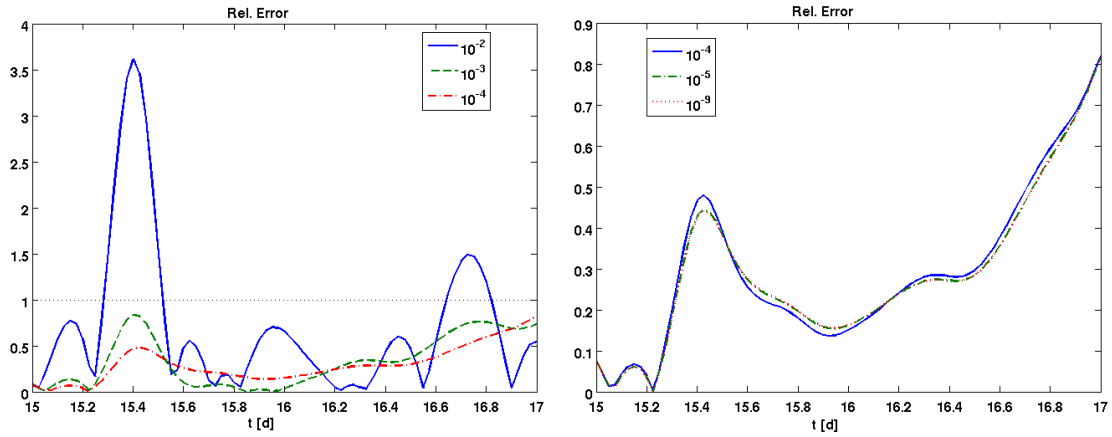

Figure 7.10. Relative error $\mathrm{err}_\nu(t)$ for forward calculations with given boundary conditions but different values for ν. Left: $\nu = 10^{-2}$ (blue), $\nu = 10^{-3}$ (dashed green) and $\nu = 10^{-4}$ (dashed red). Right: $\nu = 10^{-4}$ (blue), $\nu = 10^{-5}$ (dashed green) and $\nu = 10^{-9}$ (dashed red).

reveal how the reduction to simpler flow models changes the results of the reconstruction. Thus we devote the next subsection to show that the needed computational effort to use the whole model information in the method for the mentioned problem is justified in terms of an increased quality of the reconstruction.

7.2.2. Influence of the Flow Model in the Reconstruction Process

We simplify the configuration of the last chapter to concentrate only on the fluid model. Therefore, we assume that the intensity function is available at all times t. We denote this function by $\mathcal{I}(t)$. Thus we can directly describe the signal transport at the boundary and do not have to reconstruct this information. We then have the condition

$$\varepsilon \partial_{\boldsymbol{n}} I(t) = \frac{1}{\mu_I} \left(\mathcal{I}(t) - I(t) \right) - \frac{1}{2} \left(\boldsymbol{u}(t) \cdot \boldsymbol{n} \right) I(t), \qquad \text{on } \partial\Omega$$

in the strong formulation. Furthermore, the cost functional changes to

$$J(\boldsymbol{u}, I) = \frac{\sigma}{2} \int_0^T \| I(t) - \mathcal{I}(t) \|^2_{L^2(\Omega)} + \frac{\alpha}{2} \int_{t_0}^T \| \boldsymbol{q}_{\boldsymbol{u}}(t) \|^2_{L^2(\Gamma_{\mathrm{Con}})} \, dt.$$

Hence, the objective is now to estimate only the boundary conditions of the flow field at the left and lower boundaries to obtain the best possible recovery of the function $\mathcal{I}(t)$.

We want to compare three different physical models:

Model I: Original Flow Model for the Forward Calculation

As in the last subsection we use a weak formulation of the system of equations

$$\begin{aligned} \partial_t I - \varepsilon \Delta I + \boldsymbol{u} \cdot \nabla I = 0, \qquad & \text{in } \Omega \times (t_0, T], \\ \partial_t \boldsymbol{u} - \nu \Delta \boldsymbol{u} + \boldsymbol{u} \cdot \nabla \boldsymbol{u} + \nabla p = 0, \qquad & \text{in } \Omega \times (t_0, T], \\ \nabla \cdot \boldsymbol{u} = 0, \qquad & \text{in } \Omega \times (t_0, T], \end{aligned}$$

with the same boundary conditions as in the chapter before. Again the parameters are given by

$$\varepsilon = 10^{-3} \qquad \text{and} \quad \nu = 8.18 \cdot 10^{-9}.$$

This model represents the underlying physical model for the flow as we have described it in the forward calculation, which we used to generate our data. Thus it represents the application of the whole model.

Model II: Time-Dependent Stokes System

In the second model we skip the nonlinear term, which results in saving an essential amount of computational cost for the forward calculations in the optimisation process. The system reads as follows

$$\begin{aligned} \partial_t I - \varepsilon \Delta I + \boldsymbol{u} \cdot \nabla I = 0, \qquad & \text{in } \Omega \times (t_0, T], \\ \partial_t \boldsymbol{u} - \nu \Delta \boldsymbol{u} + \nabla p = 0, \qquad & \text{in } \Omega \times (t_0, T], \\ \nabla \cdot \boldsymbol{u} = 0, \qquad & \text{in } \Omega \times (t_0, T]. \end{aligned}$$

The parameters are chosen as follows

$$\varepsilon = 10^{-3} \qquad \text{and} \quad \nu = 1.$$

Thus the Stokes system acts in principle as regularisation, which we already mentioned in the introduction of this thesis (Chapter 1.3 and 1.4). It provides us with a flow field $\boldsymbol{u}(\boldsymbol{x}, t)$ in the space $L^2(0, T; H^1_{\text{div}}(\Omega)^2)$. However, this reduced fluid model still requires the flow field to be divergence free.

The boundary conditions are also slightly modified to

$$\begin{aligned} \nu \partial_{\boldsymbol{n}} \boldsymbol{u}(t) - p(t)\boldsymbol{n} &= \frac{1}{\mu_{\boldsymbol{u},1}} \left(\hat{\boldsymbol{u}}(t) - \boldsymbol{u}(t) \right), && \text{on } \partial\Omega \setminus \Gamma_{\text{Con}}, \\ \nu \partial_{\boldsymbol{n}} \boldsymbol{u}(t) - p(t)\boldsymbol{n} &= \frac{1}{\mu_{\boldsymbol{u},2}} \left(\left(\boldsymbol{u}^0 + \boldsymbol{q}(t) \right) - \boldsymbol{u}(t) \right), && \text{on } \Gamma_{\text{Con}}, \end{aligned}$$

with the parameters $\mu_{\boldsymbol{u},1} = h^2$ and $\mu_{\boldsymbol{u},2} = h$ chosen as before.

Remark 7.1 (Mathematical Theory for Model II). *An existence proof of at least one solution of the optimisation problem can be obtained in the same fashion as in the proof of Theorem 6.4, due to the discussion for the linear case in Chapter 5.3.*

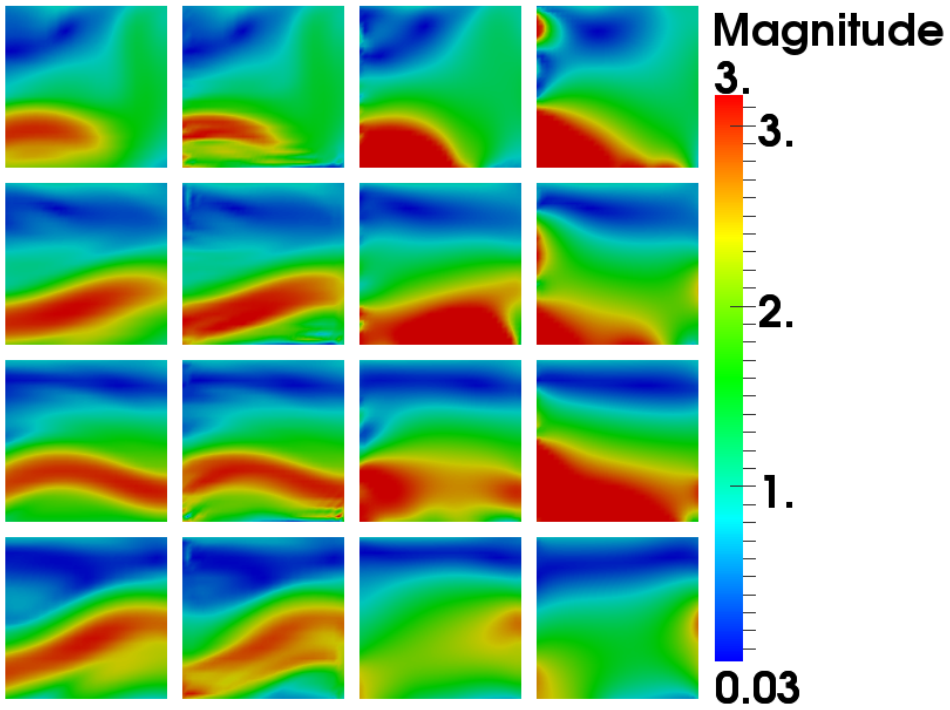

Figure 7.11. Magnitude of the transport field. Rows from top to bottom: $t_k = 15d + k0.5d$ with $k = 1, \ldots, 4$. Columns from left to right: Expected Flow ($\boldsymbol{u}_{\text{Exp}}(\boldsymbol{x}, t)$), reconstruction with Model I (Navier-Stokes system, $\boldsymbol{u}_{\text{NaSt}}(\boldsymbol{x}, t)$), reconstruction with Model II (Stokes system, $\boldsymbol{u}_{\text{St}}(\boldsymbol{x}, t)$ and reconstruction with Model III (Heat equation, $\boldsymbol{u}_{\text{Heat}}(\boldsymbol{x}, t)$).

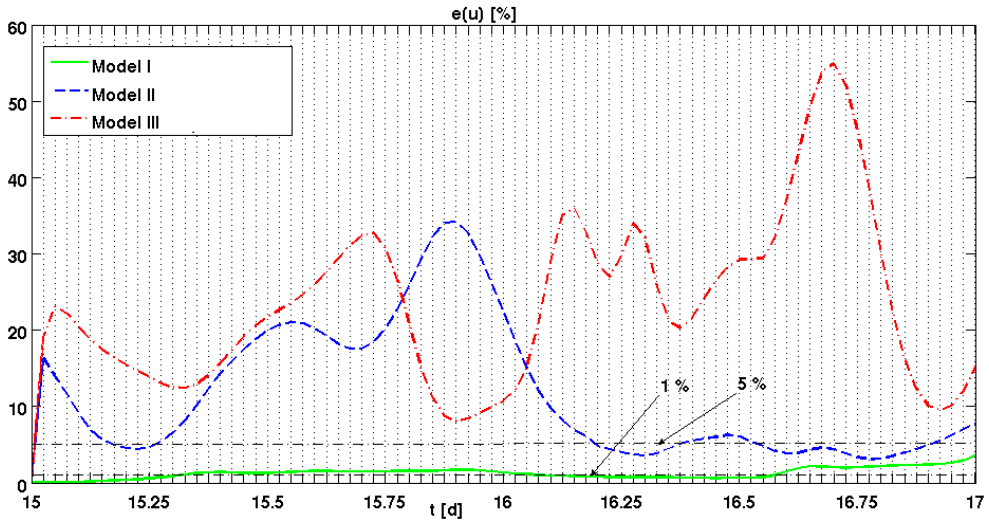

Figure 7.12. Relative error $e(\boldsymbol{u})$ (equation (7.2)) with Mod := NaSt (green curve), Mod := St (dashed blue curve) and Mod := Heat (dashed red curve).

Model III: Heat Equation

For the third flow model we simply use the heat equation

$$\begin{aligned} \partial_t I - \varepsilon \Delta I + \boldsymbol{u} \cdot \nabla I = 0, \qquad & \text{in } \Omega \times (t_0, T], \\ \partial_t \boldsymbol{u} - \nu \Delta \boldsymbol{u} = 0, \qquad & \text{in } \Omega \times (t_0, T]. \end{aligned}$$

with $\nu = 1$. In this example the heat equation has the function of temporal and spatial regularisation of the reconstruction process and the method can be interpreted as a different formulation of the optimisation problems used for optical flow estimation mentioned in Chapter 1.3. This formulation does not result in a saddle point problem. Thus the Lagrange multiplier $p(\boldsymbol{x}, t)$ is no longer needed. This leads to the following formulation of the boundary control

$$\begin{aligned} \nu \partial_{\boldsymbol{n}} \boldsymbol{u}(t) &= \frac{1}{\mu_{\boldsymbol{u},1}} \left(\hat{\boldsymbol{u}}(t) - \boldsymbol{u}(t) \right), && \text{on } \partial\Omega \setminus \Gamma_{\text{Con}}, \\ \nu \partial_{\boldsymbol{n}} \boldsymbol{u}(t) &= \frac{1}{\mu_{\boldsymbol{u},2}} \left(\left(\boldsymbol{u}^0 + \boldsymbol{q}(t) \right) - \boldsymbol{u}(t) \right), && \text{on } \Gamma_{\text{Con}}. \end{aligned}$$

Remark 7.2 (Mathematical Theory for Model III).
Here we have to be a careful since we have no longer the property:

$$\nabla \cdot \boldsymbol{u} = 0.$$

However, the equation

$$\frac{1}{2} \left(\nabla \cdot \boldsymbol{u}, I^2 \right) = \frac{1}{2} \left\langle (\boldsymbol{u} \cdot \boldsymbol{n}) I, I \right\rangle_{\partial\Omega} - (\boldsymbol{u} \cdot \nabla I, I)$$

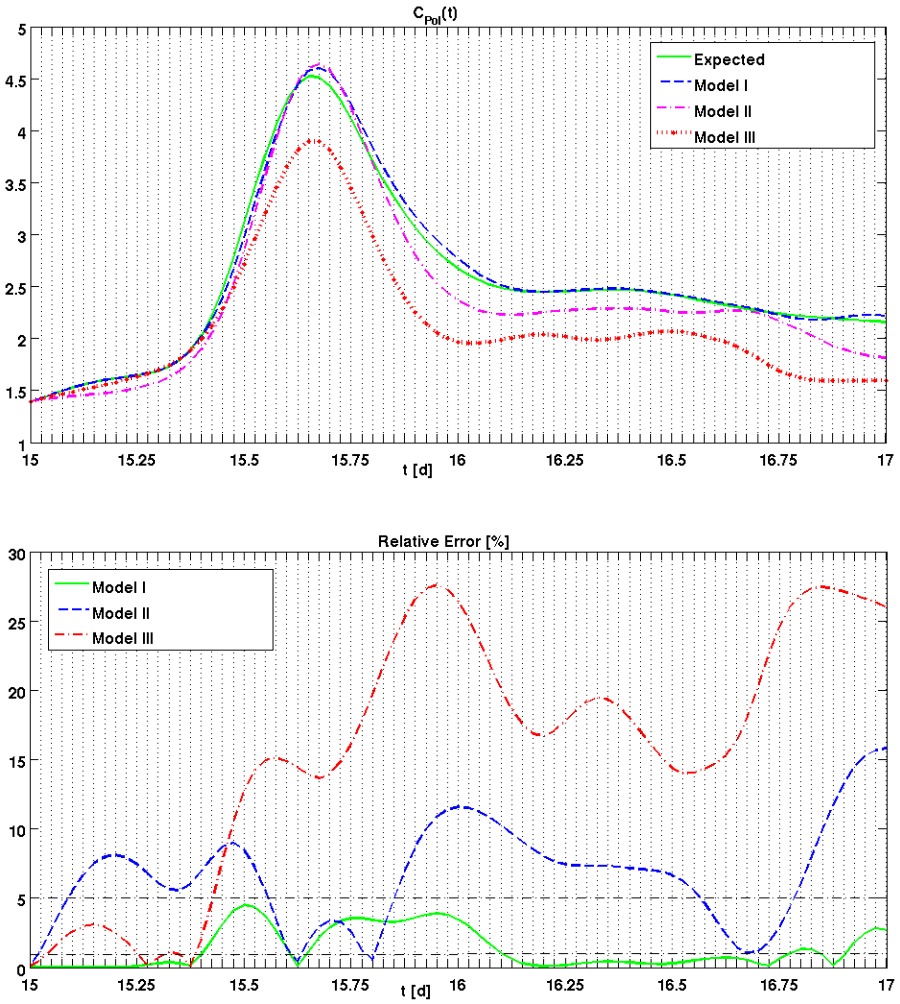

Figure 7.13. Reconstruction of $C_{\mathrm{Pol}}(t)$. Upper graph: Expected Progression (green curve), recovery with $\boldsymbol{u}_{\mathrm{NaSt}}$ (Model I, dashed blue curve), recovery with $\boldsymbol{u}_{\mathrm{St}}$ (Model II, dashed pink curve) and recovery with $\boldsymbol{u}_{\mathrm{Heat}}$ (Model III, dashed red curve). Lower graph: The relative error $\mathrm{err}(t)$ (equation (7.1)). Model I (Navier-Stokes system, green curve), Model II (Stokes system, dashed blue curve) and Model III (heat equation, dashed red curve).

is still valid and can be used to obtain the usual estimates by the standard inequalities (Young, Hölder, etc.). We find

$$\frac{d}{dt}\|I(t)\|_2^2 + \nu\|\nabla I(t)\|_2^2 + \frac{1}{\mu}\|I(t)\|_{L^2(\partial\Omega)}^2 \leq c(\nu)\|\nabla\cdot\boldsymbol{u}(t)\|_2^2\|I(t)\|_2^2 + \frac{1}{\mu}\|\mathcal{I}(t)\|_{L^2(\partial\Omega)}^2,$$

which means that we need the regularity property

$$\nabla\cdot\boldsymbol{u} \in L^2\left(0,T;L^2(\Omega)\right)$$

to obtain all usuall energy bounds by the Gronwall lemma. However, we conjecture that this property can be obtain by having a closer look on the regularity theory for the heat equation with Robin boundary conditions on our quadraliteral domain, since H^2-regularity of the flow field $\boldsymbol{u}$ should be sufficient to obtain the required regularity property. For the standard theory this is given (see Theorem 2.6).

We perform computations for optimisation problems with these three models and present the results in the following. First we compare the reconstructed flow field directly. Figure 7.11 shows the images of the magnitude of the flow fields. The first column shows the expected solution $\boldsymbol{u}_{\mathrm{Exp}}(\boldsymbol{x},t)$, the second column presents the solution of the reconstruction with the original flow model as side condition. We denote the flow field by $\boldsymbol{u}_{\mathrm{NaSt}}(\boldsymbol{x},t)$. The third column visualises the results $\boldsymbol{u}_{\mathrm{St}}(\boldsymbol{x},t)$ with the Stokes system as flow model. Finally the fourth column shows the results $\boldsymbol{u}_{\mathrm{Heat}}(\boldsymbol{x},t)$ with the heat equation as model for the flow. From top to bottom we visualise the time points $t_1 = 15.5d$, $t_2 = 16d$, $t_3 = 16.5d$ and $t_4 = 17d$ respectively in every column. Obviously all three models recover the principle movement from left to right. However, detailed features could only be recovered by using the "exact" flow model for the reconstruction. This is emphasised by Figure 7.12, where we visualised the relative error

$$e(\boldsymbol{u}) := \frac{\|\boldsymbol{u}_{\mathrm{Mod}} - \boldsymbol{u}_{\mathrm{Exp}}\|_{L^2\left(0,T;L^2(\Omega)^2\right)}^2}{\|\boldsymbol{u}_{\mathrm{Exp}}\|_{L^2\left(0,T;L^2(\Omega)^2\right)}^2}, \tag{7.2}$$

with Mod := NaSt (green curve), Mod := St (dashed blue curve) or Mod := Heat (dashed red curve). Obviously the usage of the exact model in the optimisation process outperforms the both "reduced" models

Finally we want to present how the reconstructed flow fields influence the temporal evolution of our quantity of interest $C_{\mathrm{Pol}}(t)$. We visualise a comparison between all three models and the expected curve in Figure 7.13. We see that using the original fluid model leads to a clearly better reconstruction of the quantity which stays below a threshold of 5% in terms of the relative error $\mathrm{err}(t)$ defined as in equation (7.1). Over certain subintervals of the time horizon this error drops even below 1% relative error. However, all three models can be used to obtain a qualitative impression of the progression of the curve. This is also indicated by Figure 7.14, which visualises the distribution of the pollutant in the domain of interest Ω_{Det}. Again the columns and rows are arranged as in Figure 7.11. The principle distributions look similar. However, there is a clear difference between the Model II (3rd column) and Model III (4th column), compared to the expected distribution (1st column).

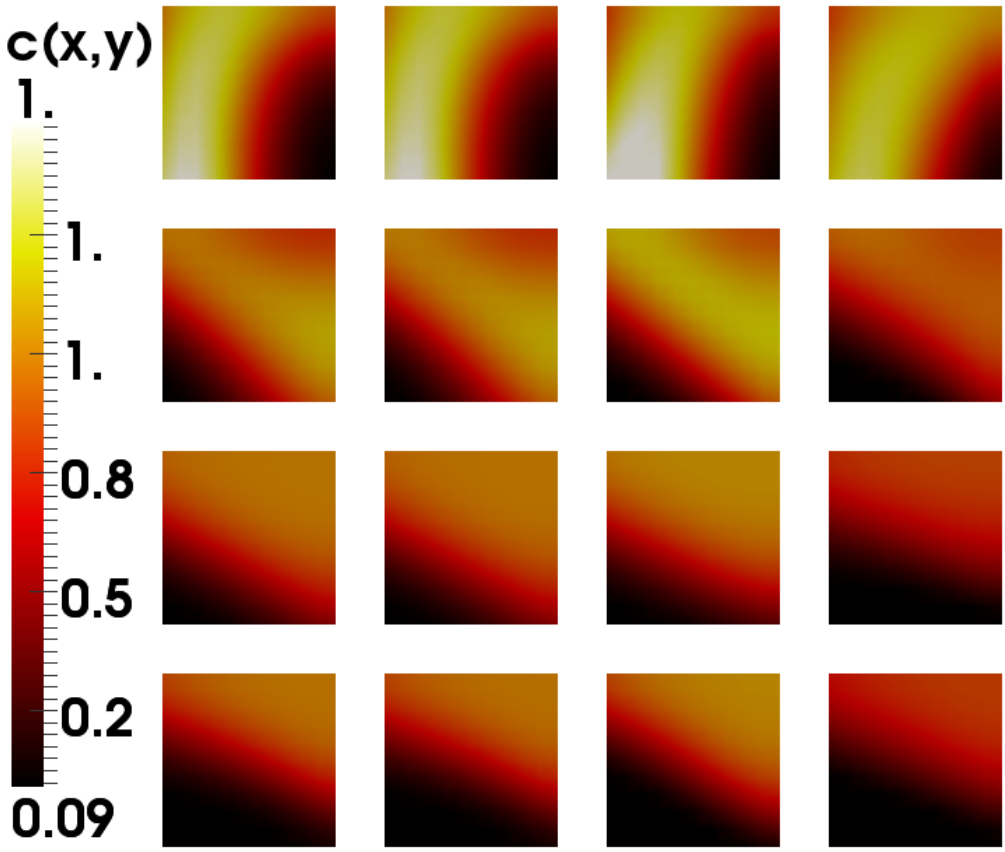

Figure 7.14. Concentration $c(\boldsymbol{x}, t)$ of the pollutant in the domain of interest $\Omega_{\text{Det}} = (0.7, 1) \times (0.7, 1)$. Rows (top to bottom): $t_k = 15d + k0.5d$ with $k = 1, \ldots, 4$. Columns from left to right: Expected flow ($\boldsymbol{u}_{\text{Exp}}(\boldsymbol{x}, t)$), computation with $\boldsymbol{u}_{\text{NaSt}}(\boldsymbol{x}, t)$ (Model I), with $\boldsymbol{u}_{\text{St}}(\boldsymbol{x}, t)$ (Model II) and with $\boldsymbol{u}_{\text{Heat}}(\boldsymbol{x}, t)$ (Model III).

Remark 7.3 (Application of Simpler Models in the Computational Process). *We want to state explicitly that in our opinion the heat equation, which introduces no model information at all seems inadequate for the target recovery process. However, the Stokes system is able to represent features of the original fluid flow. Thus it is an interesting idea to work with this simpler model (no nonlinearities) in the homotopy method to obtain a good initial value for the optimisation with the full model and a small regularisation parameter α.*

8. Conclusion

In this thesis we investigated a sophisticated time-dependent PDE-constrained optimisation problem, with a weakly coupled system of equations as side condition, which consists of two parts. First, the time-dependent Navier-Stokes system describes an underlying fluid flow in the computational domain. This velocity field is weakly coupled to a convection-diffusion equation, which describes the intensity distribution of an observable passive tracer. The mentioned optimisation problem enabled us to reconstruct features of the flow field, only by information on the temporal and spatial distribution of the passive tracer. Thus we could use the technique to compute quantities of interest that cannot be observed directly. In this final chapter we want to recall what has been achieved in this thesis and where we see possible directions for further research.

Connection to Physics-Based Optical Flow Estimation

We showed that the presented optimisation problem is closely related to variational optical flow estimators. It is an enhancement which combines two fundamental directions: On the one hand the regularisation with physical prior knowledge and on the other hand the use of PDE-based optimisation for the decoupling of time discretisation of the intensity function from the sampling rate of the given image sequence. Both techniques rely on optimal control formulations, which allowed us to combine them easily. Setting the focus on identifying boundary functions in certain model situations we chose a concrete formulation out of a broad variety of possibilities. The choice of different models for the observed flow phenomenon or the evolution of the intensity function would lead to completely different methods, which are better tailored for the respective problem.

Boundary Control I: Time-Dependent Convection-Diffusion Equation

As mentioned, the optimisation problem can be interpreted as a boundary control problem, with a sophisticated coupled PDE constraint. Before we dealt with the whole system, we considered both parts of the system independently. Thus, we began with the time-dependent convection-diffusion equation. We found a mathematically well-posed formulation of the optimisation problem by using a Robin-type formulation of the boundary conditions. This method has the advantage that it can be treated very easily from a numerical point of view, since neither additional problems nor complicated boundary integrals must be solved. Furthermore, we were able to prove that a sequence of solutions of the Robin-type problem is converging to a solution of a Dirichlet control problem with the very weakly formulated PDE as constraint when a model parameter is dropping to zero. From the numerical point of view, we were able to formulate a "general boundary" condition, which allows to switch between Robin and Dirichlet control. However, with respect to pure transport problems (e. g., the hyperbolic linear transport equation), the theoretical results were lost, even

though we could show the numerical solvability for several test cases. Here is an interesting direction for further research, especially since in the image processing community the linear transport equation as optical flow equation has a very important role.

Boundary Control II: Time-Dependent Navier-Stokes System

We were also able to deliver the existence theory for the optimisation problem with the Navier-Stokes system and Robin-type boundaries. Nevertheless, we could only prove the connection to Dirichlet controls in the Oseen case, since the very weak formulation of the Navier-Stokes equations has reduced regularity properties. However, a connection between Dirichlet controls and approximating Robin controls was indicated by our numerical experiments. Thus, further research in this direction would be interesting.

Boundary Control III: Time-Dependent Coupled System

Due to the weak coupling between the Navier-Stokes system and the convection-diffusion equation it is straightforward to prove existence of at least one solution of the optimisation problem with the coupled system and Robin-type boundary controls as constraint of the optimisation problem. Again, the connection to Dirichlet controls cannot be figured out due to a lack of regularity of the solution. However, by our numerical experiments we figured out that it is appropriate to work with the Robin-type control for the reconstruction purpose in our prototypical applications.

Physically-Based Image Interpolation Across Boundaries

After developing the method and the corresponding theory we started with a first prototypical example to present the functionality of the method. Therefore, we used a sequence of six synthetic intensity functions at six equidistant time points of the time interval. Then we reconstructed the intensity function on a finer time-grid by our method. Hereby the estimation of the flow field across the boundaries is essential. Moreover, it turned out that in the vicinity of intensity signals the method is able to reconstruct even an appropriate transport field. However, in this context the use of the fluid model acts only as a regularisation technique of the flow field and has no further physical meaning.

Benchmark with Rough Lower Boundary: Reconstruction of Drag and Lift

The second example is more focused on the influence of the fluid model. We considered a benchmark example, where the concrete choice of the physical flow model is essential. The channel is motivated by the standard obstacle benchmark in numerical fluid dynamics, which is modified by a rough bottom boundary. The boundary roughness and the choice of the viscosity clearly influences the drag and lift coefficient in this example. While the inflow and outflow conditions are fixed, the flow at the bottom boundary is not given, due to an unknown roughness. Our method was applied to reconstruct a reliable boundary function on an artificial smooth bottom boundary, only by using information on the intensity function. At first we tested the method in the context of a similar time-independent example. The method performs very well for different kinds of roughness. Thereby the reconstruction is performed by using a homotopy method for the regularisation parameter, which was stopped automatically by a heuristic, which seemed to be appropriate for the presented problem class. In a second step we could even present a segregation loop, which

is able to adjust the Reynolds number and the boundary function and yields a reliable approximation of the lift and drag coefficients. Finally we applied the methodology to a time-dependent example and showed that the method works also in this context.

Nevertheless, the example has a very synthetic character, and it would be interesting to apply the method to a more realistic problem and investigate its behaviour for such a problem class. Furthermore, the "parameter choice rule" and the segregation loop for the combined estimation of viscosity and boundary functions rely on pure heuristics. Thus a more detailed mathematical investigation is a possible direction for further research.

Prototypical Application: Interdisciplinary Example between Image Processing, Environmental Physics and Numerical Mathematics

Finally we considered a prototypical application, which is motivated by a meteorological example and combines all complexities our method is designed for. By this example we could confirm that our methodology is also working in a more complex scenario, where we have to estimate essential features of the fluid flow and signal transport across boundaries. Moreover, we emphasise that this process is also working in the case of decoupling between the sampling rate of the data and the time step size of the temporal discretisation.

However, the main result of this prototypical application is the justification of using knowledge of the underlying fluid model. We compared the use of the original fluid model (Euler-type system) to a linearised Stokes system and a simple heat equation. We showed that using the original model in the optimisation problem yields clearly the best results with respect to the reconstruction of the underlying flow. Thus the higher computational effort is justified. In addition, our experiments yield more insight for the numerical treatment of this problem classes. Using reduced fluid models to generate initial values for our numerical algorithm with the full model could be of interest in future research.

Further Directions for Future Research

Atmospheric transport fields for the distribution of pollutants is an interesting and challenging topic, and an important future problem is how to combine different measurements to achieve even improved estimates of quantities of interest. The idea is to increase the accuracy of the estimated transport field by "switching on" ground-based measurements in regions where the image data is not sufficient to identify the field. This application of additional data could also be designed in an optimisation framework, which is oriented at estimating the quantity of interest up to a certain accuracy. This could be an idea for an "optimal measurement design".

From the numerical point of view the whole reconstruction process should be designed more efficiently. For example, the Newton-type method for the optimisation problem should be adapted to the complexity of the problem. Balancing between the accuracy of the used iterative solver to solve the linearised problems in each Newton-step and the Newton residuals could possibly save a huge amount of computational effort, since we have to solve several time-dependent problems for each step of the iterative linear solver. Furthermore, the regularisation method should be investigated more systematically to reduce the amount of needed solves of optimisation problems for obtaining an adequate reconstruction. In

addition, the application of spatial and temporal adaptive techniques (cf. Becker et al. [11]) to the involved PDE problems could immensely reduce the computational effort for the considered nonlinear time-dependent PDE problems. A way towards this objective in the framework of environmental transport problems was already presented by Vihharev [103].

In the last reference it was demonstrated that information on the wind fields can be used to obtain sources for the distribution of chemical substances in the atmosphere. In case that such dense wind field information is not available it would be an interesting topic to investigate the possibility of combining the presented reconstruction techniques from this thesis with such kinds of source identification problems, e. g. by segregating the two identification processes.

Bibliography

[1] R. A. Adams and J. F. Fournier. *Sobolev Spaces*. Elsevier, 2nd edition, 2003.

[2] I. Babuška. The Finite Element Method with Penalty. *Mathematics of Computation*, 27 (12):221–228, 1973.

[3] F. E. Bachl, C. S. Garbe, and P. Fieguth. A Bayesian Approach to Spaceborn Hyperspectral Optical Flow Estimation on Dust Aerosols. *IEEE International Geoscience and Remote Sensing Symposium, IEEE*, pages 256–259, 2012.

[4] F. E. Bachl, C. S. Garbe, and P. Fieguth. Bayesian Inference on Integrated Continuity Fluid Flows and their Application to Dust Aerosols. *IEEE International Geoscience and Remote Sensing Symposium, IEEE*, pages 2246–2249, 2013.

[5] J. L. Barron, D. J. Fleet, and S. S. Beauchemin. Performance of Optical Flow Techniques. *International Journal of Computer Vision*, 12 (1):43–77, 1994.

[6] S. S. Beauchemin and J. L. Barron. The Computation of Optical Flow. *ACM Computing Surveys*, 27(3):433–467, 1995.

[7] R. Becker. Mesh Adaption for Dirichlet Flow Control via Nitsche's Method. *Communications in Numerical Methods in Engineering*, 18:669–680, 2002.

[8] R. Becker. *Adaptive Finite Elements for Optimal Control Problems*. Habilitationsschrift, Ruprecht Karls Universität, 2004.

[9] R. Becker and M. Braack. A Finite Element Pressure Gradient Stabilization for the Stokes Equations Based on Local Projections. *Calcolo*, 38, 2001.

[10] R. Becker and M. Braack. A Two-Level Stabilization Scheme for the Navier-Stokes Equations. *Enumath 2003*, 2004.

[11] R. Becker and R. Rannacher. An Optimal Control Approach to A Posteriori Error Estimation in Finite Element Methods. *Acta Numerica*, 10:1–102, 2001.

[12] R. Becker, M. Braack, T. Dunne, D. Meidner, T. Richter, M. Schmich, W. Wollner, and B. Vexler. *Gascoigne3D. High Performance Adaptive Finite Element Toolkit*. http://www.numerik.uni-kiel.de/ mabr/gascoigne/, Version 2008.

[13] F. B. Belgacem, H. E. Fekih, and H. Metoui. Singular Perturbation for the Dirichlet Boundary Control of Elliptic Problems. *ESAIM*, 37(5):833–850, 2003.

[14] M. Bergounioux. On Poincaré-Wirtinger Inequalities in Spaces of Functions of Bounded Variations. *Control and Cybernetics*, 40(4), 2011.

[15] H. Blum and R. Rannacher. On the Boundary Value Problem of the Biharmonic Operator on Domains with Angular Corners. *Math. Meth. in the Appl. Sci.*, 2: 556–581, 1980.

[16] A. Borzí, K. Ito, and K. Kunisch. Optimal Control Formulation for Determining Optical Flow. *SIAM J. Sci. Comput.*, 24(3):818–847, 2002.

[17] M. Braack, E. Burman, V. John, and G. Lube. Stabilized Finite Element Methods for the Generalized Oseen Problem. *Comput. Methods Appl. Mech. Engrg.*, 196:853–866, 2007.

[18] D. Braess. *Finite Elemente*. Springer, 4th edition, 2007.

[19] S. C. Brenner and L. R. Scott. *The Mathematical Theory of the Finite Element Methods*. Springer, 1994.

[20] M. O. Bristeau, R. Glowinski, and J. Periaux. Numerical Methods for the Navier-Stokes Equations. Applications to the Simulation of Compressible and Incompressible Viscous Flows. *Computer Physics Reports*, 6:73–187, 1987.

[21] T. Brox, A. Bruhn, N. Papenberg, and J. Weickert. High Accuracy Optical Flow Estimation Based on a Theory for Warping. In *In Proc. 8th European Conference on Computer Vision*, volume 4, pages 25–36. Springer, 2004.

[22] K. Chen and D. Lorenz. Image Sequence Interpolation Using Optimal Control. *Journal of Mathematical Imaging and Vision*, 41(3):222–238, 2012.

[23] K. Chen and D. Lorenz. Image Sequence Interpolation Based on Optical Flow, Image Segmentation, and Optimal Control. *IEEE Transactions on Image Processing*, 21(3):1020–1030, 2012.

[24] C. Clason, B. Jin, and K. Kunisch. A Semismooth Newton Method for L^1-Data Fitting with Automatic Choice of Regularization Parameters and Noise Calibration. *SIAM J. Imaging Sci.*, 3:199–231, 2010.

[25] T. Corpetti, E. Memin, and P. Perez. Dense Estimation of Fluid Flows. *IEEE Transactions on Pattern Analysis and Machine Intelligence*, 24 (3):365–380, 2002.

[26] B. Dacorogna. *Calculus of Variations*. Imperial College Press, 2004.

[27] J. I. Diaz and G. Galiano. Existence and Uniqueness of Solutions of the Boussinesq System with Nonlinear Thermal Diffusion. *Topological Methods in Nonlinear Analysis Journal of the Juliusz Schauder Center*, 11:59–82, 1998.

[28] R. J. DiPerna and P. L. Lions. Ordinary Differential Equations, Transport Theory and Sobolev Spaces. *Inventiones mathematicae*, 98:511–547, 1989.

[29] M. Dobrowolski. *Angewandte Funktionalanalysis*. Springer, 2006.

[30] A. Dróżdż and V. Uruba. Comparison of PIV and Hot-Wire Statistics of Turbulent Boundary Layers. *Journal of Physics: Conference Series*, 530, 2014.

[31] H. W. Engl, M. Hanke, and A. Neubauer. *Regularization of Inverse Problems*. Kluwer Academic Publisher, 2000.

[32] K. Eriksson, D. Estep, P. Hansbo, and C. Johnson. *Computational Differential Equations*. Cambridge University Press, 1996.

[33] L. C. Evans. *Partial Differential Equations*. American Mathematical Society, 2nd edition, 2010.

[34] R. Farwig, H. Kozono, and H. Sohr. Very Weak, Weak and Strong Solutions to the Instationary Navier-Stokes System. In P. Kaplicky and S. Necasova, editors, *Topics on Partial Differential Equations*, volume 2, pages 1–54. Publishing House of the Faculty of Mathematics and Physics Charles University in Prague, 2007.

[35] C. Fefferman. *Existence and Smoothness of the Navier-Stokes Equation*. http://www.claymath.org/millennium/Navier-Stokes_Equations/Official_Problem_Description.pdf, 2000.

[36] J. Freund and R. Stenberg. On Weakly Imposed Boundary Conditions for Second Order Problems. *Proceedings of the International Conference on Finite Elements in Fluids*, pages 327–336, 1995.

[37] E. Friedmann. The Optimal Shape of Riblets in the Viscous Sublayer. *J. math. fluid mech.*, 12:243–265, 2010.

[38] A. V. Fursikov, M. D. Gunzburger, and L. S. Hou. Optimal Dirichlet Control and Inhomogeneous Boundary Value Problems for the Unsteady Navier-Stokes Equations. *ESAIM: Proceedings*, 4:97–116, 1998.

[39] A. V. Fursikov, M. D. Gunzburger, and L. S. Hou. Boundary Value Problems and Optimal Boundary Control for the Navier-Stokes System: The Two-Dimensional Case. *SIAM J. Control Optim.*, 36 (3):852–894, 1998.

[40] H. Gajewski, K. Gröger, and K. Zacharias. *Nichtlineare Operatorengleichungen und Operatorendifferentialgleichungen*. Akademie Verlag, 1974.

[41] G. P. Galdi. *An Introduction to the Mathematical Theory of the Navier-Stokes Equations*, volume Volume I : Linearised Steady Problems. Springer, 1991.

[42] V. Girault and P.-A. Raviart. *Finite Element Methods for Navier-Stokes Equations*. Springer, 1986.

[43] A. Griesbaum, B. Kaltenbacher, and B. Vexler. Efficient Computation of the Tikhonov Regularization Parameter by Goal-Oriented Adaptive Discretization. *Inverse Problems*, 24, 2008.

[44] C. Grossmann, H. C. Roos, and M. Stynes. *Numerical Treatment of Partial Differential Equations*. Springer, 3rd (english) edition, 2007.

[45] M. D. Gunzburger, L. S. Hou, and T. P. Svobodny. Analysis and Finite Element Approximation of Optimal Control Problems for the Stationary Navier-Stokes Equations with Dirichlet Controls. *RAIRO - Modélisation mathématique et analyse numérique*, 25 (6):852–894, 1991.

[46] M. D. Gunzburger, L. S. Hou, and T. P. Svobodny. Analysis and Finite Element Approximation of Optimal Control Problems for the Stationary Navier-Stokes Equations with Distributed and Neumann Controls. *Mathematics of Computation*, 57 (195):123–151, 1991.

[47] C. Haecheon, M. Hinze, and K. Kunisch. Instantaneous Control of Backward-Facing Step Flows. *Applied Numerical Mathematics*, 31:133–158, 1999.

[48] M. Hanke. A Regularization Levenberg-Marquardt Scheme, with Applications to Inverse Groundwater Filtration Problems. *Inverse Problems*, 13 (1), 1997.

[49] P. Héas, E. Mémin, N. Papadakis, and A. Szantai. Layered Estimation of Atmospheric Mesoscale Dynamics from Satellite Imagery. *IEEE Transactions on Geoscience and Remote Sensing*, 45 (12):4087–4104, 2007.

[50] M. Heath. *Scientific Computing: An Introductory Survey*. McGraw-Hill, 2nd edition, 2002.

[51] D. Heitz, E. Memin, and C. Schnörr. Variational Fluid Flow Measurements from Image Sequences: Synopsis and Perspectives. *Experiments in Fluids*, Published Online, 2009.

[52] J. Heywood and R. Rannacher. Finite-Element Approximation of the Nonstationary Navier-Stokes Problem Part IV: Error Analysis for Second-Order Time Discretization. *SIAM Journal on Numerical Analysis*, 27 (2):353–384, 1990.

[53] J. G. Heywood, R. Rannacher, and S. Turek. Artificial Boundaries and Flux and Pressure Conditions for the Incompressible Navier-Stokes Equation. *International Journal for Numerical Methods in Fluids*, 22(5), 1996.

[54] B. K. P. Horn and B. G. Schunck. Determining Optical Flow. *Artificial Intelligence*, 17:185–203, 1981.

[55] L. S. Hou and S. S. Ravindran. A Penalized Neumann Control Approach for Solving an Optimal Dirichlet Control Problem for the Navier-Stokes Equations. *SIAM J. Control Optim.*, 36 (5):1795–1814, 1998.

[56] L. S. Hou and S. S. Ravindran. Numerical Approximation of Optimal Flow Control Problems by a Penalty Method: Error Estimates and Numerical Results. *SIAM J. Control Optim.*, 20 (5):1753–1777, 1999.

[57] K. Ito and K. Kunisch. On the Choice of the Regularization Parameter in Nonlinear Inverse Problems. *SIAM J. Optimization*, 2 (3):376–404, 1992.

[58] K. Ito and S. S. Ravindran. A Reduced-Order Method for Simulation and Control of Fluid Flows. *Journal of Computational Physics*, 143:403–425, 1998.

[59] K. Ito, B. Jin, and J. Zou. A New Choice Rule for Regularization Parameters in Tikhonov Regularization. *Applicable Analysis*, 90 (10):1521–1544, 2011.

[60] B. Jähne. *Digital Image Processing*. Springer, Heidelberg, 6th edition, 2005.

[61] B. Jin and D. Lorenz. Heuristic Parameter-Choice Rules for Convex Variational Regularization Based on Error Estimation. *SIAM Journal on Numerical Analysis*, 48 (3), 2010.

[62] V. John and E. Schmeyer. Finite Element Methods for Time-Dependent Convection-Diffusion-Reaction Equations with Small Diffusion. *Comput. Methods Appl. Mech. Engrg.*, 198:475–494, 2008.

[63] M. Juntunen and R. Stenberg. Nitsche's Method for General Boundary Conditions. *Mathematics of Computation*, 78(267):1353–1374, 2009.

[64] B. Kaltenbacher, A. Kirchner, and B. Vexler. Adaptive Discretization for the Choice of a Tikhonov Regularization Parameter in Nonlinear Inverse Problems. *Inverse Problems*, 27, 2011.

[65] R. B. Kellogg and J. E. Osborn. A Regularity Result for the Stokes Problem in a Convex Polygon. *Journal of Functional Analysis*, 21:397–431, 1976.

[66] M. Klinger. Betrachtung von Existenz- und Eindeutigkeitsresultaten der Navier-Stokes-Gleichungen auf einem künstlich beschränkten Rechengebiet. Master's thesis, Universität Heidelberg, 2009.

[67] M. Klinger. Parameter Estimation Problems in Physically Based Image Processing. In *Numerical Mathematics and Advanced Applications 2011*, pages 191–199, 2013.

[68] M. Klinger. A Variational Approach for Physically Based Image Interpolation Across Boundaries. In T. Carraro, M. Geiger, S. Körkel, and R. Rannacher, editors, *Multiple Shooting and Time Domain Decomposition Methods*, Contribution in Mathematical and Computational Sciences. Submitted, to appear in 2015.

[69] K. Kunisch and J. Zou. Iterative Choices of Regularization Parameters in Linear Inverse Problems. *Inverse Problem*, 14:1247–1264, 1998.

[70] D. Kuzmin. *A Guide to Numerical Methods for Transport Equations*. University Erlangen-Nürnberg, 2010.

[71] T. Liu and L. Shen. Fluid Flow and Optical Flow. *Journal of Fluid Mechanics*, 614:253–291, 2008.

[72] J. Lorenz. Stabilized Finite Element Methods for Dirichlet Boundary Control Problems in Fluid Mechanics. Master's thesis, Graz University of Technology, 2011.

[73] B. D. Lucas and T. Kanade. An Iterative Image Registration Technique with an Application to Stereo Vision. *Proceedings of Imaging Understanding Workshop*, pages 121–130, 1981.

[74] E. Marušíc-Paloka. Two methods for replacing dirichlet's boundary condition by robin's boundary condition via penalization. *Mathematical Communications*, 4: 27–33, 1999.

[75] E. Marušíc-Paloka. Solvability of the Navier-Stokes System with L^2-Boundary Data. *Appl. Math. Optim.*, 41:365–375, 2000.

[76] S. May, R. Rannacher, and B. Vexler. A Priori Error Analysis for the Finite Element Approximation of Elliptic Dirichlet Boundary Control Problems. *Proc. ENUMATH-2007, Graz*, pages 637–644, 2007.

[77] D. Meidner. *Adaptive Space-Time Finite Element Methods for Optimization Problems Governed by Nonlinear Parabolic Systems.* PhD-thesis, Heidelberg University, 2008.

[78] M. Menad and C. Daveau. Comparison of Several Discretization Methods of the Steklov-Poincare Operator. *Int. J. of Numer. Model.*, 19:271–287, 2006.

[79] J. Nitsche. Über ein Variationsprinzip zur Lösung von Dirichlet-Problemen bei Verwendung von Teilräumen, die keinen Randbedingungen unterworfen sind. *Abhandlungen aus dem Mathematischen Seminar der Universität Hamburg*, 36:9–15, 1971.

[80] J. Nocedal and S. J. Wright. *Numerical Optimization.* Springer, 2nd edition, 2006.

[81] D. Norman. Chemically Reacting Fluid Flows: Weak Solutions and Global Attractors. In *IMA Preprint Series No. 1487*, 1998.

[82] G. Of, T. X. Phan, and O. Steinbach. An Energy Space Finite Element Approach for Elliptic Dirichlet Boundary Control Problems. *SFB-Report No. 2009-001*, Uni Graz, 2012.

[83] N. Papadakis and E. Mémin. Variational Assimilation of Fluid Motion from Image Sequence. *SIAM J. on Image Siences*, 1 (4):343–363, 2008.

[84] A. Quarteroni, R. Sacco, and F. Saleri. *Numerical Mathematics.* Springer, Heidelberg, 2nd edition, 2007.

[85] R. Rannacher. Finite Element Solution of Diffusion Problems with Irregular Data. *Numerische Mathematik*, 43:309–327, 1984.

[86] J. Raymond. Stokes and Navier-Stokes Equations with Nonhomogeneous Boundary Conditions. *Annales de l'Institut Henri Poincare (C) Non Linear Analysis*, 24 (6): 921–951, 2006.

[87] J. C. D. L. Reyes and R. Griesse. State-Constrained Optimal Control of the Stationary Navier-Stokes Equations. *J. of Math. Anal. and Appl.*, 343 (1):257–272, 2008.

[88] RoDoBo. *Software Package for Solving Optimization Problems Governed by PDEs.* http://www.rodobo.uni-hd.de.

[89] T. Roubíček and F. Tröltzsch. Lipschitz Stability of Optimal Controls for the Steady-State Navier-Stokes Equations. *Control and Cybernetics*, 32:683–705, 2003.

[90] P. Ruhnau. *Variational Fluid Motion Estimation with Physical Priors*. PhD thesis, Mannheim University, 2006.

[91] P. Ruhnau and C. Schnörr. Optical Stokes Flow Estimation: An Imaging-Based Control Approach. *Exp. in Fluids*, 42:61–78, 2007.

[92] P. Ruhnau, A. Stahl, and C. Schnörr. Variational Estimation of Experimental Fluid Flows with Physics-Based Spatio-Temporal Regularization. *Measurement Science and Technology*, 18(3):755–763, 2007.

[93] M. Schäfer, R. Rannacher, and S. Turek. Evaluation of a CFD Benchmark for Laminar Flows. In *ENUMATH 97, 2nd European Conference on Numerical Mathematics and Advanced Applications*, pages 549–563, 1998.

[94] K. Schepanski, I. Tegen, and A. Macke. Saharan Dust Transport and Deposition Towards the Tropical Northern Atlantic. *Atmos. Chem. Phys.*, 8:16061–16096, 2009.

[95] O. Scherzer. Convergence Rates of Iterated Tikhonov Regularized Solutions of Nonlinear Ill-Posed Problems. *Numerische Mathematik*, 66, 1993.

[96] B. Schweizer. *Lineare Partielle Differentialgleichungen*. Vorlesungsskript, http://www.mathematik.uni-dortmund.de/lsi/schweizer/Skripte/pde-lin.pdf, 2012.

[97] H. Sohr. *The Navier-Stokes Equations, An Elementary Functional Analytic Approach*. Birkhäuser Verlag, 2001.

[98] I. Tegen and I. Fung. Modeling of Mineral Dust in the Atmosphere: Sources, Transport, and Optical Thickness. *Journal of Geophysical Research*, 99:22897–22914, 1994.

[99] R. Temam. *Navier-Stokes Equations*. North-Holland, AMS Chelsea edition, 1977.

[100] F. Tröltzsch. *Optimale Steuerung partieller Differentialgleichungen*. Vieweg, Wiesbaden, 1st edition, 2005.

[101] F. Tröltzsch and D. Wachsmuth. Second-Order Sufficient Optimality Conditions for the Optimal Control of Navier-Stokes Equations. *ESAIM: Control, Optimisation and Calculus of Variations*, 12(1):93–119, 2006.

[102] B. Vexler. *Adaptive Finite Element Methods for Parameter Identification Problems*. PhD-thesis, Heidelberg University, 2004.

[103] J. Vihharev. *Adaptive Methods for Modelling Chemical Transport in the Earth's Atmosphere*. PhD-thesis, Heidelberg University, 2013.

[104] D. Werner. *Funktionalanalysis*. Springer, 5th edition, 2005.

[105] J. Wloka. *Partielle Differentialgleichungen*. Teubner Verlag, 1982.

Acknowledgments

At first I would like to thank my supervisors Prof. Dr. Dr. h. c. Rolf Rannacher and Priv.-Doz. Dr. Christoph Garbe for providing me with the opportunity to work on the presented topic. The topic has an exciting physical background, which was always a good motivation to study and combine very interesting techniques from optimisation, inverse problem theory, numerical analysis and mathematical physics. However, in the beginning there was a whole manifold of possible directions in which to develop this thesis and I am very grateful that my supervisors influenced and sometimes also corrected my course over the years, by fruitful discussions and valuable hints.
Furthermore, I like to thank Dr. Elfriede Friedmann, Michael Geiger and Dr. Jevgeni Vihharev for proofreading this thesis and for the uncountable discussions about my work. Especially Michaels help with the language made it possible for me to write the thesis in English. A very big thank you for this. For the technical support with Gascoigne and RoDoBo, as well as many discussions about optimisation I am indebted to Dr. Thomas Carraro, Dr. Thomas Richter and Dr. Winnifried Wollner.
Moreover, I like to thank all members and alumni of the Numerical Analysis Group in Heidelberg, whom I met during my PhD time, for open doors in case of mathematical or technical questions.
Since I had no clue about image processing in the early phase of my work I am very grateful for the support of the members of Dr. Garbe's Image Processing and Modeling group. A special thank you goes to Dr. Karsten Staack, who had always time for my questions.
I also have to thank Prof. Dr. Guido Kanschat, who gave me the opportunity to work for him as an assistant for his lectures, which was a lot of fun. Also thanks to all members of his Mathematical Methods of Simulations group in Heidelberg.
This work has been supported by the Heidelberg Graduate School of Mathematical Computational Methods for the Sciences (HGS) at the IWR, Heidelberg University.
Beside the beauty of all insights, which I obtained during the last years there were also drawbacks and moments of disappointment as it is usual in life and also in science. In such moments my friends and my family made me keep going on instead of giving up. I will thank them in German:
Andi, Dirk, Moritz, Roman und Tobi vielen Dank für den jährlichen Städteausflug und unsere Freundschaft. Josip und Marie, danke dass ihr mich einmal von 50 Partien im Jahr beim Siedeln gewinnen lasst und die besten Gastgeber der Welt seid. Ein großer Dank geht an alle meine Freunde, die mich in den letzten Jahren immer mal wieder geerdet haben: Ben, Jule und Vanja. Lennart. Stella und dein ganzer Anhang. Christoph P., Sebastian P., David, Lam und Kluge. Die Müslibrüder und -schwestern vom Pubquiz. Meine diversen Mitbewohner(innen) und die Dienstags-Fußballgruppe. Danke Paula für die letzten Jahre, den vielen Spaß und die vielen guten Gespräche, sowohl über Fachliches als auch über Unfug. Schlussendlich danke ich meinen Eltern, Sylvia und Rudolf Klinger, dafür, dass ihr mich bei dieser ganzen "Doktor-Sache" unterstützt habt und immer für mich da seid.